UNIVERSITY OF BIRMINGHAM

Thermodynamic behaviour of supercritical water as working fluid in advanced coal-fired power plants: simulation and design study

by

Álvaro Antonio Gil-García

A thesis submitted to
The University of Birmingham
for the degree of
DOCTOR OF ENGINEERING

School of Chemical Engineering
College of Engineering and Physical Sciences
University of Birmingham
September 2016

ABSTRACT

The UK is facing an energy crisis due to the closure of old nuclear power plants which will not be replaced until Generation III nuclear reactors are built. Coal is a realistic option to fill the gap, although there is a need to use cleaner and efficient technologies as a means to comply with global environmental regulations.

Supercritical coal-fired power is a viable clean coal technology; however the UK National Grid Code is built around conventional power plants, and thus compliance is uncertain. Modelling the thermal behaviour of the supercritical boiler water cycle using computational fluid dynamics is a practical method to approach compliance.

The CFD models developed with the software Comsol Multiphysics were validated and verified using experimental and numerical data, respectively. Subsequently, a test-element representing one pipe from the water wall was scaled-down to match computational requirements, and tested at two different thermal boundary conditions. A strong, forced-convective flow was revealed, with buoyancy effects at the inlet and a considerable influence of thermal acceleration. The sharp changes of the thermo-physical properties were the most influential hydrothermal factor. Heat transfer coefficient peaked near the pipe inlet, and the outlet section showed mild hydro-thermal performance, impaired by the acceleration effects.

To my family

ACKNOWLEDGMENTS

Foremost I would like to thank my supervisor, Dr. Bushra Al-Duri, for giving me the opportunity to undertake this fascinating PhD, for believing in me and offering me not only invaluable knowledge, but also her honest friendship. Also, I would like to give my thanks to Dr. Iain Nicholas Kings, for his support, useful suggestions and feedback both during his period as a member of the project and afterwards. Likewise, I want to thank my colleague Ciprian Negoescu for the good discussions about supercritical heat transfer, and for generously sharing his knowledge with me in Computational Fluid Dynamics.

Thanks to my office mates and good friends Kostas and Alberto, who always are more than happy to give up their time to help me and deal with my stressed moods.

Moreover, I want to thank my landlady and friend Pauline Naughton. Without her I would not have been able to stay in the UK long enough to complete the thesis.

Thanks to my family for their support in the distance, as well as my best friends from Spain, Juan and Eva, for being always there.

And finally, thanks to Gaia for staying always close, supporting me and cheering me up every time.

TABLE OF CONTENTS

LIST OF FIGURES

LIST OF TABLES

1. Introduction

1.1 Background

In 2015, approximately 30% of the total energy employed in the UK to produce electricity came from gas, 25% from renewables, 20% from nuclear and another 20% from coal (Johnston, 2015). However, the UK's power generation sector is already in transition from a well-balanced mix of coal, nuclear and gas-fired power stations to one in which the old nuclear and coal-fired stations will be progressively retired in exchange of new generation nuclear power plants (NPPs) by 2030, and renewable energies by 2050.

In order to reduce the dependence on high-carbon electricity and comply with the new air quality regulations, the UK government plans on decommissioning all the coal-fired power plants (CFPPs) by 2025 (Johnston, 2015). Similarly, all the 15 existing Generation II NPPs currently operating in the UK are expected to be shut down in the period between 2023 and 2035 as they reach their natural end-of-life (World Nuclear Association, 2016).

As a result, by 2020 the UK is expected to face the risk of electrical power shortage before the arrival of new nuclear plants, known as the energy gap (Department of Energy & Climate Change, 2011), represented in Figure 1.1.

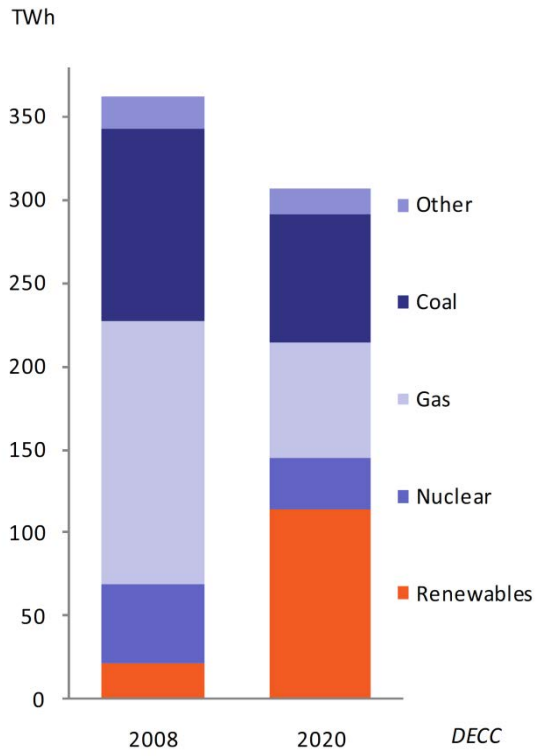

Figure 1.1 Electricity outputs in UK reflecting power gap between 2008 and forecasts for 2020 (Department of Energy & Climate Change, 2011)

In 2015, in order to bridge the energy gap resulting from shutting down the CFPPs and NPPs, the UK government directed their energy policy towards gas-fired stations and new Generation III NPPs from the mid-2020s on (World Nuclear Association, Nuclear AMRC, 2016). However, relying more on gas power plants would increase the UK dependence on an external source from the North Sea that is being exhausted (Bugge *et al.,* 2006) and thus there is only one gas plant under construction (Johnston, 2015). On the other hand, renewable energies implying technologies such as hydrogen fuel cells, biofuels, slow moving water or biomass are expected to increase their presence in power generation. However, they are not capable of generating enough electricity to fill the predicted gap.

(a)

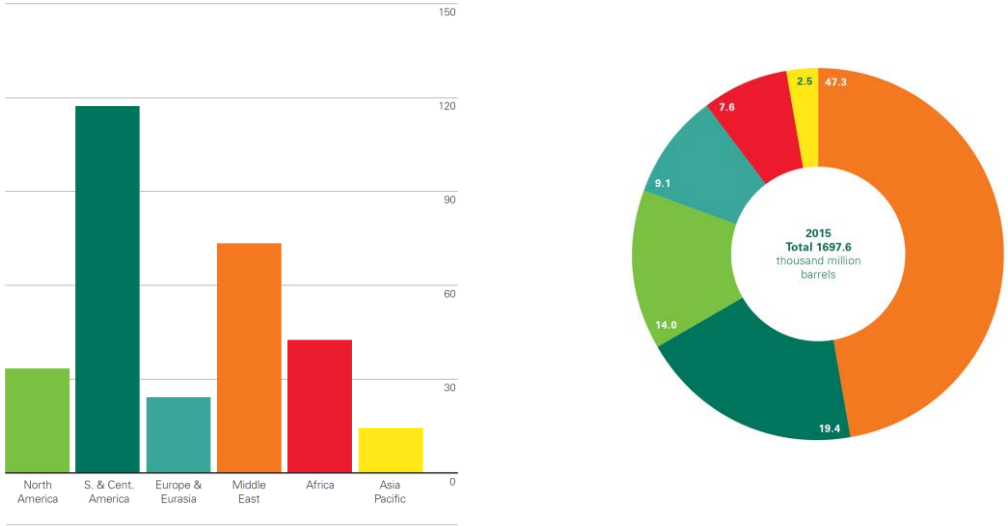

(b)

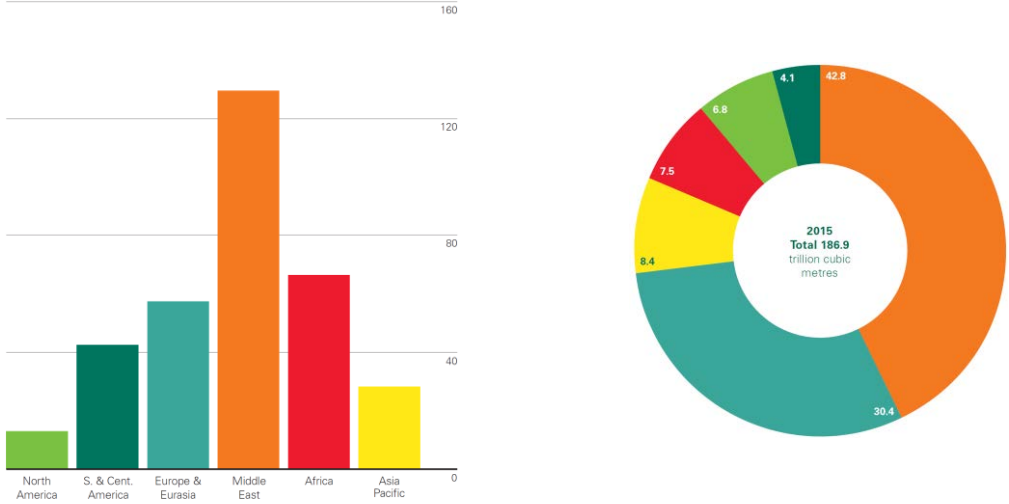

(c)

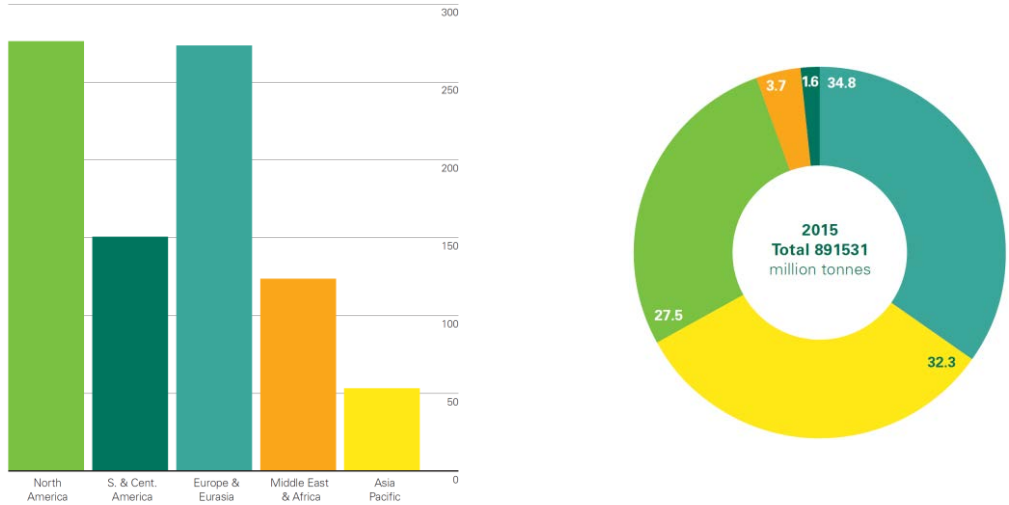

Figure 1.2 Bar charts showing reserves-to-production (R/P) ratios and pie charts showing global distributions of reserves, in 2015, for (a) oil, (b) natural gas and (c) coal (BP Statistical Review of World Energy, 2016)

Alternatively and as seen in Figure 1.2c, coal is the most abundant fossil fuel in the world in terms of reserve-to-production ratio, and also geographically spread (McMullan *et al.,* 2001). More specifically, Europe has one of the largest coal reserves (Dale, 2016) and due to its low price coal has normally been the preferred fuel (Bugge *et al.,* 2006).

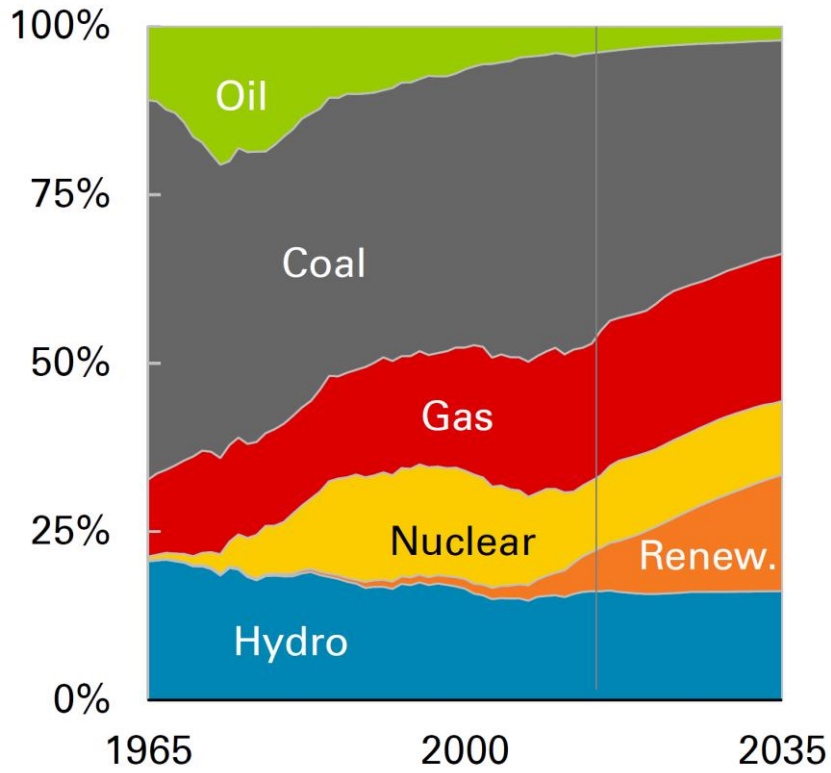

Figure 1.3 Primary inputs used for power generation in the world (BP Energy Outlook, 2016)

As a consequence, it is expected that coal will still play an important role in the future for the electricity generation (see Figure 1.3 and Figure 1.4) and therefore investment in coal technologies will be of high importance (Rukes & Taud, 2004). Coal-fired power generation is a realistic option, as a means to compensate the generation gap for the short-term development strategy in the UK.

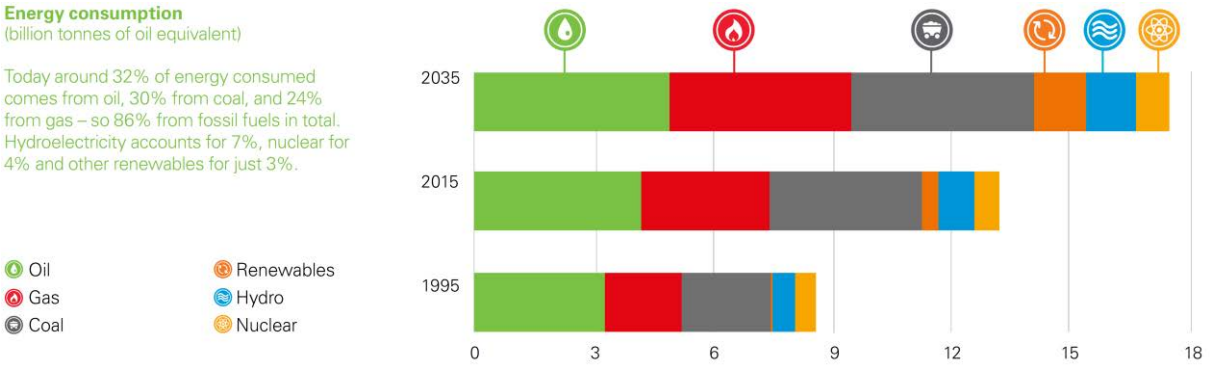

Figure 1.4 Energy consumption forecast (billion tonnes of oil equivalent) from different resources (BP Energy Outlook, 2015)

However, there is a series of concerns nowadays about the environmental impact of fossil fuel consumption, particularly CO_2 emissions and global warming. Thus, the UK government has approached a series of steps to decrease the greenhouse emissions and committed to reduce emissions by at least 80% in 2050 from 1990 levels (The committee on climate change, 2008). Consequently, cleaner and more efficient coal technologies must be established. As seen in Section 1.3, conventional CFPPs have low thermal efficiencies, producing high C flue gas and toxic emissions with an adverse environmental impact. Nevertheless, there are several clean coal technologies (CCTs) capable of optimising the efficiency of the current CFPPs in the UK and thus avoid their shut-down by 2025. The most popular CCTs are:

- Integrated gasification and combined cycle: a thermally efficient power technology, as the condensation stage is replaced by a heat exchange process, avoiding energy losses. It also allows using biomass as fuel.
- Carbon Capture and Sequestration (CCS): the CO_2 emissions from the combustion process are pressurised in solid or liquid form, and buried in cavities underground to reduce the impact on climate warming.

- Pressurized Fluidized Bed Combustion: a sand bed is fluidised inside the furnace, as a means to facilitate a homogeneous heat transfer and increase efficiency.
- Supercritical coal-fired power plants (SCCFPPs): as further explained in Section 1.3, the main feature in SCCFPPs is that the operating pressure is increased above the critical value for water (221 bar). Considering that the operating temperature is also beyond the critical point (374°C), structural simplifications in the power plant are possible, while the overall thermal efficiency also increases due to favourable variations of the thermophysical properties of water.

SCCFPP technology was considered a feasible choice for research in the present thesis due to a series of technological factors:

- While little has been developed about most of the CCTs, SCCFPPs are well-known since the 50s. In fact, they are already established in other countries such as China.
- All the knowledge gathered with SCCFPPs can be applied on the new Generation IV NPPs to be installed by 2050, as some of these nuclear reactors use SC water as coolant.
- SCCFPPs could be integrated with CCS systems.
- SCCFPPs also offer the possibility to co-fire biomass, approaching a renewable technology (Bugge *et al.,* 2006).

1.2 Conventional CFPPs

Boilers are pressurised vessels meant to produce steam at a minimum pressure of 2 bar and at a temperature ranging from saturation point to 620°C approximately (Rayaprolu, 2009). Steam is produced in two steps: first, converting the chemical energy of a fuel through combustion into radiation and heat energy to the flue gases, and second transferring this energy to the water/steam cycle by using several heat exchangers placed throughout the flue gases path. As seen in Figure 1.5, in conventional CFPPs utility boilers are used to generate steam and transform its energy into power to feed the electricity grid. Water at subcritical pressures (below 221 bar) and combustion gases flow in two different paths while exchanging heat at the same time.

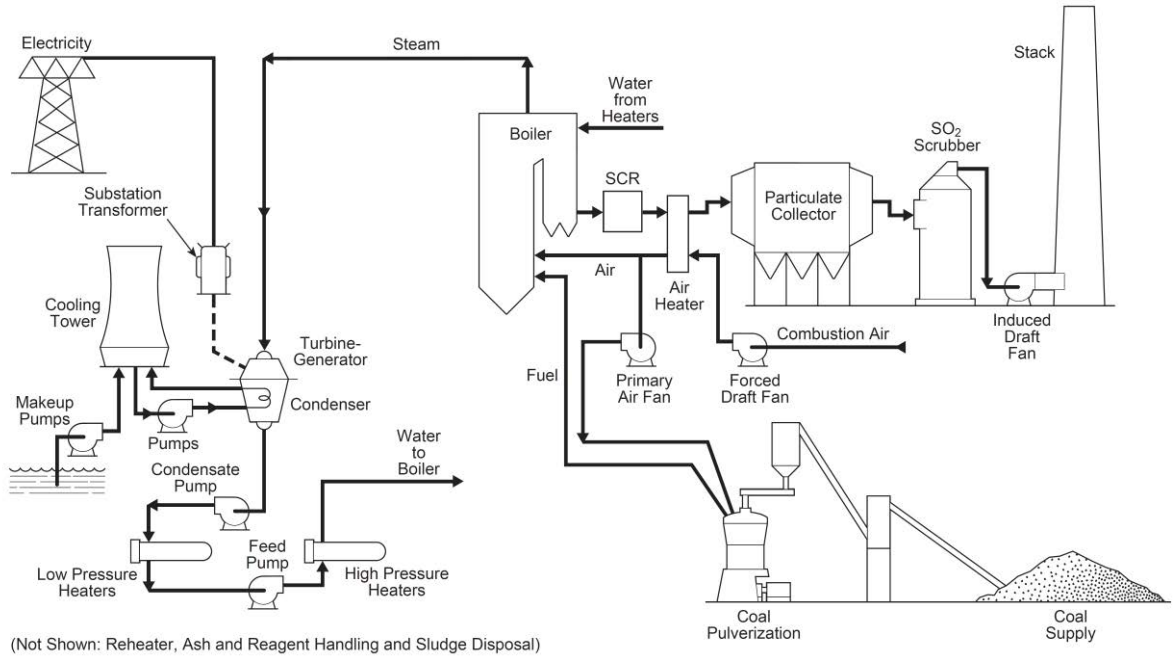

Figure 1.5 Schematic of a CFPP for power generation (Stultz *et al.*, 2005)

On the combustion side of Figure 1.5 (inside the boiler and processes depicted to the right side of the boiler), coal and air react exothermically in excess at the firing system in a chamber inside the boiler, which is the furnace. This is the hottest section of the boiler and most of the heat generated is radiant. Additionally, the chamber provides a spacious volume which increases the residence time of gases and particles, allowing (1) total consumption of coal due to the excess air, (2) reduction of the entrainment of solid particles with the rising hot gases and (3) a longer exposure of the hot gases to the heat exchangers for optimal heat transfer. The hot flue gases rise and leave the furnace passing through a series of heat exchangers as a means to transfer as much heat as possible to the hydrothermal side. When leaving the boiler tower, the flue gases are still useful to preheat the inlet combustion air and thus increase the coal combustion efficiency. Eventually, when they have transferred most of their heat, they are passed through a series of collectors, filters and scrubbers in order to reduce the particle content and the toxic potential of the emissions (CO, NO_x, SO_x, etc.) by the time they leave the stack.

The hydrothermal side of Figure 1.5 (inside the boiler and processes depicted to the left side of the boiler), also called water cycle, is composed of a pressurised vessel (drum) inside the boiler where saturated water and the generated steam are constantly derived to different paths, and a series of heat exchangers inside the boiler arranged in a fashion that maximises the absorption of radiation heat from the coal combustion and the convection heat from the flue gases produced (Rayaprolu, 2009). Drum boilers employ natural circulation, using the density differences of the

fluid as driving force, or forced circulation if the flow is facilitated with pumps (see Figure 1.6).

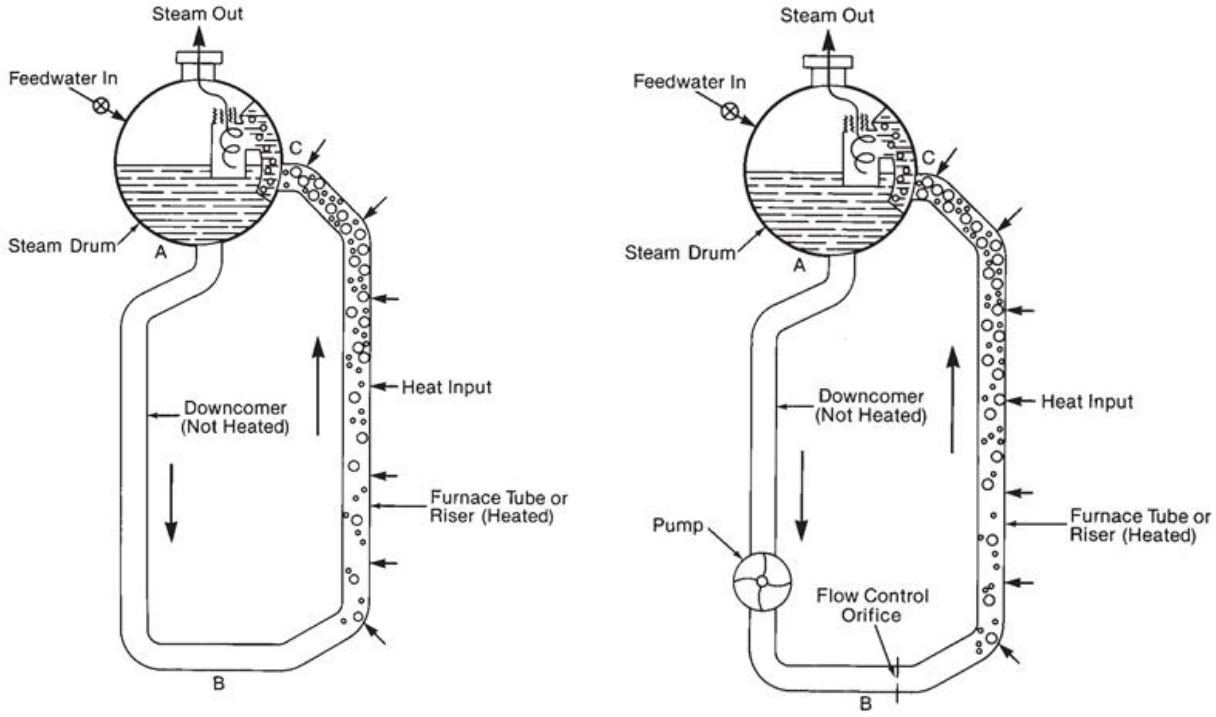

Figure 1.6 Natural (a) and forced (b) circulation in drum boilers (Stultz *et al.*, 2005)

From the drum, saturated water is naturally recirculated to the evaporator exchangers located below, where the water flow captures mostly radiant energy from the combustion as latent heat for the phase change, producing a mixture with steam. The water flow must achieve high velocities to maintain the tubes wet and thus avoid the formation of a steam layer between the pipe and the bulk of the flow, impairing heat transfer. This phenomenon is called departure from nucleate boiling (DNB), critical heat flux (CHF), dryout or boiling crisis (Stultz *et al*., 2005). There are two kinds of evaporator exchangers, located in different regions of the furnace:

- The water-cooled wall: also water wall pipes, it is composed of a series of pipes attached to the wall of the furnace structure, hence its name. They are closest to the firing system, thus absorbing radiant heat for the most part.
- The boiler bank: it is an arrangement of hanging tubes filling the furnace room and connecting the drum on the top with a smaller drum or header at the bottom of the furnace (mud drum). They are located facing the first waves of hot gases once they start rising, so they absorb heat mainly by convection.

Leaving the drum, the saturated steam generated is led to the superheater exchangers (SH) located downstream the furnace (see Figure 1.7), absorbing energy from the flue gases through convection in order to increase the steam temperature before entering the high-pressure (HP) turbines depicted in Figure 1.5. There, superheated steam expands and triggers the rotation of the turbine blades, thus transferring thermal energy into mechanical energy. At the same time, the turbines are connected by rotating shafts to power generators that convert the mechanical energy to electricity, which is delivered to the national grid.

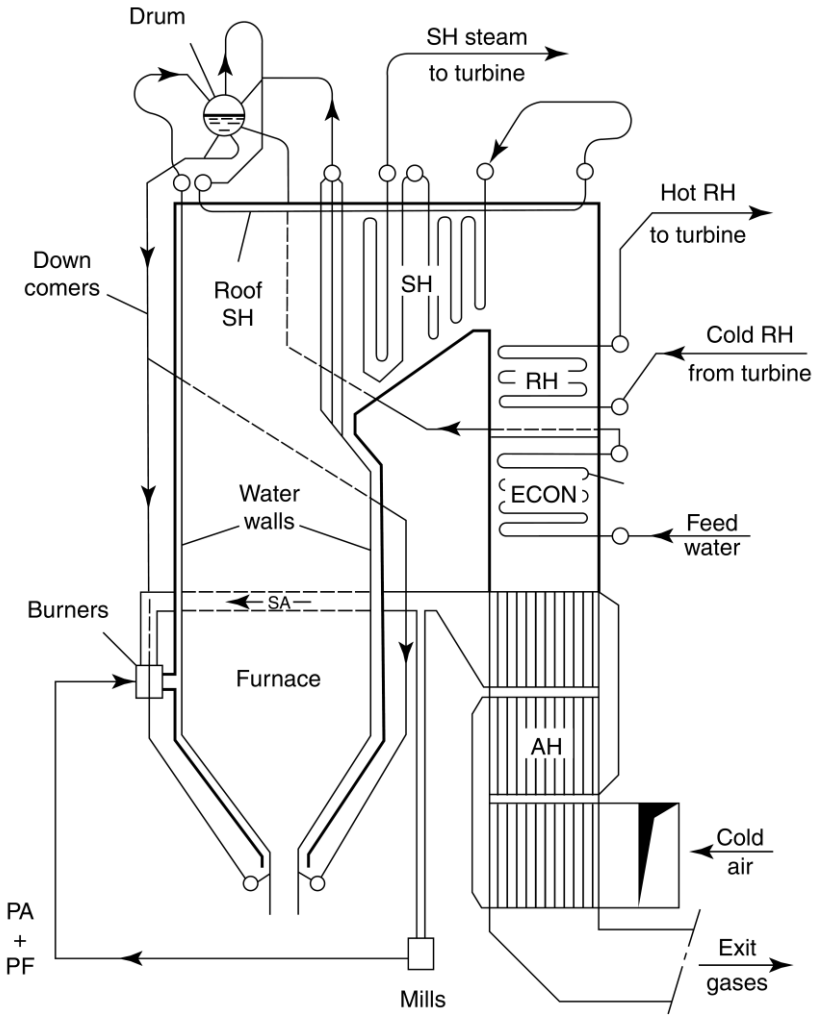

Figure 1.7 Drum-type boiler showing the heat traps (Rayaprolu, 2009)

As a means to increase the boiler efficiency, the reheater exchangers (RH) receive the steam returned from the HP turbines and deliver reheated steam to the low-pressure (LP) turbines. Cooled and depressurised steam leaves the LP turbines, and it is condensed to water using cooling towers as shown in Figure 1.5. This is an inefficient step that wastes almost 50% of the heat produced in latent heat losses to the external cooling water (Rayaprolu, 2009). This is why the efficiency of subcritical power plants makes only around 40% of the net calorific value of coal, while in cogeneration power plants where the depressurised outlet steam is used as heat

source in surrounded processes requiring heat (instead of being condensed), the efficiency increases to 85%.

The subcooled condensed water obtained is recirculated to the boiler as new feed water. At this stage, the cycle efficiency can be increased by bleeding some steam from the turbines to preheat the recycled water, thus reducing energy losses from the condensation stage. As seen in Figure 1.8a, the feed water from the condensation stage (4-5) is pressurised and preheated (5-9) using the turbine bleeds. In this process, steam is firstly bled from the LP turbines (10) to transfer its latent heat to the recycled condensate. Downstream, the procedure is repeated by bleeding steam from turbines at higher pressure (11) to preheat feed water at higher temperatures. Before feed water enters the boiler drum, receives some heat transferred from the flue gases downstream the RHs at the economiser (ECON), to cool the gases down before they leave the boiler and pass through the cleaning section and stack.

(a)

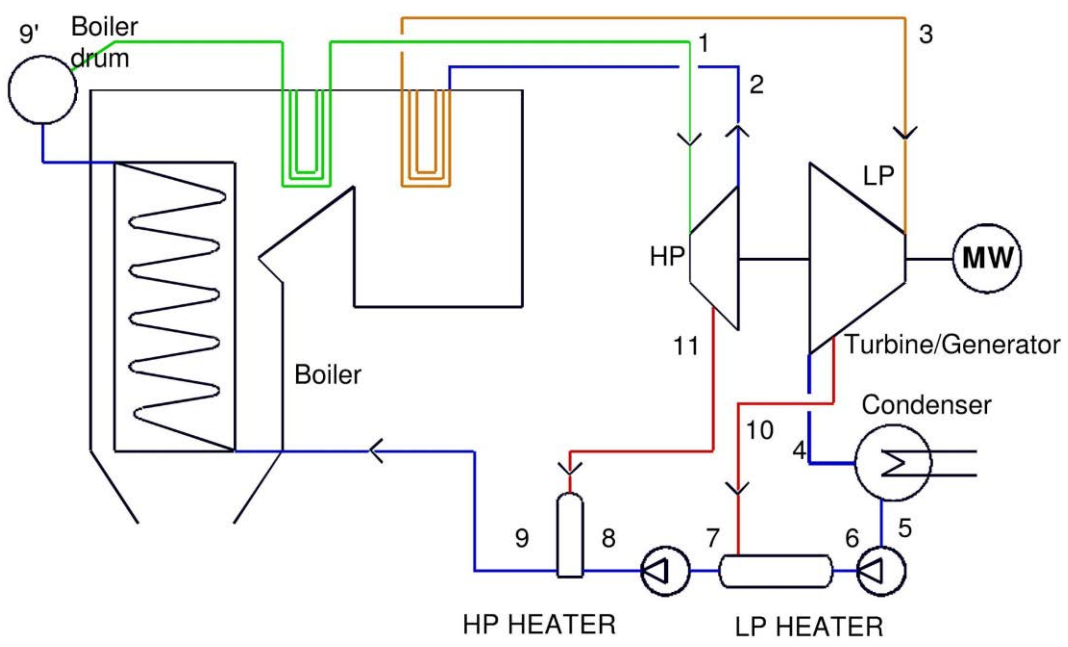

(b)

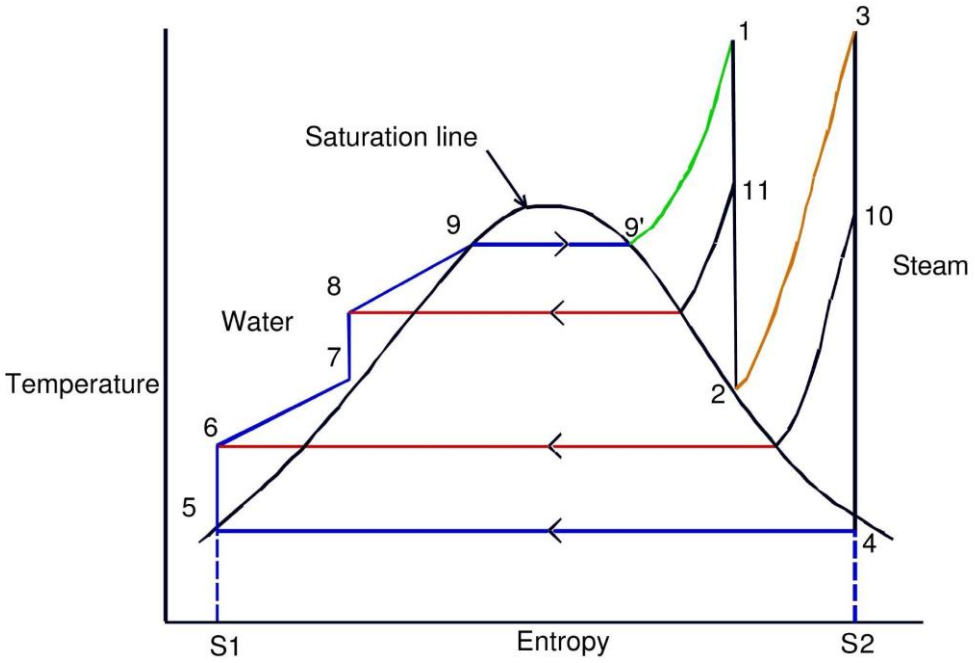

Figure 1.8 Schematic of a conventional CFPP (a) and the corresponding T-S diagram (b)

Saturated water enters the boiler drum and changes phase isothermally using the latent heat (9-9'). After the phase change, saturated steam leaves the drum and increases its temperature in the SH (9'-1). SH steam is expanded in the HP turbine, decreasing its pressure and temperature isentropically to be afterwards redirected to the boiler (1-2) and a small amount is bled to the HP preheaters (1-11). The recirculated steam enters the RH in order to increase temperature again at a lower pressure (2-3) and is eventually expanded in the LP turbine, where a portion is bled to the LP preheaters (3-10) and most of the flow is condensed to repeat the cycle (3-4). The overall steam cycle performed in the power plant is also called the Rankine cycle, and it is presented in Figure 1.8b using a temperature-entropy (T-S) diagram.

1.3 Supercritical coal-fired power plants

1.3.1 SC fluids in power engineering

The SC state of a fluid is the thermodynamic condition where the distinction between the gas and liquid phase disappears due to the rearrangement of the fluid molecular bonds. Thus, the thermophysical properties of the fluid achieve values between the two phases. A fluid becomes SC when its temperature and pressure surpass their respective critical points, which are particular to every fluid. Near the critical point, thermophysical properties such as density or heat capacity, experience large variations, while in the vicinity of pseudocritical (PSC) points, shown in the phase diagram in Figure 1.9 as an extrapolation of the saturation line, these changes become less pronounced with an increase in pressure (Pioro, 2014).

Also, the SC water cycle is represented in Figure 1.9. Water leaving the condenser is recycled in the boiler as feed water (4-5), being preheated below the critical temperature (373.95°C) and pressurised above the critical value (22.064 MPa); a phase defined as compressed water (5-6). Inside the boiler, compressed water is heated and despite achieving critical temperature, no apparent thermophysical changes occur until the PSC line is surpassed (6-1). During the HP turbine expansion (1-2), SC water decreases its pressure below the critical point, a state defined as superheated steam. Afterwards, it is redirected to the boiler RH as a means to isobarically increase its temperature again (2-3), and led to the LP turbine where the

fluid expands, decreasing its temperature below the critical point to become steam (3-4). After the expansion, the remaining steam is condensed and the cycle repeats.

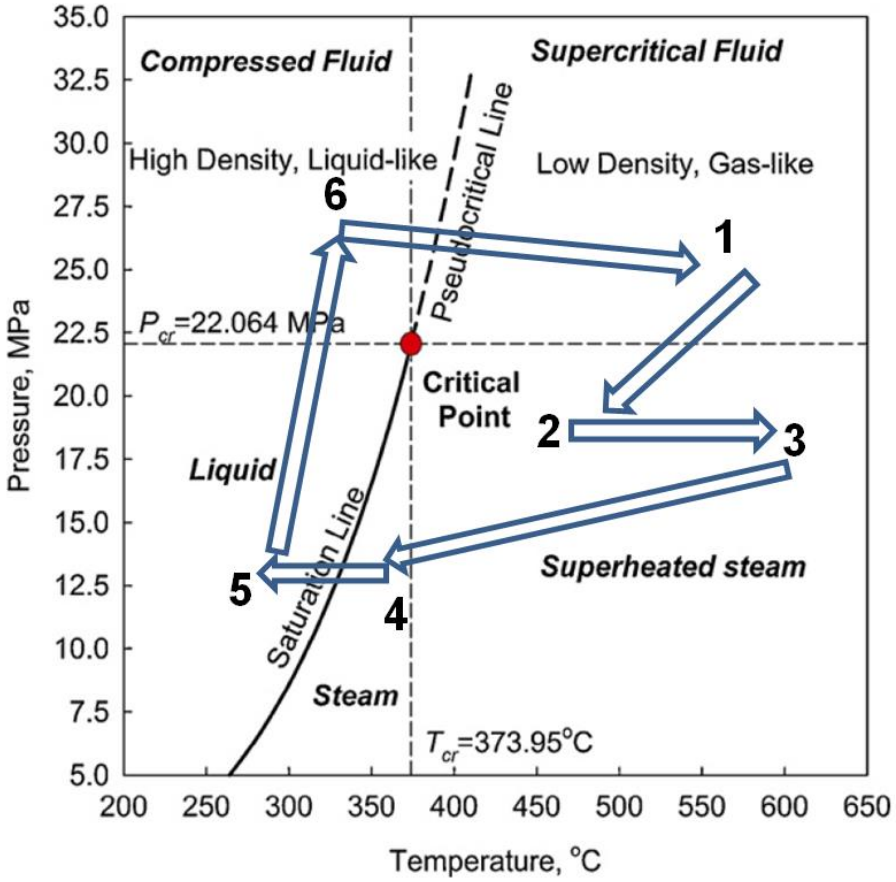

Figure 1.9 Phase diagram of water and SC water cycle. Adapted from Pioro, 2014

The role of a thermal fluid in a power plant is to transfer the energy contained in the fuel (primary energy source) to the turbine. Water is a good thermal fluid (secondary energy source), because as a liquid has high values of heat capacity to absorb and carry energy, and also good thermal conductivity to increase the heat transfer rate. Moreover, as steam displays beneficial hydrodynamic properties, such as a small density to be compressed and stored, or a lower viscosity to promote turbulence and homogenise temperature profiles.

Nevertheless, water does not experience phase change at SC pressures like subcritical water when it reaches the boiling point. Instead, when the water temperature approaches the PSC value, the thermophysical properties become very sensitive to temperature changes and experience large variations to become closer to a gas-like fluid. This transition is similar to the evaporation phenomenon at subcritical conditions, but in absence of phase change (Stultz *et al*., 2005). Due to this combination of good thermodynamic performance inherent in water and the good hydrodynamic features related to steam, SC water is a superior medium in heat cycles.

In Figure 1.10, the variations of several thermophysical properties of water with temperature are shown at critical and several PSC pressures. In Figure 1.10a it is observed that the fluid density decreases dramatically during the PSC transition. Therefore, SC water becomes highly compressible without changing phase, enabling the storage of more water in the same volume. The performance of dynamic viscosity is depicted in Figure 1.10b, which also experiences a sharp decrease. As a consequence higher turbulence is triggered, increasing the Reynolds numbers considerably and improving heat transfer.

Similarly, heat capacity and thermal conductivity profiles are depicted in Figure 1.10c and Figure 1.10d, respectively. Both properties increase significantly near the critical point due to the molecular reconfiguration of water as an intermediate phase between liquid and gas; however only the heat capacity profile reveals humps near

the PSC points. In the case of heat capacity, this feature allows the fluid to absorb more heat at a given temperature (good heat carrier). On the other hand, thermal conductivity values increase only near the critical point, and so heat transfer quality. At higher values of temperature, the thermal conductivity drops regardless of the working pressure. However, from 500°C on its value slightly commences to recover.

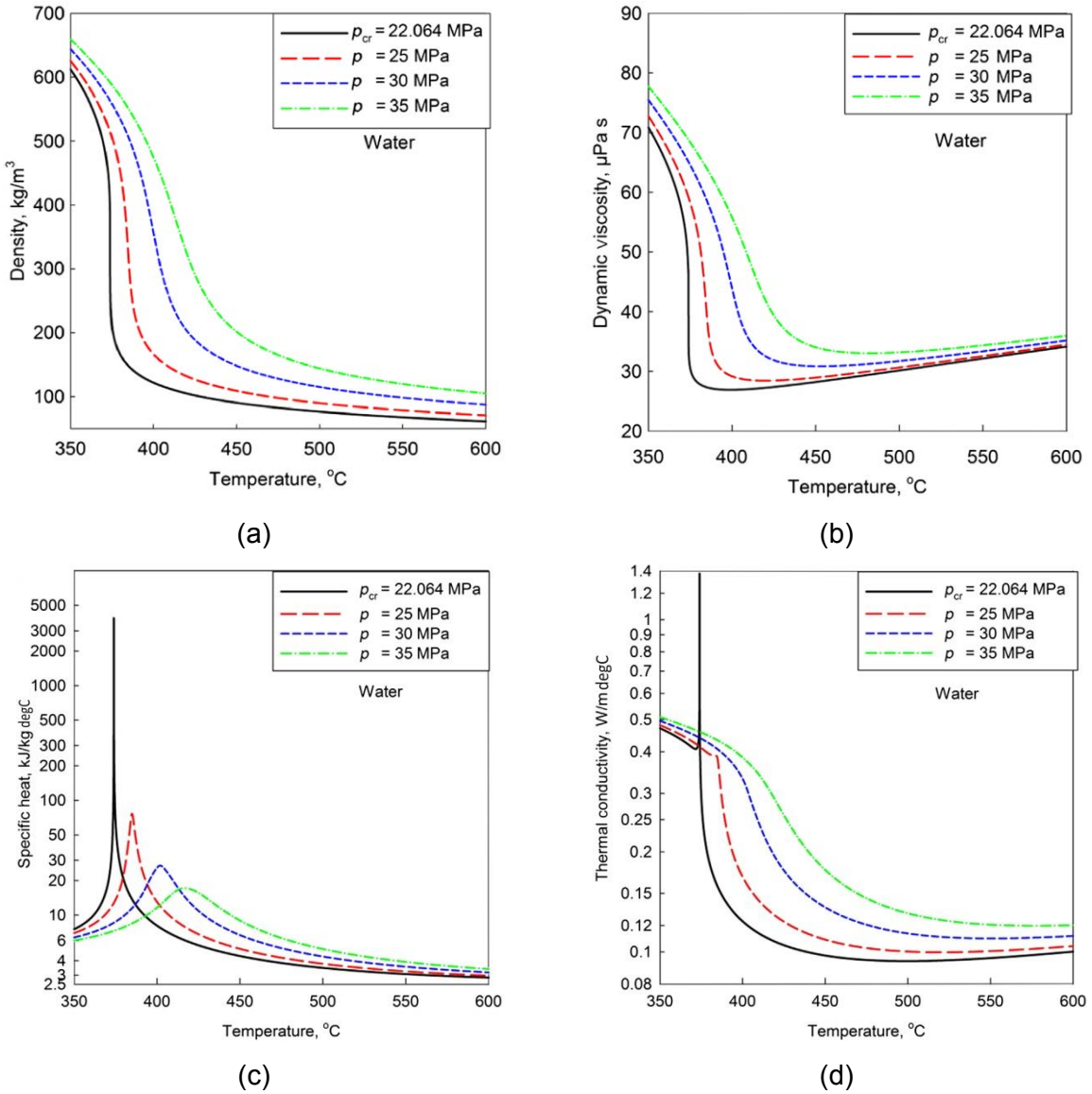

Figure 1.10 Thermophysical properties of water at critical and PSC pressures; (a) density, (b) dynamic viscosity, (c) specific heat and (d) thermal conductivity (adapted from Pioro, 2014)

1.3.2 Operational advantages of SCCFPPs

In SCCFPPs, the conventional boiler containing water at subcritical pressure is replaced by other at SC pressures, as described in Section 1.3.1. SC water has unique properties and favourable heat transfer behaviour. Thus, boilers operating at SC pressures offer a series of advantages, such as plant simplifications, a better safety and economy, and higher thermal efficiencies.

When water at SC pressure enters the boiler its temperature increases. At a certain temperature, the PSC point is reached. As defined in Section 1.3.1, the PSC points are an extrapolation of the saturation line in the SC region of the water phase diagram where the thermophysical properties progressively change towards magnitudes between a liquid and a gas without phase change. As a consequence, the drum and boiler bank are no longer required. In these conditions, the feed water pump induces a strong forced circulation and thus natural recirculation is no longer necessary, as seen in Figure 1.11. Instead, the flow passes only once through the system, hence their name once-through (OT) boilers. This configuration allows additional advantages, such as a considerable reduction in the boiler start-up times. On the other hand, the quality of water must be very high in OT boilers due to the lack of water blowdown (water intentionally wasted from the boiler) as a means to avoid build-up of impurities and eventually corrosion (Rayaprolu, 2009).

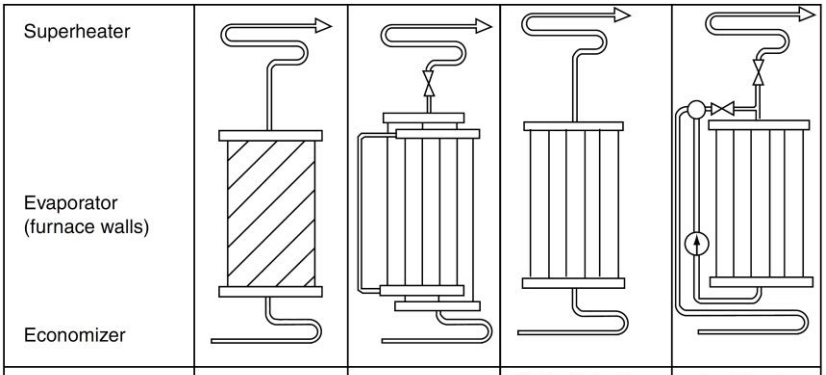

Principle	Benson	Universal pressure	OT (only for large capacity)	Combined circulation
Licensor/ manufacturer	Siemens	B&W (USA)	Alstom	Alstom
Each evaporator tube through all heating zones	Yes	No	No	No
Sliding pressure	Yes	No	Yes	No

Figure 1.11 SC circulation systems (Rayaprolu, 2009)

Moreover, SC boilers offer better safety and economy, because when the electricity demand decreases they do not need to operate at full capacity. Drum-type boilers normally produce steam at constant pressure (load-based), and thus they rely on throttle valves to vent steam out of the system in order to lower the inlet pressure at the turbine when the load demand decreases, which is a thermal waste. SC boilers, on the other hand, operate at variable (sliding) pressure, as seen in Figure 1.12. The steam flow is controlled by regulating the flow pressure provided by the feed pumps, instead of using the turbine throttle valves. This allows part-load performance, which additionally reduces thermal stress. If sliding pressure mode was used in drum-type boilers, the water levels inside the drum would be dangerously modified; and similarly sudden pressure changes could even change the boiling point of water, triggering sharp temperature profiles and thermal stress (Rayaprolu, 2009).

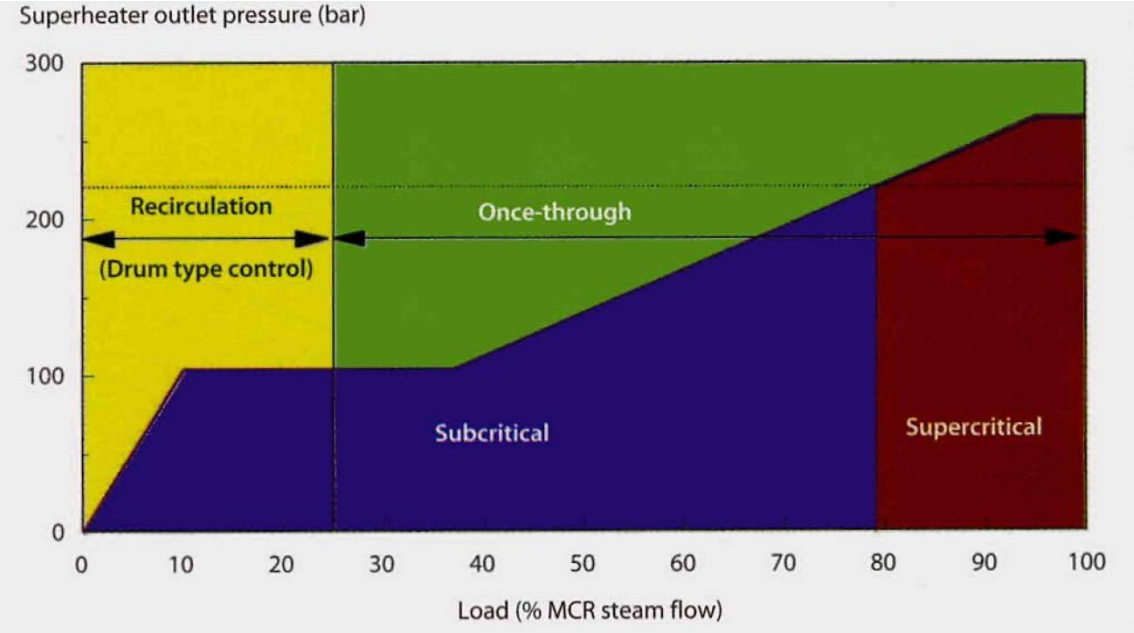

Figure 1.12 Sliding-pressure configuration in OT boilers (Goidich *et al.*, 2012)

As seen in the SC Rankine cycle in Figure 1.13b, feed water enters the boiler at SC pressures (9-1), thus avoiding the phase change as progressively increases the temperature above the subcritical value. As a consequence, the inlet temperature and pressure values of steam in the HP (1-2) and LP (3-4) turbines are higher than those in a conventional plant, as seen in Figure 1.13c. If this steam is expanded in the turbines similarly until the condensation point, the extent of energy extracted in the turbines will increase compared to a conventional plant, and thus the thermal efficiency of the plant will be higher. At the condensation stage, losses in latent heat are the same as at subcritical conditions; however the turbines are more efficient if the pressure values increase. Moreover, higher operational pressures provide the opportunity to include a double RH, further increasing the overall efficiency.

(a)

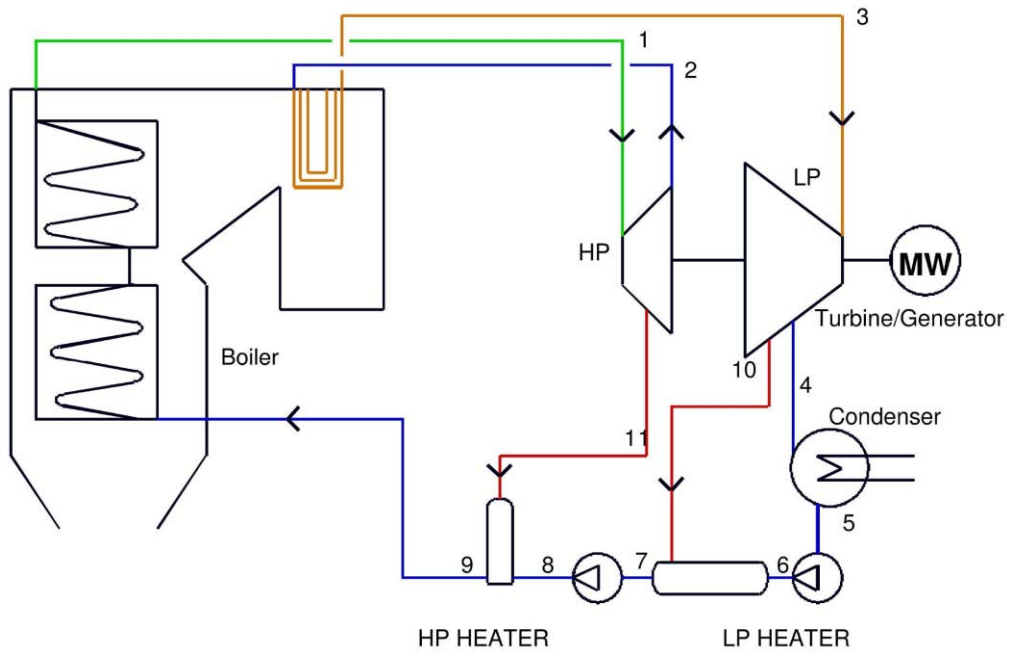
1
2
3
LP
HP
MW
Turbine/Generator
Boiler
10
4
Condenser
11
5
9
8
7
6
HP HEATER
LP HEATER

(b)

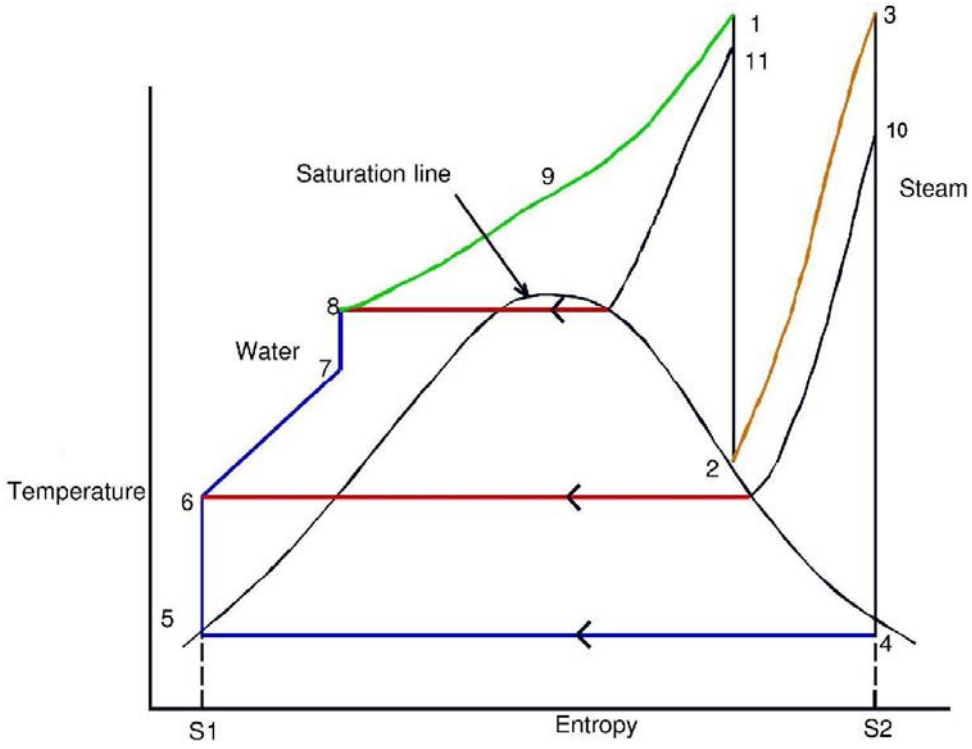
1
11
3
10
Steam
Saturation line
9
8
Water
7
2
Temperature
6
5
4
S1
Entropy
S2

(c)

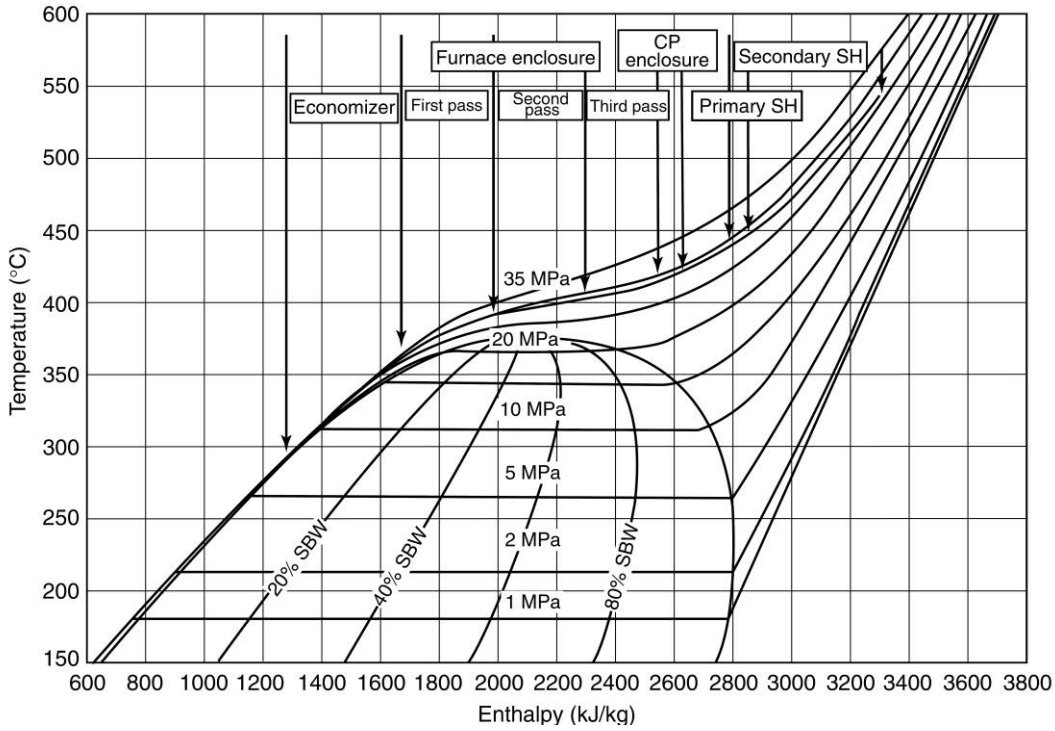

Figure 1.13 Schematic of a SCCFPP (a), the corresponding T-S diagram (b) and T-S diagram of a 1300 MW SC boiler showing operational pressures (Rayaprolu, 2009, c)

Subsequently, at SC conditions around 250 bar the thermal efficiency in the boiler increases to 43% (see Figure 1.14), compared to subcritical top efficiencies of around 37%. Increased efficiency involves the production of the same electricity as a conventional plant while burning less coal, thus reducing carbon emissions (Rayaprolu, 2009). Similarly in NPPs, SC boilers increase the efficiency from 33-35% to values approaching 45-50% (Pioro *et al.,* 2004). On the other hand, due to the high working pressures in SC boilers, the materials employed on the water cycle must be capable to resist the consequential mechanical and thermal stresses as a means to grant safety in the process.

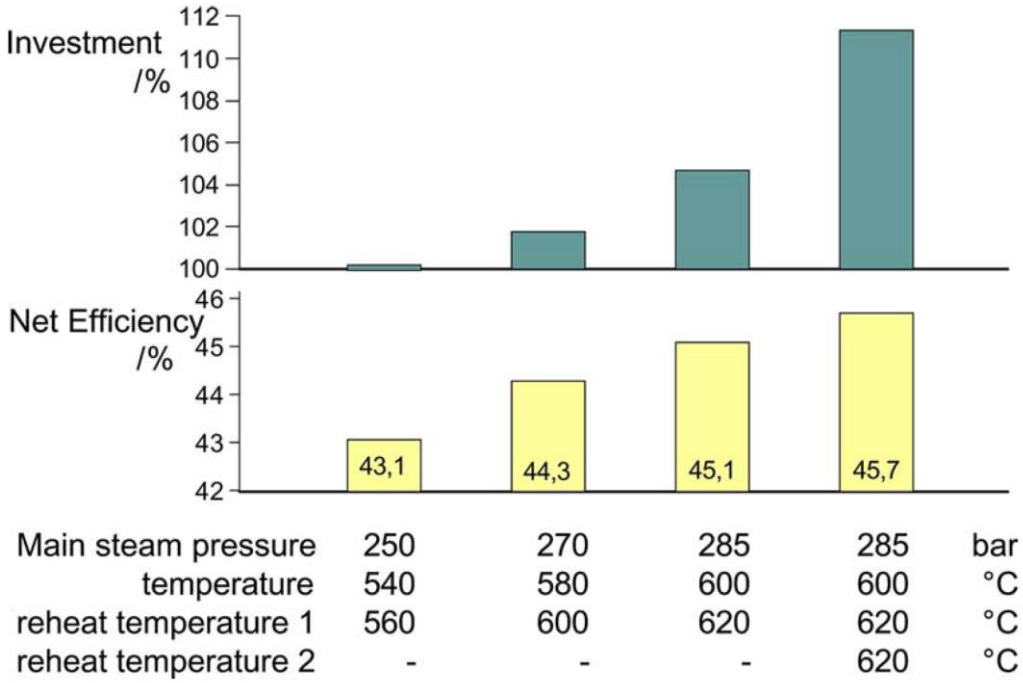

Figure 1.14 Effect of steam conditions on efficiency and investment of SCCFPPs (Rukes & Taud, 2004)

1.3.3 The water wall pipes in SC boilers

The water-cooled wall pipes, located surrounding the furnace chamber of SC boilers, is the section of the water cycle where pressurised water undergoes transition from subcritical to SC temperatures, triggering the onset of large thermophysical property variations along the flow as described in Section 1.3.1. These phenomena allow to potentially improving the heat transfer behaviour of the system. Depending on how water wall pipes are configured, the most popular furnaces are:

- Vertical-tube water wall furnaces: pipes are helically ribbed on the inside to enhance heat transfer, thus high heat fluxes can be applied while combined with low water mass fluxes. The two most common ribbed pipes are the single-lead

ribbed and the multi-lead ribbed (see Figure 1.15). The first one has a smaller diameter, which is better for OT boilers (Stultz *et al*., 2005). The most popular boiler within this category operates at sliding pressure conditions for low mass fluxes of fluid in two passes of hot gases (Kaneko *et al.*, 1996). As seen in Figure 1.16, ribbed pipes are implemented only near the combustion zone due to their cost, and mostly in SC boilers.

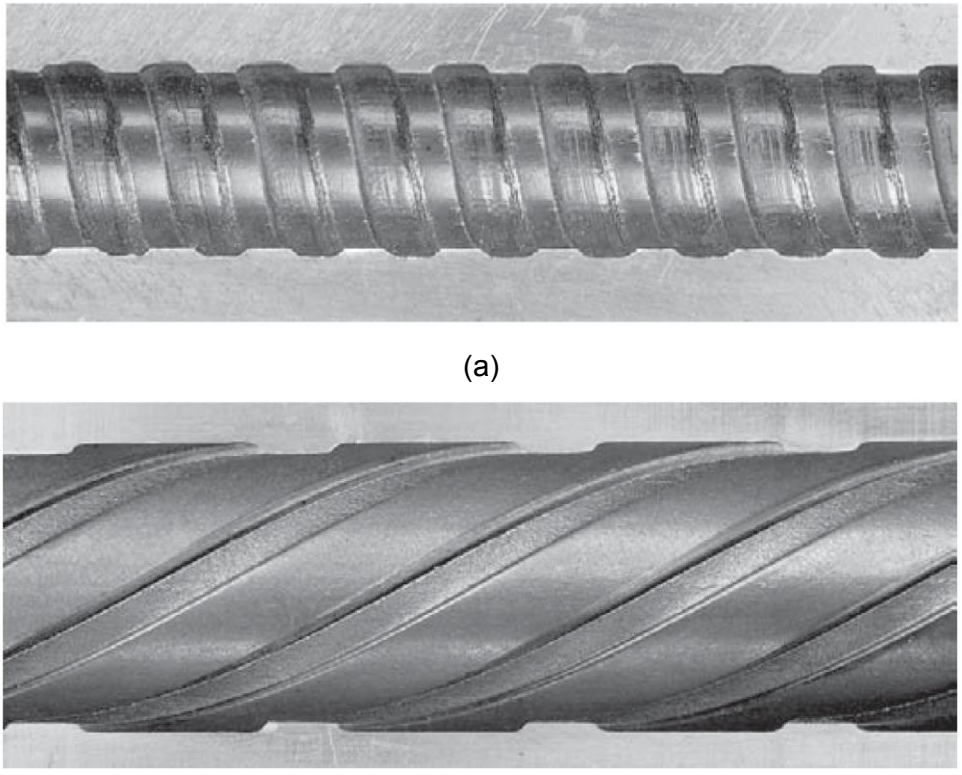

(a)

(b)

Figure 1.15 Single-lead ribbed tube (a) and multi-lead ribbed tube (b) (Stultz *et al.*, 2005)

- Upwardly spiral-wound water wall furnaces: these boilers also operate at sliding pressure conditions, and are specific for high mass fluxes of water. At the lower section of the furnace, where combustion takes place and heat flux is much higher, water wall pipes are inclined an angle between 10 and 30°, offering a

higher mass flow surface (see Figure 1.16). On the upper part of the furnace the water wall is vertical, as the heat flux is much smaller. The transition between the two sections is facilitated by placing mixing headers in-between as a means to homogenise temperatures. This arrangement is more complicated to construct, as inclined tubes are tougher to support and require extra measures that increase the cost. Pipes are normally smooth, although some new designs include ribbed pipes in the spiral section (Penati *et al.*, 2011). Because of the cost and complexity of this configuration, vertical-tube water wall furnaces using rifled tubes and low mass fluxes are preferred for the future of SCCFPPs (Rayaprolu, 2009).

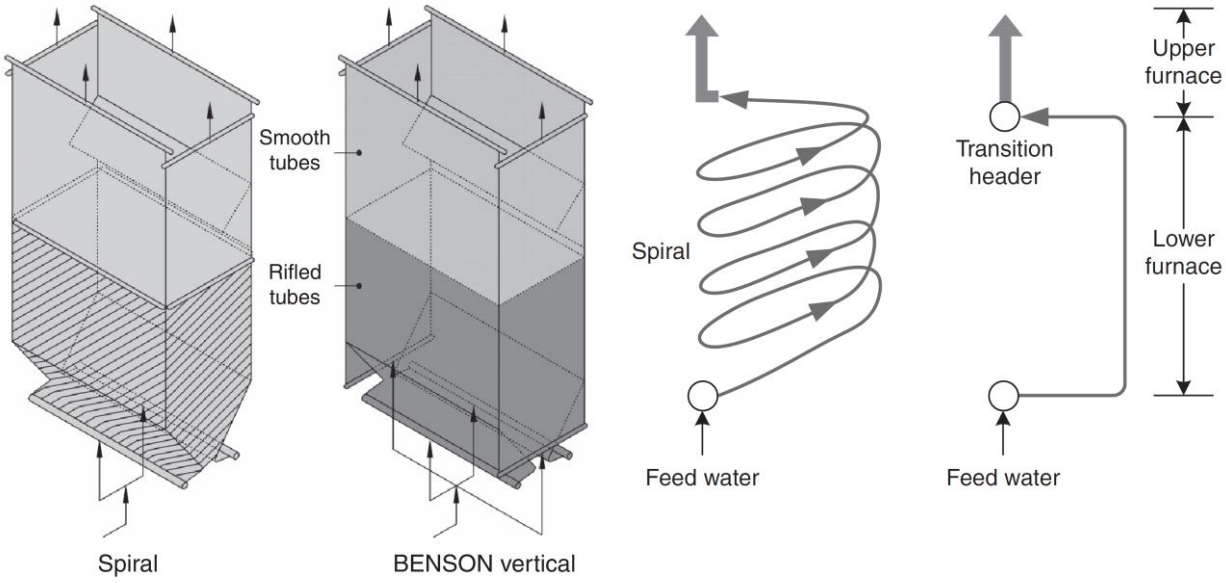

Figure 1.16 Spiral and vertical water-cooled wall configurations (Zhang *et al.*, 2013)

1.4 Compliance of SCCFPPs with the National Grid Code

Despite their numerous advantages, one of the main drawbacks of SCCFPPs with respect to subcritical plants is the lack of capacity to store energy that the drum in a conventional boiler would provide. By operating at high pressures in OT circulation the cycle efficiency increases; however energy storage is necessary for operational flexibility and rapid frequency responses in power generation.

The National Grid Code (NGC) imposes the Electricity Supply Regulations in every country, and thus power plants must comply to deliver the power dictated by pre-established dynamic frequency responses (DFRs; Nicholls, 2008). In the UK, SCCFPPs are more challenging to implement due to compliance issues with the NGC, which is more demanding than other European codes. The UK, as an isolated island, possesses a relatively small electricity network. Sudden peaks in load (electricity demand) can be sorted by switching off high power-consuming industries, such as steelworks. However, power plant DFRs must be more efficient as a means to avoid power outage or even blackouts if one or several power plants failed at providing the expected power to the grid (Fink, 1978).

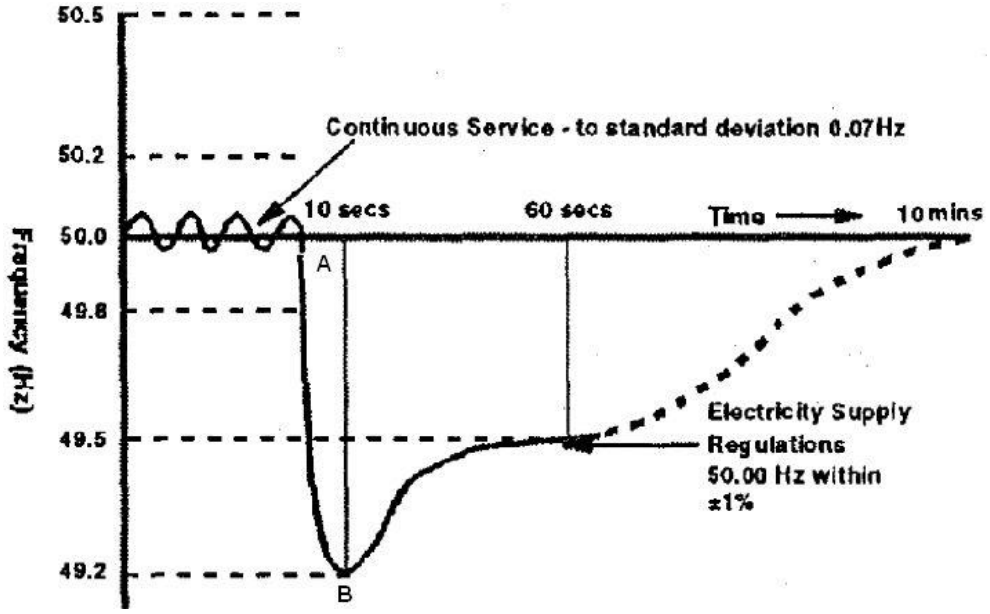

Figure 1.17 Grid frequency drop due to a sudden power demand increase, and recovery activating the two capabilities (The Grid Code, 2012)

In order to assure power plants comply with the required frequency responses at all times, the NGC in the UK introduced several minimum capabilities that any power plant must be able to achieve. This is evaluated by inducing a ramped decrease or increase in frequency of 0.5 Hz over 10 seconds, reproducing sudden changes in power demand as seen in Figure 1.17 (The Grid Code, 2012). The most relevant of these capabilities are:

a) Primary response capability: after a ramped decrease of 0.5 Hz over the standard system frequency of 50 Hz during 10 seconds, a power plant must increase at least 10% in active power output between the following 10 to 30 seconds (see Figure 1.18).

b) Secondary response capability: as a means to restore the system to the initial frequency before the ramped decrease was induced, it is a continued increase in the power output between the following 30 seconds to 30 minutes after the primary response. A boiler would increase the coal firing rate in order to comply with this capability.

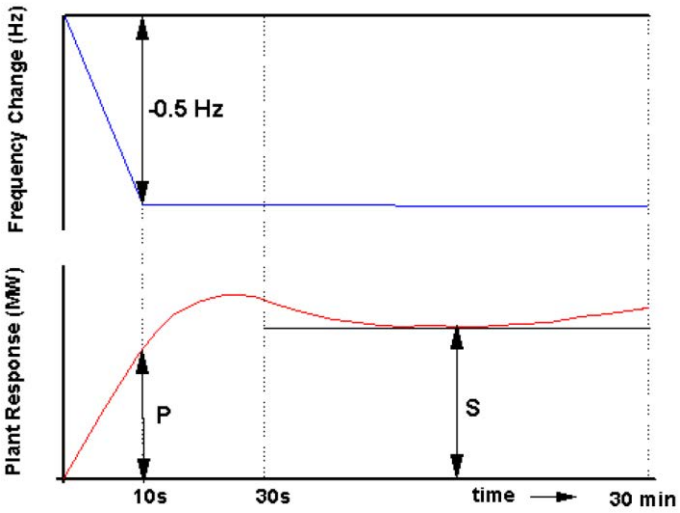

Figure 1.18 Primary and secondary frequency responses (The Grid Code, 2012)

It is well known that subcritical boilers comply with the primary response capability, because the boiler drum is able to release the stored energy by opening the turbine throttle valves and deliver more steam to the HP. However, it is not clear what the best dynamic responses can be achieved by SCCFPPs without having an energy storage system such as a steam drum (Nicholls, 2008). SCCFPPs normally operate on sliding pressure mode, i.e. adapting the system pressure to the power demand and keeping the throttle valves open. This is advantageous for secondary response capabilities. Unfortunately, the SC plant system may have difficulties to provide the

10% increase in load required by the primary response capability within the 10-30 seconds required by the NGC.

As a means to provide the additional energy required in SCCFPPs to comply with the primary response capability, several techniques have been considered. For instance, constant pressure operation as in subcritical boilers, coal firing rate increase or condensate stop (turbines stop being steam-bled in order to temporarily deliver more power). The main drawback is that, due to the technical difficulties to perform them on-site, none of these techniques has been tested yet. This limitation brings considerable uncertainties about the economy, efficiency or safety to any prospective project devoted to obtaining any operational experience on such compliance with the dynamic responses (Nicholls, 2008).

1.5 Aim of the present work

Novel research solutions must be provided to gain acceptance for this CCT in electrical power generation in the UK. To study feasible strategies to improve the dynamic responses of SCCFPPs, the aim of the research work presented in this thesis was to provide further understanding of the means to increase the thermal performance of the SC boiler and eventually approach compliance with the NGC.

Computational Fluid Dynamics (CFD) was selected to carry the research in the present thesis, as a useful tool during the product design stage of systems related to fluid dynamics and heat transfer. If a modelled system is properly validated and verified, CFD provides valuable information about phenomena occurring inside the system, such as heat transfer performance in the water cycle without the need to perform experimental tests. Also, CFD would reduce some uncertainties described in Section 1.4 such as the efficiency of the system, allowing a detailed analysis of parameters that are not measurable in test runs (Yli-Fossi *et al.*, 2011). Moreover, the information obtained can be used in SC boiler design, power plant simulation packages or validation of empirical heat transfer correlations.

As explained in Section 2.3.4, the CFD module within the simulation software Comsol Multiphysics was selected as a novel modelling technique to numerically investigate the heat transfer behaviour of a test element representing a pipe from the water wall of a SC boiler. As a result, the grid code compliance analysis would benefit from the conclusions obtained in the simulations performed.

1.6 Thesis layout

The key topics of the present thesis were revealed in the present chapter, such as SCCFPPs, supercritical heat transfer and CFD. In Chapter 2 they were explained in detail, and thus a further insight on the previous works related to SC heat transfer was provided, as well as the main features related to CFD and the numerical approaches when computing turbulence convective flows.

The objectives subject to the aforementioned aim of the research were presented in the result chapters (3, 4, 5 and 6), structured in the new writing-up style, i.e. paper format, including their own detailed literature review.

The first objective, presented in Chapter 3, was to validate the capability of the computational software Comsol Multiphysics to simulate turbulent convective flows at SC conditions, employing external experimental data. Secondly, in Chapter 4 the feasibility of simulations was further tested by verifying a numerical study under the effect of strong heating conditions. In Chapter 5, the SC boiler performance was analysed carrying a 2D study. Moreover, some SC design aspects were approached in Chapter 6 with the prospect of developing future experimental validations related to the numerical results obtained in Chapter 5.

The main outcomes of all the work performed in the thesis were summarised in Chapter 7, along with suggestions to continue with the necessary steps in the future.

A description of the simulation procedure followed within the selected CFD package was presented in the Appendix when creating and setting up a model. Aspects such as the occurring physics, the selected turbulence model and the governing equations were covered. Similarly, the three main steps in every CFD simulation (pre-processing, solving and post-processing) were further analysed within the Comsol Multiphysics environment.

1.7 Research Dissemination

a) Conference publications:

Gil-Garcia AA, Kings IN, Al-Duri B (2014). Dynamic Responses Analysis for Coal Fired Power Generation with Supercritical Units for Grid Code Compliance. 14th European Meeting on Supercritical Fluids (EMSCF)

b) Oral presentations (speaker underlined):

Gil-Garcia AA, Kings IN, Al-Duri B. Study of Supercritical Water Power Plant Cycles: Overview of Research Activities. Workshop Collaboration China-UK, Beijing (China), 2013

Gil-Garcia AA, Kings IN, Al-Duri B. Dynamic Responses Analysis for Coal Fired Power Generation with Supercritical Units for Grid Code Compliance. 14th European Meeting on Supercritical Fluids (EMSCF), Marseille (France) 2014

c) Poster presentations:

Draganescu M, Gil-Garcia AA, Wojcik JD, Kings IN, Wang J, Al-Duri B. Study of Supercritical Coal Fired Power Plant Dynamic Responses for Grid Code Compliance. RCUK UK-China: Partners in Energy Workshop, London (UK), 2014

Gil-Garcia AA, Kings IN, Al-Duri B. Study of Supercritical Coal Fired Power Plant Dynamic Responses for Grid Code Compliance. COMSOL Conference, Cambridge (UK), 2014

Gil-Garcia AA, Kings IN, Al-Duri B. Conjugate Heat Transfer Study of Supercritical Water in a Boiler Pipe by Modelling with Comsol Multiphysics. ChemEngDayUK 2015, Sheffield (UK), 2015

References

Bugge J, Kjær S, Blum R (2006). High-efficiency coal-fired power plants development and perspectives. *Energy*; 31: 1437-45

Fink DG (1978). Standard Handbook for Electrical Engineers (11th edition). Beaty HW (editor). McGraw-Hill; pp. 16-21

Goidich SJ, Docherty RJ, Melzer KP (2012). World 1st in West Virginia: Longview supercritical Benson vertical PC boiler. *Modern Power Systems*; Vol. 32, Issue 4: 29

Kaneko S, Maruta T, Hashimoto T, Sato S, Kai N (1996). 1000 MW coal fired supercritical variable pressure operation boiler with vertical furnace waterwall. Mitsubishi Heavy Industries, Ltd. Technical Review; 33: 3

McMullan JT, Williams BC, McCahey S (2001). Strategic considerations for clean coal R&D. *Energy Policy*; 29(6): 441-52

Nicholls R, Maxim C (2008). Super critical coal fired plant requirements and the Grid Code. E.ON UK

Penati M, Piasente R, Silva G, Ghirardini GV (2011). Torrevaldaliga north ultra-supercritical clean coal fired boilers: an experience overview. 19th edition of Power-Gen Europe, Milan

Pioro IL, Khartabil HF, Duffey RB (2004). Heat transfer to supercritical fluids flowing in channels-empirical correlations (survey). *Nuclear Engineering and Design*; 230: 69–91

Pioro I (2014). Application of supercritical pressure in power engineering: specifics of thermophysical properties and forced-convective heat transfer. In: Anikeev V, Fan M (editors). Supercritical fluid technology for energy and environmental applications. *Elsevier*; pp. 201-34

Rayaprolu K (2009). Boilers for power and process. *CRC Press Taylor & Francis Group*

Rukes B, Taud R (2004). Status and perspectives of fossil power generation. *Energy*; 29: 1853-74

Stultz SC, Kitto JB (2005). Steam/its generation and use. 41st edition. The Babcock & Wilcox Company

The Grid Code (2012). National Grid Electricity Transmission plc

Yli-Fossi T, Köykkä P, Majanne Y (2011). A Generalized Dynamic Water Side Model for a Once-Through Benson Boiler. 18th International Federation of Automatic Control World Congress

Zhang K, Zhang Y, Guan Y (2013). Boiler design for ultra-supercritical coal power plants. In: Zhang D (editor). Ultra-supercritical coal power plants. Materials, technologies and optimisation. *Woodhead Publishing*; pp. 104-30

Websites:

BP Energy Outlook (2015/2016). Annual report and form. Available from: http://www.bp.com/en/global/corporate/investors/results-and-reporting/annual-report.html

BP Statistical Review of World Energy (2016). Available from: https://www.bp.com/content/dam/bp/pdf/energy-economics/statistical-review-2016/bp-statistical-review-of-world-energy-2016-full-report.pdf

Dale, S (2016). BP Statistical Review of World Energy June 2016 [online]. London BP. Available from: http://www.bp.com/en/global/corporate/energy-economics/statistical-review-of-world-energy.html

Department of Energy & Climate Change (2011). The Rt Hon Chris Huhne MP's speech to CentreForum. Available from: https://www.gov.uk/government/speeches/the-rt-hon-chris-huhne-mps-speech-to-centreforum-3-march-2011

Johnston, C (2015). UK's coal plants to be phased out within 10 years [online]. London: BBC. Available from: http://www.bbc.co.uk/news/business-34851718

Johnston, C (2016). Hinkley: Why do we need the new nuclear power station? [online]. London: BBC. Available from: http://www.bbc.co.uk/news/business-35747124

Nuclear AMRC (2016). UK new build plans [online]. Nuclear Advanced Manufacturing Research Centre. Available from: http://namrc.co.uk/intelligence/uk-new-build-plans/

The committee on climate change (2008). The climate change act and UK regulations. Available from: https://www.theccc.org.uk/tackling-climate-change/the-legal-landscape/global-action-on-climate-change/

World Nuclear Association (2016). Nuclear Power in the United Kingdom. [online]. World Nuclear Association. Available from: http://www.world-nuclear.org/information-library/country-profiles/countries-t-z/united-kingdom.aspx

2. Literature Review

Abbreviations

CFD	computational fluid dynamics
DB	Dittus-Boelter
DNS	direct numerical simulation
HTC	heat transfer coefficient
HTD	heat transfer deterioration
LES	large eddy simulation
LHS	left-hand side
LPV	large property variation
NS	Navier-Stokes
PSC	pseudo-critical
RANS	Reynolds-averaged Navier-Stokes
RHS	right-hand side
SC(F)	supercritical (fluid)
SCHT	supercritical heat transfer
SCW	supercritical water

Dimensionless numbers

Gr	Grashof number
Nu	Nusselt number
Pr	Prandtl number
Re	Reynolds number

Greek symbols

β	volumetric expansion coefficient [$degC^{-1}$]
κ	wave number [-]
μ	dynamic viscosity [$kg\ m^{-1}\ s^{-1}$]
ν	kinematic viscosity [$m^2\ s^{-1}$]
ρ	density [$kg\ m^{-3}$]
τ	shear stress [Pa]

Geometric definitions

D	tube internal diameter [mm]
L	pipe length [mm]
y	radial coordinate [mm] or distance from the wall [mm]
y^+	dimensionless wall distance [-]

Roman symbols

C_p	isobaric heat capacity [J kg^{-1} degC^{-1}]
G	mass flux of water [kg m^{-2} s^{-1}]
h	enthalpy [J kg^{-1}]
I	turbulence intensity [%]
k	turbulent kinetic energy [m^2 s^{-2}]; thermal conductivity [W m^{-2} degC^{-1}]
P	instantaneous pressure [bar]
q	heat flux [kW m^{-2}]
T	temperature [K or °C]
u	local flow velocity [m s^{-1}]
$\bar{u}$	mean flow velocity [m s^{-1}]
U	instantaneous axial velocity [m s^{-1}]
$\overline{U}$	time-averaged axial velocity [m s^{-1}]
u’	fluctuating axial velocity [m s^{-1}]
V	instantaneous radial velocity [m s^{-1}]
$\overline{V}$	time-averaged radial velocity [m s^{-1}]
v’	fluctuating radial velocity [m s^{-1}]

Subscripts

$(\ldots)_b$	at bulk conditions
$(\ldots)_{lam}$	at laminar conditions
$(\ldots)_{turb}$	at turbulent conditions
$(\ldots)_w$	at inner wall conditions

2.1. Relevant turbulence phenomena

2.1.1. Development of the boundary layer in turbulent internal flows

In supercritical (SC) boilers, fluid flow is strongly turbulent within the pipes due to the inertial forces induced by the pumps. When a forced-convective flow with a flat (constant) velocity profile interacts with a wall, viscous forces appear. These are natural interactions among molecules that tend to keep the fluid as one. This phenomenon is quantified by the fluid viscosity (μ). Next to the wall, these forces are stronger and counter the dragging forces imposed by the kinetic energy of the flow, producing enough friction to stop the flow at the wall surface. This is called the no-slip effect (Çengel & Cimbala, 2006a). Away from the wall the dragging forces become more relevant, progressively overtaking the viscous effects.

This balance between viscous and inertial forces depending on the wall distance laminarises the flow, creating radial velocity gradients and producing a parabolic-like velocity profile. This is triggered because mass flow must remain constant in the pipe so the flow velocity peaks in the bulk to compensate the velocity reduction near the walls. As a consequence, two flow regions are distinguished in the velocity profile (see Figure 2.1):

- The boundary layer region: located near the wall, in this region the velocity profiles are affected by the viscous effects caused by the no-slip condition, triggering velocity gradients.

- The free stream velocity region: located at the bulk of the flow where the viscous effects are negligible and thus the velocity profile is constant. The division between these two regions takes place when the velocity profile at the boundary layer becomes 99% of the free stream velocity.

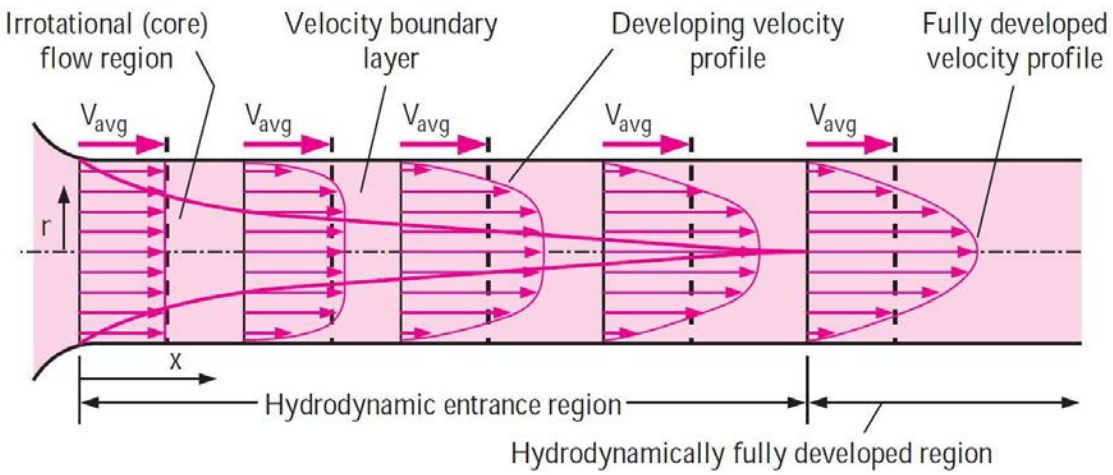

Figure 2.1 Development of velocity profile under no-slip condition (Çengel & Cimbala, 2006a)

When a flow inlet displays a flat velocity profile at the entrance of a pipe, the boundary layer is very thin, and thus the free stream velocity is developed very close to the wall in the absence of viscous forces. However, the boundary layer becomes thicker downstream due to the no-slip condition, thus pushing the free stream region towards the pipe centreline until the boundary layer overtakes the entire cross-section. At this point, the velocity profile does not change anymore axially, the viscous effects are completely established and thus the flow is considered hydrodynamically fully developed. The pipe length upstream this point is defined as the hydrodynamic entrance region, and can be expressed by a factor proportional to the pipe length over the pipe internal radius (L/D).

Because of the laminarisation effect triggered by the viscosity and the consequential creation of velocity gradients, the different layers display different flow velocities and thus friction appears between them, also known as shear stress (τ), as shown in equation (2.1).

$$\tau = \mu \cdot \frac{\partial \bar{u}}{\partial y} \quad \textbf{(2.1)}$$

Shear stress is laminar (viscous) by nature and proportional to the fluid viscosity and the local velocity gradient ($^{\partial \bar{u}}/_{\partial y}$), also called shear rate. The no-slip effect causes a sharp increase in the velocity gradients near the wall, and thus the viscous shear stress is highest in this area. As the viscous effects dissipate towards the pipe centreline, the velocity gradients decrease and so does the shear rate. When the shear rate becomes zero, the velocity profile is flat and thus the onset of the free-stream region occurs.

Moreover, due to the process by which the velocity profiles are created from the inlet, wall shear stresses (τ_w) are highest at the entrance region when the velocity gradients near the wall are sharp. As the velocity profile is established, τ_w decreases until it remains constant on the hydrodynamically fully developed region (see Figure 2.2).

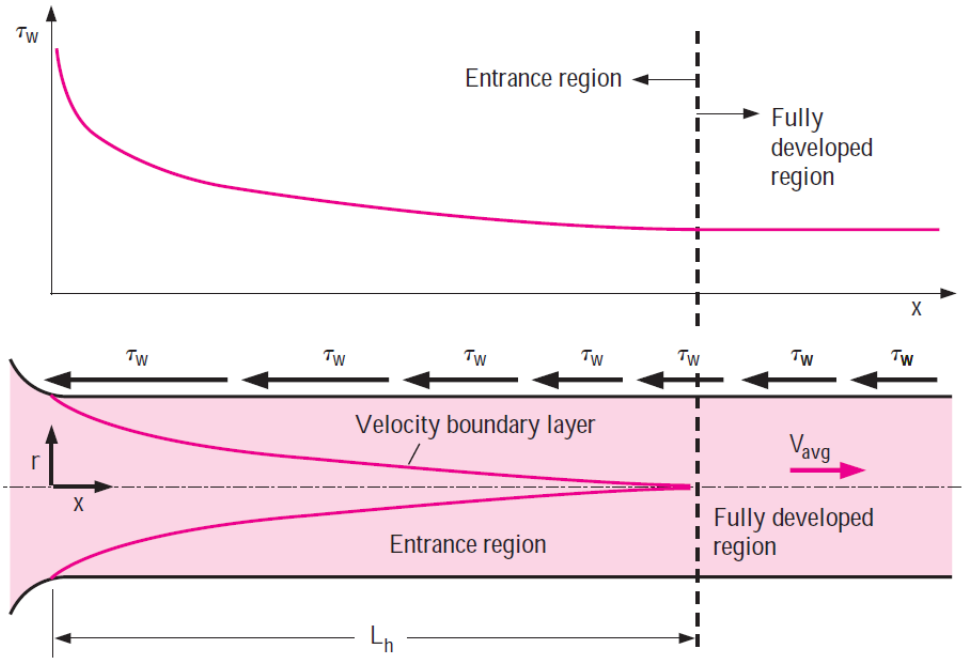

Figure 2.2 Wall shear stress at the entrance region (Çengel & Cimbala, 2006a)

If the viscous forces in the mean flow dominate over the inertial forces, the flow is considered laminar. In these cases the viscous effects reach much further into the bulk of the flow, thus the velocity gradients produce a marked parabolic shape for the velocity profile (see Figure 2.3a). On the other hand, if the inertial forces dominate over the viscous forces, the flow is considered turbulent. In this case, vortices appear in the regions away from the wall, interacting with the flow to prevent laminarisation and producing turbulent shear stress as further defined in Section 2.3.2, while the viscous effects are limited to a region close to the wall. As a result, the parabolic profile is flattened in the bulk and much steeper near the wall. This is why the viscous shear stress on the wall is much larger for turbulent profiles than laminar (see Figure 2.3b).

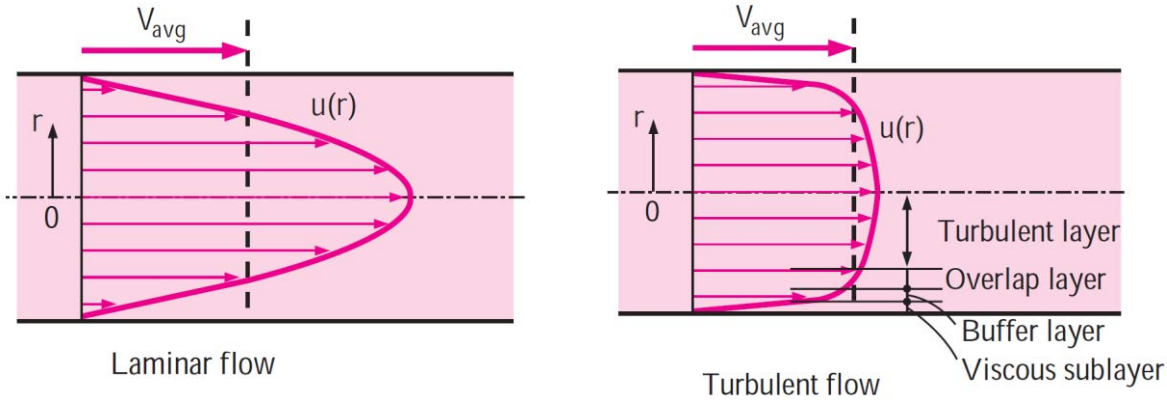

Figure 2.3 Differences between laminar (a) and turbulent (b) velocity profiles (Çengel & Cimbala, 2006a)

2.1.2. Mixed-convective turbulent flows

Some experiments in supercritical heat transfer (SCHT) that have been assumed to operate under forced convection may have ignored the presence of mixed convection (Huang *et al.,* 2008), inducing errors in the results. Turbulence is not only originated by forced convective forces transferred from the kinetic energy provided by the pumps. When pressurised water is heated and approaches the critical or pseudocritical (PSC) point, sharp drops in density and viscosity take place as explained in Section 1.3.1. The potential energy, triggered by these changes, can induce buoyancy forces due to density differences within the flow. This effect is called free or natural convection; and when forced and natural convection occur at the same time, the combined effect is called mixed convection. In any wall-bounded mixed convective flow, there are three interacting forces:

- Viscous forces (wall effects), represented by the laminar shear stress.
- Inertial forces (pumped flow), proportional to the flow density and velocity.

- Buoyant forces (heated flow), proportional to density differences in the flow, gravity and pipe diameter.

The magnitude of the viscous, inertial and buoyant forces is expressed with dimensionless numbers. The most relevant are:

a) Reynolds number (Re): expresses the balance between the inertial and viscous forces as a ratio, revealing if the system carries enough kinetic energy to produce inertial turbulence. Depending on the region of the flow to be analysed, there are different definitions for the Reynolds number (see Table 2.1):

Table 2.1 Definitions of Re based on the region considered

Region	Equation	
Mean flow	$Re_D = \frac{\bar{\rho} \cdot D \cdot \bar{u}}{\bar{\mu}}$	**(2.2)**
Bulk flow	$Re_b = \frac{\rho_b \cdot D \cdot u_b}{\mu_b}$	**(2.3)**
Local flow (from the pipe wall)	$Re_x = \frac{\rho_x \cdot 2 \cdot (R - r) \cdot u_x}{\mu_x}$	**(2.4)**
Wall-distance-based (turbulent)	$Re_y = \frac{\rho_y \cdot y \cdot \sqrt{TKE}}{\mu_y}$	**(2.5)**

Where ρ is the density of the fluid, u is the local flow velocity, y is the distance to the wall, and TKE is the turbulent kinetic energy. Equations (2.2) and (2.3) are the most commonly employed. Mean or bulk flows with a Re higher than 2300-4000 in internal flows are considered turbulent.

b) Grashof number (Gr): represents the ratio of buoyant forces due to natural convection (thermal driving) to the viscous forces. Therefore, it is equivalent to the Reynolds number in forced convection. For high values of Gr buoyancy overcomes the laminar effects and thus buoyant turbulence occurs. If Re is also high, a combined turbulence appears. In Table 2.2, several definitions of Gr are presented.

Table 2.2 Definitions of Gr depending on several criteria

Criterion	Equation	
Integrated density	$\overline{Gr_b} = \frac{(\rho_b - \bar{\rho}) \cdot \rho_b \cdot g \cdot D^3}{\mu_b^2}$	**(2.6)**
Wall-bulk temperature difference	$Gr_{\Delta T} = \frac{(T_w - T_b) \cdot \rho_b^2 \cdot g \cdot D^3 \cdot \beta_b}{\mu_b^2}$	**(2.7)**
Density difference	$Gr_b = \frac{(\rho_b - \rho_w) \cdot \rho_b \cdot g \cdot D^3}{\mu_b^2}$	**(2.8)**
Wall heat flux	$Gr_q = \frac{q_w \cdot \rho_b^2 \cdot g \cdot D^4 \cdot \beta_b}{\mu_b^2 \cdot k_b}$	**(2.9)**

In the equations in Table 2.2, β is the volumetric expansion coefficient, T_b is the bulk temperature, k is the thermal conductivity and q_w is the wall heat flux. The system geometry is paramount when determining the influence of buoyancy in SCHT. In that sense, large diameters and low velocities produce sharp temperature profiles, and thus larger density differences to trigger a dominant natural convection. In heated pipes, Gr numbers are selected depending on the kind of thermal boundary layer applied; thus equations (2.6), (2.7) and (2.8) are employed for constant wall temperature while equation (2.9) is selected for constant q_w.

c) Laminar Prandtl number (Pr): as seen in equation (2.10), Pr represents the ratio of laminar diffusion of momentum (velocity) to laminar diffusion of heat in a heated flow, i.e. how deep the velocity and thermal boundary layers in the laminar region diffuse from the wall into the flow. Heat capacity is represented as C_p.

$$Pr = \frac{{}^{\mu}/_{\rho}}{{}^{k}/_{C_p \cdot \rho}} = \frac{C_p \cdot \mu}{k} \equiv \frac{Heat\ convection\ forces}{Heat\ conduction\ forces} \quad \textbf{(2.10)}$$

For values of Pr larger than 1, the velocity gradients reach deeper into the flow than the temperature gradients, meaning the temperature gradients dissipate faster due to stronger natural heat convection. As seen in Figure 2.4, when Pr is smaller than 1, the temperature gradients take longer to dissipate than velocity because heat conduction dominates over the flow. This combined effect states if the existing natural convection boundary layer (the flow region from the wall which develops a temperature profile due to buoyancy) is turbulent or laminar, i.e. a ratio between natural convection heat transfer and conduction heat transfer.

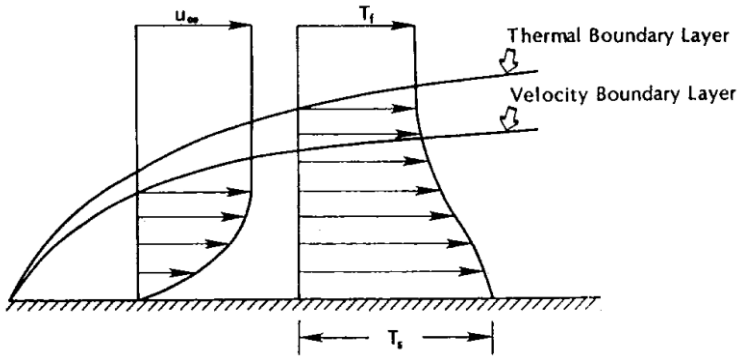

Figure 2.4 Velocity and thermal boundary layers (Hoffmann & Chiang, 2000)

2.2. Supercritical heat transfer

2.2.1. SCHT in power engineering

Schmidt *et al.* (1946) were one of the first researchers to observe the special thermal behaviour of SC fluids (SCFs). They found while researching cooling systems that the free-convective heat transfer coefficient (HTC) of a fluid near the critical point was much higher than the same at subcritical pressures. Since then, extensive research about SCFs as single-phase working fluid has been performed.

From the 50s to the 70s, SC boilers were employed in coal-fired and nuclear power plants, mainly in the USA and the former USSR, due to the advantages in thermal efficiency and structural simplification explained in Section 1.3.2. Thus, experimental research was extensively carried as a means to predict the thermal behaviour considering the differences with subcritical systems (Jäger *et al.*, 2011).

Technological limitations related to the lack of resistant materials to withstand the supercritical pressures and the onset of base-loaded nuclear power stations using subcritical boilers, the use of SCFs in power engineering declined. However, in the 90s several countries (Japan, Canada, USA and Russia) retook the research due to the development of new generation water reactors using SC boilers and the improvements in material technology (Pioro & Duffey 2005).

Nowadays, due to the development of computational fluid dynamics (CFD), new numerical studies are focused on this area, as they are more economical than the experimental works using SCFs (Rahman *et al.*, 2016).

2.2.2. Effect of parameters in SCHT performance

Yamagata *et al.* (1972) confirmed that when water was flowing vertically and horizontally at normal heat transfer conditions, the HTC increased considerably near the PSC region, peaking when the wall had surpassed the PSC temperature while the bulk temperature was below this value. However, under certain heating conditions the fluid density could change radially and axially nearby the PSC region and induce buoyancy. As a consequence, secondary flows would be triggered and the natural convection regime would commence to compete with the forced convection forces.

Additionally, when the fluid density displays non-uniform axial profiles, thermal acceleration can be caused. If the heat flux applied is large enough to increase the temperature of the bulk and thus decrease its density, bulk velocity increases axially as a means to maintain the mass flow rates constant. Subsequently, the core fluid accelerates compared to the boundary layer (Jackson & Hall, 1979). These phenomena take place when the SC conditions are surpassed and not only density, but also thermal conductivity and heat capacity drop. The overall effect is a gradual laminarisation of the flow, reducing turbulence and thus heat transfer. Unlike

buoyancy, this phenomenon is triggered in both forced-convective and mixed-convective flows.

Presently, there are no universal criteria to predict the onset of the buoyancy or flow acceleration in SCHT systems (Huang *et al.,* 2008). However, it is known that they are triggered by a series of factors which, depending on their interaction, improve or decrease the heat transfer performance. The most relevant are:

- Heat flux to mass flux ratio: as seen in Figure 2.5, if all the other parameters are fixed, lower heat fluxes produce larger peaks of HTC near the pseudo-critical point (Yamagata *et al.*, 1972). Low values of G trigger stronger buoyancy, inducing turbulence and enhancing heat transfer. Nevertheless, the most important factor is the interaction of both as ratio (q_w/G). When a convective system has a high q_w/G, sharp radial gradients of thermophysical properties occur, thus the thermophysical values near the wall can be quite different from the bulk. In this case, phenomena taking place in the boundary layer determines the heat transfer performance. In fact, heat transfer deterioration (HTD) can be triggered due to buoyancy effects if the bulk fluid temperature is below the PSC temperature. On the other hand, at low q_w/G values the radial temperature profile is uniform, and thus when the bulk temperature reaches the PSC value an improvement of heat transfer occurs due to the radial profile of large heat capacity.

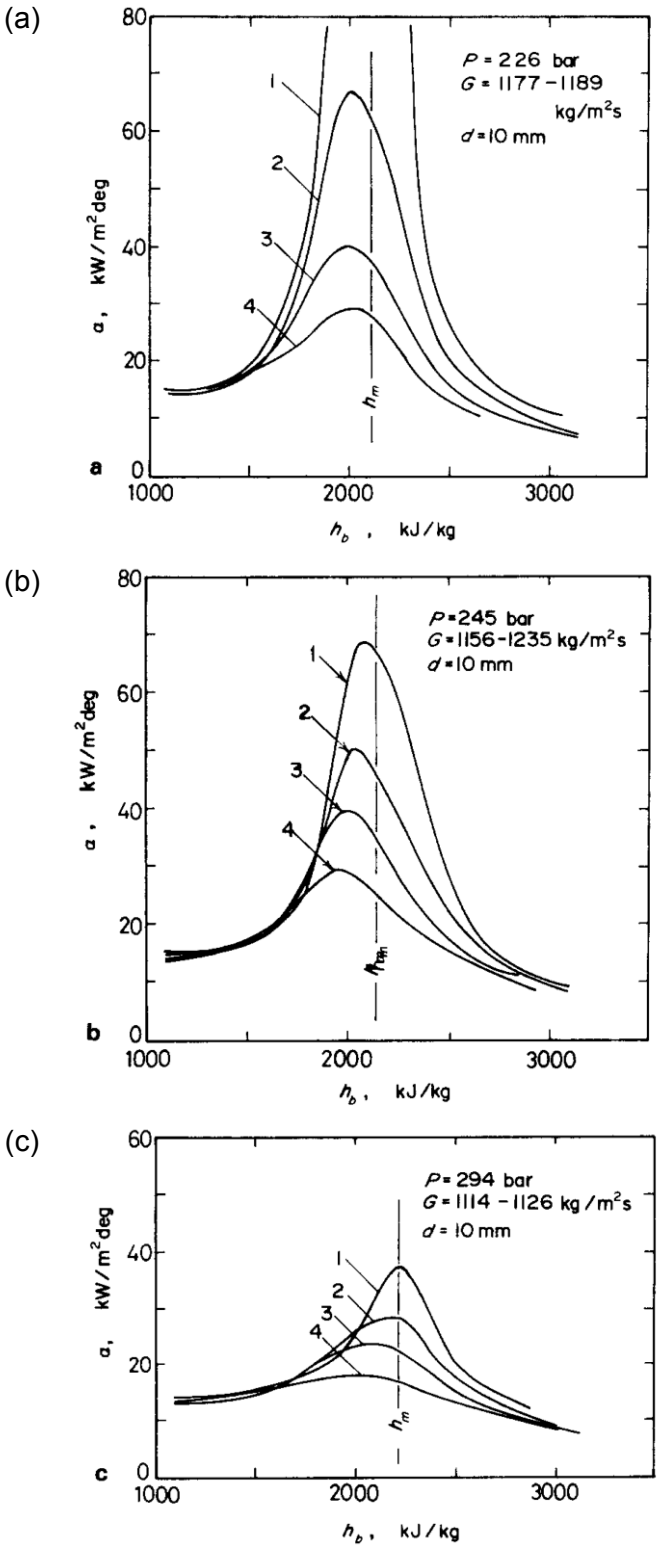

Figure 2.5 HTC (α) profiles vs. bulk enthalpy (h_b) at different heat fluxes (1. q = 233; 2. q = 465; 3. q = 698; 4. q =930 kW m^{-2}) using different pressures for an upward water flow (Yamagata *et al.*, 1972)

- Flow direction: this effect strongly depends on parameters that facilitate buoyancy, such as the q_w/G or the pipe diameter. Jackson and Hall (1979) studied the effect of buoyancy in SCHT by observing a heated upward flow. In this pipe orientation, the buoyancy force affects in the same direction as the fluid flow due to the low density. This combination of factors flattens the velocity profile near the wall, reducing shear stress and thus neglecting turbulence diffusion of heat. When the flows downwards, buoyancy and fluid flow effects are opposite, inducing shear in the velocity gradients and thus increasing the thermal efficiency. Many different buoyancy criteria have been developed to predict its onset; however there is considerable disagreement with the experimental results. Subsequently, improved criteria must be developed (Huang *et al.*, 2016).

- Pipe diameter: the diameter size is directly proportional to the effect of buoyancy and inversely proportional to thermal acceleration. Thus, small pipes are rarely subject to the effect of strong buoyancy forces, while normally suffer from thermal acceleration if strongly heated.

- System pressure: pressure variations in SCHT systems are normally not large enough to trigger buoyancy or flow acceleration effects as sensibly as the previously described factors do (Huang *et al.*, 2016). However, Figure 2.5 reveals that the closer the system pressure is to the critical point (221 bar for water), the higher the value of HTC is, due to the sharper increase in specific heat near the critical point.

When the combination of the aforementioned effects triggers HTD, it is a gradual phenomenon compared to the sharp decrease of heat transfer produced in subcritical convective flows due to dry-out. As a consequence, it is complicated to determine its onset. Vikhrev *et al.* (1967) found that at high values of q_w/G there is also HTD at the entrance region of heated tubes (L/D ≤ 40–60), due to the flow restructuration.

2.2.3. SCHT correlations

Heat transfer correlations are essential tools in the design of convective systems such as boilers, as they can predict their thermal performance. These equations are obtained by processing thermophysical properties measured in experimental tests, as a means to obtain the Nusselt number (Nu), and thus the HTC of the system. Subsequently, the prediction of the HTC is more accurate when the working conditions of the studied system are similar to those of the experiments carried to produce the correlation.

The most widely used correlation when working with heated forced-convective flows at subcritical conditions was created by Dittus and Boelter (Winterton, 1998), defined in equation (2.11).

$$Nu = 0.023 \cdot Re^{0.8} \cdot Pr^{0.4} \quad \textbf{(2.11)}$$

In (2.11), Re and Pr are the Reynolds and Prandtl numbers, representing the hydrodynamic and thermal factors, respectively. The Dittus-Boelter (DB) correlation is only valid at subcritical conditions, and once the fluid approaches the large property

variation (LPV) region nearby the PSC point it is known to overpredict the HTC (see Figure 2.6). This is due to the effect of the C_p term included within Pr in the DB correlation. In truth, additional phenomena related to the LPVs and their role triggering buoyancy and thermal acceleration affect the thermal performance depending on the system configuration. As a consequence, the experimental values of HTCs deviate from the DB correlation within the LPV region (Rahman *et al.*, 2016).

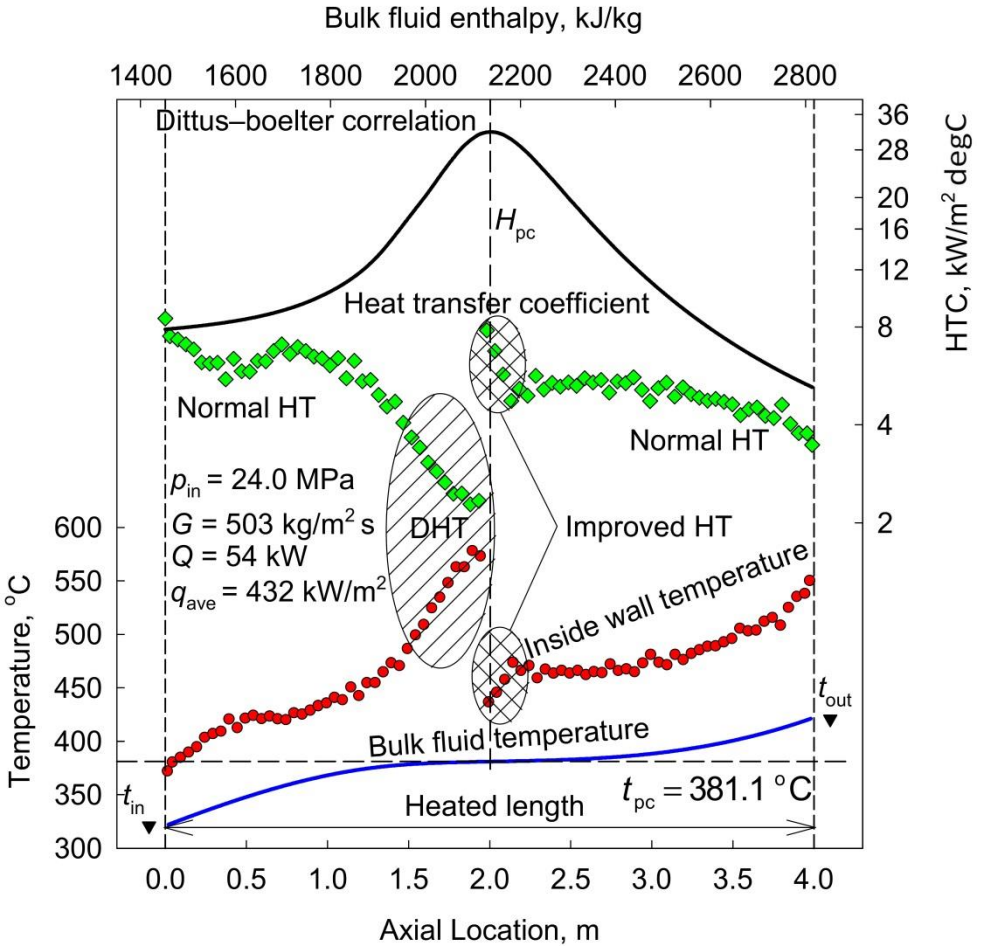

Figure 2.6 Heat transfer regimes in SC flows (adapted from Pioro, 2014)

Nevertheless, the DB correlation is important in SCHT because it is used as a reference to define the three existing SCHT regimes, also depicted in Figure 2.6 (Pioro & Duffey, 2005):

- Normal heat transfer (NHT) regime: the value of the HTC is similar to that obtained away from the PSC region, i.e. not considering LPVs and thus neglecting buoyancy and thermal acceleration effects. This is, matching the values provided by the DB correlation.

- Deteriorated heat transfer (DHT) regime: sometimes at high values of q_w the HTCs produced are lower compared to those obtained in the NHT regime, i.e. below the prediction provided by the DB correlation away from the PSC region. As a consequence, wall temperature in the affected area increases.

- Enhanced heat transfer (EHT) regime: when low q_w is applied, under certain conditions the HTCs produced are higher compared to those obtained in the NHT regime, i.e. above the prediction provided by the DB correlation away from the PSC region. Thus, wall temperature in that area decreases.

Many studies have been performed to discover a reliable correlation for SC flows, regardless of the fluid, heat flux to mass flux ratio (q_w/G), pipe orientation or diameter. In their reviews, Cheng *et al.* (2015), Jäger *et al.* (2011) and Rahman *et al.* (2016) analytically or computationally tested a series of SCHT correlations, comparing their performance with experimental data. Most of the correlations displayed a DB structure, including some of the following modifications to account for effects at supercritical conditions:

- A ratio of thermophysical properties at the wall temperature to those at the core temperature, given the case supercritical state is normally achieved first on the wall. This can be seen in equation (2.12).
- Parameters related to buoyancy or flow acceleration as a means to account for the free and forced-convective effects induced by density variation that could be triggered at certain mass fluxes.
- A geometrically dependent parameter, in order to account for possible entrance effects.

However, even the most precise correlations the aforementioned authors reviewed presented remarkable deviations nearby the PSC point, and thus new correlations with improved accuracy are necessary. On the other hand, Cheng *et al.* (2015) concluded that one of the correlations that provided the best predictions for the entire range of working conditions was that of Mokry *et al.* (2011) as seen in (2.12) for water flowing upwards. Thus, it was selected in the present thesis to predict the thermal behaviour of the modelled systems.

$$Nu_b = 0.0061 \cdot Re_b^{0.904} \cdot \overline{Pr}_b^{0.684} \cdot \left(\frac{\rho_w}{\rho_b}\right)^{0.564} \quad \textbf{(2.12)}$$

Equation (2.12) was produced at bulk conditions, where $\overline{Pr}$ is the average Prandtl number and ρ_w and ρ_b are the density at the inner wall of the pipe and the bulk, respectively. The working conditions employed to produce this correlation included vertical flows of water in smooth tubes within a diameter range of 3-38 *mm*,

pressures of 22.8-29.4 MPa, values of G of 200-3,000 kg m^{-2} s^{-1} and heat fluxes between 70-1250 kW m^{-2} (Pioro, 2014).

2.3. Supercritical boiler research using computational fluid dynamics

2.3.1. Advantages of using CFD in Process Design

Approaching turbulent flows and convective heat transfer with numerical analysis has strongly influenced the development of new technologies. Nowadays, new designs are not considered until they have been evaluated through computational analysis. CFD is a combination of disciplines (see Figure 2.7) and a powerful tool to understand the behaviour of experimental systems, validate experimental results or optimise specific designs which are complicated to scale up before industrial implementation.

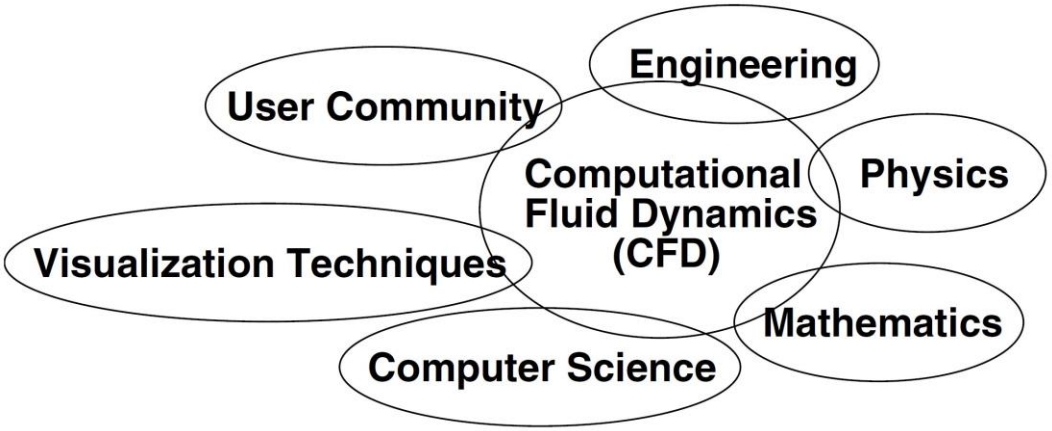

Figure 2.7 Disciplines related to CFD (Löhner, 2008)

Some CFD packages allow parametric simulations, where some key variables are modified in order to see the sensitivity of the solution to these changes (Torres & Grau, 2007). As a consequence, the number of experimental tests in the prototyping stage is reduced, saving costs and time. All these advantages highlight the importance of performing simulations in SC boiler design and operations.

The main use of CFD takes place during the Process Design stage, as a means to reveal information about the system behaviour and thus save economical efforts and time investment during test runs or the prototyping stage. Specifically in the present work, the use of CFD reveals information about the hydrothermal behaviour of SC boilers. In order to do so, a reasonable balance between computational time, model accuracy and stability must be achieved through three sequential steps:

a) Setting up the model. This is achieved when the theoretical basics of CFD and the software are understood.
b) Evaluate the reliability of the simulations through validation by measuring accuracy in relation to experimental data; and verification by using other accurate numerical solutions (Oberkampf & Trucano, 2002).
c) Obtain correct and insightful answers to the specific problem and reach conclusions.

2.3.2. Computing turbulence in CFD

In internal flow inlets, the regime can be already turbulent. In that case, the initial flat velocity profile is rapidly modified near the wall as a result of the radial mixing. Alternatively, a turbulent flow can develop from an existing laminar flow, and thus a series of oriented, organised disturbances appear inside the developing boundary layer. If the inertial forces gain importance beyond a transition range, these disturbances grow enough to disturb the layer disposition, facilitating random 3D

fluctuations known as vortices or eddies, which produce macro-mixing. The boundary layer is established as turbulent, expanding faster due to the eddies (see Figure 2.8). However, the region of the turbulent boundary layer near the wall remains laminar.

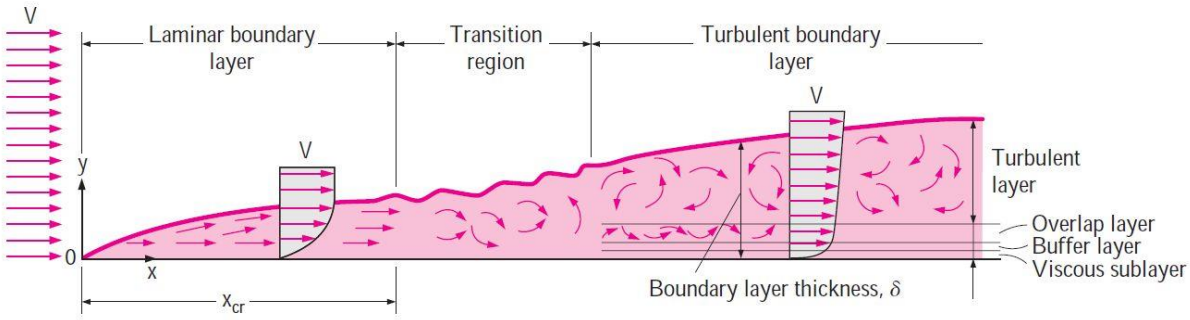

Figure 2.8 Transition from laminar to turbulent regime with creation of eddies (Çengel & Cimbala, 2006a)

The large eddies created initially stretch and tilt due to the interactions with the velocity profile, extending turbulence while new, smaller eddies appear inside them (Davidson, 2015), as seen in Figure 2.9. The difference between the initial large eddies spontaneously created and the subsequent, smaller ones obtained inside is that the former have interacted with the velocity profile and therefore are redirected and stretched (anisotropic), while the latter are independent from the mean flow (isotropic).

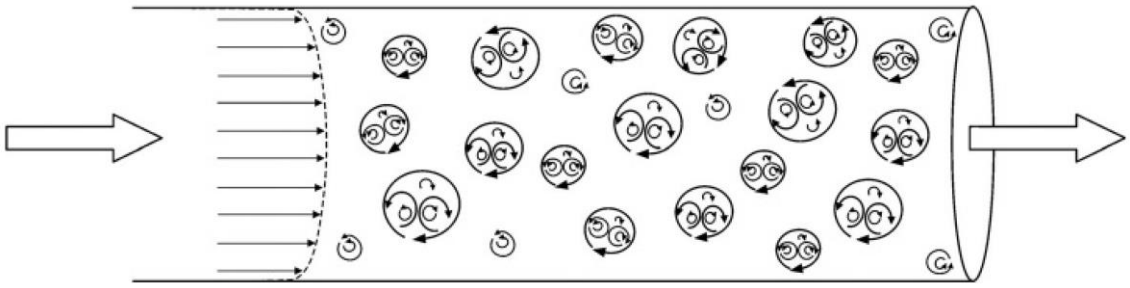

Figure 2.9 Creation of eddies in turbulent flows (Andersson *et al.*, 2012)

The largest eddies are as big as the flow geometry allows, i.e. as thick as the boundary layer. These eddies contain big amounts of kinetic energy (k) obtained from their interactions with the velocity gradients, so the sharper these gradients the higher the kinetic energy transferred. This phenomenon takes place at the velocity gradients located in the sublayers next to the wall, surpassing an interface where the viscous and forced convective forces are equally dominant. In this zone, the eddies produced by the increasing effect of the inertial forces interact with velocity gradients stemming from the viscous region. Thus, turbulent shear stress peaks and so does the turbulence intensity (I), as seen in Figure 2.10. After surpassing this zone towards the centreline of the pipe, velocity gradients decrease as the velocity profile gets flatter, and therefore eddies reduce their interaction, decreasing turbulence intensity.

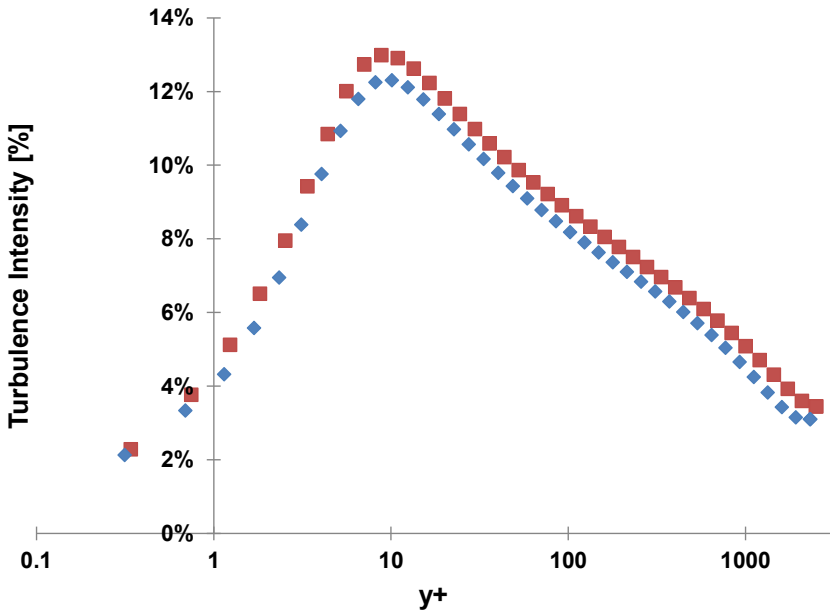

Figure 2.10 Turbulence Intensity vs. dimensionless wall distance (y^+) at two axial locations

In the regions of high turbulence intensity where eddies interact with the velocity gradients, they transfer the kinetic energy contained to the smaller eddies created inside them in a sequential process called cascade, as seen in Figure 2.11. For the biggest eddies, only a small amount of their energy is dissipated due to frictional (viscous) forces, as the inertial energy is much stronger.

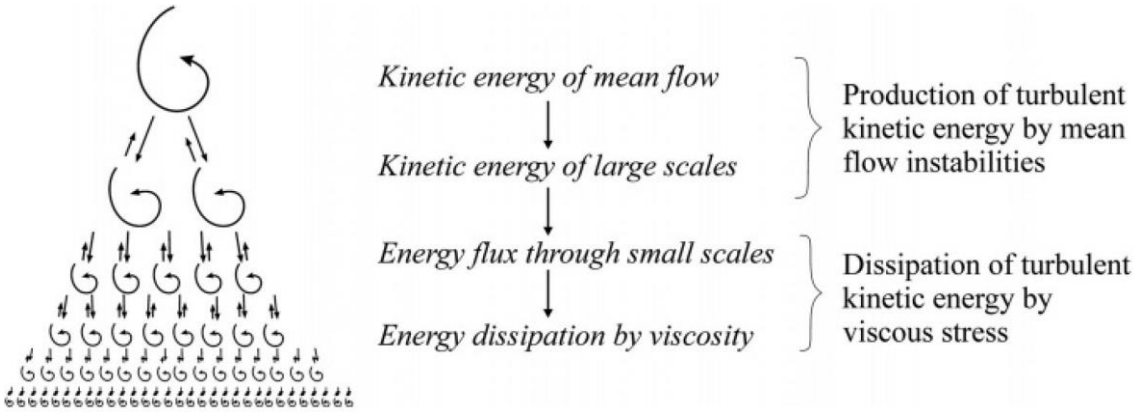

Figure 2.11 Cascade of energy from large to small scales (Andersson *et al.,* 2012)

This cascade continues until the eddies become small enough to be overcome by the viscous forces (shear stress), imposing a micro laminar regime inside as their kinetic energy is dissipated into internal energy through friction. The relationship between the energy contained within the eddies and their size is represented in a plot called *energy spectrum* (see Figure 2.12). E(κ) is the turbulent kinetic energy contained within the eddies and κ is defined as wave number (i.e. the number of spiral laps located within the eddy, inversely proportional to the eddy radius). As can be seen, the eddy production passes through four stages (from large scale to viscous subrange), giving up the energy and decreasing in size in a cascade process.

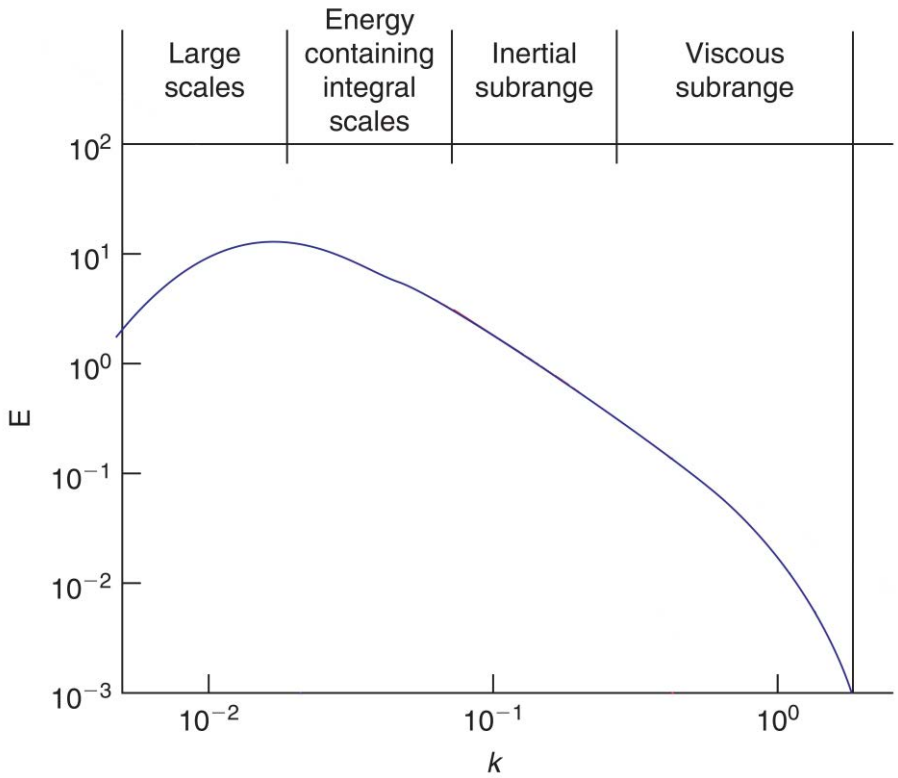

Figure 2.12 Turbulence spectrum showing turbulent kinetic energy vs. wave number (adapted from Hirsch, 2007)

In computational analysis, turbulence represents a challenge due to the chaotic character of the occurring phenomena. Still, it can be described by the Navier-Stokes (NS) equation, as represented in equation (2.13) to describe the conservation of momentum for an incompressible flow without internal energy generation. (Çengel & Cimbala, 2006b).

$$\frac{\partial u}{\partial t} + (u \cdot \nabla)u = \nu \nabla^2 u + g \quad \textbf{(2.13)}$$

$$\nabla = \frac{\partial}{\partial x} i + \frac{\partial}{\partial y} j + \frac{\partial}{\partial z} k \quad \textbf{(2.14)}$$

The first term on the left-hand side (LHS) of the NS equation represents the time-dependent nature of velocity, while the second term indicates the spatial variation of

velocity, i.e. convective effect. The symbol ∇ is the Laplacian operator, described for a 3D Cartesian system in equation (2.14). The first term of the right-hand side (RHS) of the NS equation considers the presence of diffusion effects, and thus shear stress, including the kinematic viscosity (ν). On the other hand, the second term of the RHS accounts for the presence of external sources, such as gravity.

$$\frac{\partial \rho}{\partial t} + \nabla(\rho u) = 0 \quad \textbf{(2.15)}$$

The NS equation is a second-order, unsteady partial differential equation with high nonlinearity and thus needs the continuity equation (conservation of mass), shown as equation (2.15), to be solvable. Both equations together can resolve the velocity and pressure profiles of any flow as long as velocity is time-independent, i.e. in laminar flows. However, when the flow becomes turbulent, the velocity profile randomly varies over time due to interactions with the eddies.

Nevertheless, the entire turbulent flow spectrum can be computed in CFD with the NS equation using direct numerical simulation (DNS), as seen in Figure 2.13a. Inside the smallest eddies the flow is laminar, and thus the NS equations can be employed. As a consequence, the mesh describing the fluid domain must be fine enough to consider the smallest eddies. Despite it is feasible in terms of calculation, it would render the NS equations too complex, and thus the simulation would become highly prohibitive in terms of memory demand.

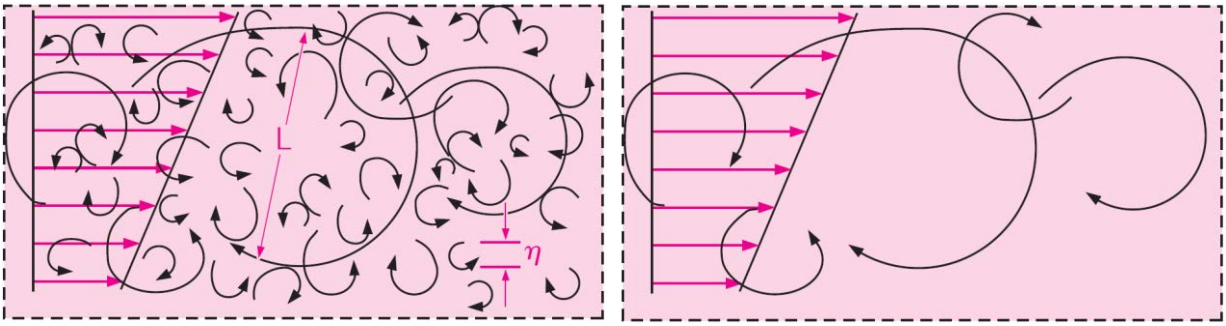

Figure 2.13 Eddies resolved by the (a) DNS approach and the (b) LES approaches (Çengel & Cimbala, 2006a)

A means to simplify the numerical analysis of the system is spatially filtering the NS equations. Only the large eddies are computed in the spectrum (see Figure 2.13b), while a series of assumptions are made for the isotropic small eddies in order to model them. This approach is called large eddy simulation (LES) and although it is not as accurate as the DNS, it is less computationally expensive.

On the other hand, the RANS approach is the most practical approach to model fluid flow from an engineering point of view, as only the largest scales are computed while all the cascaded eddies produced are modelled, as seen in Figure 2.14 along with the previous numerical approaches.

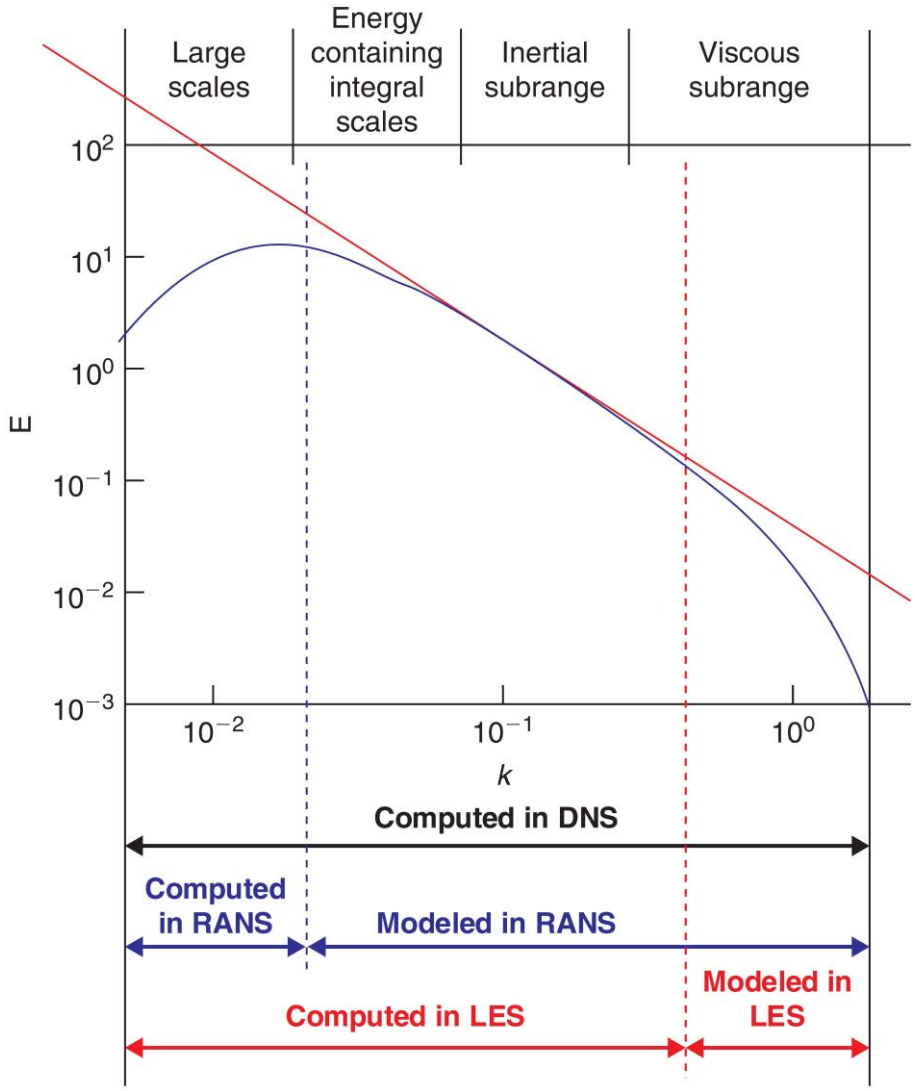

Figure 2.14 Turbulence spectrum showing turbulent kinetic energy vs. wave number, and competencies of numerical approaches (adapted from Hirsch, 2007)

2.3.3. Modelling with the Reynolds-averaged NS (RANS) equations

When modelling with the RANS equations, simulations turn feasible in personal computers in many cases. Thus, most CFD packages from commercial software are focused on turbulence models. Therefore, this approach was utilised in this research.

In RANS, the instantaneous pressures (P) and velocities (U) of the system are defined as an addition of time-averaged ($\bar{U}$, $\bar{P}$) and fluctuating (u', p') values, as seen in Figure 2.15.

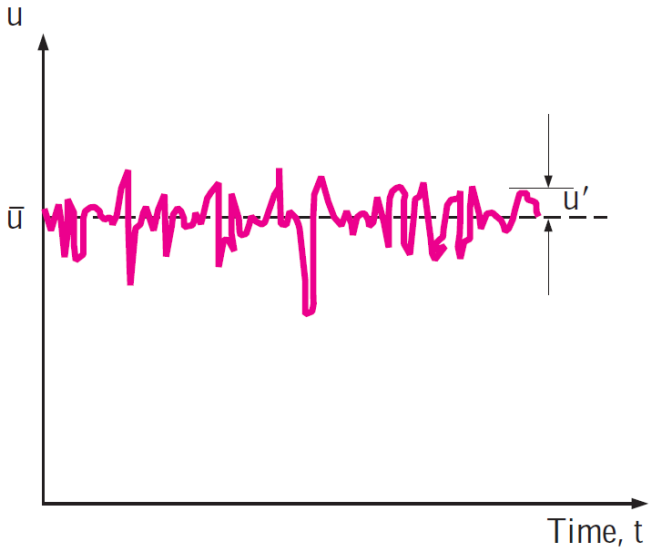

Figure 2.15 Time-averaging with the RANS formulation (Çengel & Cimbala, 2006b)

When modelling any fluid flow it is very important to know if it is going to be considered compressible or incompressible. In the present work, SC water was considered an incompressible flow at isobaric and steady conditions. Liquid water can be assumed incompressible, although upon reaching critical or PSC state, the density decreases to a state between liquid and gas and thus its compressibility must be clarified. This is important, because Comsol offers different physics options depending on this fact. A flow is considered compressible when the density is strongly dependent on the system pressure. It has been experimentally established that this compressibility onset is reached when the flow Mach number surpasses 0.3, and thus density variations in the system would become higher than ~4%. By considering a range of scenarios in the simulations, it was determined that the Mach number would be below 0.3 as long as the fluid mass flux (G) was lower than 13,000

kg m^{-2} s^{-1} approximately, which was out of the scope of the present thesis. As a consequence, the flow was established as incompressible.

Thus, for a 2D steady, incompressible flow applying the boundary layer approximation (radial velocities are negligible compared to axial velocities and axial variations are negligible compared to radial variations) the RANS equation is reorganised (Davidson, 2015) as seen in (2.16).

$$\frac{\partial \rho \bar{U}^2}{\partial x} + \frac{\partial \rho \bar{U}\bar{V}}{\partial y} = -\frac{\partial \bar{P}}{\partial x} + \frac{\partial}{\partial y}\left(\mu \frac{\partial \bar{U}}{\partial y} - \rho \overline{u'v'}\right) \quad \textbf{(2.16)}$$

$$\tau_{total} = \mu \frac{\partial \bar{U}}{\partial y} - \rho \overline{u'v'} \quad \textbf{(2.17)}$$

In equation (2.16), the LHS is composed of 2D velocity components. On the other hand, the first term of the RHS considers the pressure component, while the second term is the total shear component (τ_{total}), as seen in equation (2.17). τ_{total} is represented by a viscous term that considers the friction between layers along the flow ($\mu \frac{\partial \bar{U}}{\partial y}$), and a non-linear term that accounts for the non-computed turbulent shear stress from the friction between eddies and the mean flow, named Reynolds stress ($\overline{u'v'}$). As a means to replace the velocity fluctuations with a mean flow and close the equation, the Reynolds stress must be modelled. Depending on a linear or non-linear relationship between the Reynolds stress term and the mean flow, the accuracy and complexity of the approximations are different. As a consequence, several RANS turbulence models have been developed, as seen in Figure 2.16.

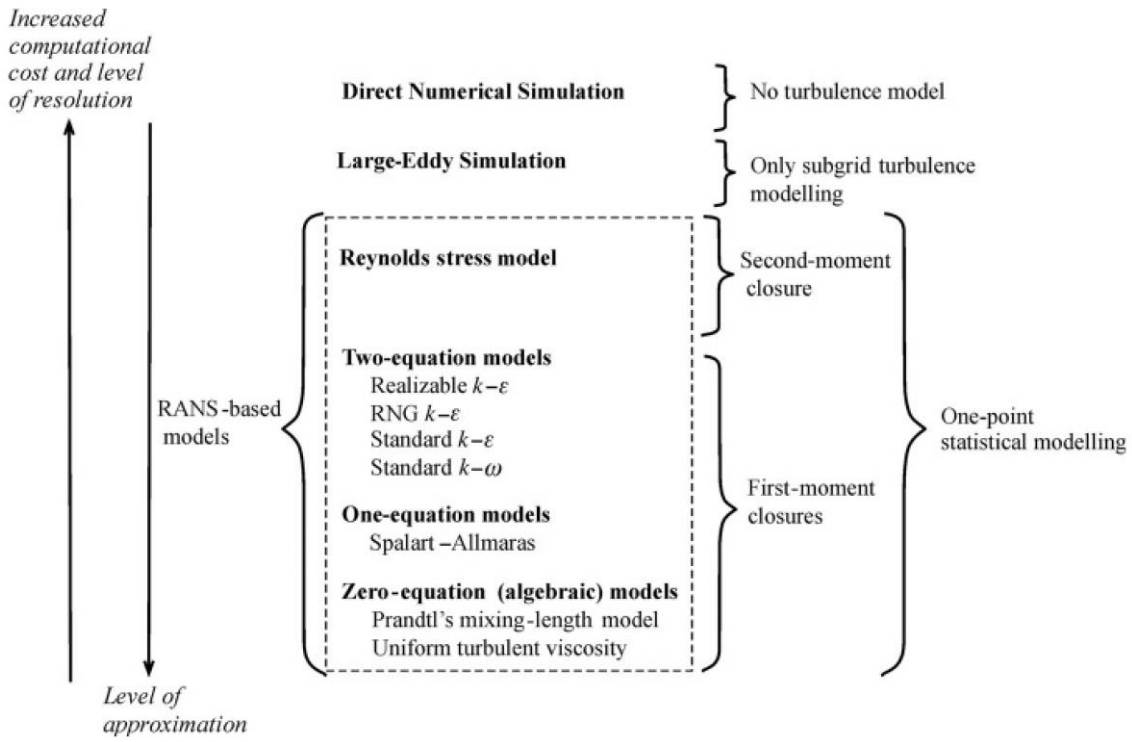

Figure 2.16 Schematic of turbulence models (Andersson *et al.*, 2012)

The most commonly employed turbulence models use the Boussinesq approximation (Wilcox, 1993), relating $\overline{u'v'}$ linearly to velocity gradients by employing a non-physical parameter, called turbulent or eddy viscosity (μ_T). This is a first-order closure method, and thus only the isotropic behaviour of turbulence is considered. As a result, they are only applicable in simple turbulent shear cases, when the model geometry does not trigger secondary flows. This is the case of internal flows using circular tubes, and because this was the main geometry employed in the present research, these were the turbulence models employed in the present thesis, further described in the Appendix. With this approximation, τ_{total} is replaced by the equation (2.18), displaying a laminar (τ_{lam}) and a turbulent (τ_{turb}) shear stress component.

$$\tau_{total} = (\mu + \mu_t)\frac{\partial \overline{U}}{\partial y} \quad \textbf{(2.18)}$$

The typical radial profiles of τ_{lam} and τ_{turb} obtained with these models are shown in Figure 2.17, where y represents the radial distance from the wall. As can be seen, τ_{total} is equal to τ_{lam} on the wall, because τ_{turb} is zero. However, further away from the wall, τ_{lam} is negligible compared to the τ_{turb} produced by the vortices.

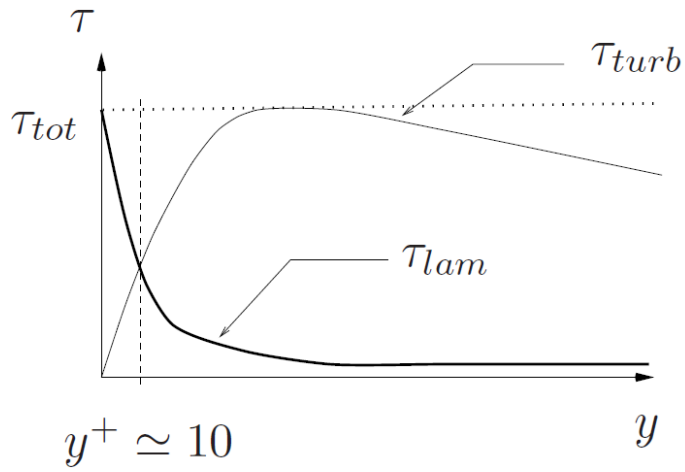

Figure 2.17 Caption showing the laminar and turbulent shear stress profiles (Davidson, 2015)

2.3.4. COMSOL Multiphysics

As further described in Section A.5 from the Appendix, when all the necessary equations to define the physics related to a model are accounted for, the system of partial derivative equations (PDEs) obtained is solved by applying a discretisation method. The three most common methods are the finite-difference method (FDM), the finite-element method (FEM) and the finite-volume method (FVM). A comparison of the three methods is represented in Table 2.3.

Table 2.3 Comparison of the main discretisation methods (adapted from Sjodin, 2016)

Discretisation Method	Finite-Difference Method	Finite-Element Method	Finite-Volume Method
Main Features	▪ Most direct approach to discretizing PDEs. ▪ Defined on rectangular CAD geometries. ▪ Continuum representation of equations in a point of space is replaced with discrete equations.	▪ CAD model subdivided in small finite-sized simple elements. ▪ A system of PDEs describes the computed physics for each element, approximating as a simple function. This gives an approximate local description of the physics. ▪ Contributions from all elements are assembled in a large sparse matrix equation system.	▪ CAD model is divided in small finite-sized simple cells. ▪ Formulation based on flux conservation equations averaged over the cells.
Advantages	▪ Easy to increase the “element order” to get higher-order accuracy. ▪ Easiest method to implement if the simulation can be fit in a rectangular geometry. ▪ Efficient and high quality results if the boundary conditions do not fail.	▪ Multi-physics analysis: the equation systems are similar to well-known methods for different physics. ▪ Adaptive mesh refinement: easy to increase the order of discretisation of the elements so the physics fields can be accurately approximated. ▪ Mixed formulations: different functions that approximate the solution within each element can be combined. This is particularly important for multi-physics analysis.	▪ Straightforward implementation. ▪ The PDEs to solve for CFD are conservation laws, natural choice for CFD problems. ▪ Local accuracy can be increased by refining the mesh.
Drawbacks	▪ Curved boundaries might give issues when defining the boundary conditions. ▪ Difficult to use for material discontinuities. ▪ Not easy to use grid refinement when solving local rapid variations.	▪ Most difficult method to implement due to the sophisticated mathematics required. ▪ Most taxing on a computer system (depends on analysis).	The functions approximating the solution are not easily made of higher order.
Applications	Large-scale simulations (meteorological, seismological, astrophysical).	Multi-physics (structural analysis, heat transfer, chemical engineering, electromagnetics, CFD).	CFD problems, also heat transfer and chemical engineering.
Packages	MATLAB	COMSOL Multiphysics	OpenFOAM, FLUENT, STAR-CCM+

Commercial CFD packages possess a series of strengths and weaknesses even if they employ the same discretisation method. In Table 2.4 a comparison is described, where the positive symbol (+) is indicative of a particular advantage, the negative symbol (-) is indicative of a weakness and the equal symbol (=) refers to an intermediate feature.

Table 2.4 Comparison of different CFD packages (adapted from Begall & Krieger, 2015)

Commercial Package	**COMSOL Multiphysics**	**Ansys FLUENT**	**OpenFOAM**
Discretisation method	FEM	FVM	FVM
Computational Cost	-	+	+
Technical Support	+	+	-
Graphical User Interface	+	=	-
Meshing	+	-	-
Mesh Integration	+	-	-
Turbulence Models	-	+	-
Customisation	-	-	+
Solver Stability	+	+	-
Programming Skills	+	=	-

Compared to the other CFD packages shown in Table 2.4, the FEM software Comsol Multiphysics (version 4.4) was selected in the present work to perform the simulations due to a series of reasons:

- Comsol Multiphysics offers the coupling of a wide range of physics (hence the name), allowing the expansion of research by adding new phenomena such as electric heating or defining a reaction within the flow.
- Comsol has a modular conception, avoiding the use of several sub-programmes for the different simulation steps, described in the Appendix.
- It offers an intuitive graphical interface which makes it approachable from any discipline of science, avoiding the need to possess programming skills.
- There are no numerical analyses related to the thermal performance of SC boilers using Comsol as a FEM analysis, thus the results obtained are expected to offer a novel approach employing a new CFD environment.

Nonetheless, Comsol Multiphysics has been employed for research purposes in a wide range of topics, from clothing technology for human comfort (Sun & Jasper, 2015) to the food industry (Sabarez, 2012).

References

Andersson B, Andersson R, Hakansson L, Mortensen M, Sudiyo R, Wachem BV (2012). Computational fluid dynamics for engineers. In: Andersson B (editor). *Cambridge University Press*

Begall M, Krieger A (2015). An Overview of CFD Tools and Comparison of a 2D Testcase. RWTH Aachen University

Çengel YA, Cimbala JM (2006a). Flow in pipes. In: Çengel, Yunus A. Fluid Mechanics. Fundamentals and applications. *McGraw-Hill*; pp. 321-82

Çengel YA, Cimbala JM (2006b). The Navier-Stokes equation. In: Çengel, Yunus A. Fluid Mechanics. Fundamentals and applications. *McGraw-Hill*; pp. 426-31

Chen W, Fang X, Xu Y, Su X (2015). An assessment of correlations of forced convection heat transfer to water at supercritical pressure. *Annals of Nuclear Energy*; 76: 451-60

Davidson L (2015). An introduction to turbulence models. Department of Thermo and Fluid Dynamics *Chalmers University of Technology*; 97/2

Hirsch, C (2007). Volume 1 – Fundamentals of Computational Fluid Dynamics. In: Butterworth-Heinemann (editor). Numerical computation of internal and external flows. *Elsevier*

Hoffmann K, Chiang ST (2000). Computational fluid dynamics Volume III. Fourth edition. In: Duvall J (editor). *Engineering Education System*

Huang D, Wu Z, Sunden B, Li W (2016). A brief review on convection heat transfer of fluids at supercritical pressures in tubes and the recent progress. *Applied Energy*; 162: 494-505

Jäger W, Sánchez-Espinoza VH, Hurtado A (2011). Review and proposal for heat transfer predictions at supercritical water conditions using existing correlations and experiments. *Nuclear Engineering and Design*; 241: 2184-203

Jackson J, Hall W (1979). Influences of buoyancy on heat transfer to fluids flowing in vertical tubes under turbulent conditions. *Turbulent Forced Convection in Channels and Bundles;* 2; 613-40

Löhner R (2008). Applied Computational Fluid Dynamics Techniques: An Introduction Based on Finite Element Methods, Second Edition In: John Wiley & Sons (editor). *Wiley*

Mokry S, Pioro I, Farah A, King K, Gupta S, Peiman W, Kirillov P (2011). Development of supercritical water heat-transfer correlation for vertical bare tubes. *Nuclear Engineering and Design*; 241:1126–36

Oberkampf WL, Trucano TG (2002). Verification and validation in computational fluid dynamics. *Progress in Aerospace Sciences*; 38: 209-72

Pioro IL, Khartabil HF, Duffey RB (2004). Heat transfer to supercritical fluids flowing in channels—empirical correlations (survey). *Nuclear Engineering and Design*; 230: 69–91

Pioro IL, Duffey RB (2005). Experimental heat transfer in supercritical water flowing inside channels (survey). *Nuclear Engineering and Design;* 235: 2407-30

Pioro, I (2014). Application of supercritical pressure in power engineering: specifics of thermophysical properties and forced-convective heat transfer. In: Anikeev V, Fan M (editors). Supercritical fluid technology for energy and environmental applications. *Elsevier;* pp. 210

Rahman MM, Dongxu J, Beni MS, Hei HC, He W, Zhao J (2016). Supercritical water heat transfer for nuclear reactor applications: A Review. *Annals of Nuclear Energy*; 97: 53-65

Schmidt E, Eckert E, Grigull V (1946). Heat transfer by liquids near the critical state. *Air Materials Command*; 527

Sun Y, Jasper WJ (2015). Numerical modelling of heat and moisture transfer in a wearable convective cooling system for human comfort. *Building and Environment*; 93: 50-62

Sabarez HT (2012). Computational modelling of the transport phenomena occurring during convective drying of prunes. *Journal of Food Engineering*; 111: 279-88

Torres R, Grau J (2007). Introduction to fluid mechanics and heat transfer with Comsol Multiphysics (Spanish version only). *Addlink media*

Vikhrev YV, Barulin YD, Kon'kov AS (1967). A study of heat transfer in vertical tubes at supercritical pressures. *Thermal Engineering*; 14(9): 116-19

Wilcox DC (1993). Chapter 3 – Algebraic models. In: Wilcox DC (editor). Turbulence modelling for CFD. *DCW Industries, Inc.*; pp. 23-67

Winterton RHS (1998). Where did the Dittus and Boelter equation come from? *International J. Heat Mass Transfer;* 41, 4-5: 809-10

Yamagata K, Nishikawa K, Hasegawa S, Fujii T, Yoshida S (1972). Forced convective heat transfer to supercritical water flowing in tubes. *Int. Journal of Heat Mass Transfer;* 15: 2575-93

Websites:

Sjodin, B (2016). What's The Difference Between FEM, FDM, and FVM? Available from: http://machinedesign.com/fea-and-simulation/what-s-difference-between-fem-fdm-and-fvm

3. Numerical validation in 2D using experimental data

Gil-Garcia AA, Kings IN, Al-Duri B

Abstract

In an approach to study the heat transfer performance of supercritical boilers, this study validates the capability of the computational software Comsol Multiphysics to simulate turbulent convective flows at supercritical conditions, employing external experimental data. A set of working conditions as well as the physical model was taken from the data produced by Yamagata *et al.* (1972). The Shear Stress Transport model was employed to simulate supercritical water implemented as new material upwardly flowing, while constant heat flux was applied on the wall at steady conditions. Using a two-dimensional geometry, several mesh distributions and near-wall refinements were attempted. Small values of y_1^+ were recommended along with second discretisation order if possible. Mild deterioration was found and several parameters accounting for buoyancy, thermal acceleration and property change were employed complemented with a study of hydrodynamic and thermodynamic properties. These parameters and properties were used to explain the heat transfer performance as a result of a balance between turbulence and large property variations. Postprocessed 2D images depicting hydrodynamic and thermal parameters were analysed, reflecting better turbulence and heat transfer performance near the wall at the entrance and outlet regions of the pipe. Moreover, some laminarisation was experienced towards the end of the pipe as a result of the bulk of the flow displaying larger values of mass flux and acceleration.

Keywords: supercritical heat transfer, turbulent convective modelling, Comsol Multiphysics.

Industrial Relevance

The importance of process simulation in both company and academia stems from the ability to foresee and assess the physical performance of the system, avoiding the scale-up procedures from laboratory to pilot plant. This allows determining if the process under study is feasible, efficient and profitable using a quicker, safer and more economical technique. Before undertaking these simulations, the software employed needs to be validated as a means to grant the veracity of the results obtained. In this work, the performance of 2D simulations with the software Comsol Multiphysics was validated by trying to reproduce similar boundary conditions employed in previous experimental studies.

Abbreviations

CFD	computational fluid dynamics
CFPP	coal-fired power plant
DB	Dittus-Boelter
DOF	degrees of freedom
HTC	heat transfer coefficient
HTD	heat transfer deterioration
HTE	heat transfer enhancement
LPV	large property variation
NHT	normal heat transfer
NPP	nuclear power plant
PDE	partial differential equation
PSC	pseudo-critical
RANS	Reynolds-averaged Navier-Stokes
SC(F)	supercritical (fluid)
SCHT	supercritical heat transfer
SST	shear stress transport
TKE	turbulent kinetic energy

Dimensionless numbers

Bo	buoyancy parameter
Gr	Grashof number
K_v	thermal acceleration parameter
Nu	Nusselt number
Pr	Prandtl number
Re	Reynolds number

Greek symbols

α	thermal diffusivity [$m^2\ s^{-1}$]
β	volumetric expansion coefficient [$degC^{-1}$]
λ	thermal conductivity [$W\ m^{-2}\ degC^{-1}$]
μ	dynamic viscosity [$kg\ m^{-1}\ s^{-1}$]
ν	kinematic viscosity [$m^2\ s^{-1}$]
π_c	dimensionless parameter measuring thermophysical changes [-]
ρ	density [$kg\ m^{-3}$]
τ	shear stress [Pa]

Geometric definitions

D	tube internal diameter [mm]
L	pipe length [mm]
R	tube inner radius [mm]
r	radial coordinate [mm]
x	axial coordinate [mm]
x/D	dimensionless pipe length [-]
y^+	dimensionless wall distance [-]
y_1^+	dimensionless wall distance of first layer to the wall [-]

Roman symbols

C_p	isobaric heat capacity [J kg^{-1} degC^{-1}]
$\overline{Cp}$	averaged heat capacity [J kg^{-1} degC^{-1}]
F	volume force vector [m s^{-2}]
G	mass flux of water [kg m^{-2} s^{-1}]
g	gravitational acceleration [m s^{-2}]
h	heat transfer coefficient [kW m^{-2} degC^{-1}]
H	enthalpy [J kg^{-1}]
I	identity matrix [-] or turbulence intensity [%]
k	turbulent kinetic energy [m^2 s^{-2}]
p	absolute pressure [bar]
q	heat flux [kW m^{-2}]
T	temperature [K or °C]
U	mean flow velocity [m s^{-1}]
u	axial flow velocity [m s^{-1}]
v	radial flow velocity [m s^{-1}]

Subscripts

$(\dots)_b$	at bulk conditions
$(\dots)_{dht}$	at deteriorated heat transfer conditions
$(\dots)_{in}$	at inlet conditions
$(\dots)_{lam}$	at laminar conditions
$(\dots)_{out}$	at outlet conditions
$(\dots)_{pc}$	at pseudo-critical conditions
$(\dots)_T$	at turbulent conditions
$(\dots)_{turb}$	at turbulent conditions
$(\dots)_w$	at inner wall conditions
$(\dots)_x$	axial increment
$(\dots)_y$	radial increment

3.1 Background

Despite the many advantages of supercritical (SC) boilers in coal-fired and nuclear power plants (CFPPs and NPPs), it is well-known that both forced and mixed turbulent flows of supercritical fluids (SCFs) suffer from heat transfer deterioration (HTD) under specific hydro-thermal conditions (Jackson, 2013; Rahman *et al.*, 2016). One of the approaches to investigate the performance of SC boilers is related to the study of the thermo-fluid dynamics within the water cycle.

When heat is transferred from the inner wall of the boiler pipe towards the bulk of the flow at SC pressure, the water temperature will firstly approach the pseudocritical (PSC) state on the viscous region of the boundary layer, inducing sharp changes in the thermophysical properties of the fluid when the temperature surpasses the PSC point. This is observed as a layer of high heat capacity (C_p), appearing initially near the wall and progressively moving along the flow towards the free stream. The area of effect and fashion of this phenomenon are dependent on the imposed convective conditions, and play a vital role on the efficiency of heat transfer in the system.

Since the first investigations related to supercritical heat transfer (SCHT) were performed in the 40's, an analogy based on SCFs behaving like a liquid-gas mixture in terms of hydrothermal behaviour was approached until the late 70's. Concepts such as pseudo-boiling and pseudo-film boiling were defined applying the knowledge established in the phase change theories. In their reviews, Hall *et al.* (1967), Pioro and Duffey (2005) and Rahman *et al.* (2016) summarised these definitions. Later, a

new approach in order to explain the peculiarities in SCHT was more widely accepted. It consisted of large thermodynamic property variations inducing thermal acceleration effects (in forced-convective flows) and buoyant forces (in mixed-convective flows). These effects combined would produce substantial changes in the shear stress and velocity profiles, and depending on their extent would therefore impair or improve the heat transfer in the system (Jackson & Hall, 1979).

Due to the importance of SCHT in many fluids and applications, and because of the lack of general agreement on the reasons by which HTD is triggered, many studies have been performed; experimentally since the 50's and also numerically since the 70's. Research on SCHT has been focused on several fluids such as water and CO_2, depending on their applications in different industry sectors (Pioro *et al.,* 2011), and the experimental data produced has been particularly useful for numerical validation. Supercritical thermal fluids are widely used in heating and cooling applications, sharing similar performance in terms of heat transfer improvement and deterioration. For instance, water is employed in SC boilers within nuclear or coal-fired power plant systems; while CO_2 is commonly used as surrogate fluid due to its milder critical conditions. Additionally, CO_2 has recently been used in solar energy powered Rankine cycles. On the other hand, helium, air, nitrogen, light hydrocarbons and refrigerants from the halocarbon family have been related to a wide spectrum of industries, ranging from automotive to air conditioning and space engineering. The present study was focused on the application of computational fluid dynamics (CFD) to investigate SCHT using two-dimensional (2D) geometries.

In terms of previous numerical works with SC water and CO_2 under forced-convective conditions, it is noticeable that some authors did not verify the possible influence of buoyancy effects and relied solely on external experimental works instead (Dang & Hihara, 2004; Gou *et al.,* 2010; Li *et al.,* 2011). Often, working conditions employed such as the thermal boundary condition, fluid mass flux, pipe geometry and flow orientation were taken from previous experimental works where only the forced convective status was verified, or at least assumed. As a consequence, this would lead to misleading results if the presence of buoyancy existed but was not accounted for upon presenting forced-convective experimental data (Huang *et al.*, 2016). In contrast, almost all the forced convective investigations found using hydrocarbons and air at SC conditions verified the existence of the convective regime, even if they utilised experimental data from external sources (Mikielewicz *et al.*, 2002; Pizzarelli, 2016). With respect to pipe configurations employed in 2D numerical studies under forced convection, both horizontal and vertical arrangements were used indistinctly, as buoyancy has little or no effect in forced convective flows.

On the other hand, supercritical mixed-convective flows (supercritical flows where forced convection and natural convection forces affect simultaneously the system to some extent) have been largely studied in 2D numerical analysis, and mostly using water as fluid (Wibisono *et al.*, 2015). This interest in researching buoyancy effects in supercritical water systems existed due to the technical difficulties to obtain experimental results compared to fluids like CO_2, which possesses milder temperature and pressure values at the critical point and thus is considered a good surrogate fluid in experimental works.

All the 2D numerical studies on SCHT found under mixed-convective conditions were carried using vertical pipes (He *et al.*, 2008). This was mainly due to two reasons. First, because buoyancy has a stronger impact in vertical configurations and thus it was better investigated. Second, because in vertical flows gravity affects homogeneously the cross-sectional area of the pipe and therefore simplifying approaches such as 2D geometry and axi-symmetry can be applied, saving considerable computational resources. This is not the case for horizontal configurations, where the effect of gravity on the flow would vary with the fluid radial position in the pipe (radial profile). Therefore, three-dimensional (3D) approaches are always recommended when modelling internal horizontal flows of SC fluids subject to buoyancy (Du *et al.,* 2010; Shang *et al*., 2008).

Among the mixed-convective studies on SCHT using 2D vertical pipe configurations, the upward flow was the most commonly studied flow direction, as heat transfer deterioration is triggered under certain heating conditions. This has been the main topic researched by many authors related to nuclear engineering. For instance, they have compared the performance of circular tubes and annular channels (Liu *et al.,* 2013), steady and unsteady behaviour (Dutta *et al.,* 2015), normal and deteriorated conditions (Jaromin & Anglart, 2013) or the interaction between buoyancy and thermal acceleration (Wen & Gu, 2011). SCHT studies devoted solely to downward flows are rare, as the phenomena occurring on this configuration is better known and predicted. Instead, they were included as part of investigations in vertical pipes (van der Kraan *et al.,* 2005).

Most of the aforementioned numerical studies have employed CFD software such as ANSYS FLUENT or STAR-CCM+. However, as far as the author is concerned, no studies have been undertaken yet within CFD when researching SC boiler performance by using the software Comsol Multiphysics.

Numerical analyses allow the validation of experimental work and also the performance of new independent studies. In any of the two cases, it is paramount to initially ensure the reliability of the numerical method by a series of procedures such as mesh independence analyses, choice of the best turbulence model and validation with former experimental data. As a consequence, the purpose of this study is to demonstrate the capacity of Comsol Multiphysics to perform simulations of mixed-convective flows at supercritical conditions. External experimental data developed at supercritical conditions was employed as reference to validate a series of SCHT scenarios. Pressurised water at 300 bar was used as fluid for the computations. Horizontal and vertical systems consisting of a 2D circular pipe were simulated for mesh analysis and experimental validation, respectively. The turbulence model SST was mainly employed and the conjugate heat transfer module was selected. This validation, along with the model verification undertaken in Chapter 4 using reliable numerical data, gave way to the numerical analyses performed in Chapter 5 at real boiler conditions.

3.2 Computational methods

3.2.1 Physical model

The experimental data chosen for validation belongs to the work of Yamagata *et al.* (1972). Due to the working conditions they employed, a certain extent of buoyancy forces affected the system without triggering considerable HTD. These are the boundary conditions this chapter aimed to numerically reproduce. As a consequence, the physical model and the computational domain were adapted from one of their set of working conditions. In their system, a steady, pre-heated turbulent flow of water entered a circular, smooth test section with 7.5 *mm* of internal diameter and 1,500 *mm* of length, heated by applying a low-voltage direct current (heat flux) and mounted either horizontally or vertically upwards. The flow would be circulated in a series of loops in order to increase the bulk temperature enough to reach and surpass the PSC value.

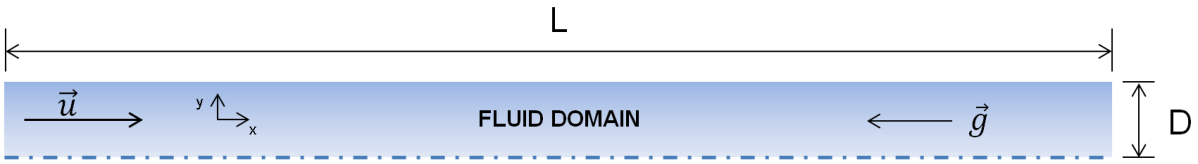

Figure 3.1 Computational domain for the upward flow numerically studied

Nevertheless, in order to save memory resources the present simulations were focused solely on the test section, as shown in Figure 3.1. Axial symmetry was applied and only the fluid domain was considered so the heat flux was applied directly on the flow. Zhang *et al.* (2010) took a similar approach when validating their

model with data from Yamagata *et al.* (1972). In the present study, the same internal diameter of 7.5 *mm* (D) was kept for the test element in order not to modify the balance of forces in the system (viscous, inertial and gravitational), but the required temperature increase could not be achieved in only one pass of the loop for the given combination of heat and mass fluxes. Thus, a pipe long enough to grant the PSC transition in the bulk was investigated at the required working conditions, resulting in a pipe length (L) of 8,000 *mm.* This length provided a continuous wall and bulk temperature curve and also allowed the development of the boundary layer.

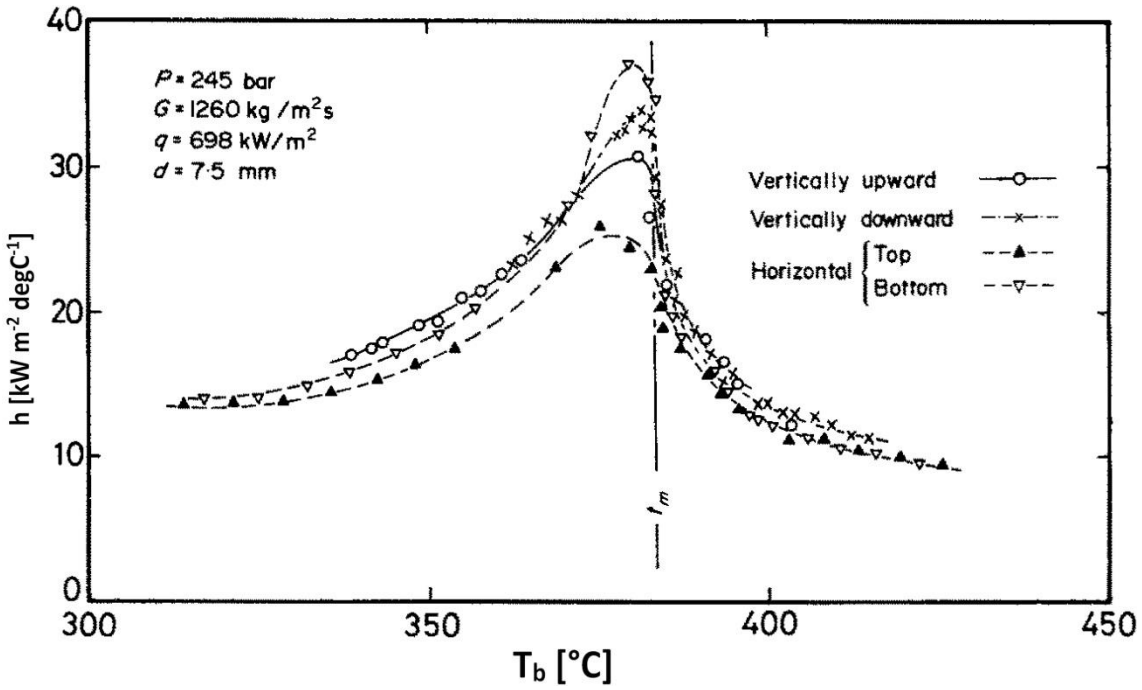

Figure 3.2 HTCs vs. bulk temperature at the selected conditions (adapted from Yamagata *et al.*, 1972)

The heat transfer coefficient (HTC) obtained by Yamagata and colleagues using the experimental rig at the selected working conditions is presented in Figure 3.2. As observed, different results were obtained for the horizontal configurations at the top and the bottom of the pipe; also the vertical configuration revealed different

performance comparing upward and downward flows. As a consequence, their system was affected by buoyancy forces. In vertical flows, buoyancy affects evenly the cross-sectional area of the flow, thus allowing a series of simplifications such as the use of a 2D geometry as well as the application of axial symmetry. These simplifications considerably reduce the computational cost of the simulation and thus were applied in the investigation, employing upward flows to research the possible phenomena affecting the system performance. On the other hand, simulations of horizontal flows subject to buoyancy forces cannot compute the different phenomena accurately using 2D geometries. In these cases, a symmetrical geometry will not produce symmetrical profiles of velocity or temperature if the interaction of the flow with the buoyancy forces is strong.

3.2.2 Governing equations

In these simulations, heat flux was applied on the internal wall of the pipe (solid-fluid interface), so it was transferred to the turbulent flow through convection. As explained in Chapter 2, the equations of mass, momentum and energy balance describing the system were defined applying the Reynolds-averaged Navier-Stokes (RANS) approach and the Boussinesq assumption in order to account for the turbulent phenomena. Shown as equations (3.1), (3.2) and (3.3), respectively, they are further explained in the Appendix.

$$\nabla \cdot (\rho U) = 0 \quad \textbf{(3.1)}$$

$$\rho(U \cdot \nabla)U = \nabla \cdot \left[-pI + (\mu + \mu_T)(\nabla \mathrm{U} + (\nabla \mathrm{U})^T) - \frac{2}{3}(\mu + \mu_T)(\nabla \cdot U)I - \frac{2}{3}\rho k 2I\right] + F \quad \textbf{(3.2)}$$

$$\rho C_p U \cdot \nabla T = -\nabla \cdot q \quad \textbf{(3.3)}$$

3.2.3 Solution methodology

The equations in Section 3.2.2 were coupled with the equations provided by the turbulence model and the system was solved by using the finite element method, implemented in the simulation software Comsol Multiphysics version 4.4. The physical model was converted to a domain wherein discretised elements contained calculation nodes (or degrees of freedom, DOF). In these nodes, the partial differential equations (PDEs) related to the physics of the system were solved using the Newton series. To solve the whole domain the node solutions were interpolated between calculation points using polynomials.

Besides the option to solve the pertaining PDEs from the different physics involved individually and then couple them separately, Comsol offered the possibility to couple them efficiently inside a single package, hence the Multiphysics name. In this case, the Non-Isothermal Flow package was selected to couple turbulent flow with heat transfer in fluids. Simulations were run on an Intel Core i7-3770 processor at 3.40 GHz clock rate with an installed RAM memory of 32 GB on a 64-bit operating system using Windows 7.

3.2.4 Turbulence model

When heating a turbulent flow whose temperature is approaching near the PSC region, also called large property variation (LPV) region, wall effects are very important and will determine the performance of heat transfer. Thus, they must be captured as best as possible in the computations. As further explained in the Appendix, for the present simulations it was decided that the turbulence model had to solve the entire flow field (low-Re model), instead of applying wall functions near the wall. Amongst the low-Re turbulence models available in Comsol, the Shear Stress Transport k-ω (SST k-ω) model was selected (Menter, 1993) because it combined the best features of two turbulence models thus it was capable of accurately solving flows near the wall until the log-law layer (k-ω model) and progressively switch to the k-ε model to solve the free-stream. Many authors have selected it due to its good performance in predicting deterioration in supercritical flows (Rahman *et al.*, 2016), and succeeding at spotting the qualitative trends. The transport equations related to the SST k-w model are described in-detail in works such as the one from Podila *et al. (*2015).

3.2.5 Boundary conditions

The boundary conditions were also adapted from one of the test conditions employed by Yamagata *et al.* (1972). A summary of the boundary conditions defined in the simulations is shown in Figure 3.3. Due to the application of axial symmetry, the pipe

centreline was located on the edge at the bottom of the geometry, while the internal wall was placed at the top.

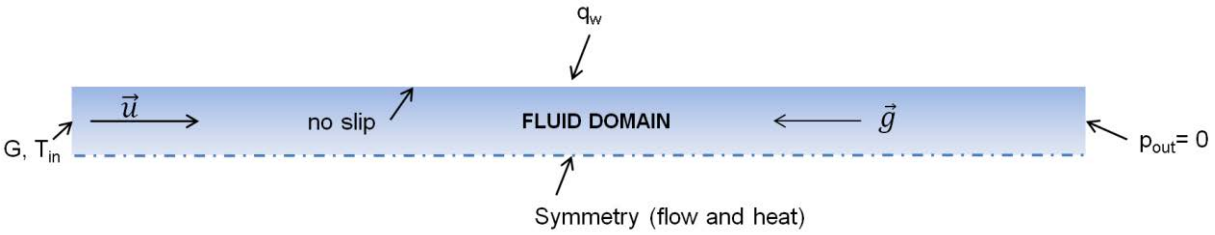

Figure 3.3 Boundary conditions for the upward flow to be computed

Consequently, the water inlet conditions were specified by a flat velocity profile corresponding to a mass flux (G) of 1260 kg m^{-2} s^{-1} and a flat temperature profile of 315°C, coupled with a pressure condition that imposed a value of 0 bar at the outlet. The thermal boundary condition applied on the wall was a heat flux of 698 kW m^{-2}. Due to the consideration of upward flow, axial symmetry was applied at the centre-line of the fluid domain, both for heat and for flow performance. Moreover, no-slip condition was considered at the fluid-solid boundary, and thus strong viscous effects existing near the wall progressively decreased the velocity profile until it reached zero value exactly at the wall surface.

3.2.6 Initial conditions

The program offered the possibility to select the initial conditions for every simulation; however due to the use of a ramping technique, this was used only at the beginning when an isothermal profile was firstly obtained to set the initial temperature. On the following simulations heating was step-wisely applied in magnitude, thus the

isothermal solution (velocity profiles and turbulent parameters) was employed first as initial condition and the solution obtained was used as initial condition for the following simulation and so on. Ramping the thermal boundary condition involved a progressive increase in the fluid temperature, normally between 50 and 200° C depending on the proximity of the system temperature to the pseudocritical point. As the fluid viscosity was defined as a polynomial function dependent on the system temperature, a consequential decrease in viscosity would be triggered step-wise, so turbulence would not be abruptly established. This is considered a good practice in simulation procedures, as it avoids convergence issues with stability given the complex coupling of heat transfer with turbulence over a flow experiencing sharp changes in thermophysical properties.

3.2.7 Implementation of fluid properties

Supercritical water was defined as a material in Comsol by focusing on the isobaric transition region from subcritical to supercritical conditions, where large changes in the thermophysical properties take place. Thus, the thermophysical properties of water were considered to depend only on temperature while the assumption of an isobaric system was made because the test section was short enough to consider pressure drop negligible. In addition, the thermophysical properties of fluids are strong functions of temperature but weak functions of pressure (Withag *et al.*, 2012). By using piece-wise polynomials dependent only on temperature, the material properties were initially defined within a range of temperature that would safely contain all the computed temperatures in the system.

It is worth noting that the selected reference pressure was 245 bar, as Yamagata *et al.* (1972) employed in their experiment, although the research focused on a working pressure of 300 bar as a means to test the implementation of supercritical water as material at a pressure matching the boiler conditions selected for future simulations (300 bar). At 300 bar, the PSC point is triggered at 401.9°C approximately, as obtained from the NIST Standard Reference Database Number 69 by Lemmon *et al.* (2015). Logically, this variation in pressure compared to 245 bar would produce differences in HTC values between simulation and experimental work, given how much the thermophysical properties change as the pressure values surpass the critical point at 220.6 bar, as shown in Figure 3.4.

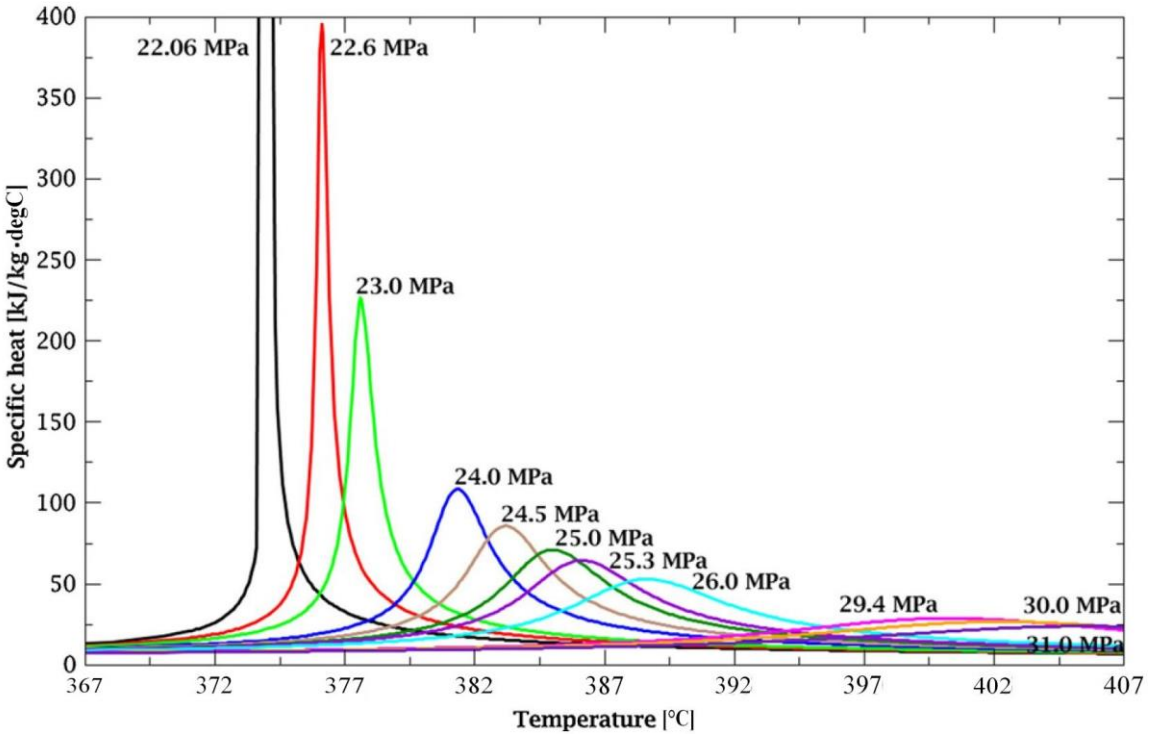

Figure 3.4 Variation of heat capacity along temperature at different pressures (adapted from Jäger *et al.*, 2011)

Compared to the system performance at 245 bar (24.5 MPa), the thermophysical property changes are considerably smoother when the flow temperature is near the LPV region at 300 bar, thus muffling the influence of parameters such as buoyancy or flow thermal acceleration. Nevertheless, comparisons were based on qualitative trends at different pressures rather than quantitative, and taking into account the different system responses. As a matter of fact, Yamagata and colleagues did carry experimental works at conditions close to 300 bar (at 294 bar), however the data presented was scarce and difficult to extract from the produced plots. On the other hand, the data they obtained and presented at 245 bar was prone to more accurate interpretations.

3.2.8 Discretisation

Thermophysical properties of water depend on the temperature profiles obtained, and therefore on the solution, making the problem non-linear. In an attempt to keep a balance between computational time and accuracy, it was established to keep a first-order discretisation in all the simulations. In those conditions, the discretised domain was around one million of DOF for the mesh employed and the computational time was 24 hours. Some simulations were computed using a second-order discretisation, and it was observed that the number of DOF increased to 3.5 million for the same mesh, and the computation time was 1.5 times higher.

3.2.9 Mesh generation and distribution

Given the computational domain in 2D was rectangular, the mesh was created by using a mapped technique with a standard axial distribution of 4,000 elements displaying an element ratio of 5 distributed arithmetically and symmetrically. This was selected with the intention to make the inlet and outlet sections more refined in order to improve accounting for effects like the development of the boundary layer at the inlet or the achievement of the PSC transition near the end of the pipe.

The radial distribution of the mesh was more relevant due to the wall effects produced by the applied heat flux affecting the thermophysical properties and eventually turbulence near the wall. Unlike what happens in 3D geometries, if no mesh was specified for the fluid domain in a 2D geometry, the software assigned the boundary layer (produced to refine the layers near the wall) to overtake the rest of the fluid domain. This was used to the user's advantage, for a better definition of the radial mesh by controlling two of the parameters in the *Boundary Layer* nodule, namely the number of layers and the stretching factor. These values were adapted from the work of Zhang *et al.* (2010), so initially 40 layers were selected with a stretching factor of 1.2 to completely mesh the radial length of the pipe. In Figure 3.5, an example of the first 7 *mm* at the inlet section of the 2D test element was captured. The pipe inlet was located on the edge at the left side while the pipe centreline was placed on the edge at the bottom side. The wall of the pipe, with a refined grid, was on the edge at the top side.

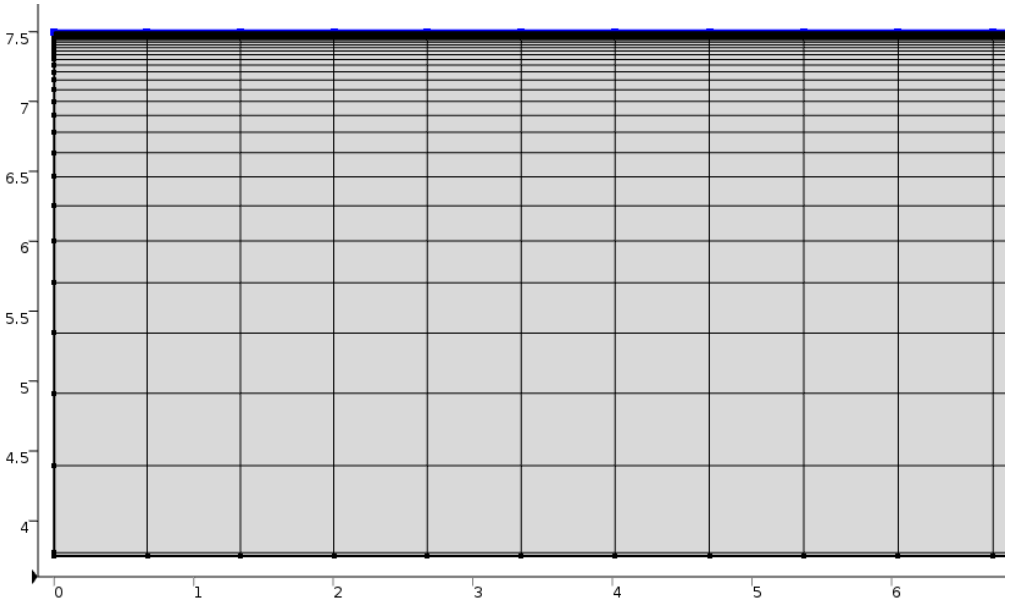

Figure 3.5 Example of the 2D mesh distribution (y-axis as diameter, x-axis as pipe length). Axes shown in *mm*

3.2.10 Near-wall and mesh refinement studies

When modelling heated turbulent flows reaching PSC state with a low-Re turbulence model, the thickness of the first layer, i.e. the dimensionless distance to the wall of the first layer (y_1^+), is more important than the number of radial elements because it determines the extent of consideration of the different phenomena taking place from the wall. This is the third parameter that defined the boundary layer in the program. Following the comments from Zhang *et al.* (2010), a value of y_1^+ below 1 should be chosen if accurate, quantitative results are required.

Similarly, the effect of several axial and radial refinements was tested in order to observe their impact on the results. A mesh is considered independent when a computed parameter such as the temperature profile is plotted throughout different

simulations using finer meshes each time and the differences obtained with respect to the previous simulation drop below a pre-established threshold.

3.2.11 Solver approach

The problem was computed at stationary conditions. As further explained in the Appendix, the solver process was divided in two stages; first to establish the wall distances for the viscous and turbulent interactions, and then proceeding to solve the discretised domain. In both cases, the chosen solvers were direct PARDISO. When the DOF surpasses a certain number, the software would select an iterative solver by default for the second stage as a means to decrease computation time; however that would decrease the convergence stability. Thus, the solver was manually switched to direct.

In the wall distance initialisation stage, the direct solver used a *Full Coupled* nodule to solve the PDEs, as the calculation process in this stage was not complex. However, in the second stage the PDEs were solved in different groups employing a segregated nodule. Three segregated groups were created, each of them employing independent PARDISO solvers and their damping factors were slightly decreased in order to gain stability for the Newton series (explained in the Appendix).

As for the termination technique, a relative tolerance of $1x10^{-6}$ was chosen for both solver stages. Sometimes in the ramping sequence this tolerance could not be

achieved, thus the termination technique was determined by establishing a maximum number of iterations instead.

3.3 Results and discussion

3.3.1 Effect of pressure

The effect of two different system pressures, namely at 245 and 300 bar is investigated. In order to study this effect and also those researched between Sections 3.3.2 and 3.3.4, the 2D simulations were performed horizontally while using the experimental set of conditions used by Yamagata *et al.* (2010) at 245 bar for reference. As previously explained in Section 3.2.1, horizontal configurations under the effect of buoyancy forces should be computed using 3D geometries in order to appropriately capture the different phenomena. However, in this case the study was focused on the performance of the near-wall mesh rather than the interpretation of the quantitative value of the HTC. Moreover, at 300 bar the expected thermophysical changes are not as sharp as at 245 bar, thus the buoyancy effect decreases. As explained in Section 3.2.4, the turbulence model SST was selected to carry the research, although the Low Reynolds (Low Re) model was also employed in certain simulations for comparison purposes.

For a first discretisation order with a y_1^+ of 0.36, a fixed radial distribution of 40 elements and a fixed axial distribution of 4,000 elements, the results are shown in Figure 3.6 representing the HTC (h) versus the bulk temperature (T_b). As can be observed, at 245 bar, the quantitative values of the HTC are only relatively close to the experimental results from Yamagata and colleagues when the T_b is away from the LPV region, although the peaks obtained in the HTC at both pressures are

triggered for every system at values of T_b approaching the corresponding PSC state. As will be explained in Sections 3.3.2 to 3.3.4, these differences between the experimental values and the simulation results are mainly caused by the lack of mesh refinement and the discretisation order. Moreover, the results at 245 bar using the SST the Low Re models reveal very similar performance using the present mesh conditions (refinement and discretisation order).

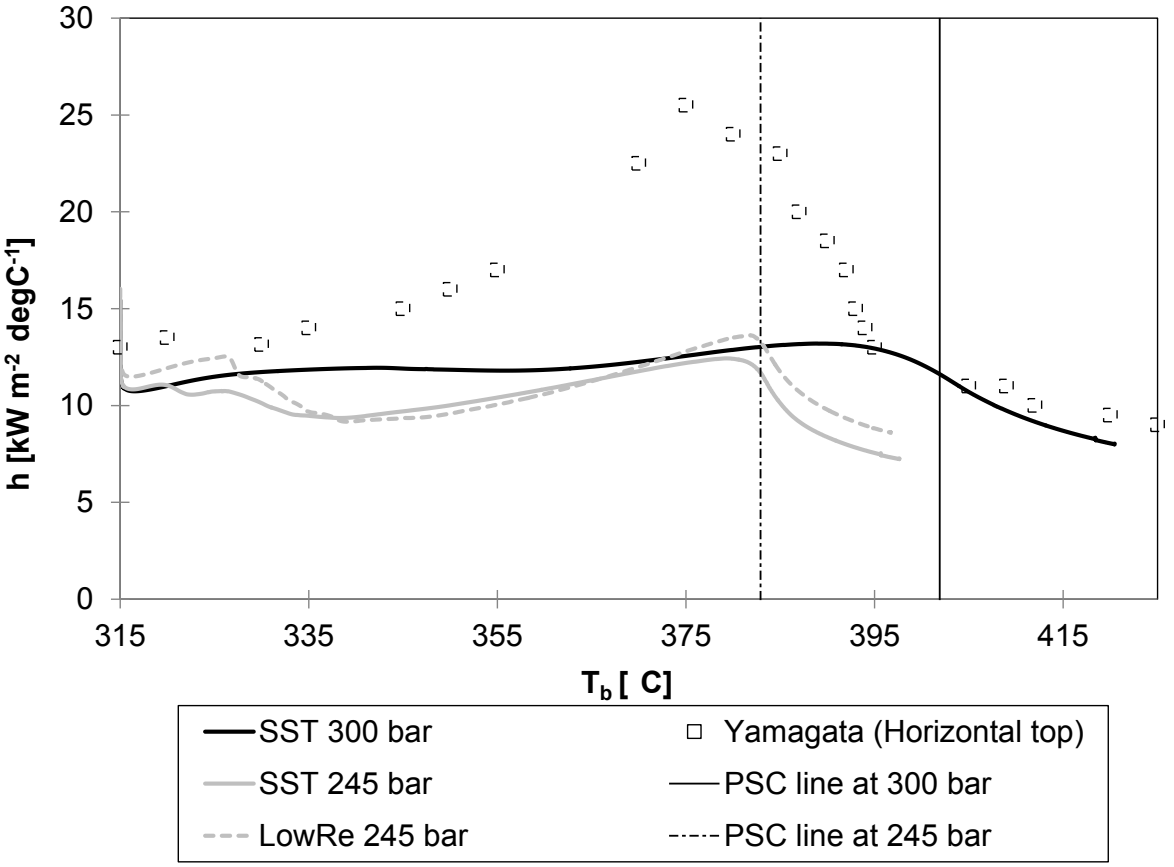

Figure 3.6 Effect of pressure on the HTC profile (245 and 300 bar)

3.3.2 Effect of near-wall refinement

In order to study the impact of the first-layer thickness on the computational results at 300 bar, four different values for y_1^+ were tested at the *Boundary Layer* nodule,

namely 0.36, 1, 5 and 15. Using the flat-plate boundary layer theory (White, 2011) described in the Appendix, the values of y_1^+ were converted to *mm* and specified in the description section of the mesh nodule. As in the previous subsection, a first discretisation order with a fixed radial distribution of 40 elements and a fixed axial distribution of 4,000 elements was researched, only at 300 bar and using the SST model in this occasion. The results are shown in Figure 3.7, representing the HTC (h) versus T_b.

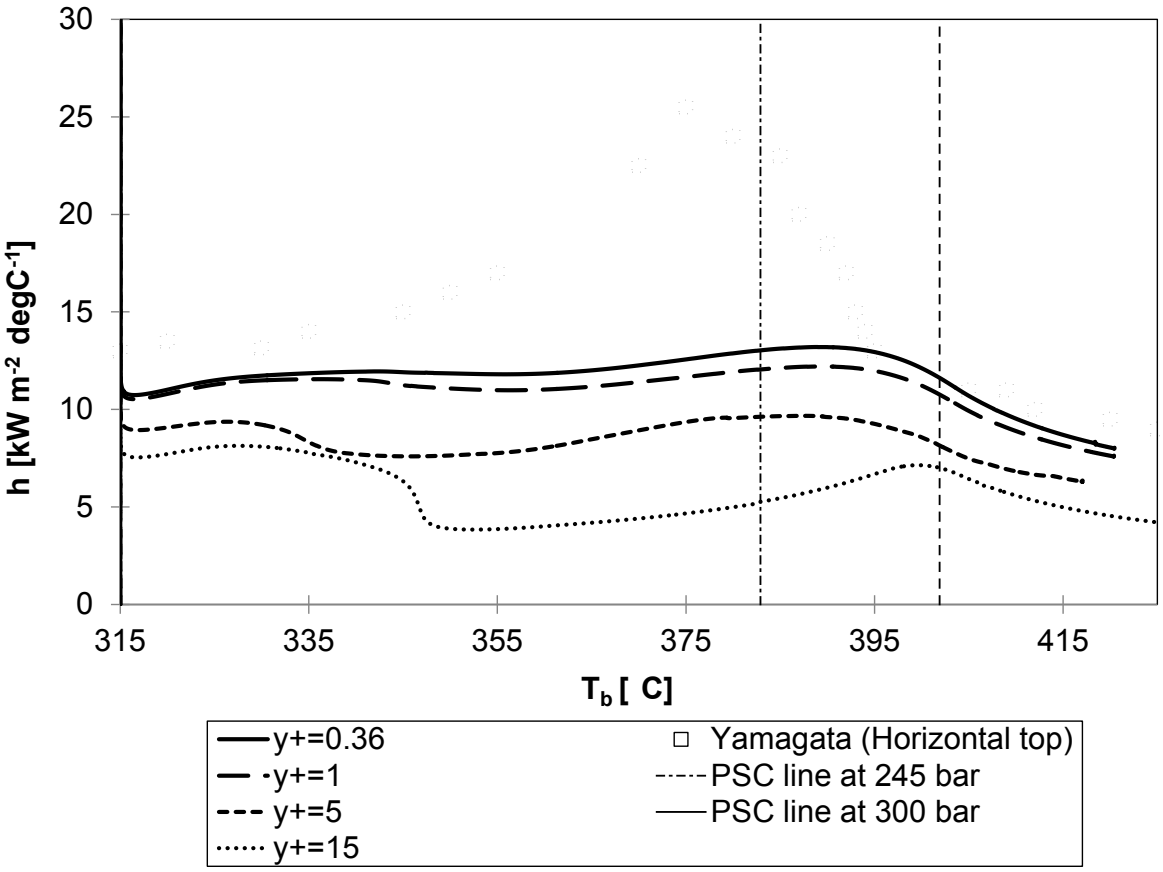

Figure 3.7 Impact of the first-layer thickness on the HTC profile at 300 bar

As can be observed, not only the quantity but also the trend of quality in the HTC results changed with different values of y_1^+, from the thinnest layer (y_1^+=0.36, i.e.

5.07x10^{-4} mm) to the thickest one at the buffer zone (y_1^+=15, i.e. 2.1x10^{-2} mm). The relative error of the HTCs obtained when reducing the values of y_1^+ is observed in Table 3.1. As can be seen, these relative errors decrease to 7.5% and below when comparing simulations whose meshes possess values of y_1^+ below 1, and within this range the highest relative errors are produced when T_b is approaching the PSC value due to the large variations in thermodynamic properties.

Table 3.1 Relative error of HTC values obtained with the refinement near the wall

y_1^+ comparison	T_b [°C]					
	315	**335**	**355**	**375**	**395**	**415**
15 - 5	11.5%	6.5%	50.2%	50.1%	27.8%	23%
5 - 1	14.6%	28%	29.4%	19.8%	22.7%	20.6%
1 - 0.36	3.2%	2.6%	6.9%	7.2%	7.5%	6.2%

All the values of HTC were calculated using the computed results of heat flux on the wall (q_w), the wall temperature (T_w) and T_b as shown in equation (3.4):

$$h = \frac{q_w}{(T_w - T_b)} \tag{3.4}$$

As expected and due to the pressure differences, mild improvements of HTC were triggered for all the values of y_1^+ before the bulk of the flow reached the PSC temperature at 300 bar. These peaks were much smaller compared to the sharp HTC peak obtained by Yamagata *et al.* (2010) before the bulk flow reached the PSC temperature (at 245 bar). Upstream and downstream the point where the bulk flow

surpassed the PSC temperature at 300 bar, the HTC of both experimental results at 245 bar and numerical at 300 bar showed similar values for the smallest values of y_1^+, when the thermophysical properties do not change sharply. On the other hand, when larger values of y_1^+ were employed the quality of the near-wall mesh decreased, and thus an impression of HTD appeared at values of T_b between 335 and 355°C. In that case, misconceptions in heat transfer performance would be induced, accentuated if the results were interpreted using a mesh with y_1^+ in the buffer zone.

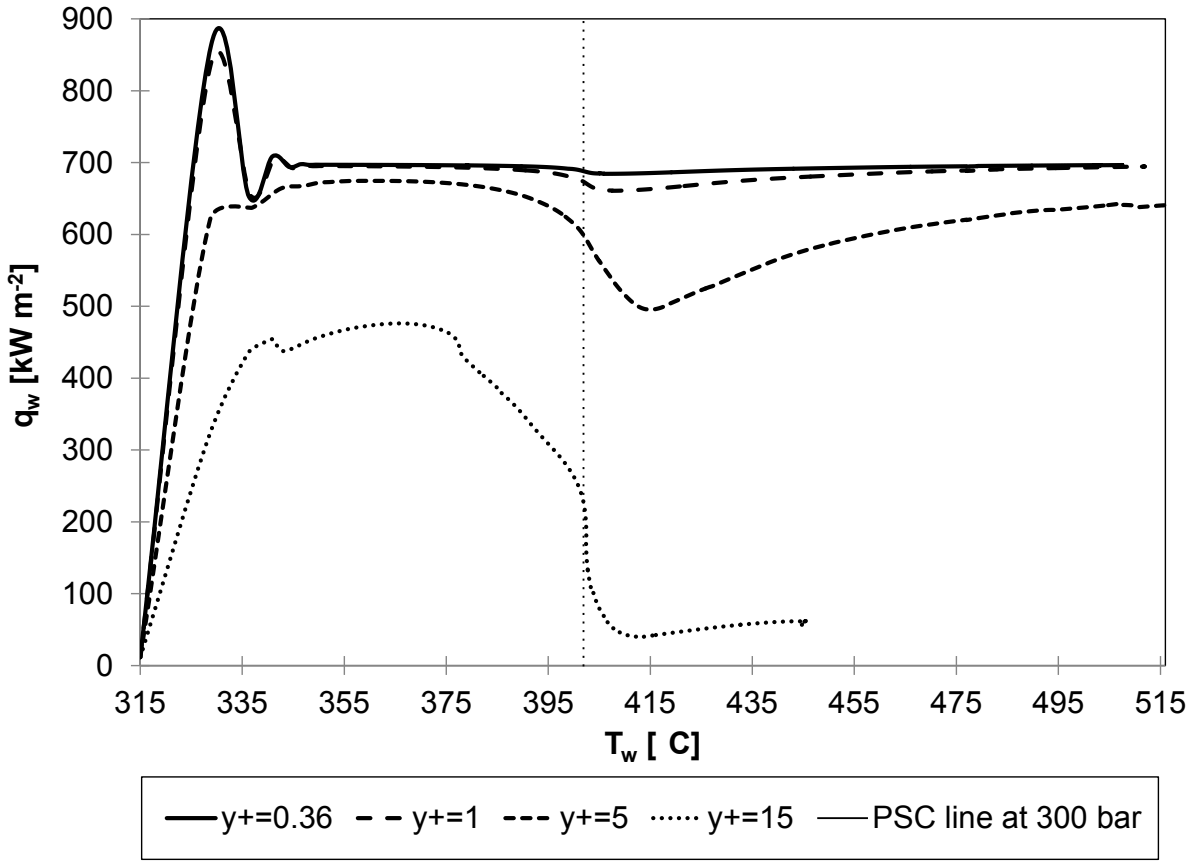

Figure 3.8 Effect of y_1^+ on the performance of the applied q_w at 300 bar

The reason for these deviations relies on the heat flux computed, as depicted on Figure 3.8 from the simulations at 300 bar. The heat flux should remain constant along the wall at a value of 698 kW m^{-2} as it was imposed. At values of y_1^+ equal to 1 or below, the deviation was small, apart from the inlet effects and thus was recommended. However, as the value increased beyond 5, the heat flux profile was dramatically deviated, happening mostly when the PSC temperature was achieved on the wall, triggering sharp changes in the thermophysical properties that could not be accounted for with a poor mesh near the wall. At y_1^+=15 the heat flux was considerably deviated due to the fact that this wall distance fell on the buffer zone, a transition region between viscous and turbulent performance where the law of the wall could be applied.

3.3.3 Effect of mesh refinement

For the study of the mesh performance when modifying axial elements, a value of 0.36 for y_1^+ and 40 radial elements were fixed for the simulations at 300 bar using the SST model. Two axial distributions of 4,000 and 8,000 elements were tested, as well as the effect of refining the inlet and outlet axial distribution with the specifications described in the computational methods. Initially, the results obtained when plotting HTC vs. T_b did not show any noticeable difference between the various axial configurations. But if the heat flux was plotted against the wall temperature, the results are shown in Figure 3.9.

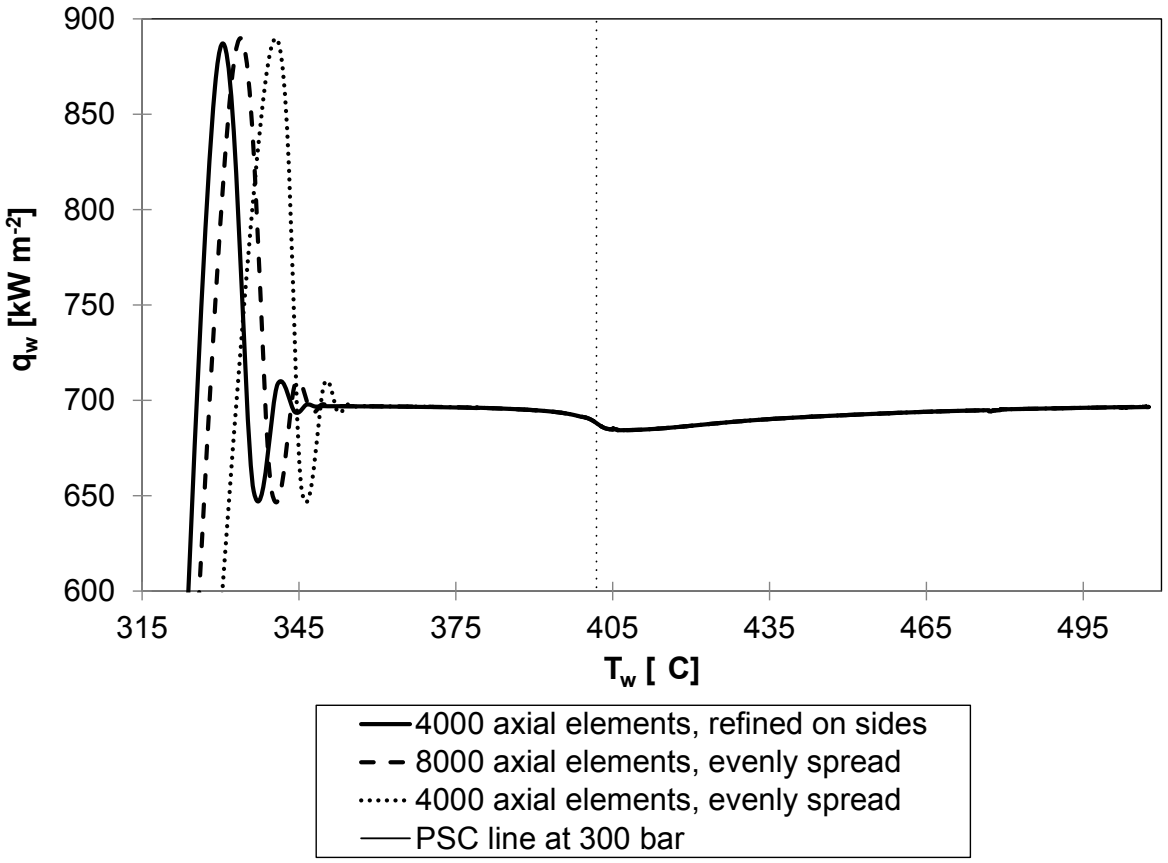

Figure 3.9 Effect of different axial distributions on the wall heat flux at 300 bar

As it is observed in Figure 3.9, the axial mesh of 4,000 elements refined on the inlet and outlet (defined as *refined on sides*) provided stabilisation of the inlet effects at lower values of T_w along the wall before achieving a relatively constant value close to 698 kW m^{-2}. On the other hand, outlet effects did not seem to have any presence, regardless of the distribution. Overall, refining the inlet area seemed to be more efficient than evenly increasing the number of axial elements. This could be seen comparing the previous results with an axial distribution using 8,000 elements evenly spread. This phenomenon likely occurred because the inlet did not present a developed flow combined with the heat shock at the entrance of the pipe.

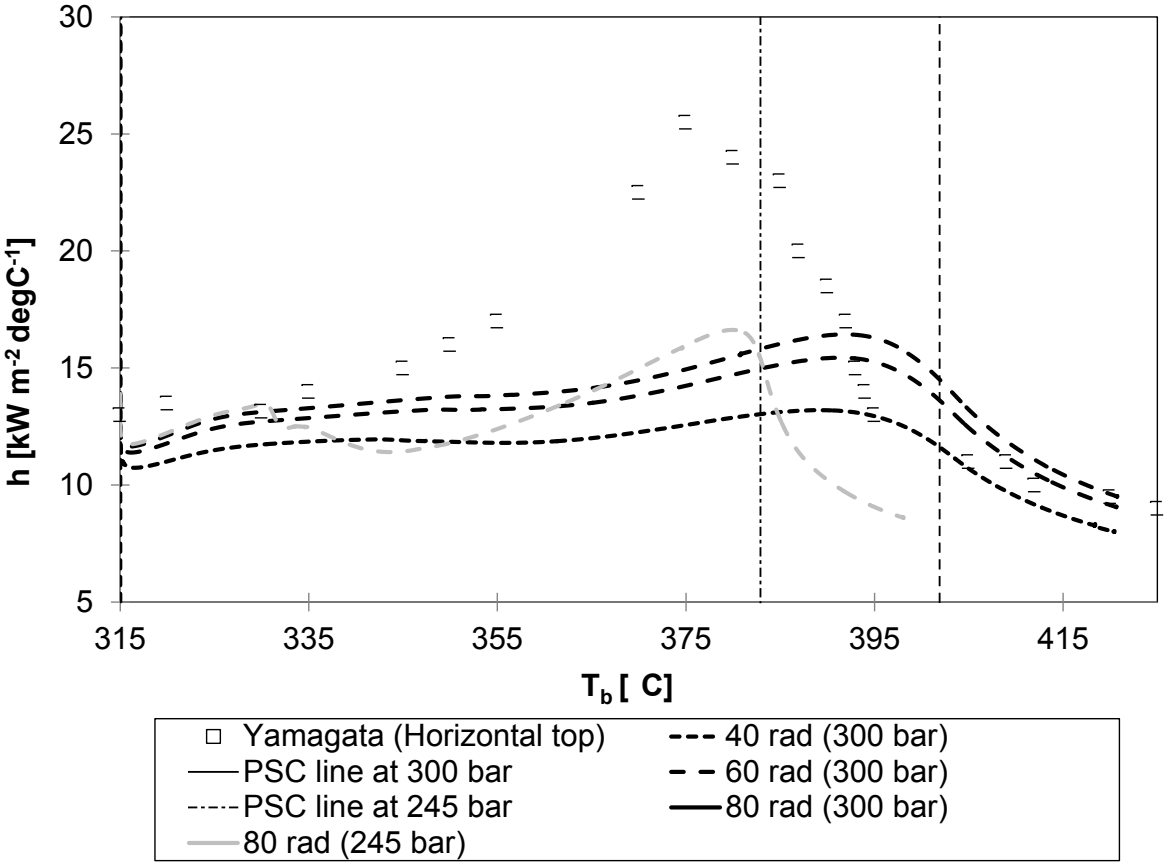

Figure 3.10 Effect of the radial mesh distribution on the HTC profile (245 and 300 bar)

Moreover, the influence of several radial meshes at 245 bar (80 elements) and 300 bar (40, 60 and 80 elements) was tested by fixing the same y_1^+ of 0.36 and an axial distribution of 4,000 elements with the SST model. The simulation results are presented in Figure 3.10, showing an improvement in the values of HTC towards the experimental results at 245 bar using 80 radial elements, compared to the results from Figure 3.6 using 40 radial elements, increasing from approximately 11 to around 17 kW m^{-2} $degC^{-1}$. Similarly, a clear influence of the refinement on the radial mesh distribution is presented at 300 bar, and thus the HTC peak of around 13 kW m^{-2} $degC^{-1}$ shown at 40 radial elements increased to 17 kW m^{-2} $degC^{-1}$ approximately when doubling the radial distribution. In this case, the mesh near the wall did not have any influence on this improvement, as plotting q_w against the T_w did not show

differences for the different radial distributions. Nevertheless, different effects on the bulk flow were found by plotting q_w vs. T_b for the simulations at 300 bar with the SST model, as depicted in Figure 3.11.

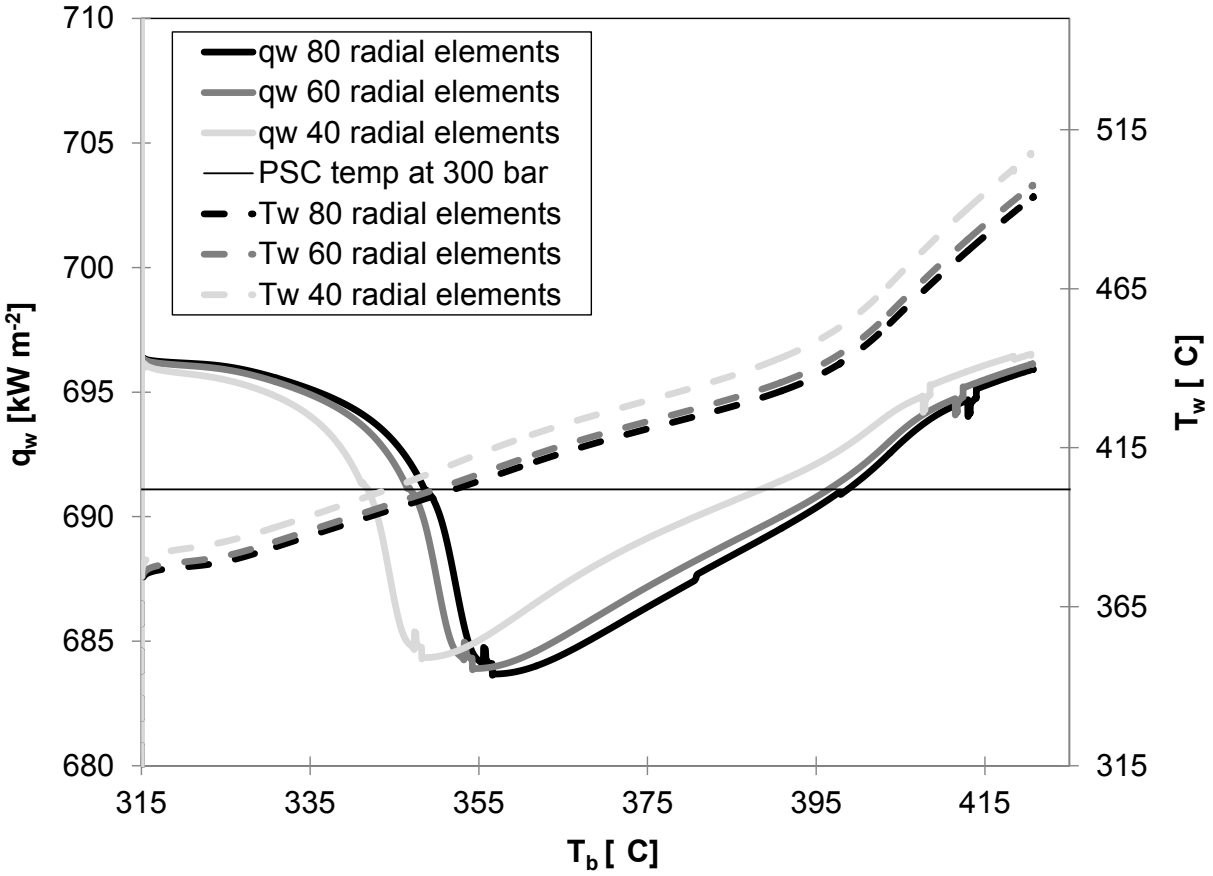

Figure 3.11 Effect of radial distributions on the wall heat flux when computing at 300 bar

As it is observed, wall heat fluxes plotted from simulations using higher number of radial elements dropped at higher values of T_b when the values of T_w had just surpassed the PSC value (due to large thermophysical changes taking place decreasing the performance of the mesh). In this situation, the radial mesh improved near the bulk, and although the impact on HTC was not as strong as when varying y_1^+, the influence could still be seen.

3.3.4 Discretisation study

The effect of increasing the discretisation order was investigated. First and second orders were employed at 245 and 300 bar, using the Low Re and SST models for the same horizontal simulation with a y_1^+ of 0.36, 4,000 axial elements and 40 radial elements. The comparison is shown in Figure 3.12. Prior the LPV region, the results using second order discretisation are very similar to those from Yamagata, regardless the different pressure values and models. Moreover, an increase on the HTC values was depicted in both pressure systems for the second discretisation case, approximating the results to the experimental conditions at 245 bar. However, if both turbulence models produced very similar values of HTC at 245 bar when using first order discretisation, the same simulations with second order discretisation revealed a better performance of the SST model as it approaches more closely the experimental results.

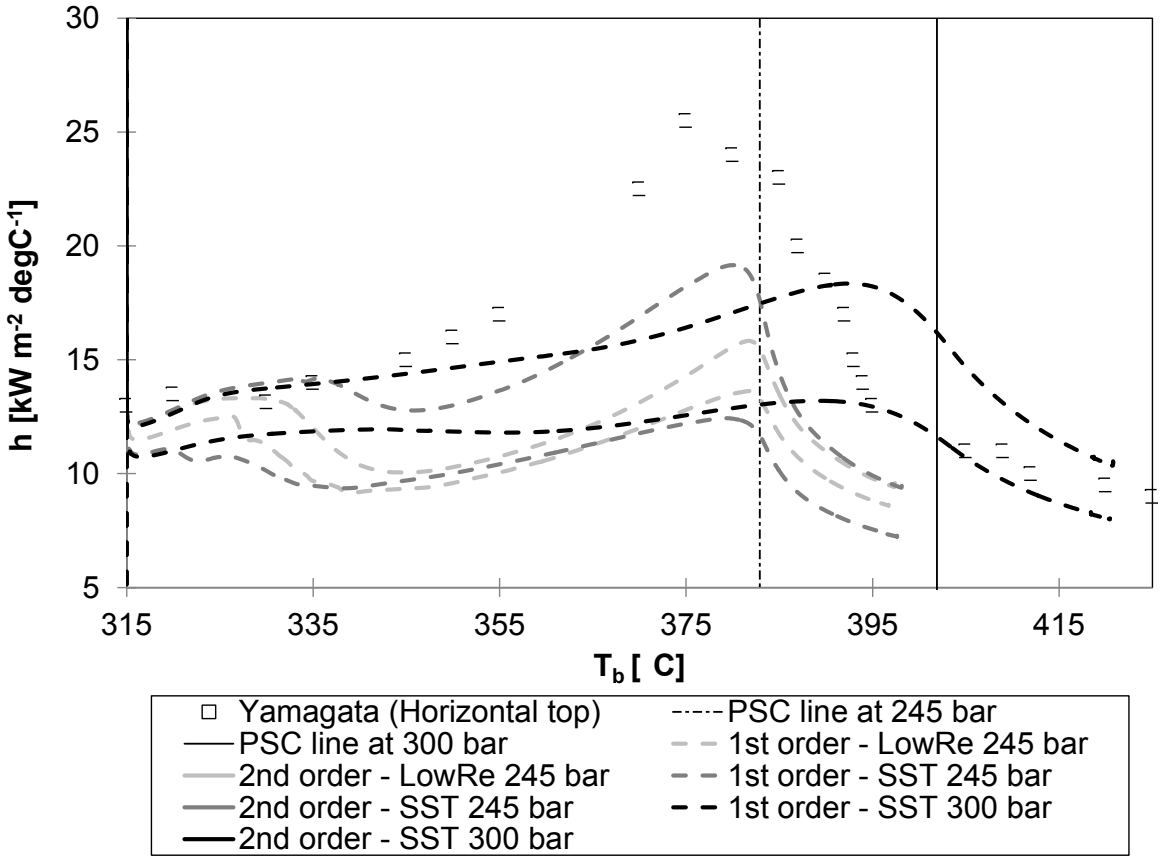

Figure 3.12 Effect of first and second discretisation orders on the HTC profile (245 and 300 bar)

When plotting the profile of the wall heat flux obtained at 300 bar with the SST model against the wall temperature (Figure 3.13), the simulation using second discretisation order revealed a smoother inlet effect, stabilising afterwards on a constant value of heat flux of 698 kW m^{-2} which was not even disturbed by the onset of the PSC point on the wall. The end-value of T_w was around 20°C below using second-order discretisation, which means heat was better transferred to the flow as the higher values of HTC show in Figure 3.12. The most important drawback when using second discretisation order was the increase of the computation time.

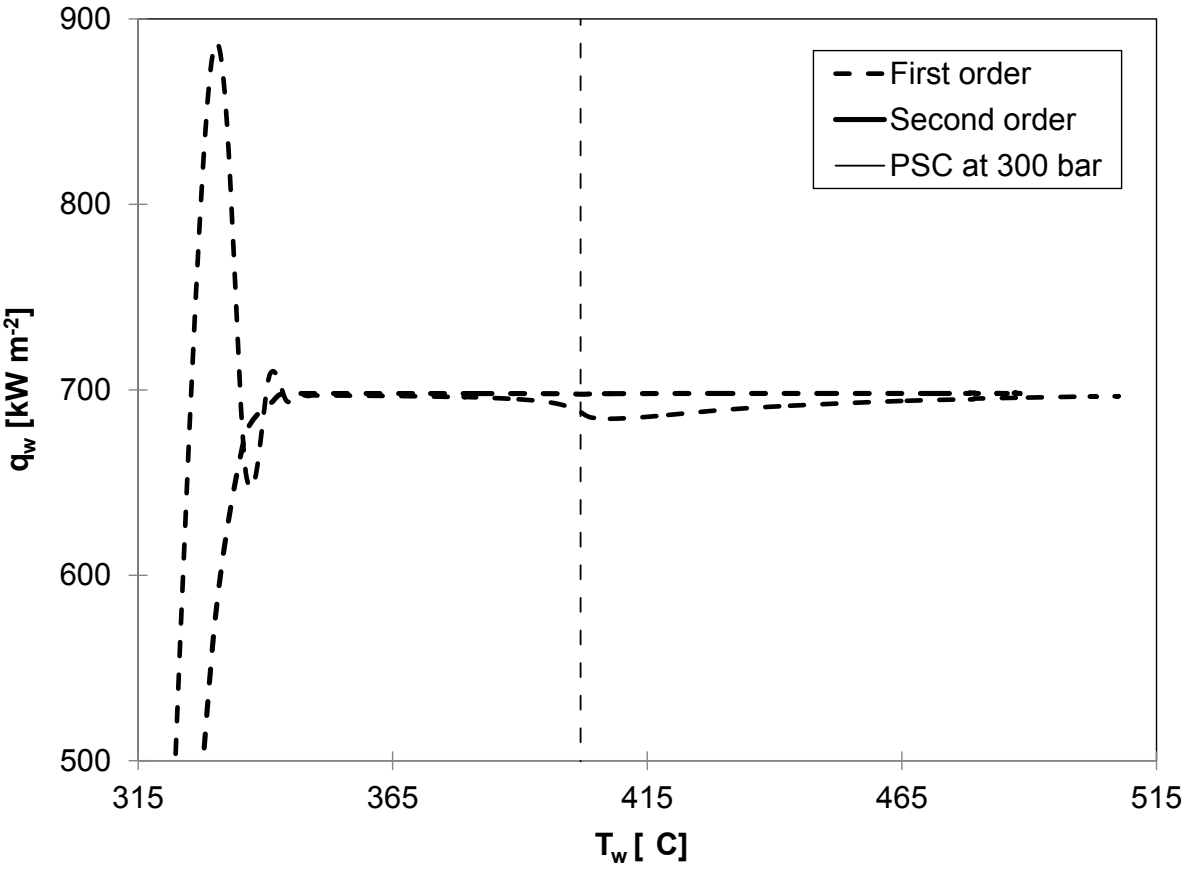

Figure 3.13 Effect of the discretisation order on the wall heat flux obtained at 300 bar

3.3.5 HTD criteria

In their review, Huang *et al.* (2016) highlighted the most relevant correlations created to detect the onset of HTD for a given combination of q_w and G in vertical pipes. These could be also used for horizontal pipes as a conservative criterion, given HTD is always more likely to be produced in upwardly vertical pipes due to buoyancy. Those correlations for water systems and the calculated values for the onset of deteriorated heat flux (q_{dht}) in the present system conditions are summarised in Table 3.2.

Table 3.2 Selected correlations to predict the onset of HTD (q: kW m^{-2}, G: kg m^{-2} s^{-1})

Correlation	Authors	q_{dht} at simulation cond.
$q_{dht} = (1/2.16) \cdot G$	Yin *et al.* (2006)	583.3
$q_{dht} = 0.2 \cdot G^{1.2}$	Yamagata *et al.* (1972)	1050.7
$q_{dht} = 0.58 \cdot G$	Styrikovich *et al.* (1967)	730.8
$q_{dht} = -58.97 + 0.745 \cdot G$	Mokry *et al.* (2011)	879.7

As can be seen, the correlations by Yin *et al.* (2006) and Styrikovich et al. (1967) showed proximity to the onset of deterioration (698 kW m^{-2}) while the other two left some margin before the onset. Therefore, after analysing the aforementioned correlations it could be said HTD might be mildly triggered at the present working conditions.

When HTD is triggered, there are three possible factors involved in SCHT as previously described in Section 3.1; namely large property changes, thermal acceleration of the flow and buoyancy due to gravitational forces. In order to achieve a better understanding in the present simulations about the influence of these factors in the heat transfer phenomenon, some parameters quantifying the aforementioned factors were considered. The property variation parameter π_c, shown in equation (3.5), was developed by Cheng *et al.* (2009) as a means to demonstrate the extent of the large changes in thermophysical properties over the deterioration or heat transfer enhancement (HTE) of heat transfer in the system.

$$\pi_C = \frac{\overline{Cp}}{Cp_b} \tag{3.5}$$

Where $\overline{Cp}$ was the averaged heat capacity, defined by equation (3.6).

$$\overline{C_p} = \frac{H_w - H_b}{T_w - T_b} \quad \textbf{(3.6)}$$

The thermal acceleration effect was measured by employing parameter K_v, as seen in equation (3.7).

$$K_v = \left(\frac{\nu}{U_b^2}\right) \cdot \left(\frac{dU_b}{dx}\right) \quad \textbf{(3.7)}$$

The buoyancy effect for vertical configurations was quantified by the buoyancy parameter (Bo), created by Jackson (2010) and defined in equation (3.8). It compares the relative importance of the buoyant turbulence with the inertial turbulence as a ratio, showing which is more significant.

$$Bo = \frac{Gr_q}{Re^{3.425} \cdot Pr^{0.8}} \quad \textbf{(3.8)}$$

As described in equation (3.9), the definition of the dimensionless value Gr_q involved the consideration of a constant heat flux as thermal boundary condition while all the parameters were evaluated at bulk conditions.

$$Gr_q = \frac{\rho_b^2 \cdot g \cdot \beta_b \cdot q_w \cdot D^4}{\mu_b^2 \cdot \lambda_b} \quad \textbf{(3.9)}$$

Several authors have experimentally obtained various thresholds for which these parameters induce HTD or HTE in SCHT works (Huang *et al.*, 2016). In numerical analysis, although the qualitative trends of a system can be obtained with relatively coarse meshes, the quantitative results are always dependent on the quality of the mesh. For practical reasons, in the present study the mesh refinement was constrained to maintain a balance between computational times ranging from hours to several days and overall performance. Therefore, the aforementioned thresholds were not considered as reference because the quantitative results obtained could be misleading. Instead, the studies were devoted to the analysis of the qualitative trends obtained.

The simulation for the presented study on HTD was carried using the SST model for an upwardly vertical geometry and a mesh with a y_1^+ of 0.36 containing 4,000 axial elements refined on the inlet and outlet, and 80 radial elements. This simulation gave the best results among all the choices using the first discretisation order, although as it was shown in Section 3.3.4 the second discretisation order provided better performance for the horizontal geometry even with a fewer number of radial elements. In order to understand the tendencies of the different phenomena involved, it was decided to focus on the qualitative trends rather than relying on quantitative values, given the system constraints. In Figure 3.14 the results obtained for the computed T_w and T_b and the calculated HTC are shown along the dimensionless pipe length (x/D). The ratio x/D was selected to define the axial coordinates from the perspective of the inlet effects, rather than normalising the pipe length. As can be observed, a slight increase in HTC was produced before the T_w achieved the PSC

value, while a stronger improvement was triggered when the region upstream the bulk approached the PSC point.

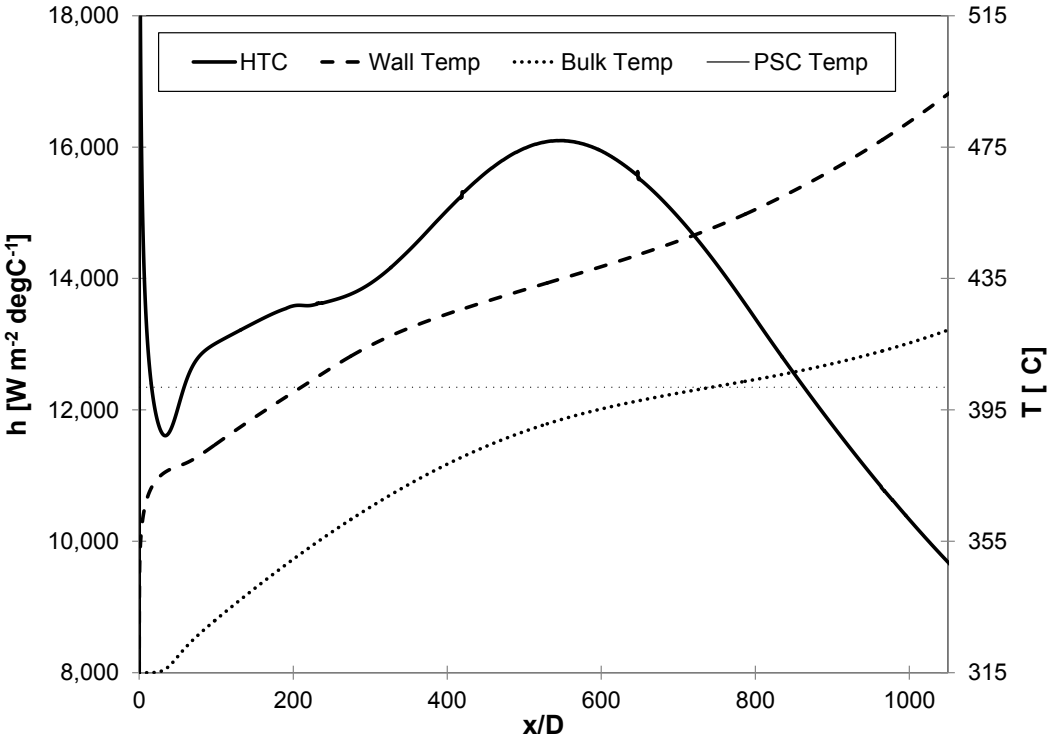

Figure 3.14 Axial profiles of h, T_w and T_b for the upward flow using first-discretisation order

By using several empirical correlations, further described in Section 2.2.3, the system performance at supercritical conditions was compared to an equivalent subcritical system. The correlation by Dittus-Boelter (Winterton, 1998), henceforth called DB correlation, was conceived for forced-convective flows at subcritical conditions considering constant thermophysical properties. As shown in Figure 3.15, as long as the working conditions were away from the LPV region, the DB correlation was closer in magnitude to the computed results, with a HTC of 20,000 W m^{-2} $degC^{-1}$ approximately at the inlet (x/D=0) until an axial location of x/D close to 400 approximately. That was the region under the normal heat transfer (NHT) regime.

Downstream this point, the bulk of the flow started approaching the LPV region and thus the DB correlation was no longer valid, diverging from the computed result. Once the LPV region was being surpassed, at an axial location near the outlet, the NHT regime was recovering again and thus the HTC from the DB correlation was starting to stabilise.

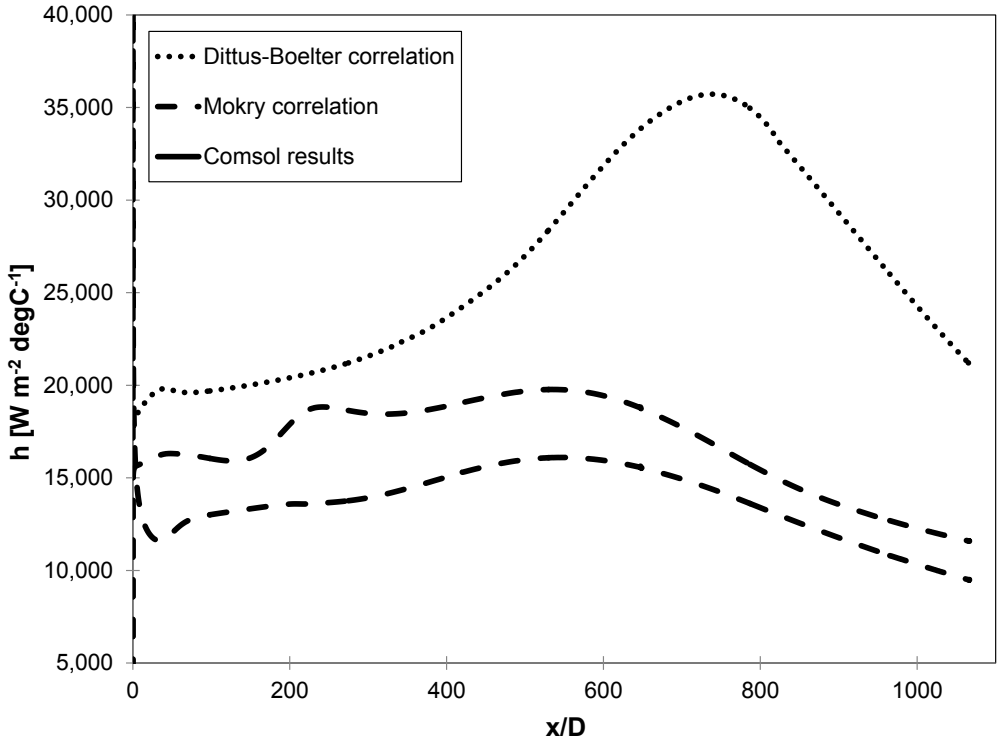

Figure 3.15 Axial profiles of HTC produced with two empirical correlations and the simulation results

On the other hand, the supercritical correlation by Mokry *et al.* (2011), henceforth called Mokry correlation, was defined in Section 2.2.3 along with its range of operating conditions. After comparison, this correlation was considered applicable in the present computations and produced an axial profile of HTC much closer to the computed values than the results from the DB correlation, also defined in Section 2.2.3, as shown in Figure 3.15. Nevertheless, the Mokry correlation was created for

supercritical flows under forced-convective conditions, i.e. accounting for large thermophysical property changes only and excluding additional forces such as buoyancy or thermal acceleration. Thus, any noticeable difference in the HTC profile compared to the computed results can be considered to be caused by the aforementioned effects. Moreover, at the pipe outlet when leaving the LPV region, the HTC profiles from the computed results and the Mokry correlation showed smaller values compared to the inlet prior to the LPV region, which revealed some kind of deterioration.

In order to interpret if the HTC profile was affected by the aforementioned parameters, a series of Nusselt numbers (Nu) related to the DB and Mokry correlations and the computed results (Nu_{DB}, Nu_{Mokry} and Nu_{Comsol}, respectively) were calculated and displayed in ratios depending on the effects of interest. Figure 3.16 shows the Nu_{Comsol} over the Nu_{DB} along the pipe (henceforth defined as Nu ratio).

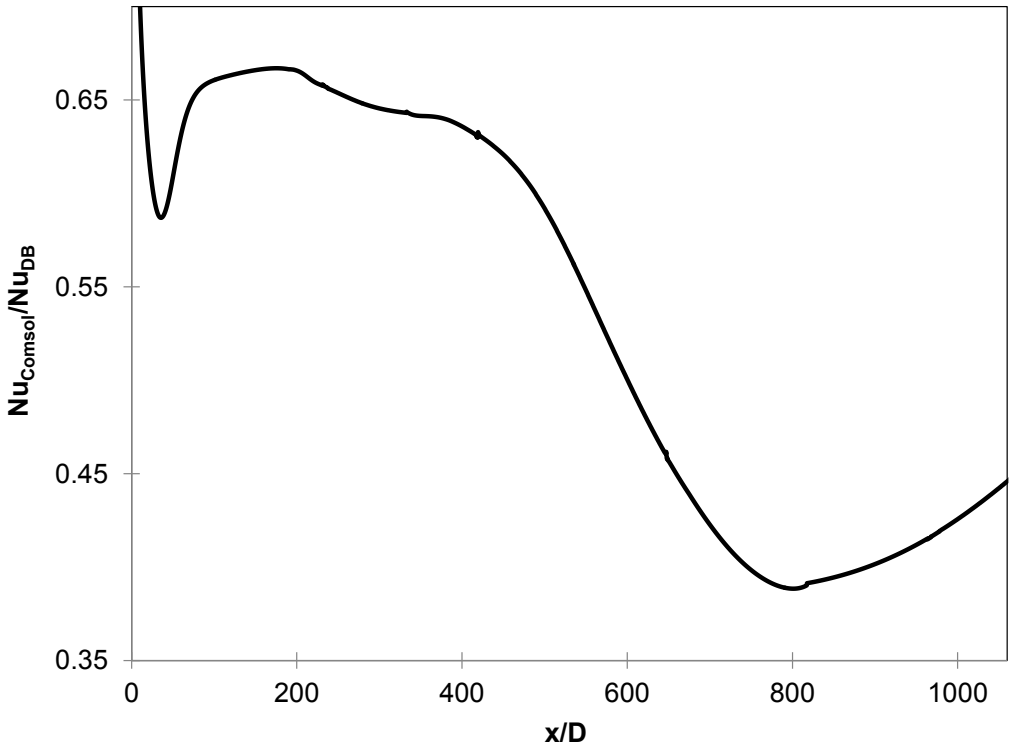

Figure 3.16 Ratio of Nu for supercritical and subcritical conditions along the axial length

As expected, the pipe section from the inlet to the middle value, around x/D=500, provided better results at supercritical conditions in terms of heat transfer efficiency, while downstream the second HTC peak displayed in Figure 3.14, Nu ratio decreased dramatically because the DB correlation was not valid any longer and overestimated the HTC values until the outlet, where Nu ratio showed a smaller value compared to the inlet, as explained in Figure 3.15. These phenomena were due to a combination of factors previously described in this section and could not be distinguished using this Nu ratio. As explained, the DB correlation only considers constant thermophysical properties while the computation produced results considering large property changes, buoyancy and thermal acceleration, as seen on Figure 3.15 by comparing the computed results with the HTC results provided by the Mokry correlation.

As a consequence, specific Nu ratios were necessary. In order to focus on the effect of LPVs, Nu_{Mokry} and Nu_{DB} were displayed as a ratio because the former was obtained in supercritical forced-convective flow and in absence of HTD conditions (thus accounting exclusively for large property changes) while the latter was meant for subcritical flows without property changes or other effects. The produced Nu ratios were plotted with the π_c parameter, defined in equation (3.5), as shown in Figure 3.17.

(a)

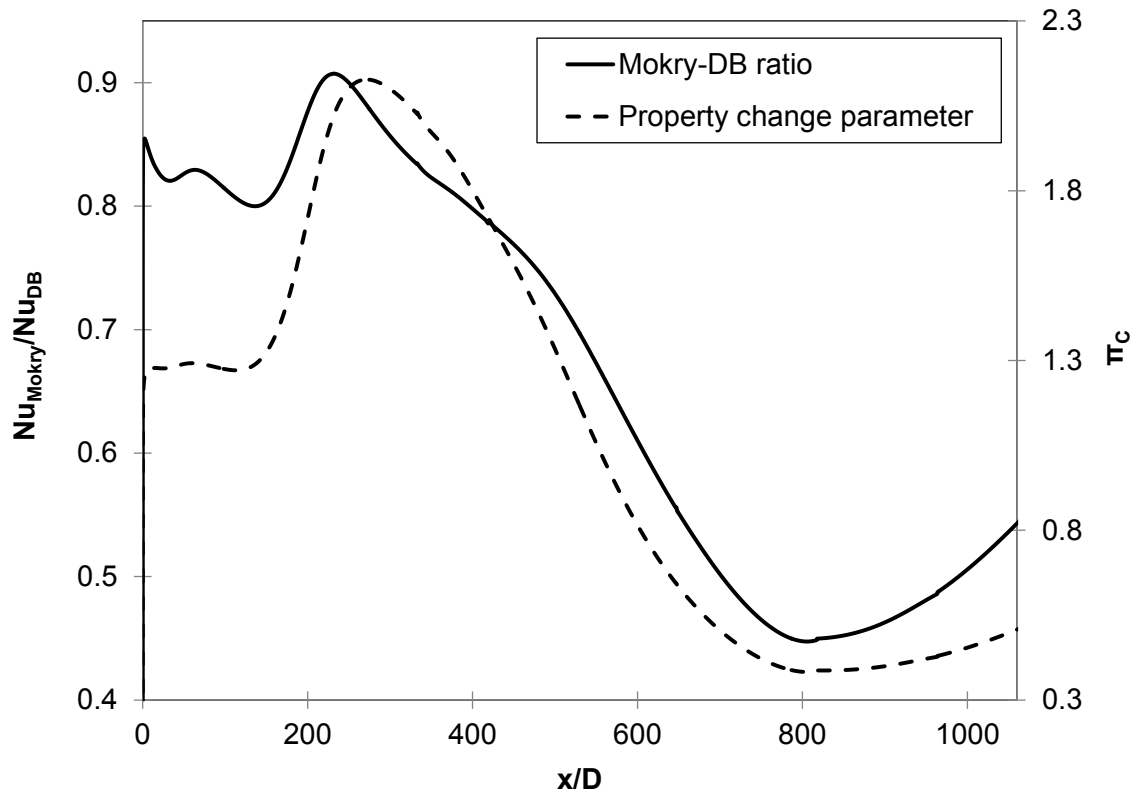

(b)

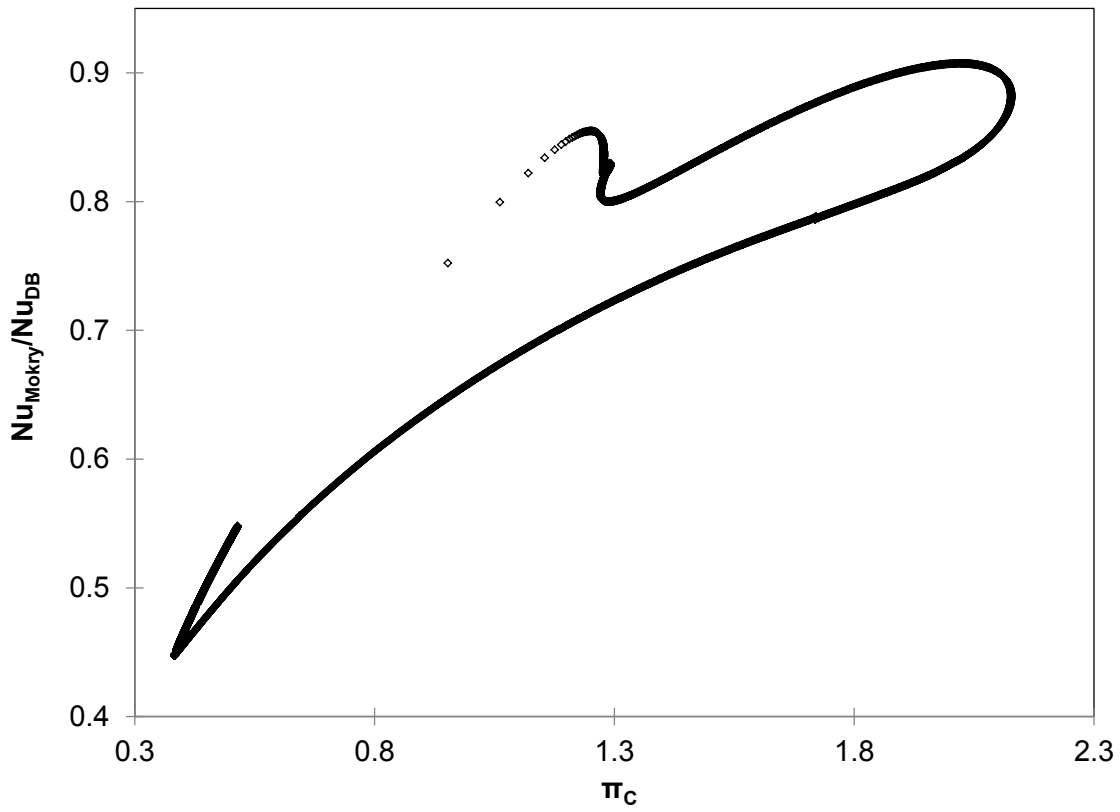

Figure 3.17 Effect of property changes on heat transfer performance

On Figure 3.17b the relation between Nu ratio and the π_c parameter was captured, and thus an increase in property changes increased the ratio. On Figure 3.17a this relation was displayed along the pipe. Nu ratio captured reasonably well the pattern induced by the property changes. From the inlet section of the pipe until x/D=500 approximately, heat transfer performance increased due to property changes. Normally, the HTC increases at the axial location where the wall reaches the PSC temperature, and more visibly upstream the point where the bulk temperature reaches the PSC value. These increases are triggered when the property changes are large (Yamagata *et al.*, 1972), as shown on Figure 3.10. In this case, the overall effect of property variations near the wall influenced positively (led by high values of

C_p near the wall to absorb more energy), however the same effect near the bulk would reduce temperature gradients, impairing heat transfer.

In order to observe the effect of buoyancy on heat transfer, the Nu_{Comsol} was displayed as a ratio over the Nu_{Mokry} (Nu_{Comsol}/Nu_{Mokry}). Both Nu numbers were specified for supercritical conditions and accounted for large property changes. However, Nu_{Comsol} also accounted for buoyancy and flow acceleration. To focus on buoyancy performance, this specific Nu ratio was plotted vs. Bo in Figure 3.18. The performance of SCHT under buoyancy effects for upward flow was depicted in Figure 3.18b, revealing three main areas. For low values of Bo, Nu ratio was somewhat close to a value of 1 as without the influence of buoyancy the Mokry correlation could predict the forced-convective performance. This was also represented on Figure 3.18a, coinciding at x/D=900 approximately, downstream the PSC point. At that point, the buoyancy effect decreased substantially and thus the flow could be considered to have entered the forced-convective regime; coinciding with the fact that the density has become homogeneous again downstream the PSC point. However, the Nu ratio showed a hump also nearby x/D=900 and did not match with the HTC trend, which was decreasing as shown in Figure 3.16. This was likely due to other external factors or poor mesh performance towards the end of the pipe.

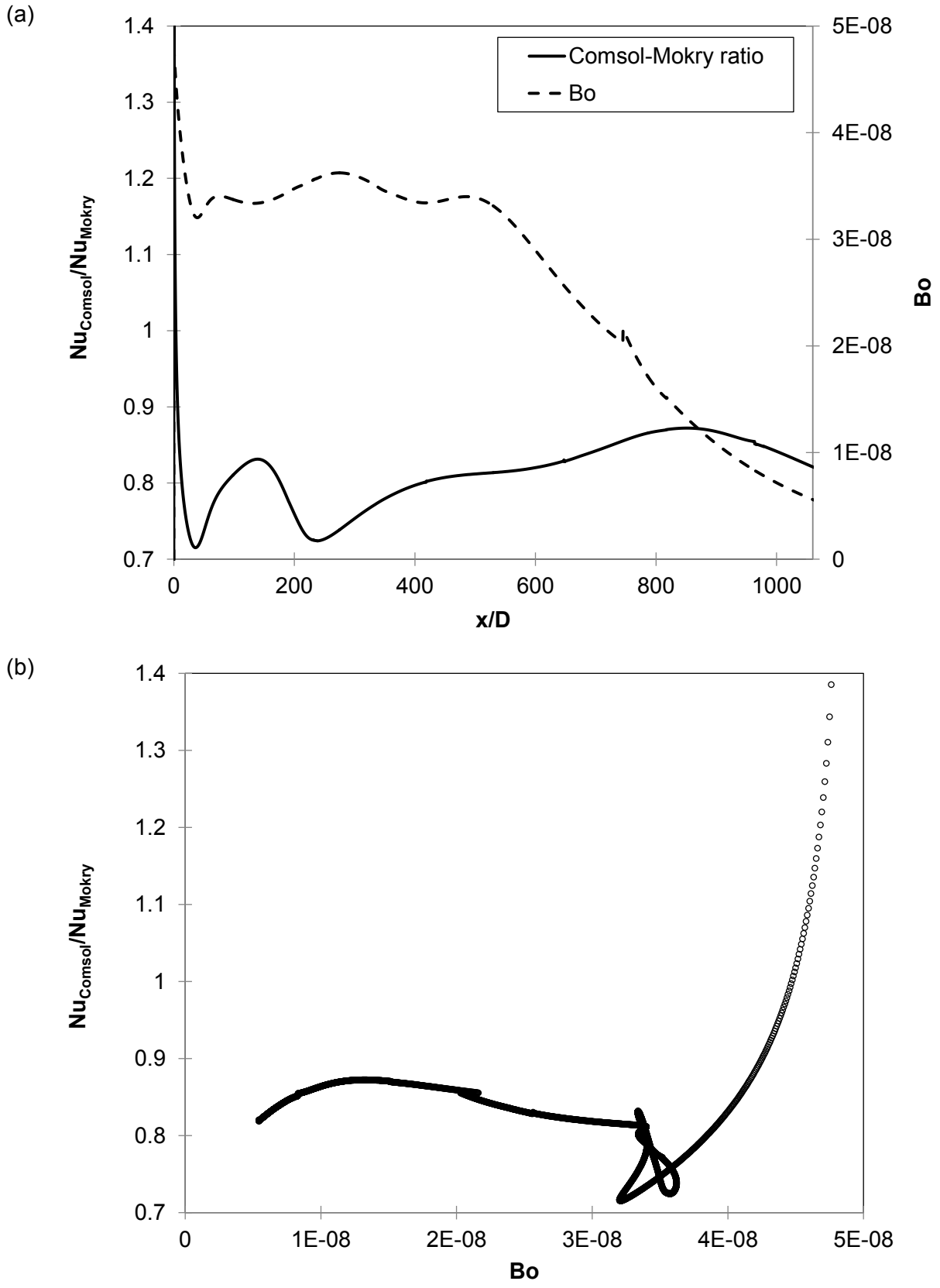

Figure 3.18 Effect of buoyancy on heat transfer regimes

When Bo increased, reaching a certain value between $3x10^{-8}$ and $3.5x10^{-8}$, Nu ratio experienced a clear decrease on the pipe section between the inlet and x/D=200, only interrupted by the HTE produced when the wall and bulk temperatures approached the PSC value. When Bo surpassed a value of approximately $4x10^{-8}$, an increase in buoyancy enhanced the heat transfer performance as Nu ratio increased considerably. This was correctly represented by Nu ratio and it occurred at the entrance section of the pipe, when the wall started being heated and strong buoyancy was triggered.

Similarly, the thermal acceleration effect was interpreted using the same Nu ratio as previously with the buoyancy but using the parameter K_v (thermal acceleration) instead. The results are shown in Figure 3.19b, where a strong dependence of Nu ratio on K_v was revealed. In Figure 3.19a, it can be seen that large values of K_v as well as the large Nu ratios were localised at the pipe entrance, while downstream at x/D=50 approximately K_v dropped along with Nu ratio, coinciding with the HTC values in Figure 3.14. The peaks of Nu ratio at x/D=150 approximately coincided with the recovery of K_v. The smooth increase of Nu ratio produced at the end of the axial length did not coincided with the HTC curve due to external factors as well as mesh performance. This factor does not seem to represent properly the presence and behaviour of flow acceleration in the system, as it looks quite unresponsive compared to other parameters measuring the same effect in Section 3.3.6.

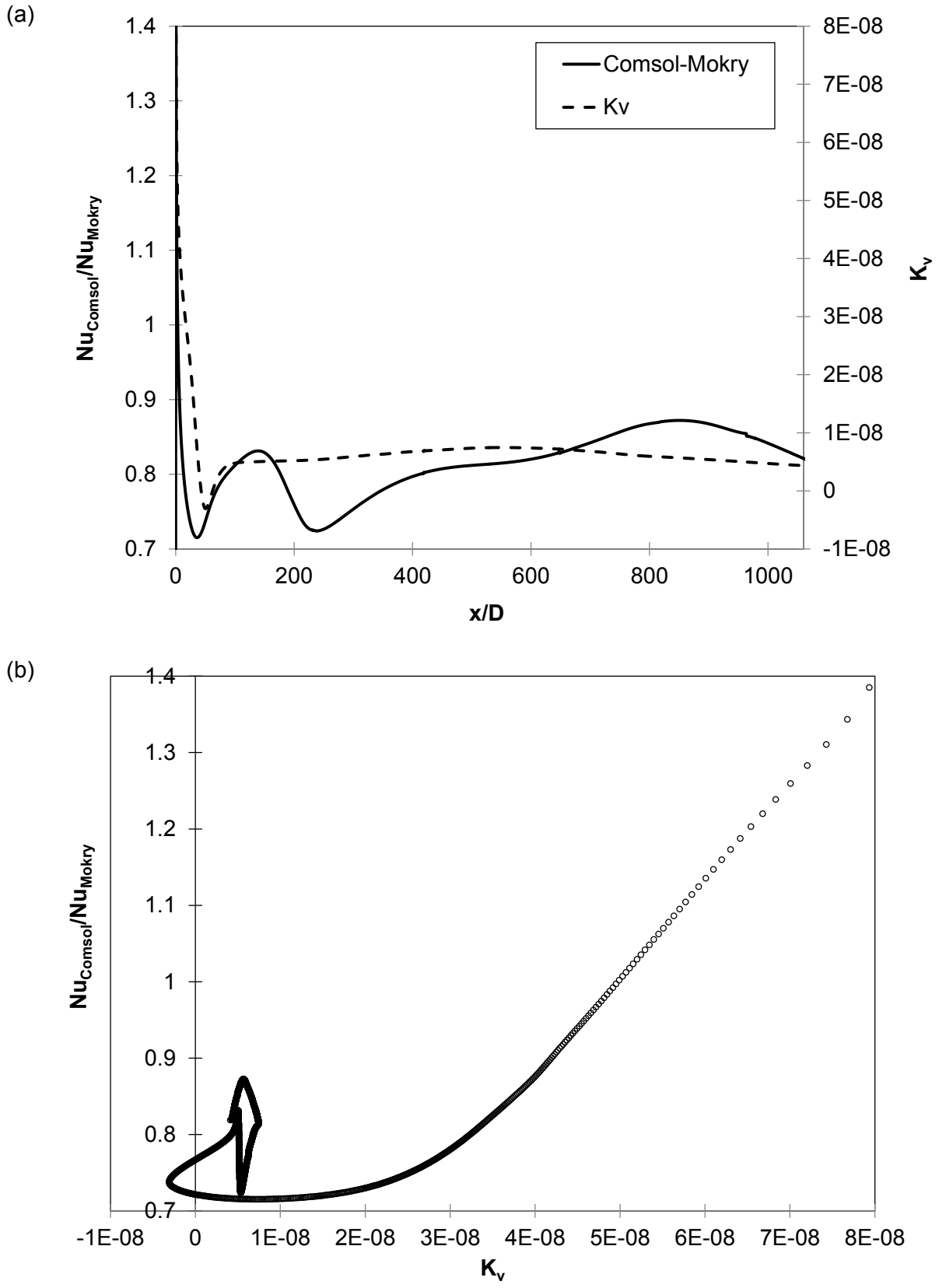

Figure 3.19 Impact of thermal acceleration on SCHT

Buoyancy and thermal acceleration are normally triggered by the decrease in density induced within the LPV region, which could affect the flow if the gravitational forces are strong in the first case, or accelerate the flow due to modifications in the velocity profile in the latter. Sometimes thermal acceleration is facilitated by buoyancy, and sometimes it is triggered independently if the pipe diameter is small enough to neglect buoyancy. In Figure 3.20, Bo is plotted vs. K_v as a means to see their relation. When buoyancy was low, thermal acceleration was hardly responsive, however when Bo approached around $3.5x10^{-8}$, flow acceleration was triggered and sharply increased. These values of Bo and K_v were achieved at the entrance region, and considerably improved the HTC.

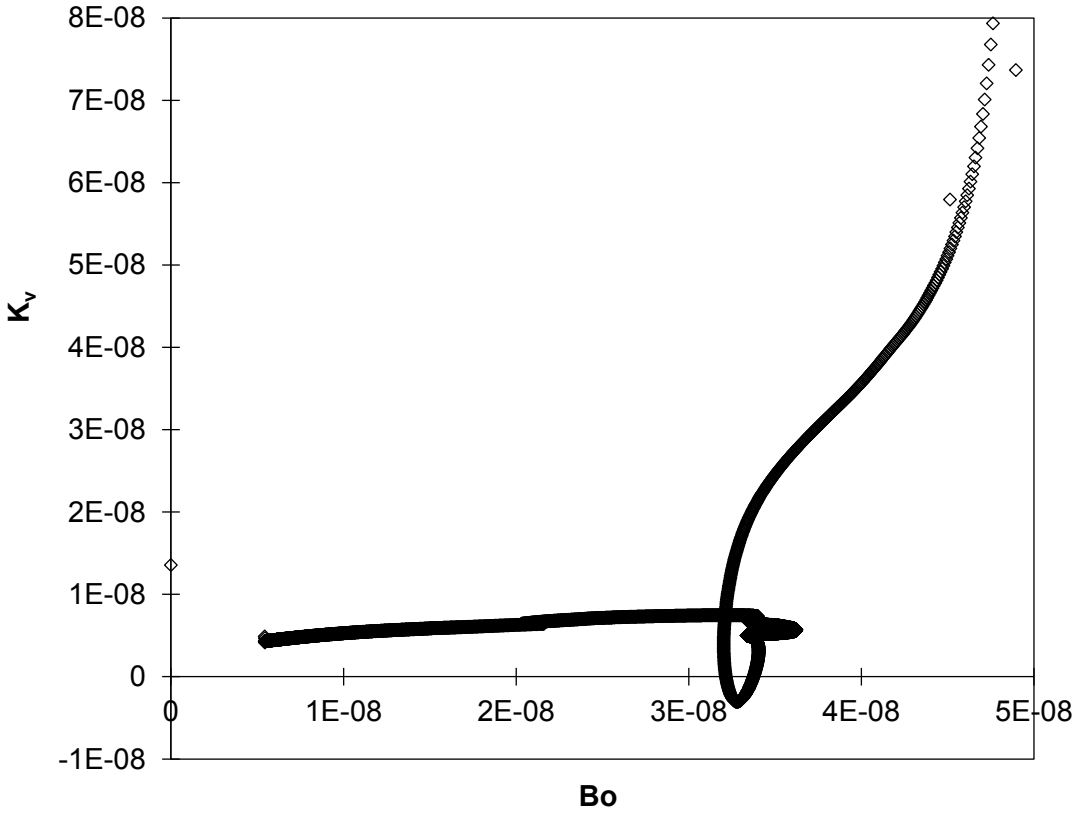

Figure 3.20 Effect of buoyancy on thermal acceleration

3.3.6 Hydrothermal study

The hydrothermal performance of any flow system related to SCHT is the result of a series of phenomena interacting in a complex manner. The location where the thermophysical properties pass through the LPV region depends on factors such as the inlet temperature, the thermal boundary condition and the G. At the same time, entrance effects such as the inlet velocity profile or the axial distance before the heat source is applied will impact turbulence. Moreover, a portion of the radial flow is normally accelerated when the T_b surpasses the PSC point, impairing the turbulence production downstream. On the other hand, some sections of the cross-sectional flow normally decelerate upstream that point, improving turbulence.

Due to these interactions, sometimes a flow region experiencing turbulence might not have a good thermal performance, and vice versa. In order to support the previous studies and further understand the performance of the HTC curve, additional analyses were undertaken displaying several hydrodynamic and thermal parameters in postprocessed 2D plots of the solved fluid domain. The 2D plots were presented applying a 1:1 aspect ratio (length-diameter) in order to capture the full geometry of the system. The flow inlet was depicted on the left edge of each image, while the top edge was the wall boundary and the bottom edge was the bulk of the flow.

Figure 3.21 shows the 2D plots for some hydrodynamic parameters such as G, axial velocity gradients (u_x), radial velocity gradients (u_y), turbulent shear stress (τ_{turb}) and turbulence intensity (I). The equations for I and τ_{turb} are defined on (3.10) and (3.11),

where both the turbulent viscosity (μ_T) and the turbulent kinetic energy (k) are parameters belonging to the turbulent model and were described in the Appendix.

$$\tau_{turb} = \left(\frac{du}{dy} + \frac{dv}{dx}\right) \cdot \mu_T \quad \textbf{(3.10)}$$

$$I = \frac{\sqrt{\frac{2 \cdot k}{3}}}{U} \quad \textbf{(3.11)}$$

Figure 3.21a reveals the G map, aided with isolines. As can be seen, the biggest changes took place near the bulk of the flow. Near the pipe entrance G experienced a sharp increase at the bulk because the flow near the wall was increasing the temperature already while heat had not been transferred yet to the bulk of the flow. The flow density was changing more noticeably than the velocity profile, thus G dropped near the wall and as a consequence G had to increase at the core as a means to keep the mass flow constant. This phenomenon coincided with the HTC drop at the same axial location shown in Figure 3.14. Downstream, at an axial location of 1,500-2,000 *mm* the value of G dropped at the bulk after T_w achieved the PSC point and the HTC experienced an improvement. At an axial range between 4,000-8,000 *mm*, G smoothly increased around the location where T_b approached the PSC point because the flow velocity increase at the core was more relevant than the density drop, slightly laminarising the flow profile.

(a)

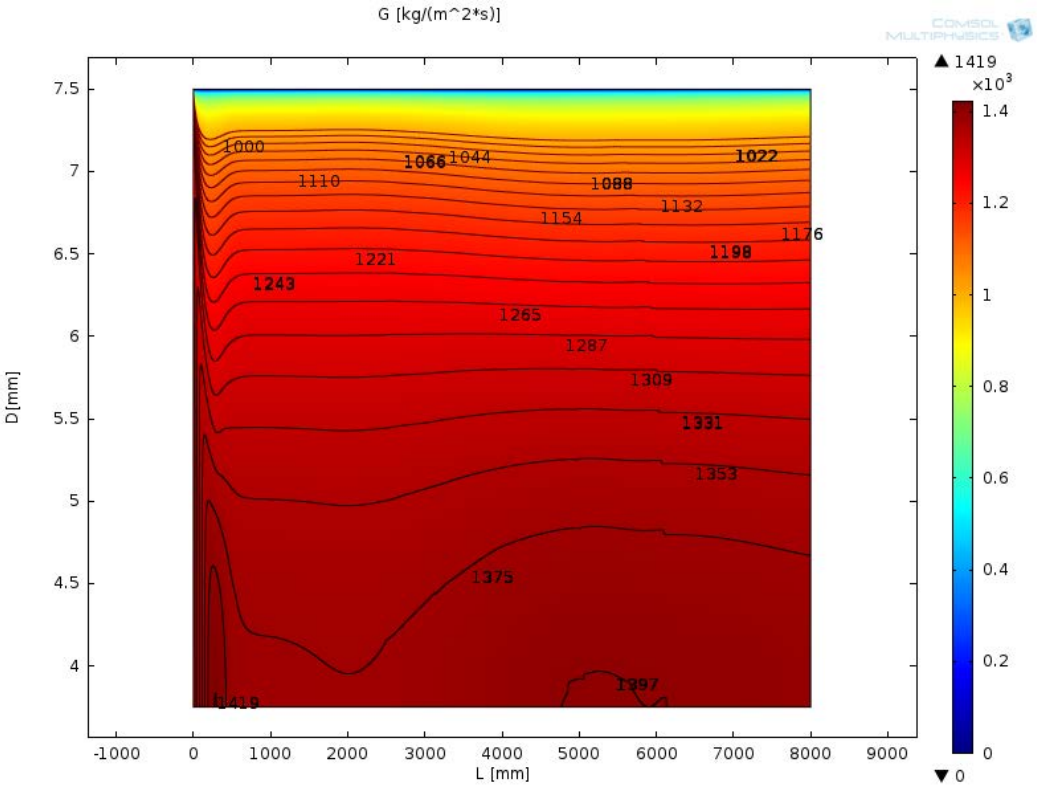
G [kg/(m^2*s)]
▲ 1419
×10^3
1.4
1.2
1
0.8
0.6
0.4
0.2
0
▼ 0
1000
1044
1066
1022
1110
1088
1132
1154
1176
1198
1221
1243
1265
1287
1309
1331
1353
1375
1397
1419
D [mm]
L [mm]
7.5
7
6.5
6
5.5
5
4.5
4
-1000
0
1000
2000
3000
4000
5000
6000
7000
8000
9000

(b)

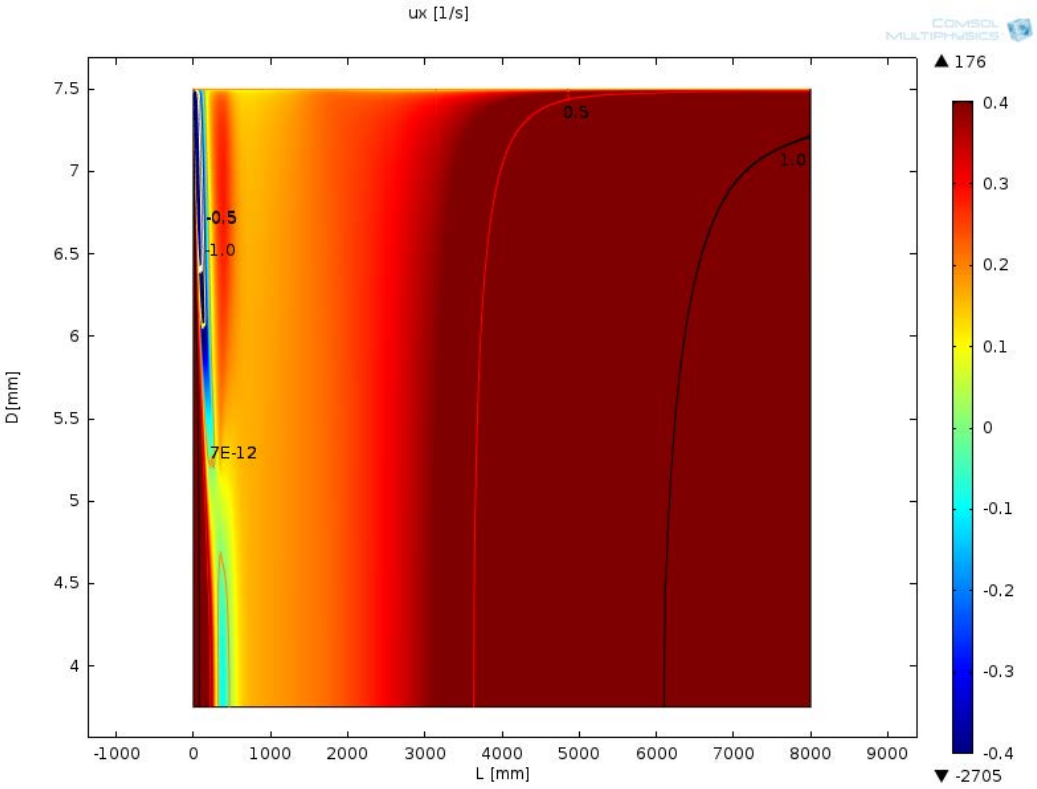
ux [1/s]
▲ 176
0.4
0.3
0.2
0.1
0
-0.1
-0.2
-0.3
-0.4
▼ -2705
0.5
1.0
-0.5
-1.0
7E-12
D [mm]
L [mm]
7.5
7
6.5
6
5.5
5
4.5
4
-1000
0
1000
2000
3000
4000
5000
6000
7000
8000
9000

(c)

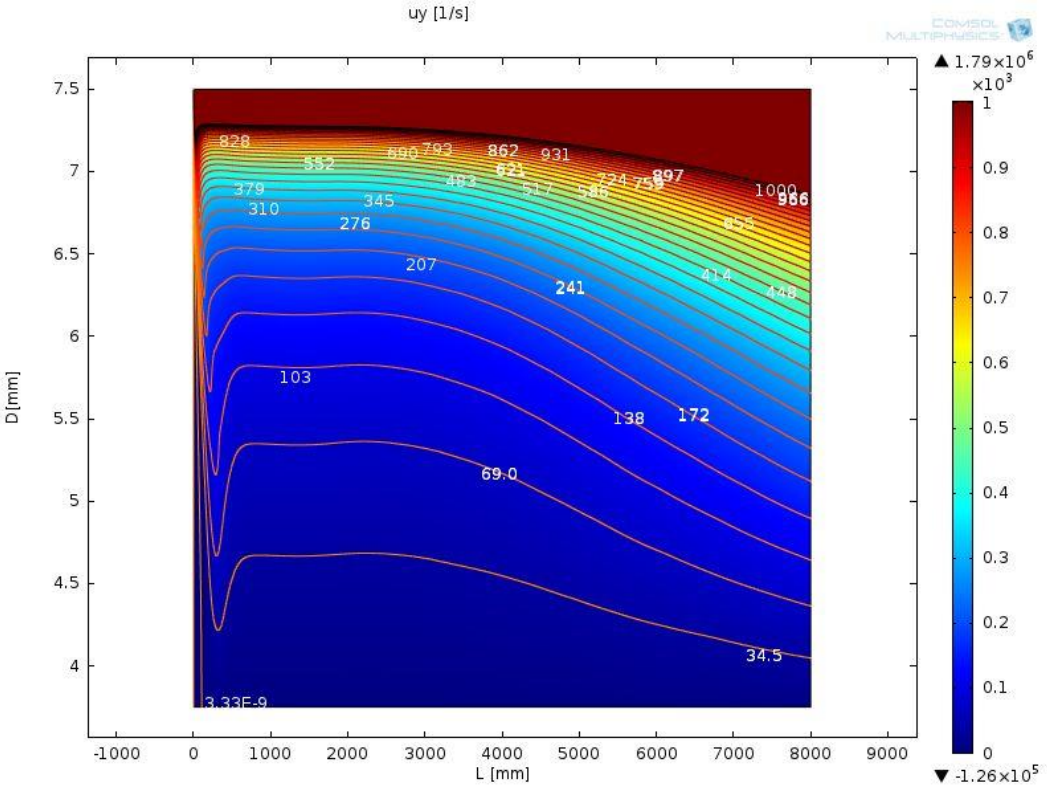
uy [1/s]
▲ 1.79×10^6
×10^3
▼ -1.26×10^5
D[mm]
L [mm]
828
552
379
310
345
276
207
241
103
138
172
69.0
34.5
3.33E-9

(d)

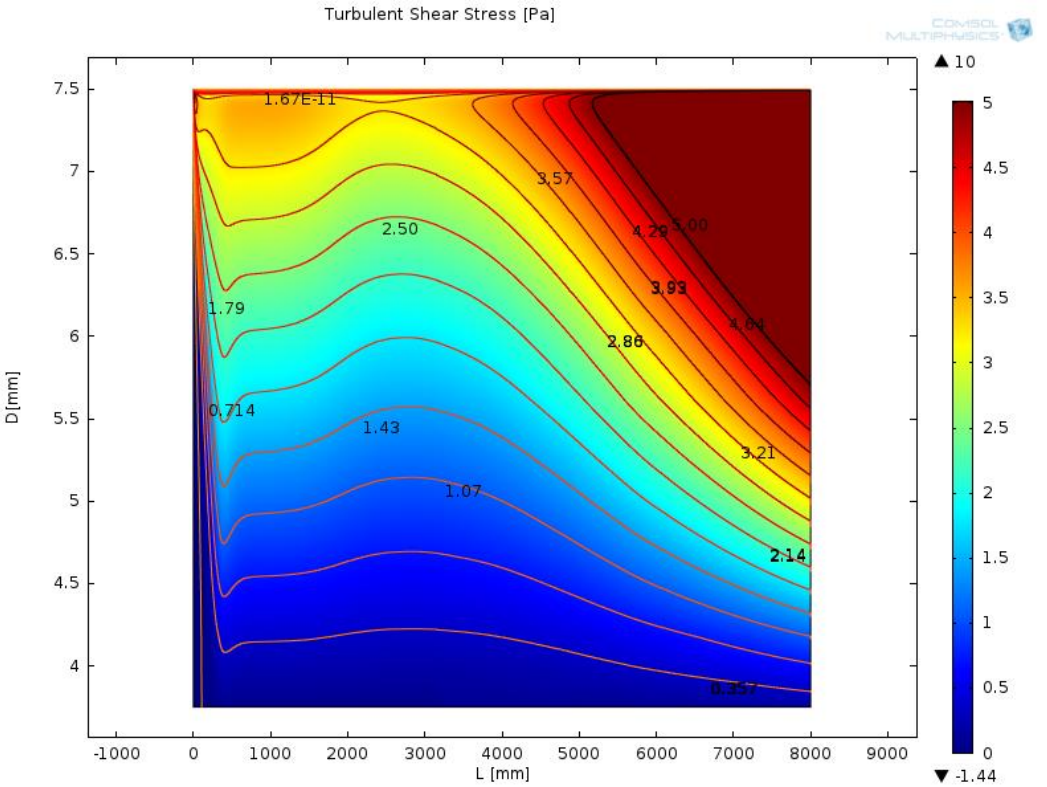
Turbulent Shear Stress [Pa]
▲ 10
▼ -1.44
D[mm]
L [mm]
1.67E-11
3.57
2.50
1.79
0.714
1.43
1.07
3.21
2.14
0.357

(e)

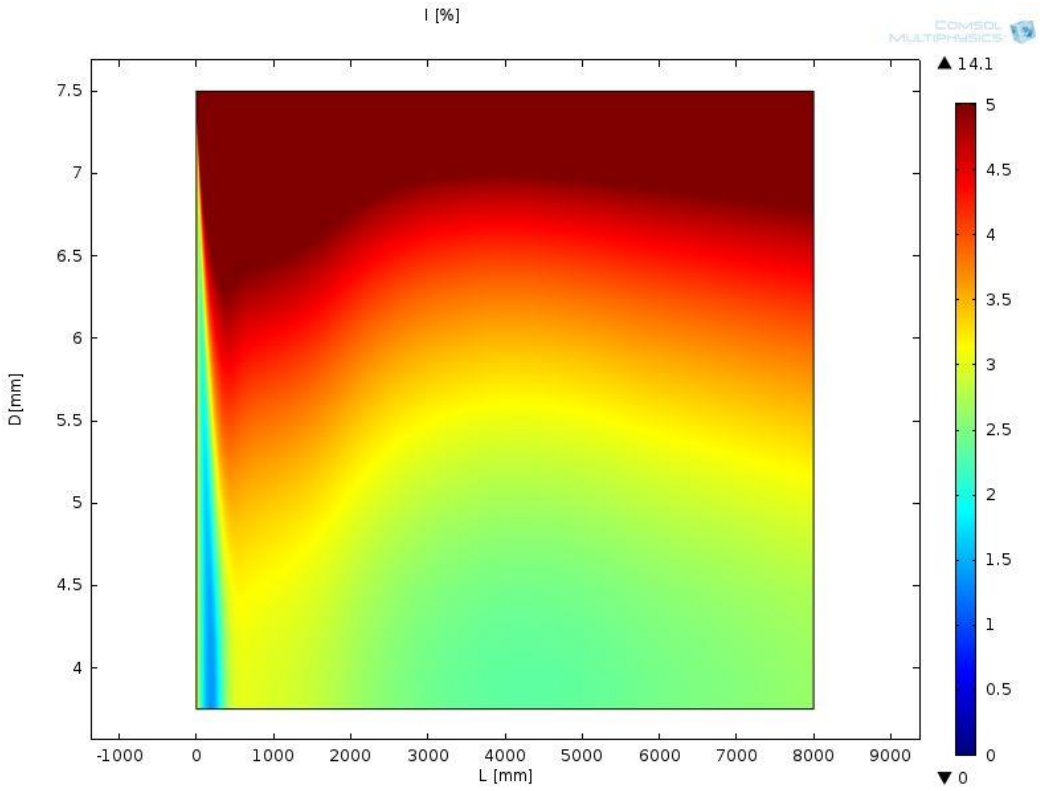

Figure 3.21 Postprocessed 2D plots of hydrodynamic parameters showing G (a), u_x (b), u_y (c), T_{turb} (d) and I (e)

Figure 3.21b, showing u_x, confirmed the previous discussion; as the areas near the wall and near the core were balancing at the entrance. The flow area at the entrance near the wall decelerated due to the density drop while the core accelerated. Downstream, at an axial length of a few hundreds of *mm* up to 500 *mm* approximately, the flow profile was reconfigured in an attempt to balance the mass flow and the core decelerated. Once the entrance effects vanished, the flow evenly and progressively accelerated along the pipe due to the PSC transition to a gas-like fluid. Due to the fact that the G and u_x increased more at the bulk compared to the area near the wall towards the pipe outlet, some laminarisation was triggered and thus the HTC dropped towards the end of the pipe. This can be seen in Figure 3.14,

as the T_w had a higher slope than the T_b close to the outlet. This is a common factor in HTD as heat is not properly transferred.

Figure 3.21c, d and e, showing u_y, τ_{turb} and I respectively, depicted a similar trend. There were two regions where the u_y and thus the τ_{turb} showed better results, namely the areas near the wall before the T_w achieved the PSC value and after the T_b did the same. In fact, Figure 3.21e depicted stronger turbulence near the wall on the region once the entrance effects adjusted, upstream the T_w reaching the PSC point. On the other hand, the area near the wall and upstream the bulk achieving the PSC reflected a decrease in turbulent shear stress which did not agree with the HTC profile. In this area, the LPVs outweighed the hydrothermal performance. Nevertheless, downstream this section the HTC dropped due to the acceleration in the flow core, while turbulence improved near the wall towards the end of the pipe. The SCHT parameters employed in Section 3.3.5 could predict the good overall performance at the pipe entrance, although there were some disagreements near the outlet; for instance K_v did not reflect the acceleration increase along the pipe.

With respect to thermal performance, the values of momentum diffusivity (represented by the kinematic viscosity, ν, as natural convective force), C_p, thermal diffusivity (represented by α, as conductive force), axial temperature gradients (T_x) and radial temperature gradients (T_y) were analysed as shown in Figure 3.22. The equations for the diffusivity parameters are shown in (3.12) and (3.13).

$$\upsilon = \frac{\mu}{\rho} \tag{3.12}$$

$$\alpha = \frac{\lambda}{C_p \cdot \rho} \tag{3.13}$$

Figure 3.22a displays the values of ν, and as can be seen the natural-convective performance of the flow is favoured downstream due to the sharp decrease in density after the flow surpassed the LPV region. Nevertheless, as seen in Figure 3.18 and Figure 3.21a and b, the increase of G and u_x along the pipe induced a dominant forced-convective flow towards the end of the pipe, inducing low values of Bo at the outlet. Figure 3.22b and c reflected the fact that near the LPV region the value of α decreased due to the reduction in the capacity of the fluid to increase the temperature while absorbing the same amount of heat flux. This is favourable for storing energy, but it also induces low temperature variations.

(a)

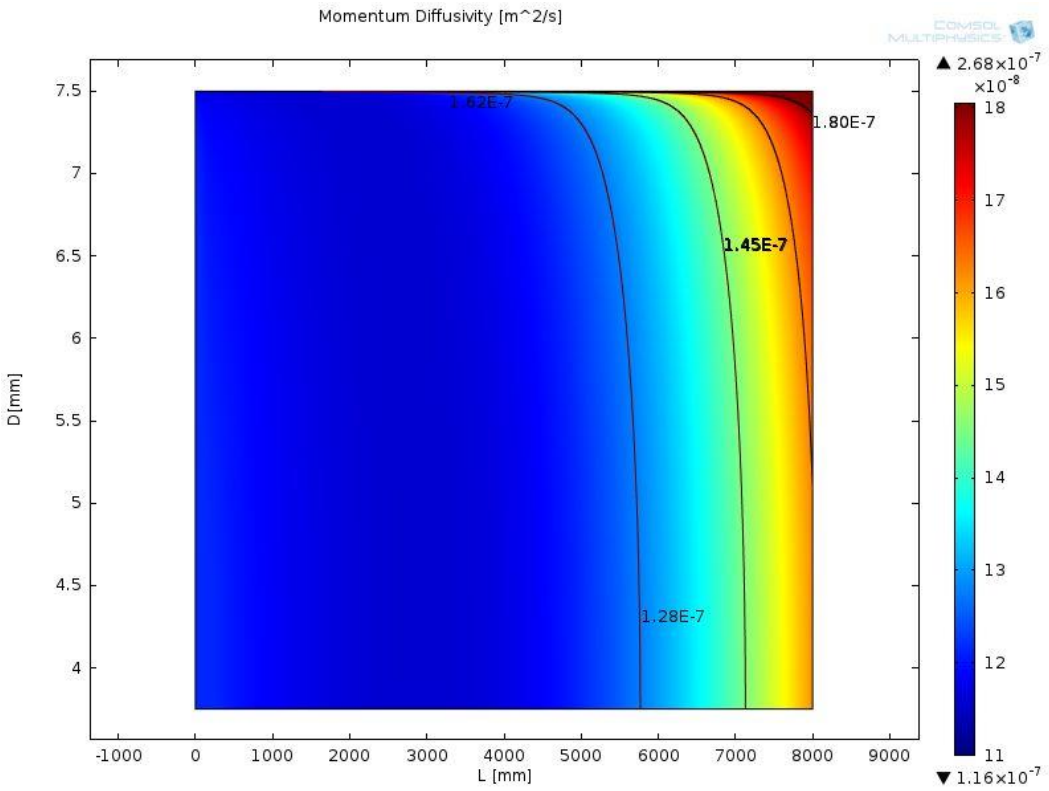

(b)

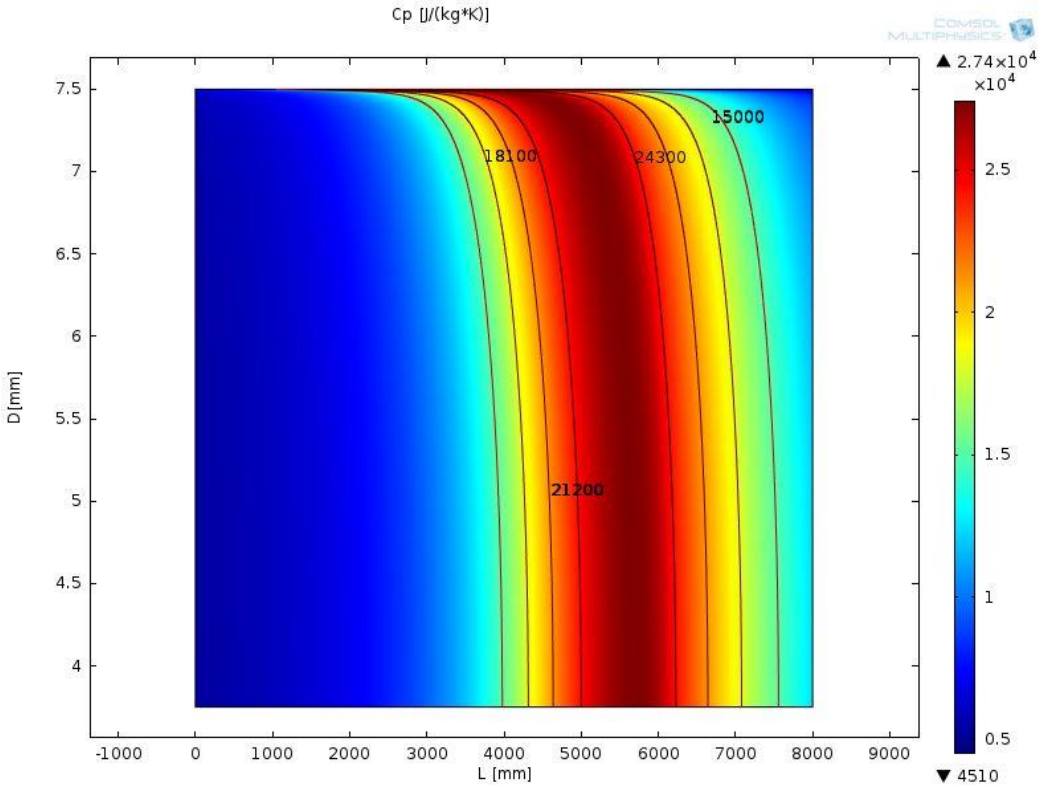
Cp [J/(kg*K)]
▲ 2.74×10^4
×10^4
2.5
2
1.5
1
0.5
▼ 4510
15000
18100
24300
21200
D [mm]
L [mm]

(c)

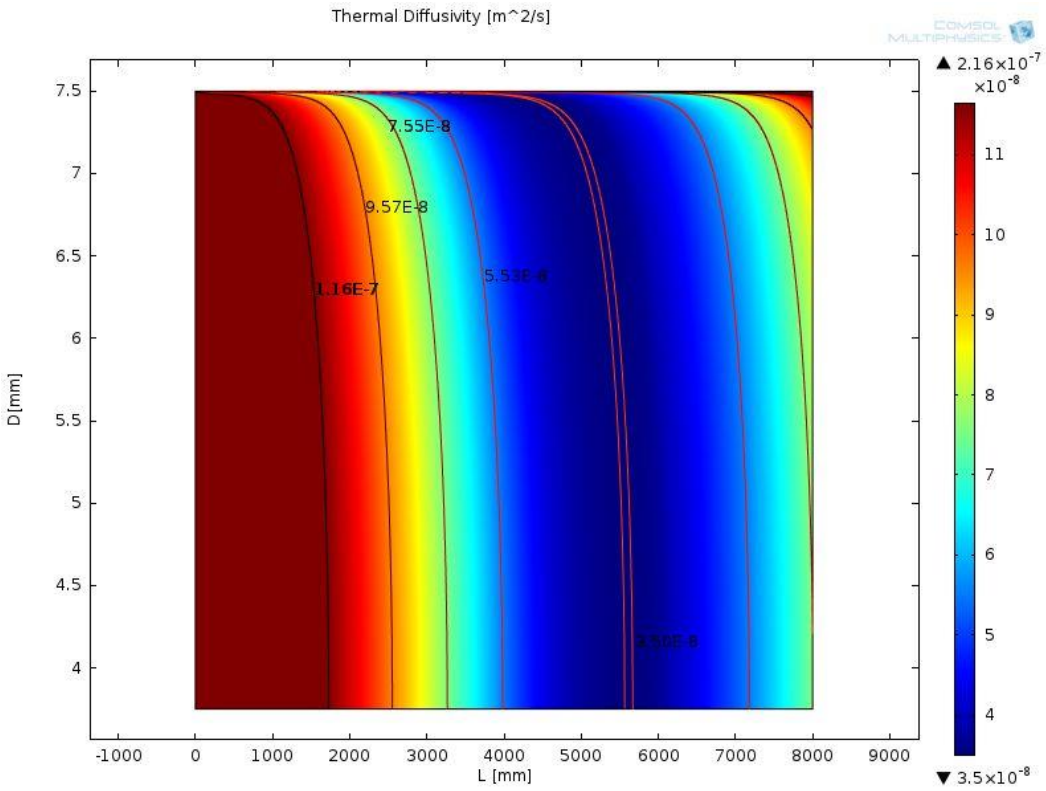
Thermal Diffusivity [m^2/s]
▲ 2.16×10^-7
×10^-8
11
10
9
8
7
6
5
4
▼ 3.5×10^-8
7.55E-8
9.57E-8
1.16E-7
D [mm]
L [mm]

(d)

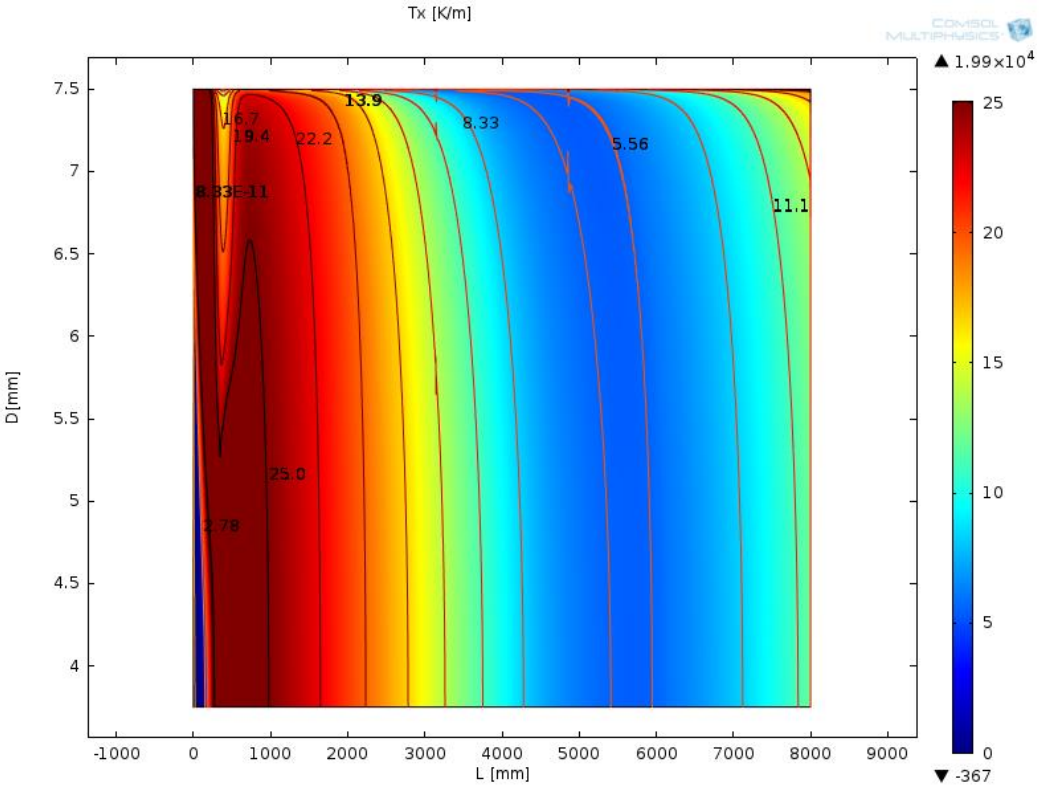

(e)

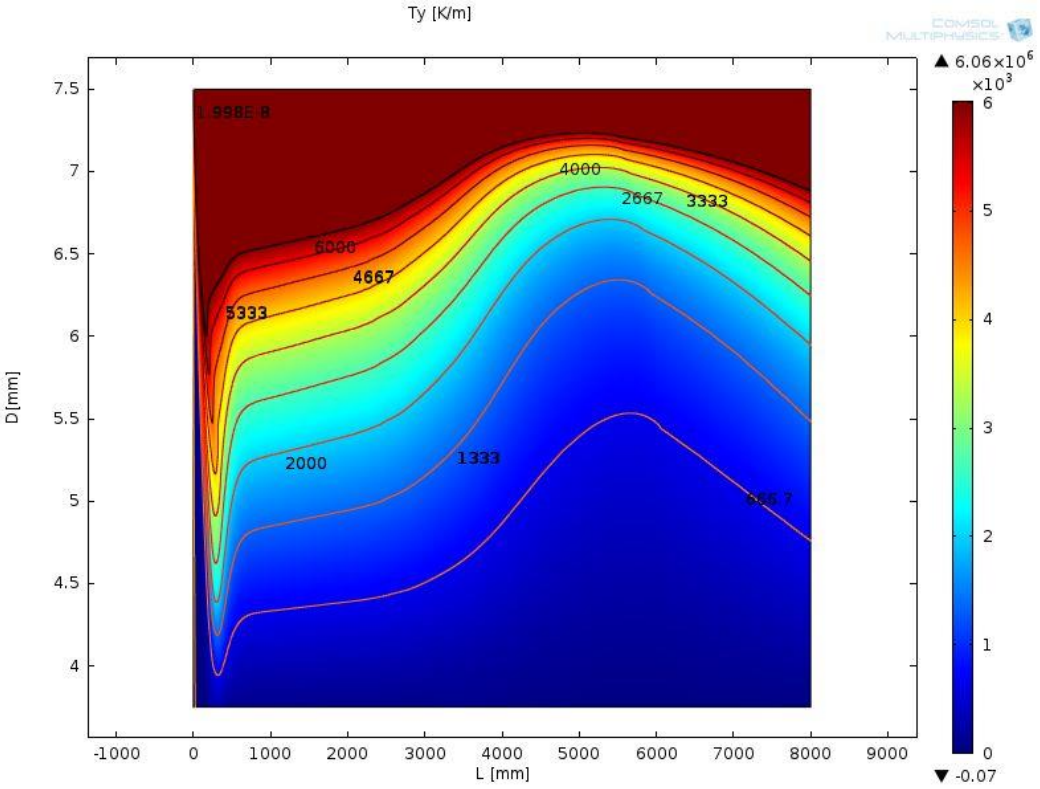

Figure 3.22 Postprocessed 2D plots of thermal parameters showing ν (a), C_p (b), α (c) T_x (d) and T_y (e)

Figure 3.22d and e confirmed the aforementioned phenomenon and also agreed with the turbulence performance previously discussed from Figure 3.21e. As it happened with the hydrodynamic study, the entrance area depicted the best values of T_y, as seen in Figure 3.22e, due to the balancing of the entrance effects and the onset of the PSC point in the T_w. Figure 3.22d revealed a small region near the wall with lower values of T_x compared to the surroundings, which coincided with Figure 3.21b as a region with higher flow acceleration as a product of the entrance effects, thus heat transfer was only locally deteriorated.

It was concluded that the entrance and outlet regions presented better hydrothermal behaviour near the wall compared to the section of the flow undergoing LPVs. Nevertheless, the core of the flow at the outlet experienced more acceleration which laminarised the flow and decreased the HTC value. The large peak in the HTC, shown in Figure 3.14 at x/D=550 approximately, was favoured partly due to the onset of the PSC point in the bulk triggering large property changes upstream (as seen on Figure 3.17a); and also partly due to the reduction of T_x at the wall (based on the HTC formula, depicted in equation (3.4)).

3.4 Summary

A near-wall refinement study was performed while using the SST turbulence model in order to verify the improvement produced on the results when decreasing the value of y_1^+. A value of y_1^+below 1 was recommended to appropriately capture important effects on the viscous layer, given the impact on the computations of q_w.

Several mesh distributions were employed both axially and radially. The impact of an axial refinement was small when obtaining values of HTC. Nevertheless, the use of a refined axial mesh focused on the inlet region could improve possible deviations caused by inlet effects. Refining the radial distribution caused a noticeable impact on the mesh performance due to the improvements on the bulk, but not as considerably as decreasing y_1^+.

The use of a second discretisation order was recommended when computing turbulent convective flows, as it produced better results than refining the same mesh with first order. However, computational times can be prohibitive.

Several correlations were employed to verify if the system was subject to HTD; the correlations by Yin *et al.* (2006) and Styrikovich et al. (1967) showed proximity to the onset of deterioration (698 kW m^{-2}). In order to test this phenomenon, several parameters measuring property changes, buoyancy and thermal acceleration were employed with Nu ratios in order to capture qualitative trends. It was observed that

several factors not included within these parameters might possibly affect the heat transfer performance.

For better understanding, further studies were undertaken displaying some hydrodynamic and thermal properties in 2D plots postprocessed from the software. The plots revealed that turbulence and heat transfer were favoured at the entrance and outlet regions near the wall and slightly weaker within the LPV region of the flow. Still, a large HTC peak was achieved near this hydrothermally impaired area due to the fact that the growing rate of T_w decreased and the favouring effect of the property changes on the onset of the PSC point in the bulk of the flow. Towards the end of the pipe, the core of the flow experienced some acceleration which laminarised the flow, triggering a drop in the local HTC.

References

Cheng X, Yang YH, Huang SF (2009). A simplified method for heat transfer prediction of supercritical fluids in circular tubes. *Annals of Nuclear Energy;* 36: 1120-28

Dang C, Hihara E (2004). In-tube cooling heat transfer of supercritical carbon dioxide. Part 2. Comparison of numerical calculation with different turbulence models. *International Journal of Refrigeration;* 27: 748-60

Du Z, Lin W, Gu A (2010). Numerical investigation of cooling heat transfer to supercritical CO_2 in a horizontal circular tube. *The Journal of Supercritical Fluids*; 55: 116-21

Dutta G, Maitri R, Zhang C, Jiang J (2015). Numerical models to predict steady and unsteady thermal-hydraulicbehaviour of supercritical water flow in circular tubes. *Nuclear Engineering and Design;* 289: 155-65

Gou J, Shang Z, Ishiwarari Y, Oka Y, Yamakawa M, Ikejiri S (2010). CFD analysis of heat transfer in subchannels of a Super Fast Reactor. *Nuclear Engineering and Design;* 240: 1819-29

Hall WB, Jackson JD, Watson A (1967). A review of forced convection heat transfer to fluids at supercritical pressures. *Proc Instn Mech Engrs;* 182 Pt 3 I: 10-22

He S, Kim WS, Bae JH (2008). Assessment of performance of turbulence models in predicting supercritical pressure heat transfer in a vertical tube. *International Journal of Heat and Mass Transfer;* 51: 4659-75

Huang D, Wu Z, Sunden B, Li W (2016). A brief review on convection heat transfer of fluids at supercritical pressures in tubes and the recent progress. *Applied Energy*; 162: 494-505

Jackson JD (2010). Evaluation of a new equation for variable property mixed convection heat transfer in vertical tubes. *In:* Bilbao y León, S (editor). *Technical meeting on heat transfer, thermal-hydraulics and system design for supercritical water cooled reactors. International atomic energy agency; pp. TM-38683-1*

Jackson JD (2013). Fluid flow and convective heat transfer to fluids at supercritical pressure. *Nuclear Engineering and Design;* 264: 24-40

Jackson J, Hall W (1979). Influences of buoyancy on heat transfer to fluids flowing in vertical tubes under turbulent conditions. *Turbulent Forced Convection in Channels and Bundles; 2; 613-40*

Jäger W, Sánchez-Espinoza VH, Hurtado A (2011). Review and proposal for heat transfer predictions at supercritical water conditions using existing correlations and experiments. *Nuclear Engineering and Design*; 241: 2184-203

Jaromin M, Anglart H (2013). A numerical study of heat transfer to supercritical water flowing upward in vertical tubes under normal and deteriorated conditions. *Nuclear Engineering and Design;* 264: 61-70

Lemmon EW, McLinden MO, Friend DG (2015). Thermophysical Properties of Fluid Systems. In: Linstrom PJ (editor). NIST Standard Reference Database Number 69. *NIST Chemistry WebBook*

Liu L, Xiao Z, Yan X, Zeng X, Huang Y (2013). Heat transfer deterioration to supercritical water in circular tube and annular channel. *Nuclear Engineering and Design;* 255: 97-104

Li X, Huai X, Cai J, Zhong F, Fan X, Guo Z (2011). Convective heat transfer characteristics of China RP-3 aviation kerosene at supercritical pressure. *Applied Thermal Engineering*; 31: 2360-66

Menter FR (1993). *Higher order turbulence model predictions for complex 2D and 3D flow fields. In: Martelli F & Rodi W (editors). Proceedings of the Second International Symposium on Engineering Turbulence Modelling and Measurements. Engineering turbulence modelling and experiments; pp. 229-38*

Mikielewicz DP, Shehata AM, Jackson JD, McEligot DM (2002). Temperature, velocity and mean turbulence structure in strongly heated internal gas flows. Comparison of numerical predictions with data. *International Journal of Heat and Mass Transfer; 45: 4333-52*

Mokry S, Pioro I, Farah A, King K, Gupta S, Peiman W, Kirillov P (2011). Development of supercritical water heat-transfer correlation for vertical bare tubes. *Nucl Eng Des; 241: 1126-36*

Pioro, I (2014). Application of supercritical pressure in power engineering: specifics of thermophysical properties and forced-convective heat transfer. In: Anikeev V, Fan M (editors). Supercritical fluid technology for energy and environmental applications. *Elsevier;* pp. 225

Pioro IL, Duffey RB (2005). Experimental heat transfer in supercritical water flowing inside channels (survey). *Nuclear Engineering and Design;* 235: 2407-30

Pioro I, Mokry S, Draper S (2011). Specifics of thermophysical properties and forced-convective heat transfer at critical and supercritical pressures. *Rev Chem Eng*; 27: 191-214

Pizzarelli M (2016). A CFD-derived correlation for methane heat transfer deterioration. *Numerical Heat Transfer, Part A*, vol. 69, 3: 242-64

Podila K, Rao YF (2015). CFD analysis of flow and heat transfer in Canadian supercritical water reactor bundle. *Annals of Nuclear Energy;* 75: 1-10

Rahman MM, Dongxu J, Beni MS, Hei HC, He W, Zhao J (2016). Supercritical water heat transfer for nuclear reactor applications: A Review. *Annals of Nuclear Energy;* 97: 53-65

Shang Z, Yao Y, Chen S (2008). Numerical investigation of system pressure effect on heat transfer of supercritical water flows in a horizontal round tube. *Chemical Engineering Science;* 63: 4150-58

Styrikovich MA, Margulova TK, Miropolskiy ZL (1967). Problem in the development of designs of supercritical boilers. *Thermal Engineering;* 32: 4-7

Van der Kraan M, Peeters MMW, Fernandez-Cid MV, Woerlee GF, Veugelers WJT, Witkampa GJ (2005). The influence of variable physical properties and buoyancy on heat exchanger design for near- and supercritical conditions. *J. of Supercritical Fluids;* 34: 99-105

Wen QL, Gu HY (2011). Numerical investigation of acceleration effect on heat transfer deterioration phenomenon in supercritical water. *Progress in Nuclear Energy;* 53: 480-86

Wibisono AF, Addad Y, Lee JI (2015). Numerical investigation on water deteriorated turbulent heat transfer regime in vertical upward heated flow in circular tube. *International Journal of Heat and Mass Transfer*; 83: 173-86

White FM (2011). The flat-plate boundary layer (Flow past immersed bodies). In: Lange M (editor). Fluid Mechanics, 7th Edition. *McGraw-Hill;* pp. 467-75

Winterton RHS (1998). Where did the Dittus and Boelter equation come from? *International J. Heat Mass Transfer;* 41, 4-5: 809-10

Withag JAM, Sallevelt JLHP, Brilman DWF, Bramer EA, Brem G (2012). Heat transfer characteristics of supercritical water in a tube: Application for 2D and an experimental validation. *J. of Supercritical Fluids;* 70: 156-70

Yamagata K, Nishikawa K, Hasegawa S, Fujii T, Yoshida S (1972). Forced convective heat transfer to supercritical water flowing in tubes. *Int. Journal of Heat Mass Transfer;* 15: 2575-93

Yin F, Chen TK, Li HX (2006). An investigation on heat transfer to supercritical water in inclined upward smooth tubes. *Heat Transfer Engineering;* 27: 44-52

Zhang B, Shan J, Jiang J (2010). Numerical analysis of supercritical water heat transfer in horizontal circular tube. *Progress in Nuclear Energy*; 52: 678-84

4. Numerical verification in 2D using computational data and 3D analysis

Gil-Garcia AA, Kings IN, Al-Duri B

Abstract

In this study, numerical verification was performed using a 2D analysis from previous authors. Aiming to further verify the feasibility of simulations using the software Comsol Multiphysics, the selected system was under the effect of supercritical heat transfer at higher q_w/G ratios. Boundary conditions and geometry from the previous work were taken as reference using different turbulence models (Low-Re and SST), first and second discretisation order and different thermal boundary conditions. The second-order discretisation simulation provided the best verification, showing the same trends from the selected study. Deterioration was found due to sharp decreases of property changes at the inlet of the heated section, while strong buoyancy and acceleration affected the axial range between the inlet and 1,250 *mm*, inducing M-shaped velocity profiles and improving hydrothermal performance. This free convection regime quickly diminished along the pipe length, so at the axial range between 1,250 *mm* and the outlet had already turned to forced-convective. In this region, the HTC experienced an improvement due to the bulk of the flow achieving the PSC state at the outlet. For comparison purposes, the system was computed using 3D analysis, showing a better verification on the free-convective section of the pipe, while the forced-convective section did not reflect the performance of the data source. Moreover, HTE techniques were computed on 3D simulations by attaching ribs on the internal walls. Higher turbulence was found, although the selected helical ribs did not exceed the performance of the straight ribs due to the short pipe length.

Keywords: Comsol Multiphysics, conjugate heat transfer, supercritical heat transfer deterioration, three-dimensional turbulence modelling, internally-ribbed tube.

Abbreviations

2D	two-dimensional
3D	three-dimensional
BC	boundary condition
CFD	computational fluid dynamics
CHT	conjugate heat transfer
DB	Dittus-Boelter
DNS	direct numerical simulation
DOF	degrees of freedom
HTC	heat transfer coefficient
HTD	heat transfer deterioration
HTE	heat transfer enhancement
IRT	internally-ribbed tube
LPV	large property variation
PDE	partial differential equation
PSC	pseudo-critical
RANS	Reynolds-averaged Navier-Stokes
SC	supercritical
SCW	supercritical water
SCHT	supercritical heat transfer
SST	shear stress transport
TKE	turbulent kinetic energy

Dimensionless numbers

Bo	buoyancy parameter
Gr	Grashof number
K_v	thermal acceleration parameter
Nu	Nusselt number
Pr	Prandtl number
Re	Reynolds number

Greek symbols

α	thermal diffusivity [$m^2\ s^{-1}$] or helical rib angular displacement [°]
δ	pipe wall thickness [mm]
ε	rate of dissipation of kinetic energy [$m^2\ s^{-3}$]
μ	dynamic viscosity [$kg\ m^{-1}\ s^{-1}$]
π_c	dimensionless parameter measuring thermophysical changes [-]
ρ	density [$kg\ m^{-3}$]
τ	shear stress [Pa]
ϕ	circumferential angle between the centres of two rib root widths [°]

ω rate of dissipation of kinetic energy [$m^2\ s^{-3}$]

Geometric definitions

D tube inner diameter [mm]
D_o tube outer diameter [mm]
e rib height [mm]
L total length of section [mm]
L_{entr} unheated entrance section of pipe [mm]
L_{hot} heated section of pipe [mm]
R_i tube inner radius [mm]
R_o tube outer radius [mm]
r radial coordinate [mm]
w rib root width [mm]
x axial coordinate of heated section in 2D, axial/radial in 3D [mm]
x/D dimensionless heated pipe length [-]
y radial coordinate [mm]
y^+ dimensionless wall distance [-]
y_1^+ dimensionless wall distance of first layer to the wall [-]
z axial/radial coordinate in 3D [mm]

Roman symbols

C_p isobaric heat capacity [$J\ kg^{-1}\ degC^{-1}$]
G mass flux of water [$kg\ m^{-2}\ s^{-1}$]
g gravitational acceleration [$m\ s^{-2}$]
h heat transfer coefficient [$W\ m^{-2}\ degC^{-1}$]
H enthalpy [$J\ kg^{-1}$]
I turbulence intensity [%]
k turbulent kinetic energy [$m^2\ s^{-2}$]
p absolute pressure [bar]
q heat flux [$kW\ m^{-2}$]
T temperature [K or °C]
u axial flow velocity in 2D, radial flow velocity in 3D [$m\ s^{-1}$]
U flow mean velocity [$m\ s^{-1}$]
v radial flow velocity [$m\ s^{-1}$]
w axial flow velocity in 3D [$m\ s^{-1}$]

Subscripts

$(\ldots)_b$ at bulk conditions
$(\ldots)_{dht}$ at deteriorated heat transfer conditions

$(\dots)_{in}$ at inlet conditions
$(\dots)_{iw}$ at inner wall conditions
$(\dots)_{out}$ at outlet conditions
$(\dots)_{ow}$ at outer wall conditions
$(\dots)_{r}$ radial increment in 3D
$(\dots)_{turb}$ at turbulent conditions
$(\dots)_{T}$ at turbulent conditions
$(\dots)_{x}$ axial increment
$(\dots)_{y}$ radial increment in 2D
$(\dots)_{\infty}$ at surrounding temperature conditions (furnace chamber)

4.1. Background

In Chapter 3, a two-dimensional (2D) numerical validation employing imported experimental data was performed in order to validate the computational fluid dynamics (CFD) code COMSOL Multiphysics under conditions of supercritical heat transfer (SCHT) in turbulent convective flow. The 2D physical model had to be limited to a vertical flow due to the heterogeneous effect of gravity on the cross-sectional area of a horizontal flow, making also unrealistic the application of mesh-simplifying techniques such as axial symmetry (Du *et al.,* 2010; Shang *et al*., 2008).

Nevertheless, when studying SCHT many authors employed three-dimensional (3D) numerical analysis as a means to not only investigate horizontal flows but also obtain more realistic results in terms of buoyancy for vertical flows, allowing comparisons with their equivalent 2D studies in order to validate their performance. In general, the use of 2D analysis in SCHT was found more widespread than 3D due to their less demanding computational requirements. However, the cost to produce experimental results with SC water (SCW) makes 3D analysis an appealing alternative to study buoyancy-affected flows.

Because the area of interest in the present investigation was related to water cycles in supercritical (SC) boilers, 3D studies on SCHT previously performed by other authors were divided into forced-convective and mixed-convective regimes. At the same time, these two convective modes were sub-classified in four categories of investigation, namely 1) those tackling the effects of parameters such as buoyancy

and thermal acceleration, and their effect when producing new correlations, 2) the effects of heat transfer deterioration on the hydrothermal performance, 3) the influence of heat transfer enhancing techniques and 4) performance analysis of specific turbulence models.

When observing 3D numerical works on SCHT possessing a flow described as forced-convective (meaning pipe orientation should not affect performance), it is worth mentioning that many authors did not provide any verification on the effect of buoyancy being negligible when presenting their results. Instead, they relied on the conditions provided by imported experimental sources. In Chapter 3, the working conditions imported from Yamagata *et al.* (1972) were not considered to be generally affected by heat transfer deterioration (HTD), however as it was shown in terms of qualitative trends, some sections of the flow were more likely to be affected by slight deterioration even after replacing the working pressure (24.5 MPa) with a higher value (30 MPa), further away from the critical point.

As an example among the 3D forced-convective studies devoted to parameter effects and correlations, Li *et al.* (2011) developed a new correlation for CO_2 employing their own experimental data supported by numerical simulation, although the absence of buoyancy was not confirmed at any stage in the process. However, Li *et al.* (2016) developed a semi-empirical correlation for CO_2 and they considered a buoyancy parameter (Bo), from Jackson *et al.* (2009), as a means to verify that the flow regime was only affected by forced convection. Moreover, there were previous studies on HTD performed in 3D forced convection, referring to either property changes only

(Urbano & Nasuti, 2013) or thermal acceleration (He *et al.*, 2013) as the main causes.

When modelling complex geometries, numerical research takes advantage of the 3D analysis. Thus, several authors investigated the improvement of the heat transfer coefficient (HTC) by the enhancing the flowing system with the application of internally-ribbed tubes (IRTs). Pioro and Duffey (2005) presented a brief review of experimental heat transfer enhancement (HTE) for vertical and horizontal pipes, and Huang *et al.* (2016) published a review devoting a section to such techniques, including also numerical works. Nonetheless, not many numerical investigations employing IRTs were found at forced-convective conditions. Xu *et al.* (2015) performed numerical research of SCHT using methane flowing in an IRT at zero gravity with the CFD code FLUENT and they confirmed the presence of HTE, the weakening of HTD and the exact rib height to obtain optimal thermal performance.

On the other hand, the most common studies employing IRTs at forced-convective studies were found to be experimental, with the fluid flowing upwards (as one of the most common water-wall configurations as explained in Chapter 1), although none of them verified the presence of buoyancy effects either. Among them, it is worth mentioning the work carried by Zhang *et al.* (2015), as besides HTD and HTE studies they additionally developed a piece-wise correlation. Taklifi *et al.* (2016) and Tang *et al.* (2007) tested inclined orientations for IRTs (some new supercritical boiler designs combine inclined spiral pipes at the water wall with IRTs) despite the lack of buoyancy criteria. Also, in the investigation by Wang *et al.* (2011) they compared

subcritical and SCW performance in heated upward IRTs to find that there was no strong deterioration in any case, although the HTCs at subcritical conditions were larger compared to the best results of SCW. In addition, they found that the SC flow suffered HTD in a similar fashion as it occurs at subcritical conditions.

Three-dimensional analysis is also useful to validate the accuracy of turbulence models utilising either experimental data (in-house or imported) or empirical correlations. It offers advantages as it provides geometrical aspects that cannot be considered in two dimensions. Literature considering these aspects was found in forced convection, like the work of Cheng *et al.* (2007) and Wang *et al.* (2016) where both studies modelled SCHT and showed a better performance of the so-called Reynolds Stress Models compared to Low-Re ω-type models (described in the Appendix) which highly depended on the mesh structure. Kiss and Aszódi (2009) researched the effects of creating the material property definitions through different methods, to prove that the material table IAPWS-IF97 best defined SCHT as it also accounts for pressure variations; and also compared three turbulence models (k-ε, k-ω and Shear-Stress Transport k-ω (SST k-ω)) with experimental data in smooth upward flow to reach the conclusion that none of them was particularly better for the given conditions.

The literature found on 3D analysis of SCHT at mixed-convective conditions was considerably larger. Two general aspects to highlight are the existence of several investigations employing horizontal configurations, which is logical considering the aforementioned issues with such geometries in 2D; and the widespread investigation

of upward flows, given the necessity to understand the effects of gravitational forces on the flow in terms of heat transfer impair and deterioration.

One of the most relevant 3D mixed-convective studies on correlations and the effect of parameters was carried by Li *et al.* (2014). Employing the SST k-ω model, they studied numerically the SCHT of water flowing in vertical circular tubes not uniformly heated. They provided literature of previous studies where the SST model was capable of predicting HTD induced by buoyancy and thermal acceleration, and revealed that their system suffered a milder degree of HTD produced by buoyancy compared to uniform heating when heat input was increased. Also, they experienced a stronger effect of buoyancy in upward flows compared to downward flows. In terms of SC correlations, the one provided by Mokry *et al.* (2011) was proven useful to predict HTC. Finally, they revealed that radial distributions of velocity and turbulent diffusion were affected by HTD related to buoyancy.

Additionally within the studies of parameter effects, Forooghi and Hooman (2013) investigated the SCHT of CO_2 flowing in inclined pipes under the effect of considerable buoyancy. In order to isolate the gravitational effect, they applied the Boussinesq approximation (not to be mistaken for the Boussinesq assumption that defines the turbulent viscosity, described in Chapter 2) where all the thermophysical properties were kept constant but the density included in the gravity term in the momentum equations. They obtained heterogeneous values of HTC due to asymmetry of the buoyancy in inclined pipes and a similar deterioration mechanism compared to vertical upward flows (90°), although for inclinations below 60° this

effect started to disappear. Another important parameter, the pipe diameter, was investigated in 3D SCHT by Shang and Chen (2011) using water in horizontal pipes. They confirmed that large diameters (above 10 *mm*) would trigger strong buoyancy effects, while high values of mass flux would eliminate any HTD for diameters below 10 *mm*. In terms of the effect of pressure, Shang *et al.* (2008) studied numerically SCW flowing inside a horizontal round pipe of inner diameter (D) of 6.3 *mm* and 3 *m* in length (L) with the CFD code STAR-CD using different pressures and heat flux-mass flux ratios. It was shown that only when the buoyancy was insignificant, different values of system pressure would modify considerably the heat transfer performance. Also, higher system pressures would impair HTD at strong buoyancy conditions.

The number of works found related to HTD in 3D mixed convection was considerably larger compared to the ones using forced convection due to the effect of buoyancy on the enhancement or deterioration of heat transfer. As a consequence, it was extensively studied even employing Direct Numerical Simulation (DNS) like the research of Nemati *et al.* (2015). Focusing on the relevant literature found in turbulence modelling, Podila and Rao (2015) studied the HTD onset of SCW flowing vertically in a nuclear reactor bundle with the code STAR-CCM+ and the SST turbulence model employing values of the dimensionless wall distance of first layer to the wall (y_1^+) below 1. They discovered that in presence of high heat flux-mass flux ratios, an effective method to reduce the onset of HTD was to increase the temperature inlet beyond the corresponding pseudo-critical (PSC) value in order to

avoid instabilities at the entrance region, and also increase the system pressure to reduce the magnitude of property changes.

Moreover, several studies employed HTD conditions as stress tests for turbulence models. The numerical and experimental investigation by Wang *et al.* (2015) of annular flows in vertical pipes showed that among three different turbulence models, the SST successfully predicted the onset of HTD. Moreover, Sharabi *et al.* (2008) numerically predicted the 3D SCHT to CO_2 flowing in upward pipes with strong buoyancy-induced HTD using several k-ε models, and the low-Re formulation performed the best despite some overestimation of wall temperatures.

Similar to forced convection, investigations in mixed-convective flows were also performed employing HTE techniques only feasible in a 3D analysis. Li *et al.* (2015) compared the performance of heated SCW flowing in vertically smooth and IRTs utilising the SST k-ω model, and besides verifying the milder effect of buoyancy on the HTC of IRTs, they also revealed the applicability of the buoyancy criterion proposed by Jackson (1979), initially meant for smooth tubes, on such riffled pipes. Also Li et al. (2016) studied helically IRTs (3D) and transversally ribbed pipes (2D) for the same pipe orientation and turbulence model, observing the range of the buoyancy parameter by Jackson (1979) that would be beneficial on HTE and the role of rotational flows as a the reason for such HTE in helically IRTs. Also, they noticed that turbulence was intensified specifically on an area of the log-law region within the boundary layer.

The performance of turbulence models was also found to be assessed in several 3D numerical studies at mixed-convective conditions, often utilising complex geometries unfeasible in 2D analysis. A detailed numerical SCHT study by Podila and Rao (2016) was focused on a fuel rod bundle containing water flowing upwards, comparing the bare rod performance with another one including a wire-wrapped inside, as a means to improve turbulence. For this purpose, they imported experimental conditions and employed the SST k-ω and another Reynolds-averaged Navier-Stokes (RANS) model, named v^2-f, which utilises a nonlinear definition of eddy viscosity. They undertook sensitivity analysis for the mesh independence, for the effect of conjugate heat transfer (CHT) and for the effect of modifying the turbulent Prandtl number (Pr_t) included in the models, as this is normally a fixed value of 0.9 but can be modified in order to better match the experimental results. The SST k-ω model was found to better represent the SC conditions, and a Pr_t value of 1.5 was reported as ideal for the SC experiments. Similarly, Wang *et al.* (2015) employed a 3D approach to numerically investigate the performance of several turbulence models representing SCHT of a CO_2 flow in helically coiled tubes. Again, the SST model provided the best prediction compared to the experimental data. Nonetheless, in this case for such a complex geometry a buoyancy criterion commonly employed in straight pipes was found useless and modifying the Pr_t value was found irrelevant in terms of results.

In order to further validate the performance of the simulation software Comsol Multiphysics in conditions of SCHT with respect to the Chapter 3, in the present chapter a 2D numerical verification was firstly carried employing the boundary

conditions from the numerical study by Withag (2013). Although employing a different Low-Re turbulence model, it was the only numerical research found employing Comsol Multiphysics on SCHT. Moreover, Withag's working conditions were much more likely to be affected by buoyancy forces and HTD than the experimental conditions imported in Chapter 3. Boundary conditions similar to the present 2D studies were transferred to an equivalent 3D geometry and the computed results were compared. Furthermore, HTE techniques were investigated by comparing the smooth internal pipe surface with an array of straight and helicoidal IRTs displaying a shorter pipe length in order to save memory power, which were expected to promote turbulence and thus increase the HTC values. To the author's knowledge, no other 3D numerical analyses have been performed under supercritical conditions using the simulation software Comsol Multiphysics, so this was considered a novel area of investigation.

4.2. Computational methods

4.2.1. Physical models

The working conditions employed for all the geometries in this verification study were imported from the numerical analysis performed by Withag (2013). The computational domain involved a 2D vertically upward flow in a circular pipe employing axi-symmetry around the pipe centreline (thus only half the geometry was computed). In addition, the model included the pipe wall; therefore it was a CHT problem (conduction and convection). Moreover, an unheated length at the pipe entrance (L_{entr}) was included in order to allow the hydrodynamic boundary layer to develop. The L_{entr} had a value of 100 *mm* and the heated section (L_{hot}) measures 2400 *mm*. The value of D was 10 *mm* and the outer pipe diameter (D_o) was 16 *mm*. The 2D analysis in the present work is depicted in Figure 4.1.

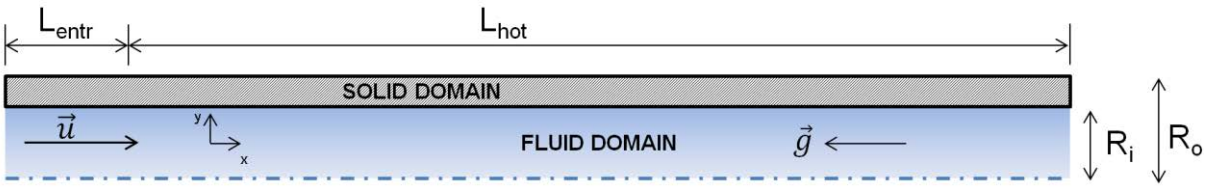

Figure 4.1 Computational domain employed in the 2D analysis, adapted from Withag (2013)

Afterwards, the computational domain was converted into a series of different 3D geometries employing (1) a smooth pipe and also ribbed pipes such as (2) a straight IRT and (3) a helical IRT as a means to research the improvement in heat transfer due to the turbulence induced by the ribs. For the smooth pipe and due to both the geometry and the vertical configuration, the flow could be considered completely

symmetrical, in terms of buoyancy forces too. Thus, it was modelled employing a quarter of the meshing domain as shown in Figure 4.2, keeping the same pipe length and diameters.

(a)

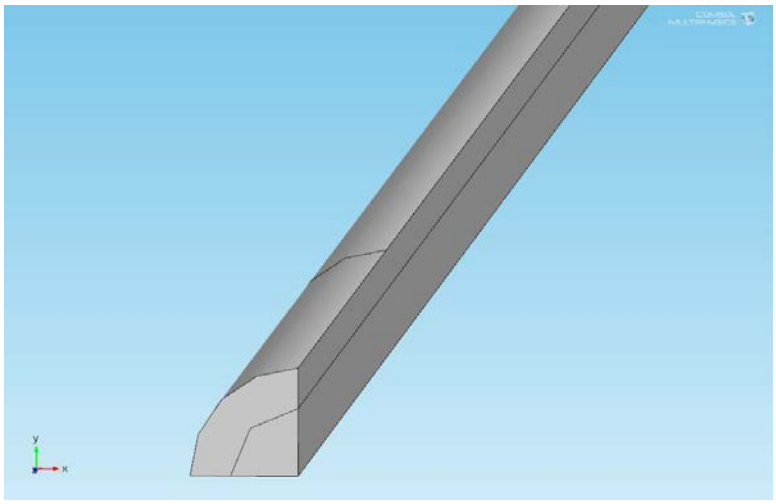

(b)

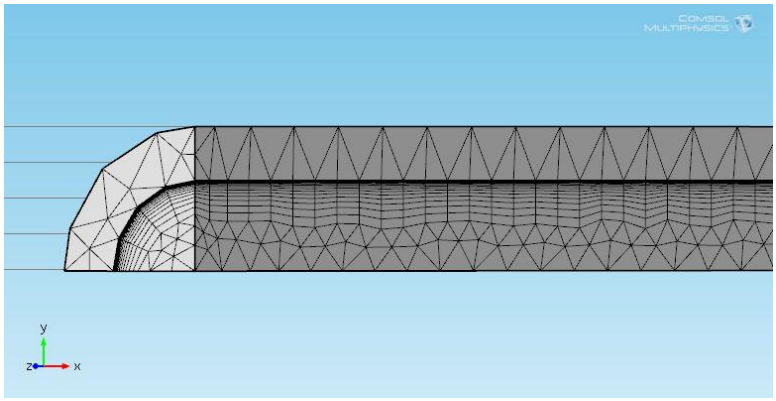

Figure 4.2 Detail of the smooth pipe geometry domains (a) and mesh (b)

The straight IRT, shown in Figure 4.3, also conserved geometrical and buoyant symmetry for the same reasons; however the helical IRT (Figure 4.5) did not due to the spiral configuration itself and the rotational flow induced as secondary effects. As a result, the full radial profile needed to be modelled in the helical IRT, which involved a memory-expensive 3D mesh. This constraint and the computational limitations present in the study led to an axial simplification of the geometry, thus only the first

400 *mm* of L_{hot} after the 100 *mm* of L_{entr} were modelled (around 17% of the full length) in order to maintain a reasonable balance between computational time and capture of the qualitative trends. It was decided that for the straight IRT, despite being completely symmetrical, this simplification would also be applied. Thus, a finer mesh could be selected in order to better capture the expected improvements in turbulence and thermal performance, and later compare it to the helical IRT.

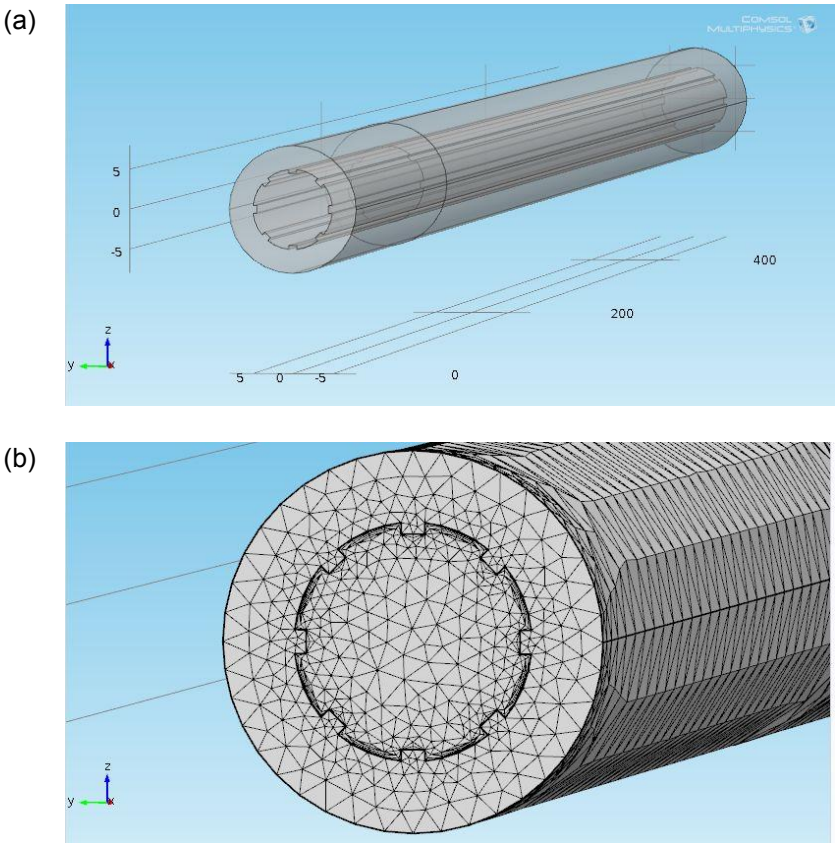

Figure 4.3 Detail of the straight IRT geometry domains (a) and mesh (b)

Moreover, the simulations with the IRTs displayed 8 ribs and their dimensioning was defined employing a cross sectional specification similar to that depicted in Figure 4.4 from the work of Li *et al.* (2016). The rib height (e) was 0.5 *mm* and the rib root width

(w) had a value of 1 *mm.* The circumferential angle between the two centres of w (φ) was 45°.

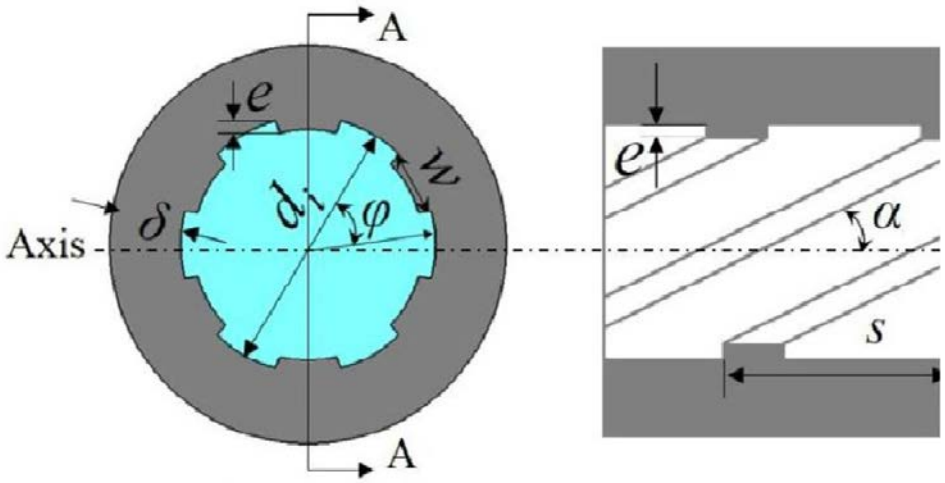

Figure 4.4 Cross section for an IRT (left) and A-A section (right), adapted from Li *et al.* (2016)

Both the 3D straight and helical IRTs were obtained by utilising the same 2D work plane (cross section) within the geometry section, extruding it afterwards into a 3D pipe. The only difference was that for the helical IRT, a "helix angle" feature was included, selecting an angular displacement of 15° along the axial section (α in Figure 4.4) during the extrusion between the initial work plane position and the final distance extruded. As appreciated in Figure 4.5, the spiral configuration was applied only after the end of the L_{entr} section of the pipe, namely at the beginning of the heated section, in order to allow a more stable development of the boundary layer at the inlet.

(a)

(b)

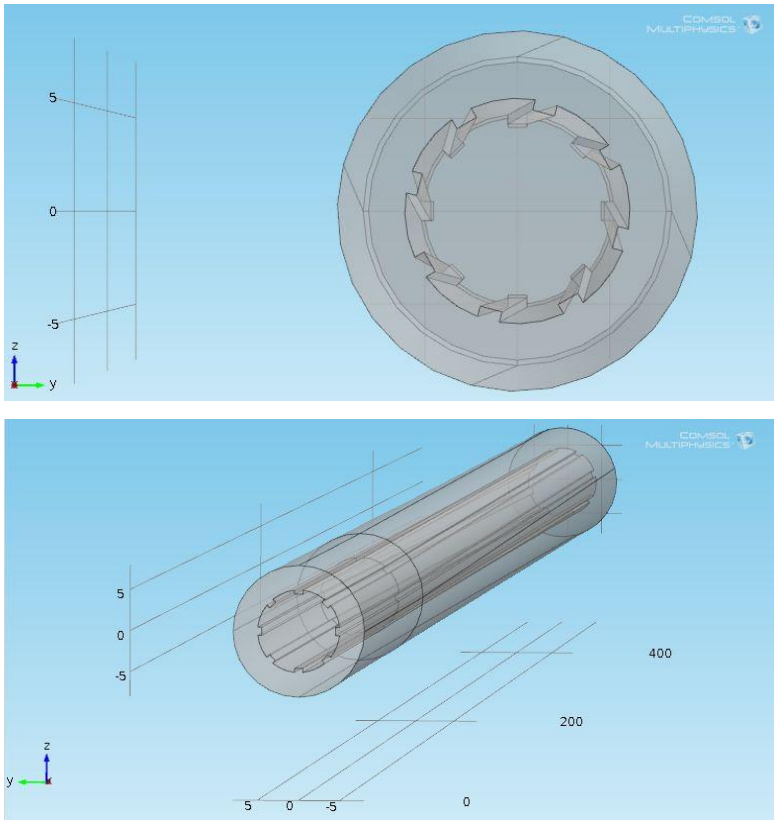

Figure 4.5 Detail of the helical IRT geometry inlet (a) and domains (b)

4.2.2. Governing equations

The governing equations of mass, energy and momentum for the fluid flow were the same as those previously described in the system computed in Chapter 3. On the energy equation however (namely equation 3.3), the heat flux (q) was not applied directly, but it came from the conduction through the solid domain as a part of the CHT process. This energy transferred from the solid to the fluid flow is represented by the Fourier's law, as shown in equation 4.1.

$$q = -k\nabla T \tag{4.1}$$

4.2.3. Boundary conditions

The selected boundary conditions were adapted from the work of Withag *et al.* (2012), which is summarised in Table 4.1. Additionally, they imported the fluid data containing all the thermophysical properties at a fixed pressure of 300 bar, which coincides with the reference pressure employed in the present study.

Table 4.1 Boundary conditions for the numerical verification, adapted from Withag (2013)

Boundary	Condition	Symbol and unit	Value
Inlet	Mass flux	G [kg m^{-2} s^{-1}]	200
Inlet	Temperature	T_{in} [°C]	350
L_{hot}	Temperature	T_{ow} [°C]	600
Outlet	Relative pressure	p_{out} [bar]	0

A 2D depiction of the boundary conditions used in the present studies is presented in Figure 4.6. This depiction could be also considered for all the undertaken 3D works, despite not displaying the rib geometries for those cases using IRTs.

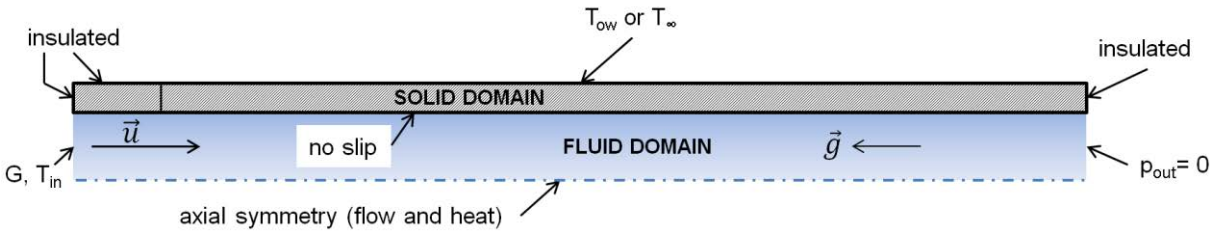

Figure 4.6 Boundary conditions, adapted from the work of Withag (2013)

A mass flux (G) of 200 kg m^{-2} s^{-1} enters the pipe flowing vertically upwards at an inlet temperature (T_{in}) of 350°C. With the values of density and viscosity at such

temperature, obtained from the NIST Standard Reference Database Number 69 by Lemmon *et al.* (2015), the normal inflow velocity (U_{in}) and thus the inlet Reynolds number (Re) were calculated. Two different thermal boundary conditions were selected on the outer wall of the L_{hot} section, giving way to two different simulation groups. The first followed exactly the same thermal boundary condition employed by Withag (2013); applying a constant external wall temperature (T_{ow}) of 600°C in a 2D approach and considering the same turbulence model they selected (Low Re k-ε) along with the SST model. The second thermal boundary condition, selected in the second section of the study, was an external convective heat flux defined by an external HTC (h_∞) of 4,800 W m^{-2} $degC^{-1}$ and external temperature (T_∞) of 650°C. In this case, the axial temperature profile of T_{ow} varies depending on both the T_∞ and the temperature of the fluid flowing inside. This thermal boundary condition was selected to compare results between 2D and 3D systems, because it represents a more realistic boiler system.

4.2.4. Initial conditions

The ramping technique utilised in Chapter 3 was also applied in the present investigation as a means to reach the desired values of thermal boundary conditions without issues in convergence. Therefore the selection of any initial conditions other than the previous computed solution was of little use. Moreover, the first computations were performed at isothermal conditions so all the fluid domain was set at T_{in}, away from the region of large changes induced by the PSC conditions at 401.9°C.

Besides the addition of a L_{entr} section at the inlet, a developed inflow was also intended in order to increase stability at the entrance where the development of the boundary layer and the applied heat flux might interact. Consequently, inflow parameters such as U_{in} and the turbulent kinetic energy (k) and energy dissipation (ω or ε) from the employed turbulence models were intended to be mapped (imported rather than roughly estimated) from a previous computed model at isothermal conditions. This was fully or partially achieved for simple inflow geometries such as the 2D simulations or the 3D smooth pipe, but for complex geometries such as the 3D ribbed pipes this feature was not successfully achieved.

4.2.5. Material properties and implementation

In the present study supercritical water was not the only material implemented as in Chapter 3, but also a nickel-based super-alloy for the solid domain named Inconel 625. This material was initially selected bearing in mind prospective validations with in-house experimental work. Inconel 625 was preferred in most experimental rigs due to its high electrical resistivity, which due to the Joule effect produces large amounts of energy dissipation, thus heating the fluid flow inside the pipe. For the implementation of Inconel 625 in the simulation software Comsol Multiphysics, the same methodology as in Chapter 3 for supercritical water was utilised to define the thermophysical properties using technical information from piping vendors; creating a series of temperature-dependent piecewise polynomials interconnected by coupling their temperature ranges as a continuum.

4.2.6. Mesh generation and performance

The 2D meshes employed for the cases applying constant T_{ow} and convective heat flux as thermal boundary conditions were composed of a free triangular mesh for the solid domain and a mapped mesh for the fluid domain. The free triangular mesh is an unstructured, versatile mesh that the software selects by default, and thus it was assigned to the solid domain in order to save memory power where the property profiles are not relevant. The mapped mesh on the other hand is very efficient when refining squared geometries, and thus it was selected for the fluid domain in order to customise the areas where property profiles were expected to experience sharp slopes. In that sense, mesh refinement was applied near the inner wall, as a means to better capture the phenomena occurring within the viscous layer. For this purpose, the mapped mesh in the fluid domain was distributed manually due to its easy configuration, instead of creating a boundary layer nodule. The free triangular mesh was distributed with a fixed number of elements, while the mapped mesh for the fluid domain was slightly refined in the axial direction towards the inlet and outlet by employing an arithmetic sequence with a moderate element ratio. Bearing in mind the results from Chapter 3, the radial mesh strongly influenced on the results. Thus, it was composed of 40 elements, with a geometric sequence of a higher element ratio towards the inner wall. Figure 4.7 depicts the first 15 *mm* of L_{entr}, shown in the x-axis of the axy-symmetric 2D geometry, and on the y-axis the upper radial half of the pipe D (from 5 to 10 *mm*) including the solid domain of the pipe (from 10 to 13 *mm*). Thus, the dotted horizontal line at y= 5 mm represented the bulk of the flow. This mesh was

selected because showed a good balance between performance and reasonable simulation times (not more than a few hours, as seen on Table 4.2) and results.

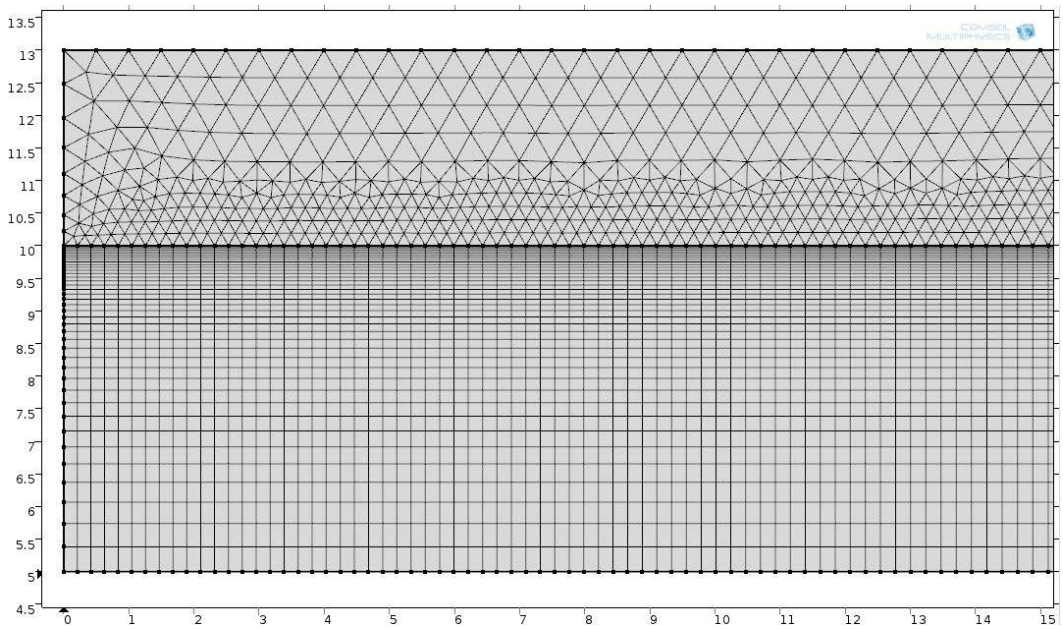

Figure 4.7 2D mesh at inlet section showing solid and fluid domains (axes in *mm*)

Due to its high sensitivity, it was discovered that a good parameter to measure the mesh response to thermal stress was the conductive heat flux applied on the outer wall of the solid domain (q_{ow}), which transfers from the solid domain into the fluid domain and increase the temperature. On Figure 4.8 two plots depicting different values of T_{ow} (Figure 4.8a at 600°C and Figure 4.8b at 900°C) show the q_{ow} transfer from the solid domain (diameter range of 10-13 *mm*) towards the fluid domain (diameter range of 5-10 *mm*) for the 2D simulation employing constant T_{ow}. The original aspect ratio of the geometry (L/D) was visually reduced to 1:1 for convenient depiction of the full pipe (solid domain on the top side and pipe inlet on the vertical left side). As can be seen, Figure 4.8b with T_{ow} at 900°C shows a red trail of spontaneous and physically meaningless high heat flux close to the inner wall, on a

zone of the fluid domain known as the large-property-variation (LPV) region, where the thermophysical properties start to considerably change due to proximity of the PSC point. This trail was much weaker as shown in Figure 4.8a with T_{ow} at 600°C, shown in yellow, as the thermal stress was milder so the mesh could process more appropriately the computation and consequently the q_{ow} transfer occurs smoothly.

(a)

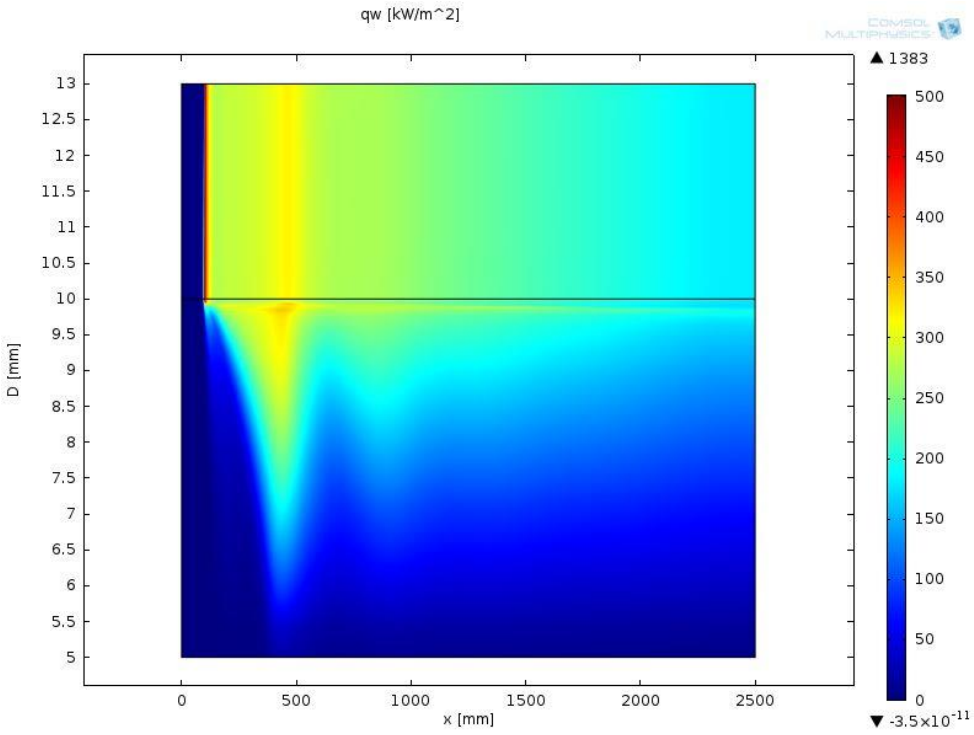

(b)

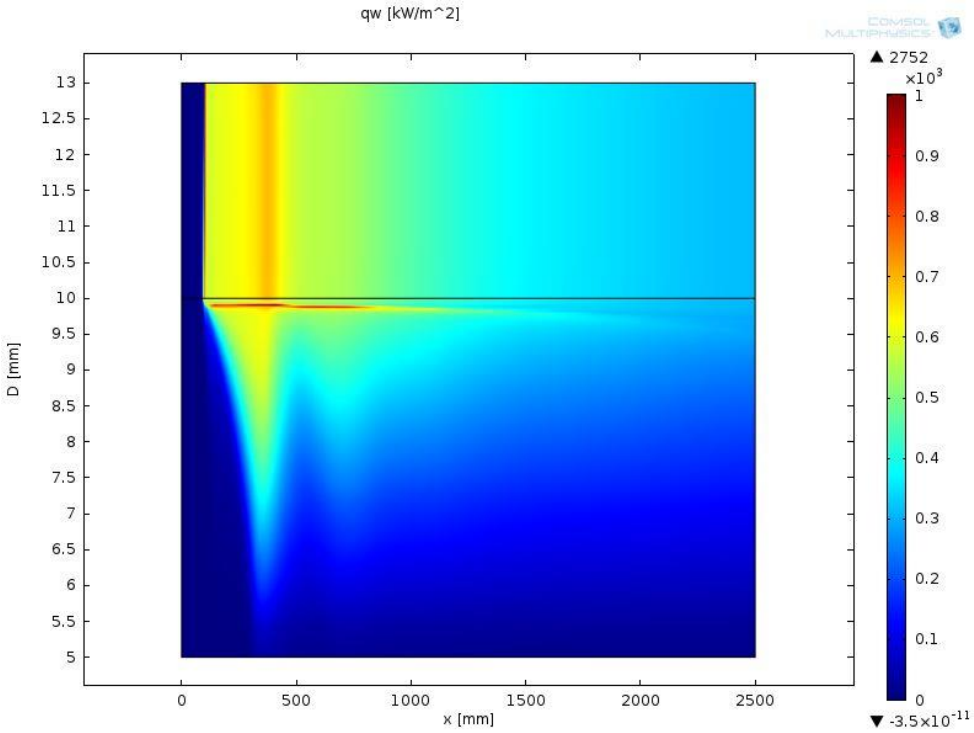

Figure 4.8 Thermal stress on mesh, at T_{ow}=600°C (a) and T_{ow}=900°C (b)

The 3D geometries were produced by a physics-controlled sequence in order to reinforce mesh stability. Despite the application of geometrical simplifications such as axial symmetries on the smooth pipe to compute a quarter of the volume, or a reduction of approximately 80% in the pipe length for the IRTs, the mesh element sizes had to be coarse in all the 3D analyses in order to reduce computational times. Mapped or quadrangular meshes, which allowed a better manual distribution in 2D studies, were not feasible when applying 3D symmetry or IRTs, thus the final 3D meshes were composed by a series of unstructured, tetrahedral elements in both the solid and fluid domains and a boundary layer nodule composed of 14 layers (prism elements) as can be observed in Figure 4.2b for the smooth pipe and Figure 4.3b for the straight IRT.

Moreover, mesh sensitivity studies were carried in order to prove the capability of the 3D meshes to capture qualitative trends. Figure 4.9a and Figure 4.10a show the axial profiles, at isothermal conditions, of the mean flow velocity at the pipe centreline for the 3D smooth pipe and the 3D straight IRT, respectively; while Figure 4.9b and Figure 4.10b depict turbulent viscosity at the same conditions. In every plot, two isothermal scenarios at 350°C were compared. One of them employed a geometry with finer mesh (cases 3D-E in Figure 4.9 and 3D-G in Figure 4.10, as described in Table 4.2) while the other system used slightly coarser 3D meshes, utilised for the non-isothermal simulations (cases 3D-F in Figure 4.9 and 3D-H in in Figure 4.10, also described in Table 4.2). As a consequence of mesh refinement, cases 3D-E and 3D-G were expected to provide more accurate trends. As can be seen, the cases 3D-F and 3D-H, while having coarser meshes, still provided very similar qualitative trends. It is worth mentioning that the case 3D-G shown on Figure 4.10 had a pipe length twice the case 3D-H for computational reasons, thus the different profile lengths.

(a)

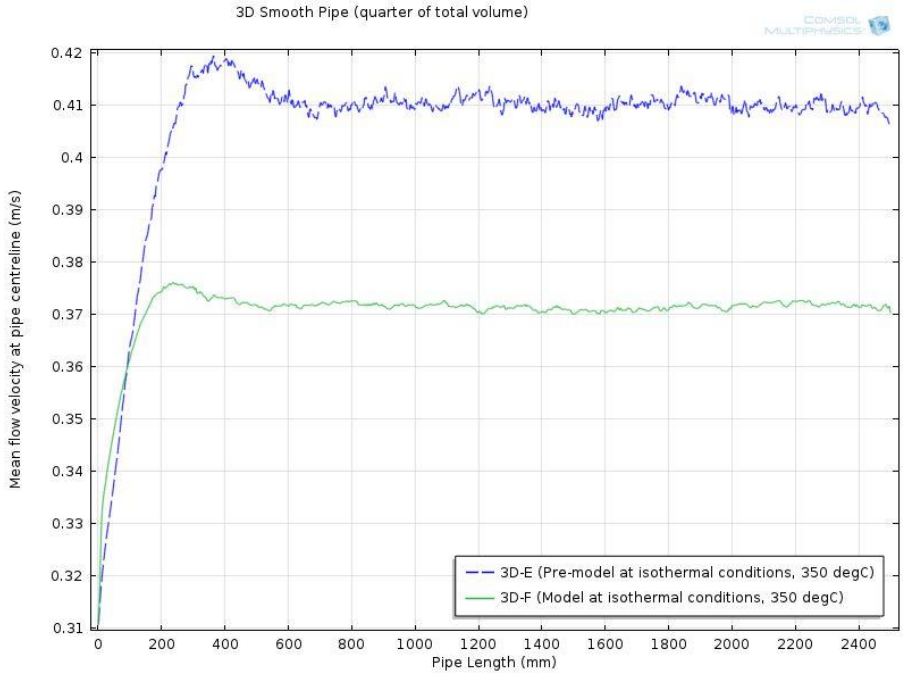

(b)

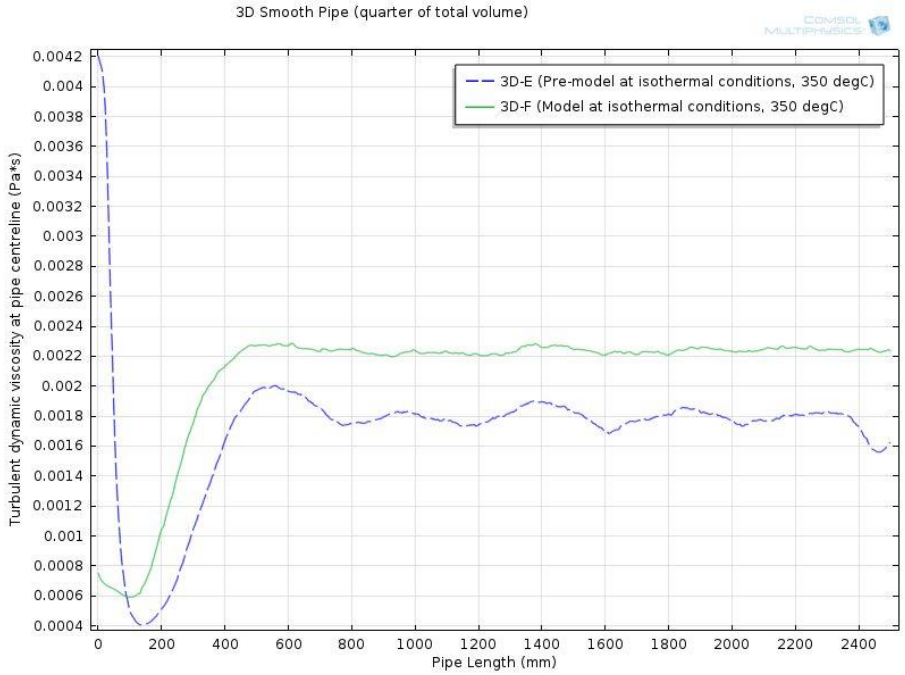

Figure 4.9 Performance of mean flow velocity (a) and turbulent viscosity (b) for cases 3D-E and 3D-F, using the 3D smooth pipe

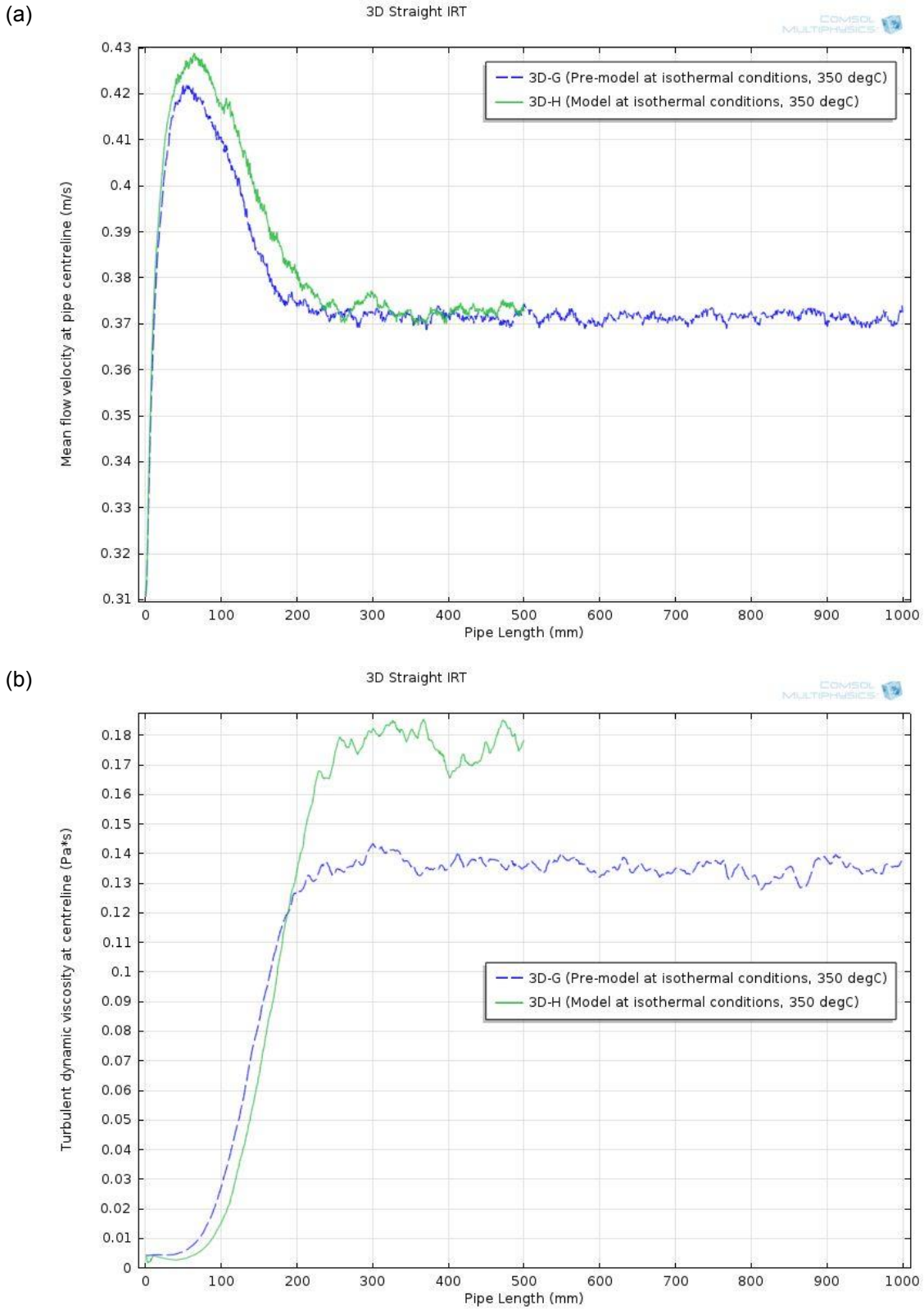

Figure 4.10 Performance of mean flow velocity (a) and turbulent viscosity (b) for cases 3D-G and 3D-H, using the 3D straight IRT pipe

In terms of y_1^+, despite the relatively coarse meshes employed, the low values of G were beneficial towards the mesh performance and thus the 2D simulations had an averaged value of 4 approximately. The 3D results for the smooth pipe revealed a y_1^+ between 4 and 6. On the other hand, the 3D ribbed meshes displayed heterogeneous values of y_1^+ due to the surface of the internal wall containing many edges from the ribs. Nevertheless, the edge between the ribs and the internal pipe diameter, which was meant to possess a larger value of y_1^+ due to geometrical limitations, was tested and revealed a y_1^+ of 3.7 approximately.

4.2.7. Solution methodology, turbulence model and discretisation

In terms of the procedure within Comsol Multiphysics, the solution methodology followed the same features as described in Chapter 3. In the present work however, the selected package was CHT instead of Non-Isothermal Flow, in order to couple the heat conduction through the solid domain with the turbulent convection in the fluid domain. For computer specifications refer to Chapter 3. Similarly, the SST k-ω was selected due to the advantageous features for the given conditions as described in the Appendix and the extensive literature highlighting the successful applicability of the model in SCHT, as presented in Chapter 3 and the introduction of the present study. Only some results for the 2D numerical verification employed the Low-Re k-ε model, in order to match the computing conditions of Withag (2013).

A description of the different cases studied and their performance is summarised in Table 4.2 and Table 4.3, respectively. All cases employ the same 2D or 3D geometry

and only differ on aspects such as meshing, discretisation order and turbulence model. Because the 2D simulations using first-order Lagrange elements as discretisation technique required less computational power, a second order simulation was attempted employing the first-order discretised solution as initial condition and a convergence criterion (relative error) of $1x10^{-6}$. However, the case 2D-A failed due to instabilities and the cases 2D-B and 2D-D never managed to converge below the error criterion of $1x10^{-6}$ (some segregated groups of equations did not reduce their residual errors below $1x10^{-3}$ and $1x10^{-2}$, respectively). Still, the modified case 2D-B using second-order discretisation provided a solution that, although not complying with the established convergence criterion, produced more accurate results than the initial first-order simulation. Thus, it was presented as case 2D-C. In order to reach a solution using second-order discretisation in all cases, this procedure should have been implemented at the beginning of the ramping process at isothermal conditions, instead of overwriting the first-order discretisation in the last simulation. However, the computational time would have been prohibitively high.

Table 4.2 Description of the different cases studied

Case	Dimensions	Discretisation	Model	Thermal BC
2D-A	2D	1st order	Low-Re k-ε	T_{ow}
2D-B	2D	1st order	SST	T_{ow}
2D-C	2D	2nd order	SST	T_{ow}
2D-D	2D	1st order	SST	T_{∞}
3D-E	3D smooth (pre-model)	1st order	SST	T_{∞}
3D-F	3D smooth	1st order	SST	T_{∞}
3D-G	3D straight IRT (pre-model)	1st order	SST	T_{∞}
3D-H	3D straight IRT	1st order	SST	T_{∞}
3D-I	3D helical IRT	1st order	SST	T_{∞}

Nevertheless, all the computed results shown by Withag *et al.* (2012) employed second-order discretisation, and the selected convergence criterion was a relative error of 1×10^{-3}. The 2D mesh they generated for the geometry consisted of 115,717 triangular elements for the solid domain and 585,000 quadrilateral elements for the fluid domain. This means that their computation employed a finer mesh than the present cases, depicted in Table 4.3.

Table 4.3 Performance of the different cases studied

Case	Residual error	DOF	Solid elements	Fluid elements	Memory [GB] (physical/virtual)	Solution time [h]
2D-A	$1x10^{-3}$	$1x10^{6}$	$5.1x10^{4}$	$1.6x10^{5}$	6.9/7.3	8
2D-B	$1x10^{-3}$	$1x10^{6}$	$5.1x10^{4}$	$1.6x10^{5}$	6/8.2	7
2D-C	$1x10^{-3}$	$3.5x10^{6}$	$5.1x10^{4}$	$1.6x10^{5}$	20.2/20.9	∞
2D-D	$1x10^{-3}$	$1x10^{6}$	$5.1x10^{4}$	$1.6x10^{5}$	7.7/12.2	2
3D-E	$1x10^{-3}$	$3.7x10^{6}$	-	$1.5\ x10^{6}$	30.7/46.3	51,5
3D-F	$1x10^{-3}$	$3.9x10^{5}$	$1x10^{4}$	$9.1x10^{4}$	8.5/22.8	5.5
3D-G	$1x10^{-3}$	$2.3x10^{6}$	-	$1.5\ x10^{6}$	23.8/25.7	17
3D-H	$1x10^{-3}$	$1.2x10^{6}$	$2x10^{5}$	$6.7x10^{5}$	28/35	15
3D-I	$1x10^{-3}$	$1.1x10^{6}$	$1.8x10^{5}$	$5.7x10^{5}$	25.6/36.9	12

The 3D analyses were also limited to first-order discretisation for the same computational limitations. The case 3D-F (3D smooth pipe) employed the full pipe length due to the use of only a quarter of the meshable volume by applying axi-symmetry. However, compared to the 3D IRTs cases (3D-G to 3D-I) the latter revealed a much higher number of degrees of freedom (DOF) and elements despite computing only around 17% of the meshable volume using full 3D analysis (thus, larger computational times). As a means to increase stability, prior to modelling the hydrothermal process of each simulation case an isothermal run was computed

employing finer geometries and longer pipes lengths looking for a prospective mapping of the developed hydrodynamic parameters to the flow inlet of the heated pipe in the following simulation. Therefore, these pre-models involved a sensitive increase in the computational time, i.e. cases 3D-E and 3D-G.

4.2.8. Solver approach

The solver configuration was very similar to the one described in Chapter 3. A direct solver (Pardiso) replaced the iterative solvers assigned by default in order to gain robustness against the high non-linearity and the unstable coupling of different physics such as convective heat transfer and turbulent flow, in exchange of higher memory consumption. Moreover, consistent stabilisation techniques such as the use of streamline and crosswind diffusions were applied without modifying the initial transport equation.

After the wall initialisation stage, the segregated partial differential equations (PDEs) were only manually modified for the 3D analyses, in the fashion of Chapter 3, in order to grant higher stability. For the termination technique, a relative tolerance of 10^{-3} was chosen at all times in order to maintain a reasonable computation time.

4.3. Results and discussion

4.3.1. Numerical verification with 2D studies

The computed results obtained by Withag *et al.* (2012) are depicted in Figure 4.11. The x-axis displayed the axial location within L_{hot}, known as x in the present chapter. The HTC, as well as the internal wall temperature (T_{iw}) and the axial flow temperature (named bulk temperature in the present study, T_b), are shown on the left y-axis while the conductive heat flux transferred throughout the wall to the flow (q_w) is displayed on the right y-axis. The values of q_w, T_{iw} and T_b were obtained from the computation, while the HTC (h) was obtained from equation (4.2).

$$h = \frac{q_w}{(T_{iw} - T_b)} \quad \textbf{(4.2)}$$

During the first 250 *mm* approximately, entrance effects were triggered as a result of the q_w producing a rapid increase of the T_{iw} beyond the PSC point. At 250 *mm* approximately, T_b started rising and thus a sharp peak in the HTC was produced. From this point to an x of 1750 *mm* approximately, the HTC decreased as a result of the T_b increasing towards the value of T_{iw}, which at the same time decreased the driving force in terms of q_w. Nevertheless, at 1750 *mm* approximately the T_b reached values within the LPV region and the HTC started increasing until the outlet of the pipe which, as explained in Chapter 3, should coincide with a value of T_b a few decrees earlier than the PSC temperature (approximately at 401.9°C or 675 K at a pressure of 300 bar). This peak in HTC, at 950 W m^{-2} $degC^{-1}$ approximately,

increased the heat transfer performance and thus the heat flux increased in a similar fashion.

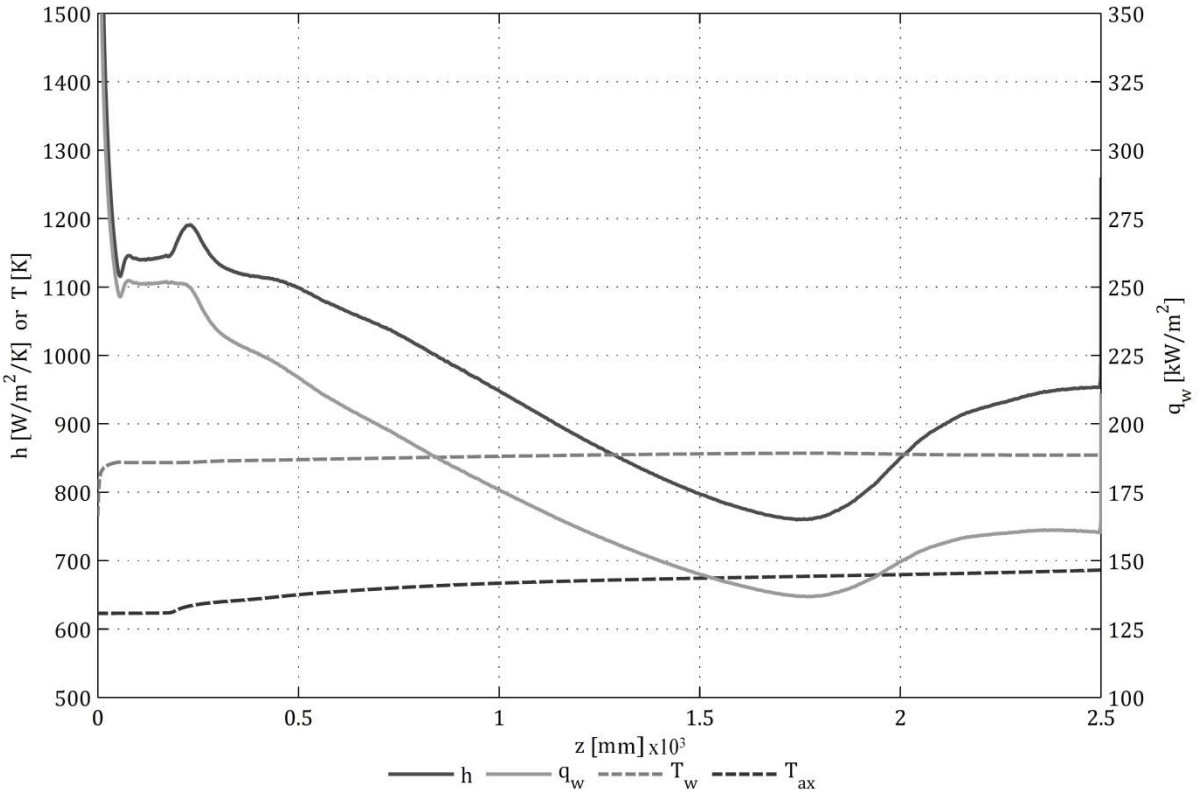

Figure 4.11 Plot adapted from Withag *et al.* (2012), showing the axial values of h, T_{iw} and T_b (left y-axis) as well as q_w (right axis) for constant T_{ow} as thermal boundary condition

Figure 4.12 reveals the computed results obtained for the case 2D-A, defined in Table 4.2 and Table 4.3. This case used the same turbulence model as Withag and co-workers, although the mesh was coarser and first discretisation order was applied. Compared to the results from Withag and colleagues, these simplifications led to a sensible overestimation of q_w and thus of the HTC throughout L_{hot}, although the qualitative trends were maintained at the axial range approximately between the inlet and 1,250 *mm*. Nevertheless, despite the T_b values reached the LPV region approximately within the axial range between 1,200 *mm* and the outlet and also were

very close to the PSC point at the pipe outlet, the case 2D-A was not able to reproduce the consequent HTC recovery.

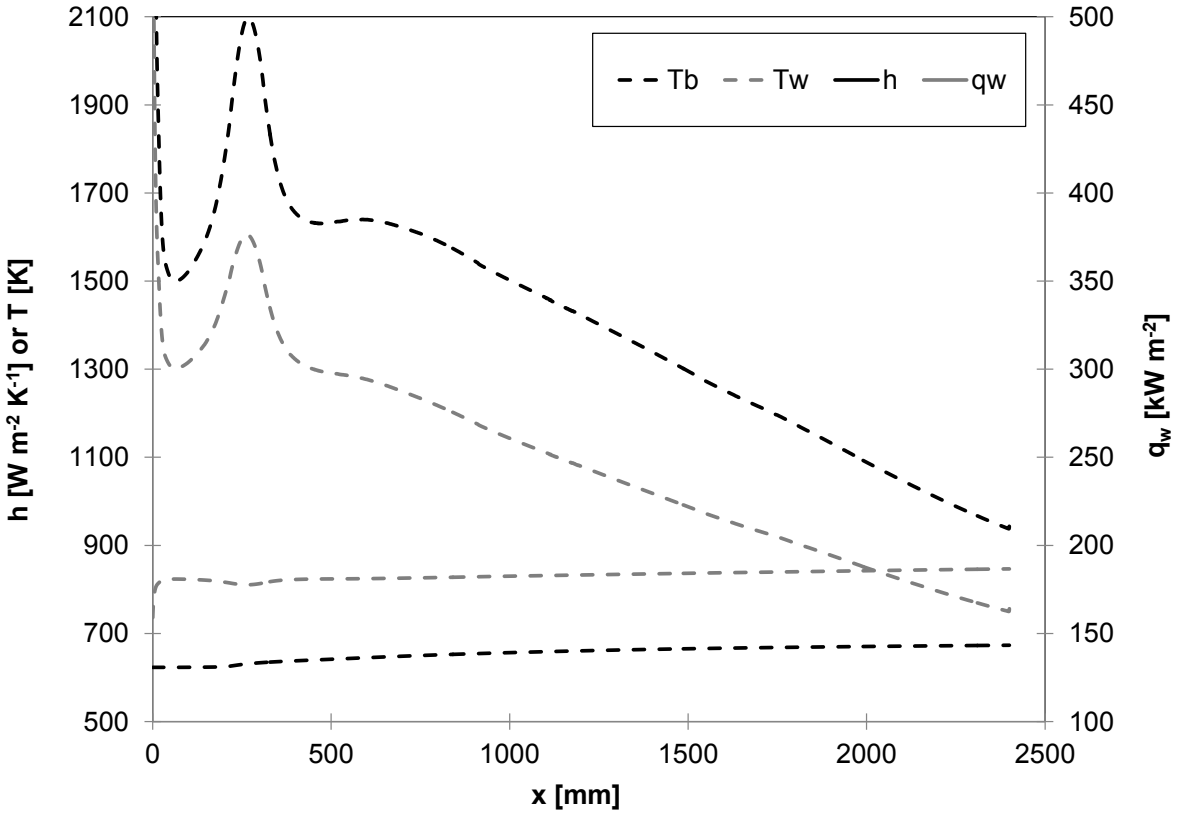

Figure 4.12 Plot displaying the results from case 2D-A as in Figure 4.11

The case 2D-B is depicted in Figure 4.13. This case used the same mesh and discretisation order as in case 2D-A, but the SST turbulence model was employed. The results shown display a similar pattern as in Figure 4.12 and very similar values of T_b along the centreline, although the overestimation of q_w and HTC was milder and a slight recovery of the HTC value was captured at the outlet. These results reveal a better performance of the SST model than the Low-Re k-ε model in the same computational conditions, when compared to the work of Withag and colleagues. Nevertheless, a second HTC peak seems to appear shortly after the highest, at 800

mm approximately. This peak was almost not reproduced in the simulation by Withag and collaborators or in case 2D-A, both using the Low-Re k-ε model.

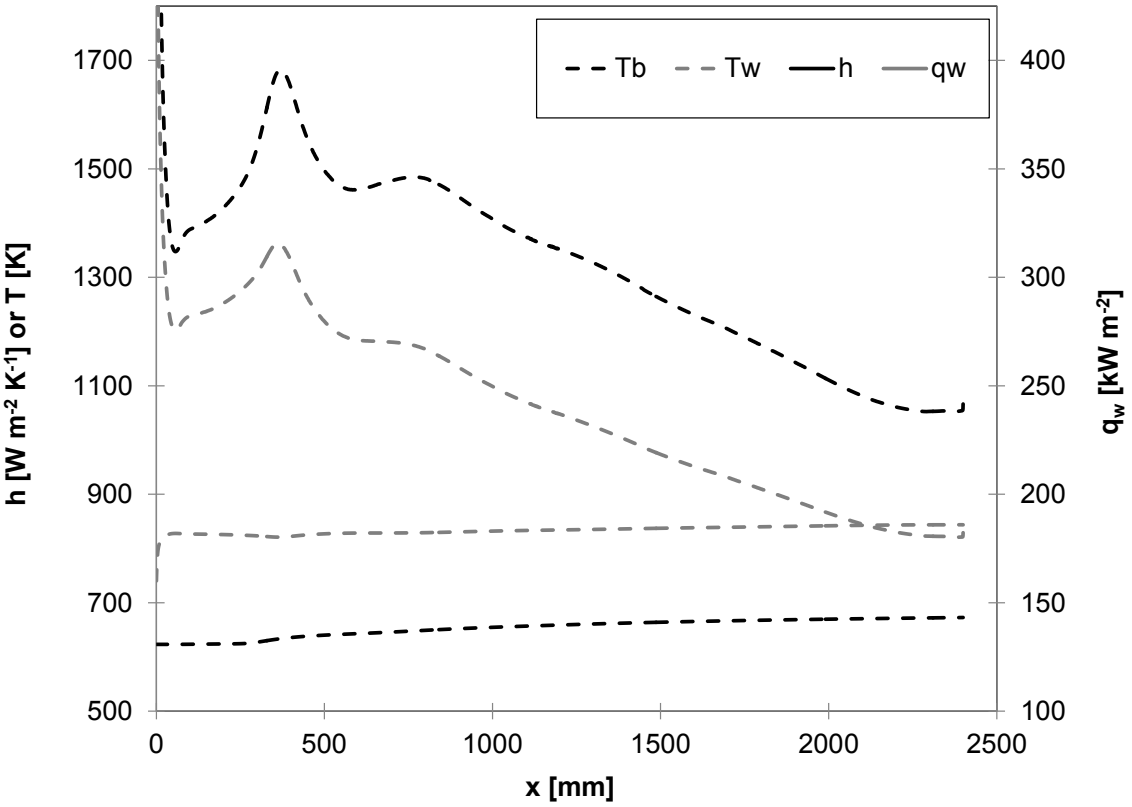

Figure 4.13 Plot displaying the results from case 2D-B as in Figure 4.11

In Figure 4.14 the results for the case 2D-C are presented. This case used the same mesh and turbulence model as in case 2D-B, but employed a second discretisation order. Even in these conditions, overestimation of q_w was still present, which seems to be inherent to the SST model. However, this case computed higher values of T_b, so the core of the flow had just surpassed the PSC point at the outlet because the model was capable of fully capturing the qualitative trend approximately within the axial range between 1,200 *mm* and the outlet, including the HTC recovery. As a result, using a second-order discretisation was useful in terms of better representing the coupling between the conductive heat applied and the turbulent fluid flow, i.e. the

heat transfer from the solid to the fluid domain. Again, a second HTC peak was produced, at x= 900 *mm* approximately, when using the SST model and therefore some attention was focused around this area on further analyses.

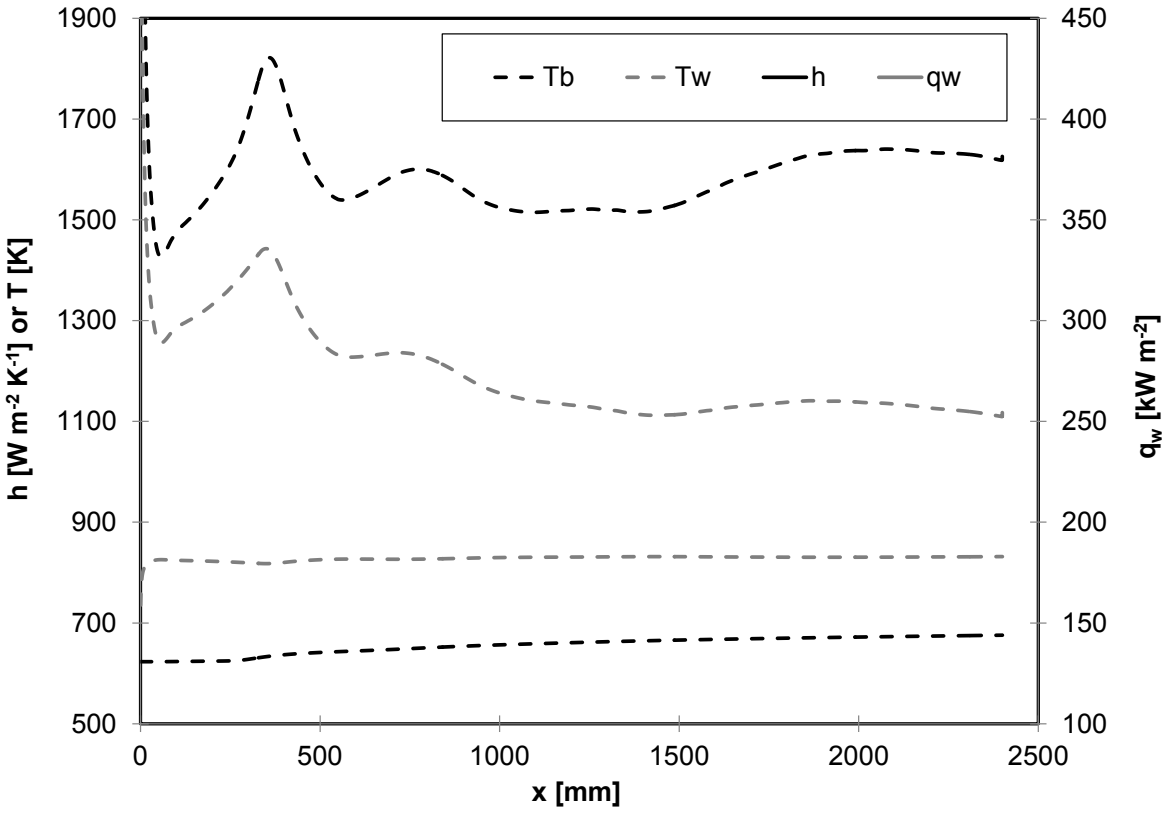

Figure 4.14 Plot displaying the results from case 2D-C as in Figure 4.11

Moreover, the case 2D-D included a modification of the thermal boundary condition selected by Withag and colleagues, choosing external convective heat flux as a more realistic heat source than a constant T_{ow}. A value of 4800 W m^{-2} $degC^{-1}$ was estimated for the h_∞ by assuming furnace chamber conditions, and a T_∞ of 650°C was considered in order to allow comparison with the previous cases. The results are shown in Figure 4.15. The mesh, discretisation and turbulence model were the same as in case 2D-B so only the heat source method was replaced. As can be observed,

the differences with respect to the case 2D-B were minimal, however the mesh refinement and mostly the discretisation order should be further increased in order to properly capture possible differences.

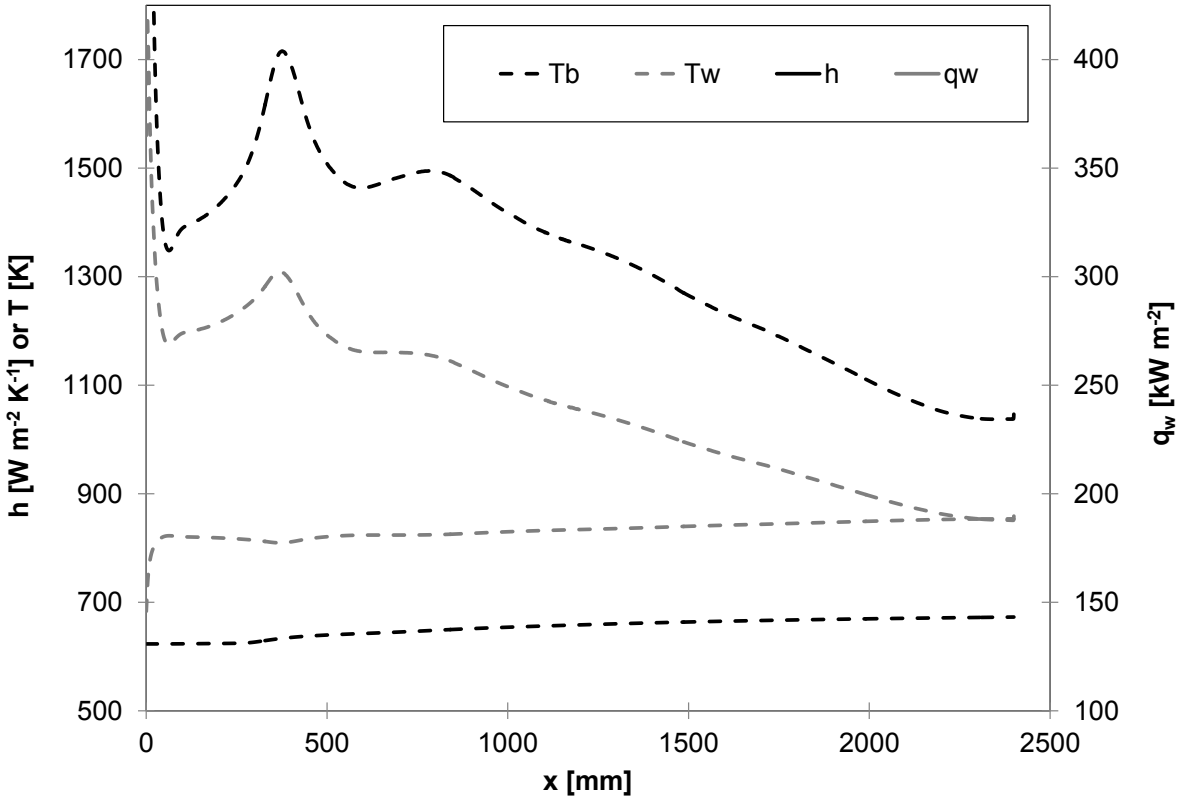

Figure 4.15 Plot displaying the results from case 2D-D as in Figure 4.11

4.3.2. 2D heat transfer deterioration study

The case 2D-C was chosen for the HTD study due to the good performance reproducing the results from Withag *et al.* (2012) seen in Figure 4.11. The correlations employed in Chapter 3 to determine the onset of the HTD (Table 3.2) were applied for a G of 200 kg m^{-2} s^{-1}, obtaining a range of heat fluxes at the onset of deterioration (q_{dht}) between 90 and 116 kW m^{-2}. By checking the results for the q_w in

the different plots between Figure 4.11 and Figure 4.15, it can be appreciated that all the cases largely surpass this range of q_{dht} and thus buoyancy and or thermal acceleration were influential. The same parameters used in Chapter 3 accounting for the three factors affecting HTD (property changes, buoyancy and thermal acceleration) were considered. These were the property changes parameter (π_c), the buoyancy parameter (Bo) and the thermal acceleration parameter (K_v). The only difference is that in the present study heat flux was not imposed as constant. Instead, constant external wall temperature (case 2D-C) was applied so the driving force was progressively reduced along the pipe, as the fluid temperature converges towards the external wall temperature. Thus, the Grashof number (Gr) contained within the formula for Bo had to be redefined to another one accounting for density instead (Gr_ρ), as shown in equation (4.3). The symbols contained within were properly defined in the nomenclature section.

$$Gr_\rho = \frac{g \cdot \rho_b \cdot D^3 \cdot (\rho_b - \rho_w)}{\mu_b^2} \quad \textbf{(4.3)}$$

In order to research the influence of each of the three factors, different Nusselt numbers (Nu) displayed as ratios (henceforth, known as *Nu ratios*) in the fashion of Chapter 3 were used by employing the Dittus-Boelter (DB) correlation (Winterton, 1998, described in Section 2.2.3) to account for the subcritical performance at constant properties and the Mokry correlation (Mokry *et al.,* 2011, described in Section 2.2.3) for the supercritical performance considering property changes. The range of parameters for the Mokry correlation to be applicable was described in Chapter 2, and could be also applied in the present chapter.

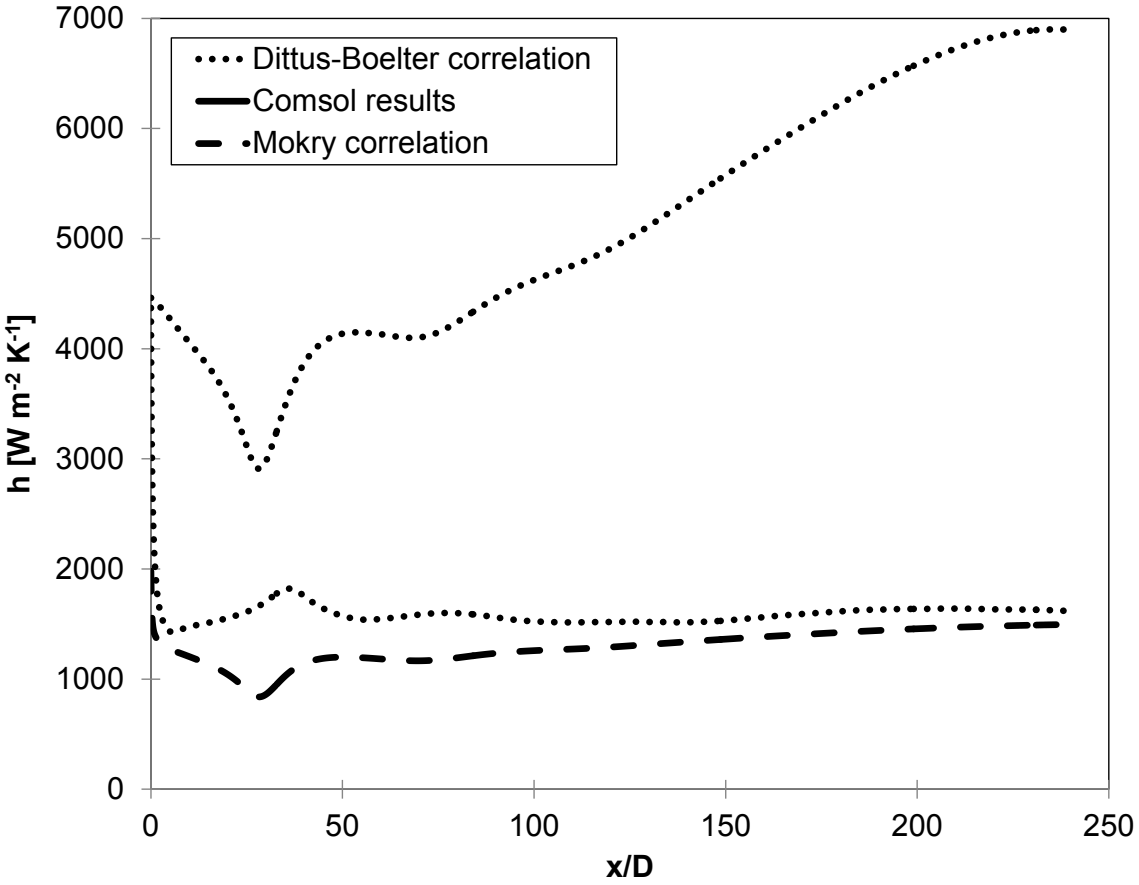

Figure 4.16 HTCs obtained from several correlations and the simulation results

In order to see the overall perspective, Figure 4.16 shows the HTCs obtained by both correlations and the simulation results. From the entrance region of L_{hot} to a dimensionless heated pipe length (x/D) close to 75, the DB correlation seems to reveal a normal heat transfer (NHT) regime at a HTC value of 4,000 W m^{-2} $degC^{-1}$ approximately. From that point on, the HTC from the DB correlation started sharply rising as the flow temperature approached the LPV region and therefore this correlation was no longer valid for the rest of L_{hot}. Nevertheless, within the NHT regime the HTC values from the Mokry correlation and the computation results appeared considerably below the value shown from the DB correlation, which

suggests the heat transfer regime was deteriorated. This is shown in Figure 4.17b, using Nu ratio accounting for the property changes (Nu_{Mokry}/Nu_{DB}) which was well below 1 in the NHT region. Beyond x/D=50 approximately, the Nu ratio was no longer valid.

On the other hand, the π_c parameter was applied along the entire pipe length and revealed larger property changes at the entrance region of L_{hot}, but as the T_b approached the PSC value, π_c dropped. This trend was due to the fact that the π_c formula was based on the heat capacity (C_p), whose axial gradients decrease on the onset of the peak achieved before the PSC point. In the plot shown in Figure 4.17a the NHT regime laid from a value of π_c equal to 1.1 onwards approximately. At the very beginning of L_{hot} region the property changes were large, which gave the highest values of Nu ratio (0.45) but still below 1. However, when approaching a value of π_c approximately around 1.3 this relation disappears and seems to be inverted until the NHT regime disappears at a π_c of 1.1. Overall, using this analysis approach it could be concluded that the sharp drop of the π_c parameter at the beginning of L_{hot} induced a HTD regime in terms of property changes.

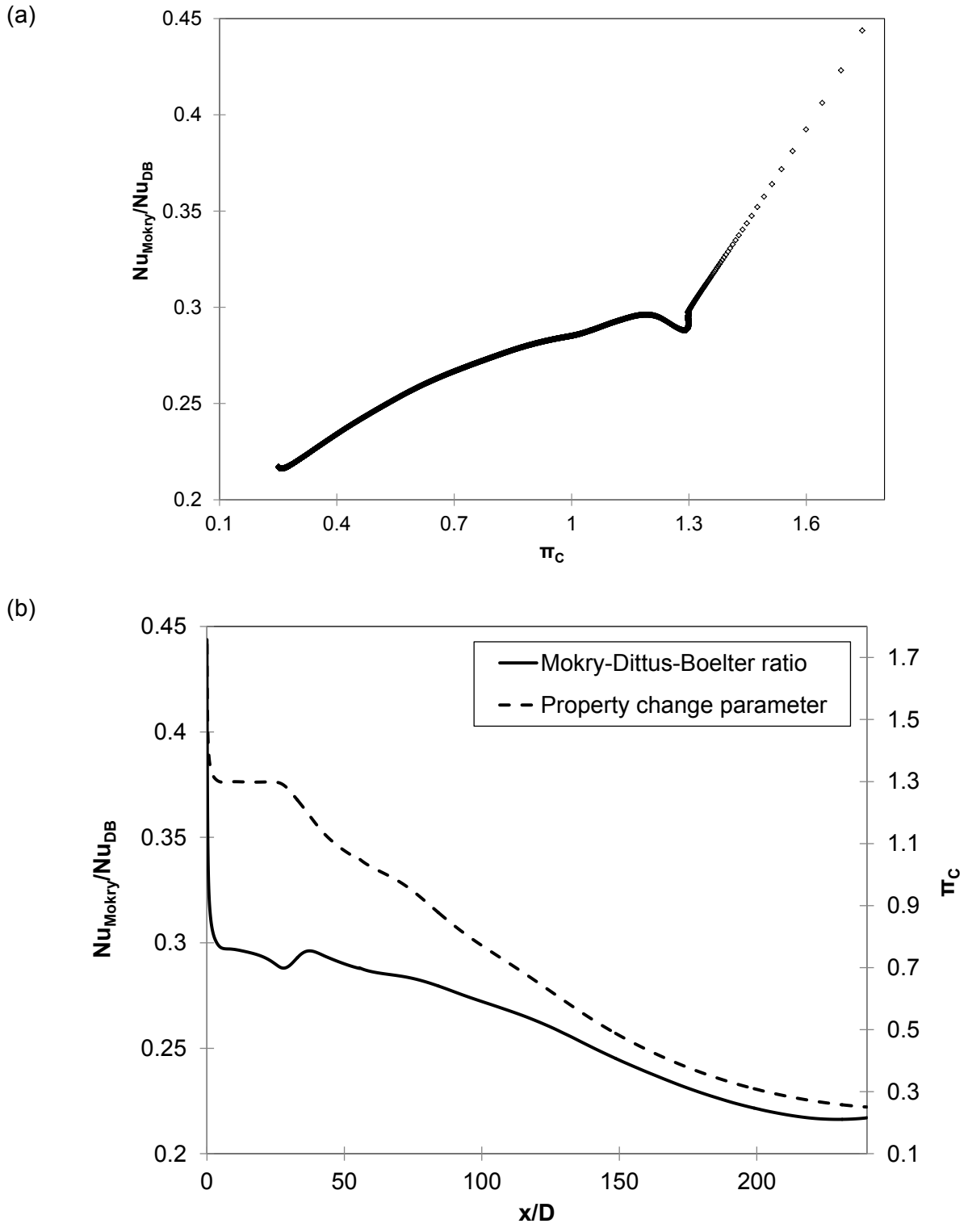

Figure 4.17 Effect of property changes represented by the Mokry-DB Nu ratio vs. π_c (a) and their separate effect along x/D (b)

Nu ratios representing the buoyancy and thermal acceleration effects are displayed in Figure 4.18. Both plots present Nu ratios above 1 and moreover the peaks and trends shown by both variables occur at the same values of x/D, which means an increase in buoyancy and thermal deceleration facilitate better thermal performance. Nevertheless, the axial region approximately between x/D= 125 and the outlet revealed a drop in both parameters (Bo and K_v) and also Nu ratios become stable close to a value of 1, showing how the flow turned rapidly from mixed-convective to forced-convective throughout L_{hot}.

(a)

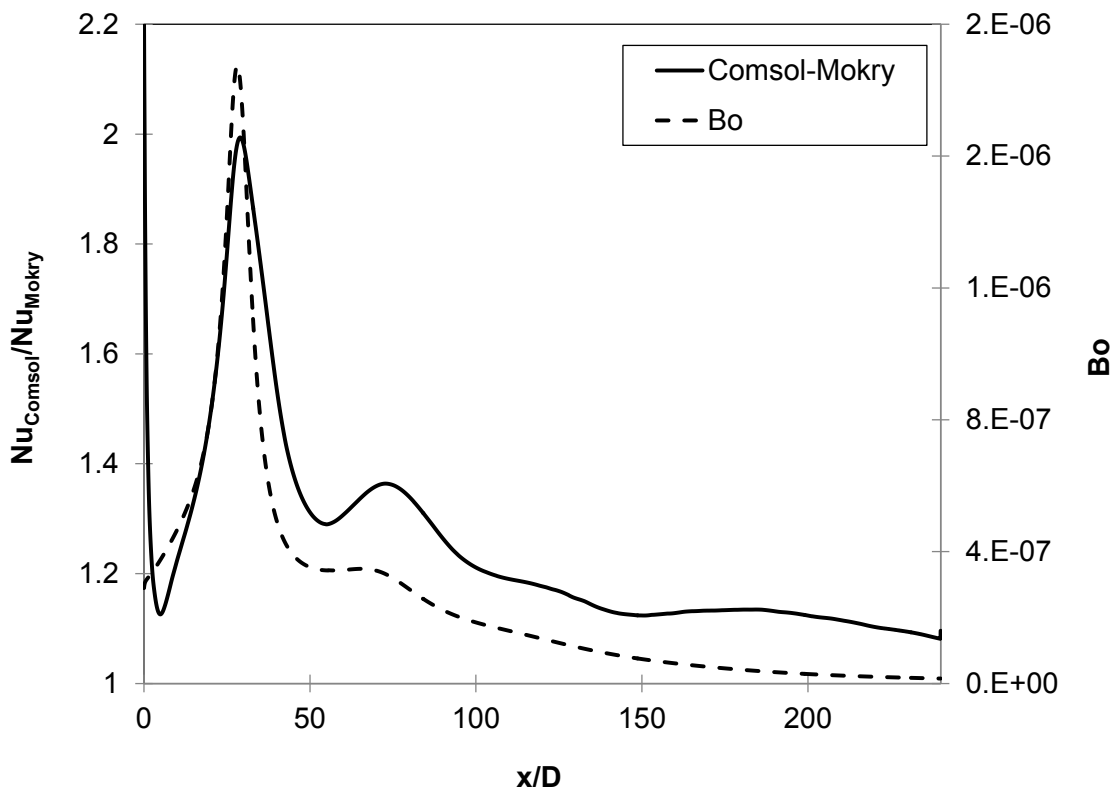

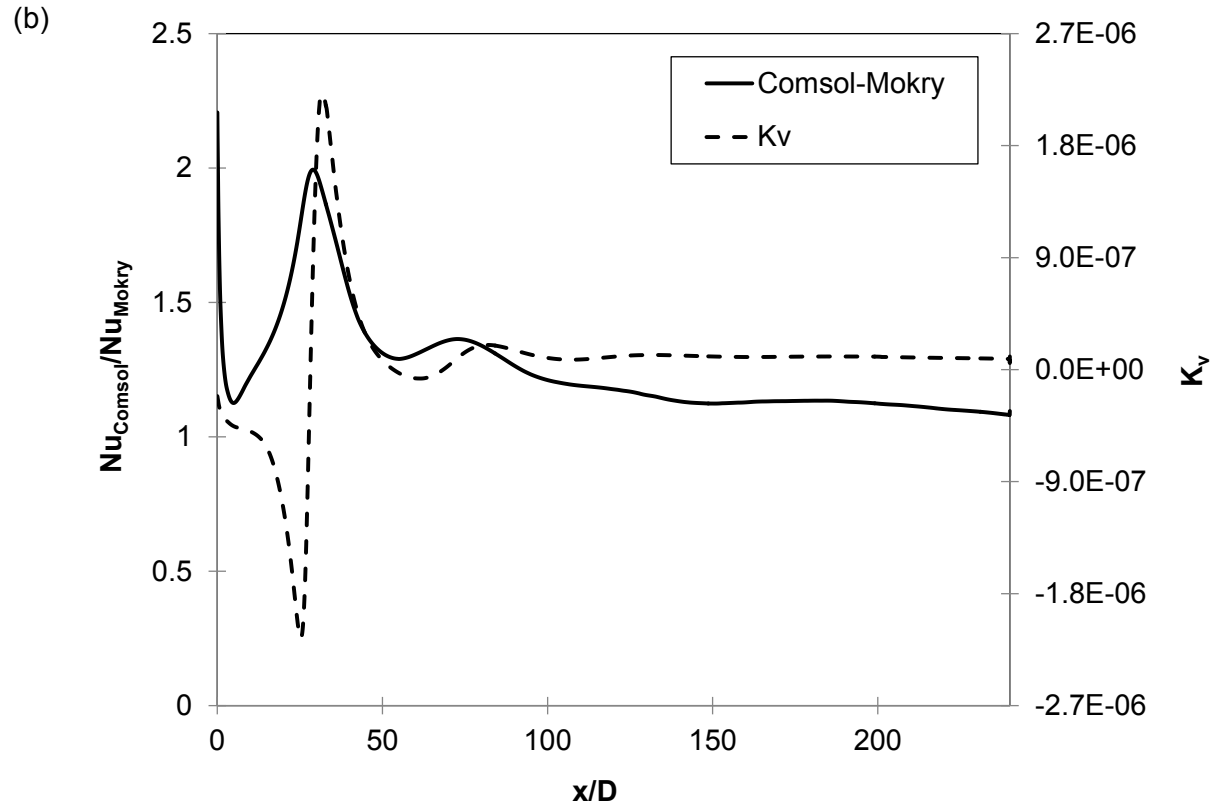

Figure 4.18 Nu ratios depicting the influence of buoyancy (a) and thermal acceleration (b)

After the main factors affecting HTD were determined for the case 2D-C, four radial locations of interest were selected for further study. Observing Figure 4.14, these were the sharp drop in the HTC occurring close to the entrance of L_{hot} ($x \approx 60$ *mm*), the first HTC peak ($x \approx 360$ *mm*), the second HTC peak ($x \approx 775$ *mm*) and the smooth recovery of the HTC when T_b approached the PSC point ($x \approx 2000$ *mm*).

(a)

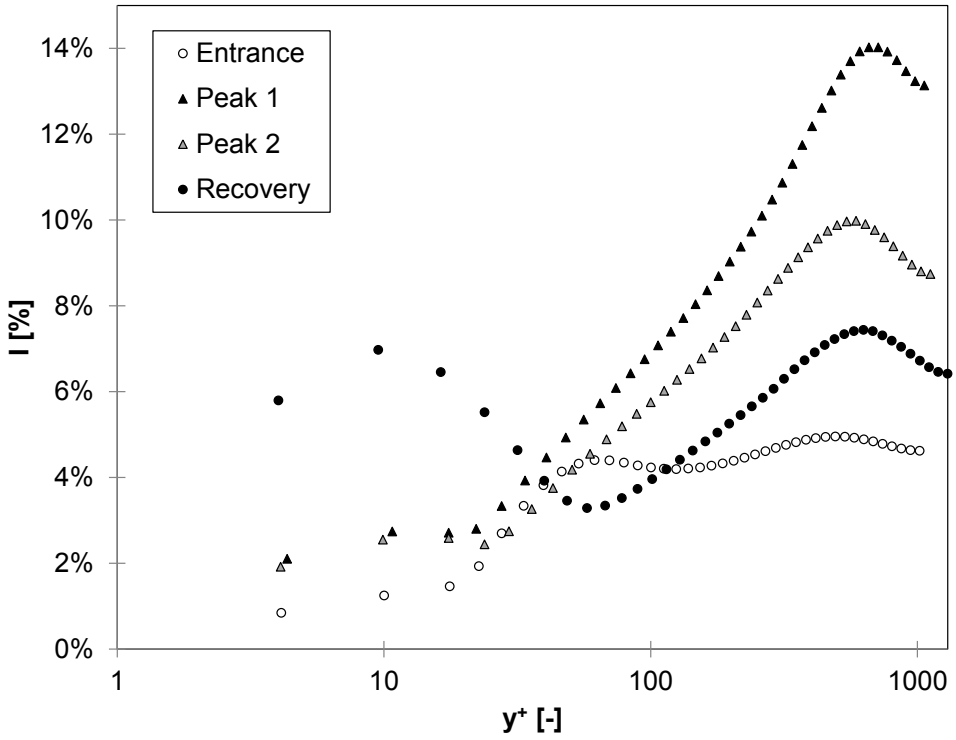

(b)

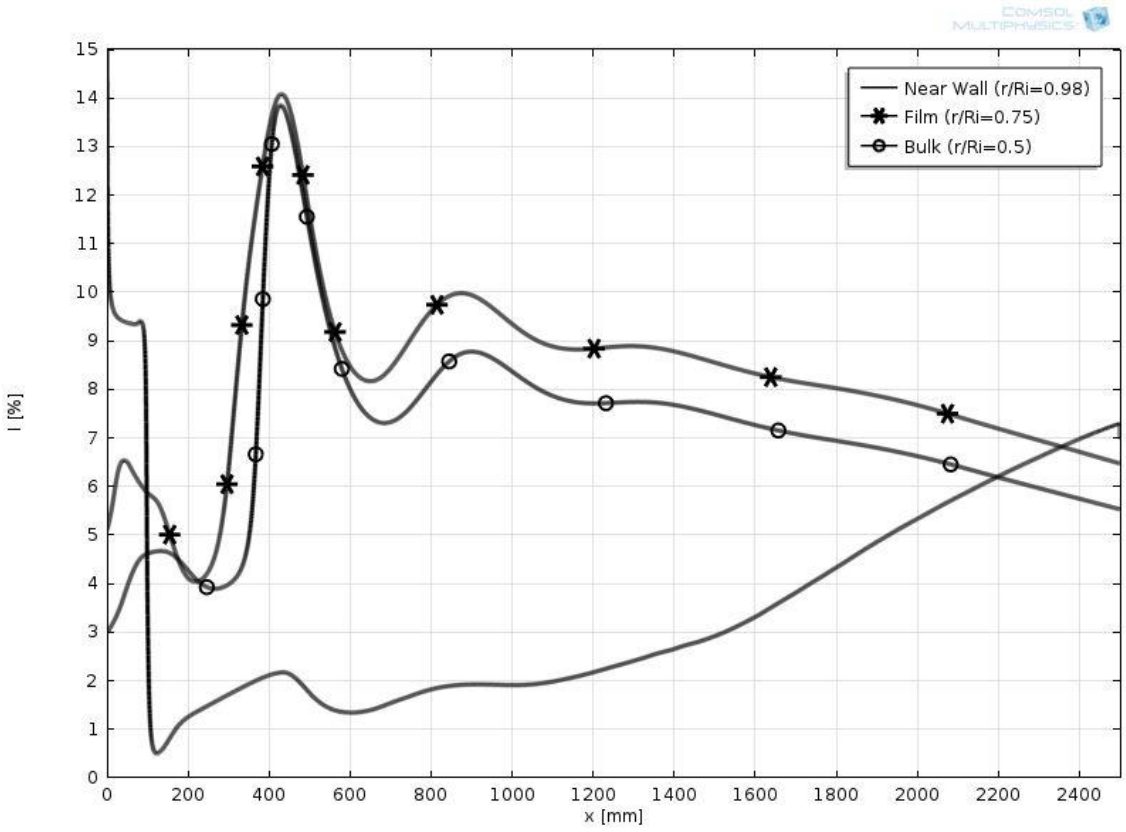

Figure 4.19 Radial (a) and axial (b) profiles of turbulence intensity at different locations

In Figure 4.19a the radial profiles for turbulence intensity (I) are shown, and a strong laminarisation was triggered from the entrance region of L_{hot} to the second HTC peak, where turbulence was stronger at the core than near the wall. A sharp increase in turbulence occurs near the core for the two HTC peaks, while the recovery region revealed an improvement in turbulence near the wall as well as near the core. Figure 4.19b displays the values of I for different axial locations of the full pipe (L_{entr} + L_{hot}), confirming the previous discussion. Moreover, convergence in radial turbulence was achieved near the pipe outlet. This laminarisation effect was similarly observed in Figure 4.20, depicting the values of G and C_p for the fluid domain of the geometry only and keeping the geometrical aspect ratio of 1 (inlet on the vertical left side, inner wall of the pipe on the horizontal top side). As displayed in Figure 4.20a, the radial location of the first HTC peak includes a high G produced near the wall and thus the centreline flow must keep the mass balance with a low value. Figure 4.20b offers a clear view of the LPV region (in red) affecting the flow; confirming the presence of a layer of low density and high C_p near the wall, within an axial region approximately between the inlet and 1,250 mm, that triggered laminarisation and tends to insulate the wall from the bulk of the flow. Downstream, within an axial region approximately between 1,250 mm and the outlet, the LPV region was spread throughout the pipe radius as T_b approached the PSC point, thus homogenising turbulence and thermal performance.

(a)

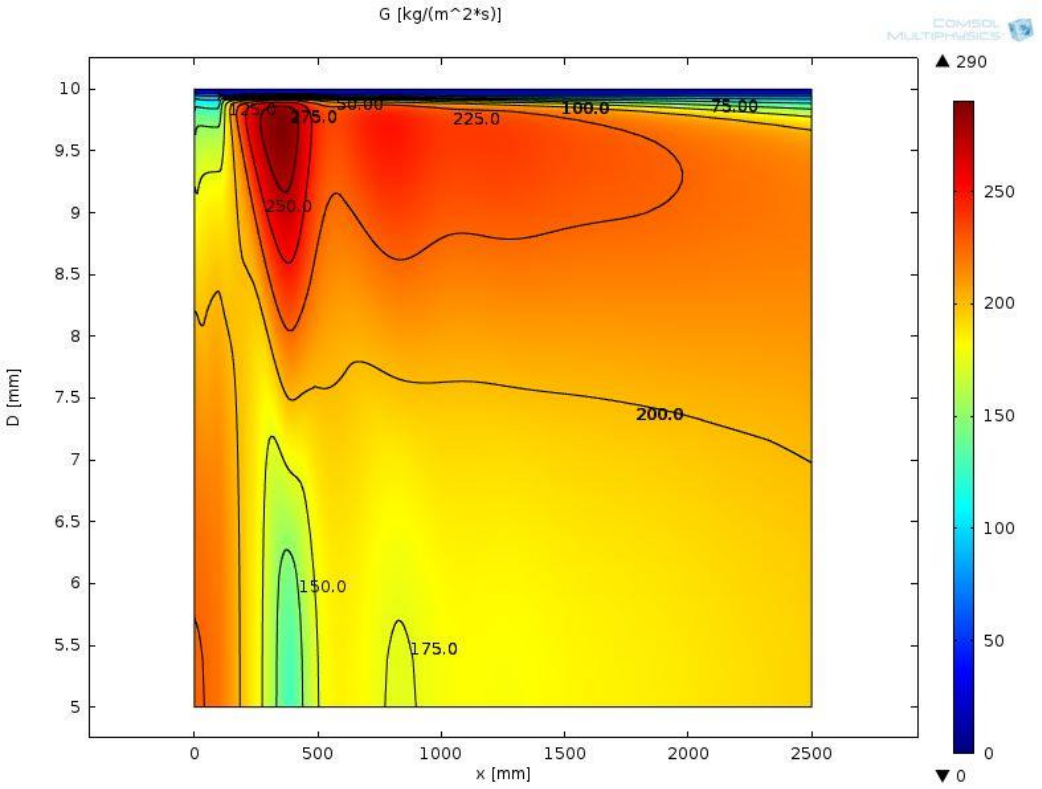

(b)

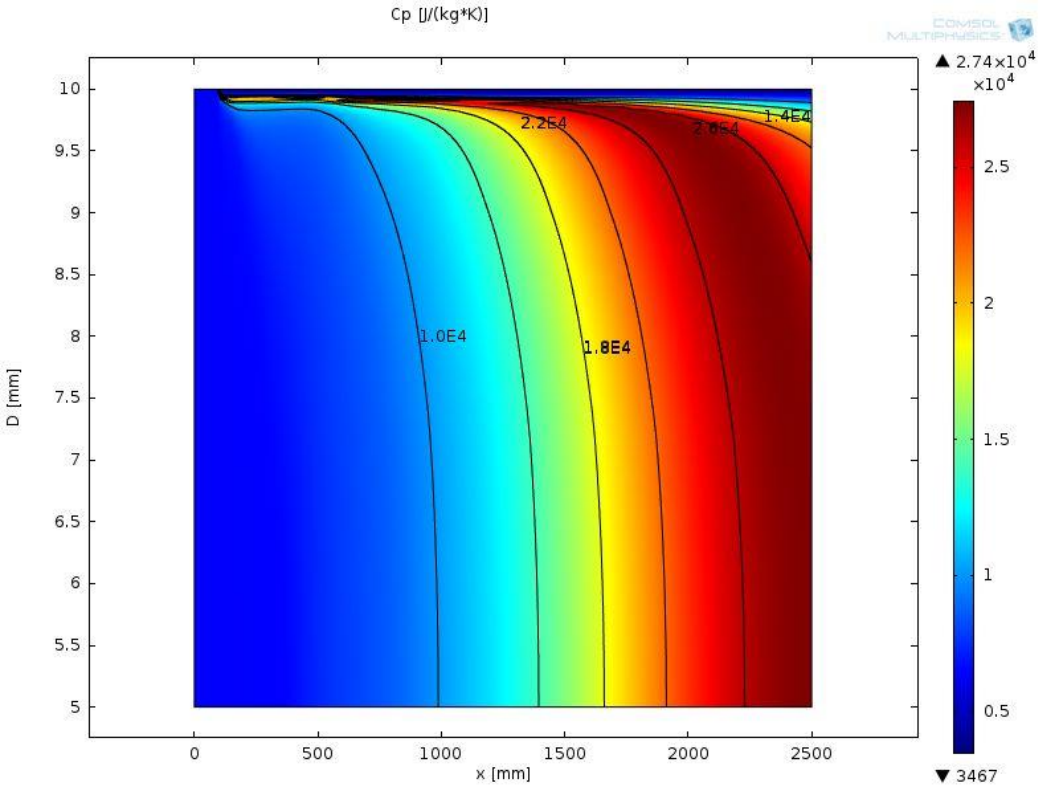

Figure 4.20 Values of G (a) and C_p (b) in rainbow colours and isolines employing the postprocessing tool within Comsol

The radial profiles of flow mean velocity (U) depicted in Figure 4.21 are characteristic of a mixed-convective flow under strong buoyancy and have been widely researched in HTD studies related to strong gravitational forces, such as the works from He *et al.* (2008), Forooghi and Hooman (2013), Zhang *et al.* (2012), Jaromin and Anglart (2013), Hall and Jackson (1969), Wen and Gu (2010), and van der Kraan *et al.* (2005). In upward flows, buoyancy could induce either HTD or THE depending on the q_w/G ratio. Moderate ratios induce low buoyancy, which eventually would trigger flat velocity profiles, neglecting shear stress and provoking some extent of HTD as the one present in Chapter 3. However, high values of q_w/G (as the ones existing in the present chapter) trigger strong buoyancy effects due to sharp changes in density across the boundary layer near the LPV region.

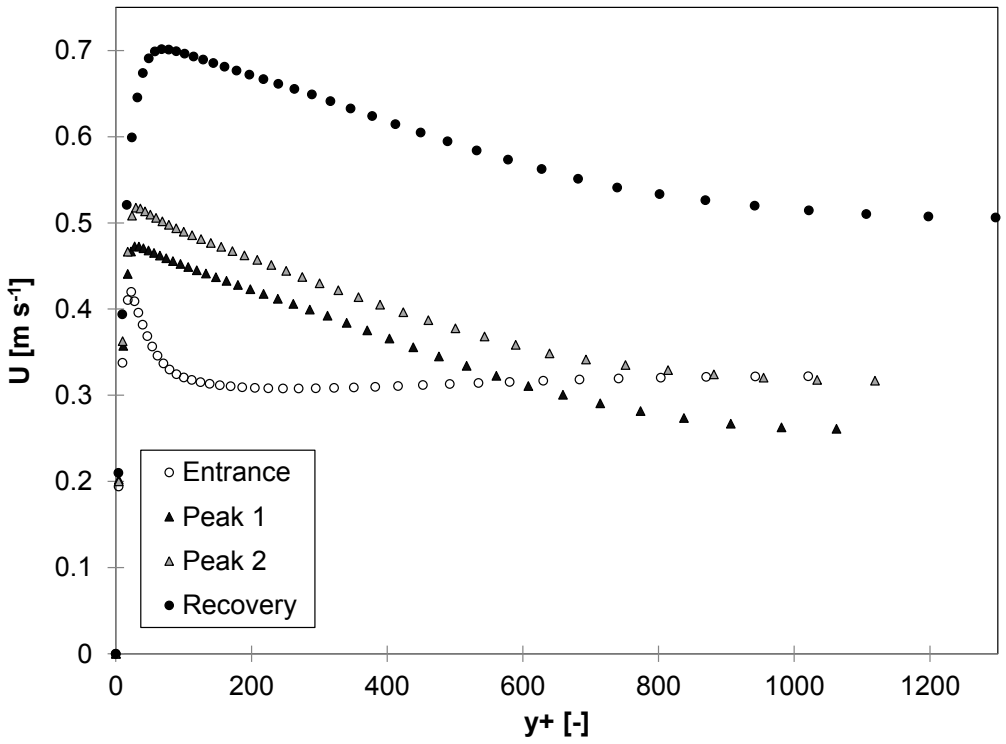

Figure 4.21 Radial profiles of flow mean velocity at several locations

The effects commence with a sharp increase of U near the wall, which in order to comply with the conservation of mass flattens the rest of velocity profile as the entrance velocity profile depicts, triggering laminarisation. In turn, these phenomena reduced the turbulent shear stress as presented in the entrance radial locations in Figure 4.22b, impairing turbulence and decreasing the heat transfer efficiency with an increase in wall temperature and a drop in the HTC value as in the entrance radial location.

(a)

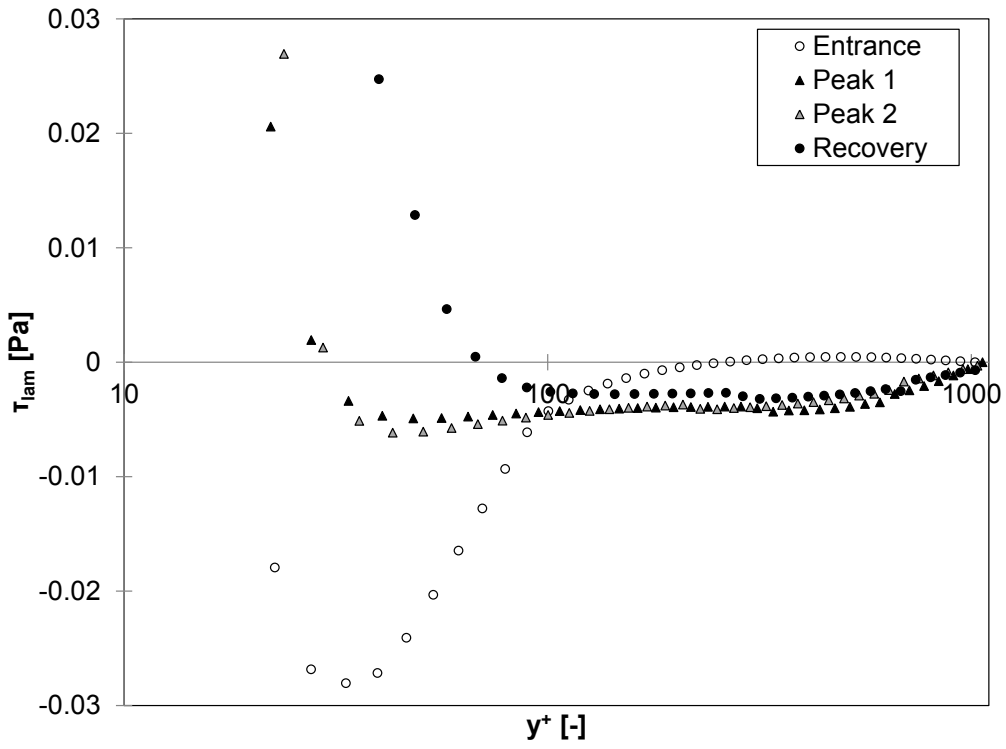

(b)

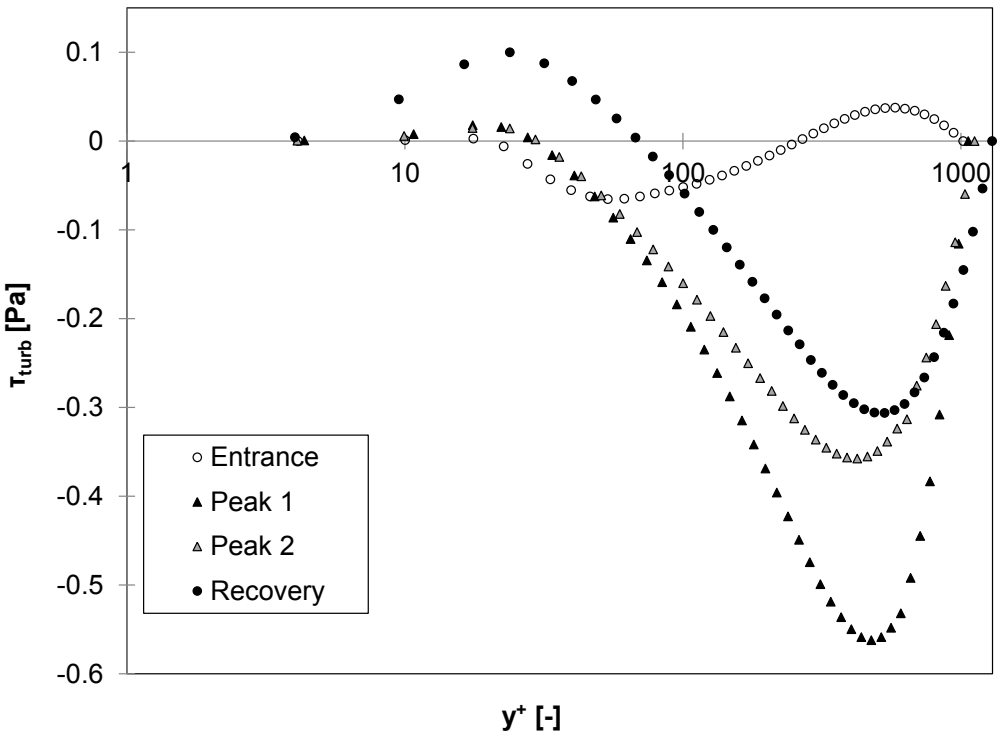

Figure 4.22 Radial profiles of laminar (a) and turbulent (b) shear stress

Downstream the entrance section the velocity profile was restructured and inverted in an M-shape fashion as observed for the other radial locations in Figure 4.21. These new velocity gradients induce positive shear stress near the wall and negative shear stress near the bulk (W-shaped), as observed in Figure 4.22. This facilitated turbulence and heat transfer, so the wall temperature decreased and the HTC increased as the radial gradient of peak 1 revealed in Figure 4.21. Downstream the HTC peak 1 the M-shape was maintained in the velocity profile, although T_b had increased as a consequence of the improved HTC and so the bulk velocity, reducing the velocity profile gradients (u_y) as observed in Figure 4.23a.

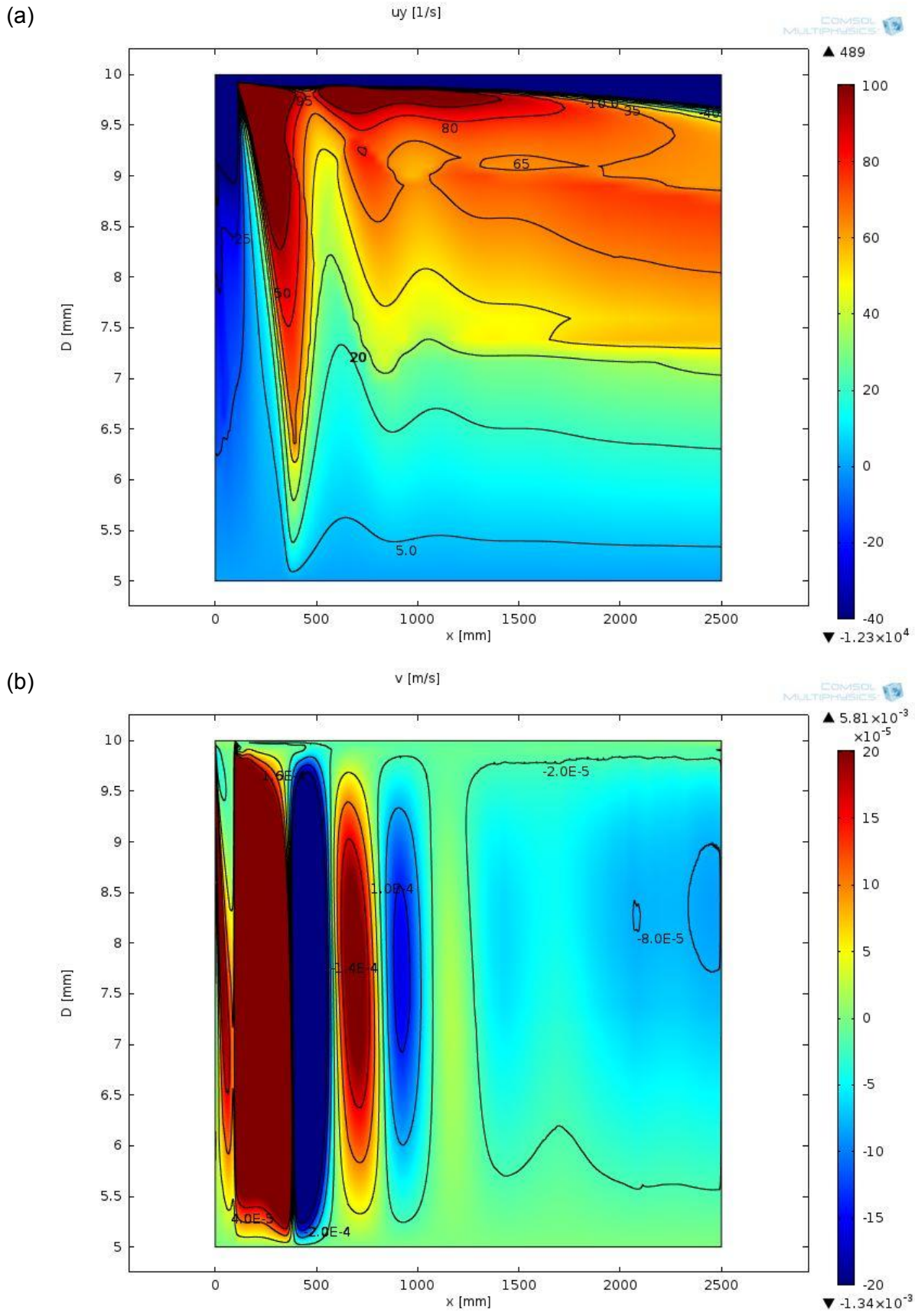

Figure 4.23 Postprocessed plots of U gradients (a) and radial velocity (b)

This reduction of radial velocity gradients caused the shear stress and turbulence to be diminished again, although slighter than the first onset upstream. Consequentially, a slight HTD region was triggered and the cycle was repeated again as the presence of a second HTC peak demonstrates. As T_b progressively approached T_{iw} in the process, the radial temperature profile would become uniform eventually. As a result, the radial density variations would decrease and the buoyancy forces would eventually recede as shown in Figure 4.18a. This cycle phenomenon is supported by Figure 4.23b depicting the radial velocity values (v); showing a cyclic combination red colours for positive velocities (flowing upwards) and blue for negative values (flowing downwards). Downward velocities bring hot flow from the wall into the core, improving heat transfer and thus coinciding with the locations of better values of HTC.

The acceleration effects were not expected to be the cause of HTD due to the low value of G with respect to the applied q_w, as Figure 4.18b depicted. In fact, they only affected the entrance region, as seen in Figure 4.24b, while the effect vanished quickly downstream. In Figure 4.24a flow deceleration is appreciated on a large extent of the radial profile at HTC peak 1, which improved the heat transfer performance.

(a)

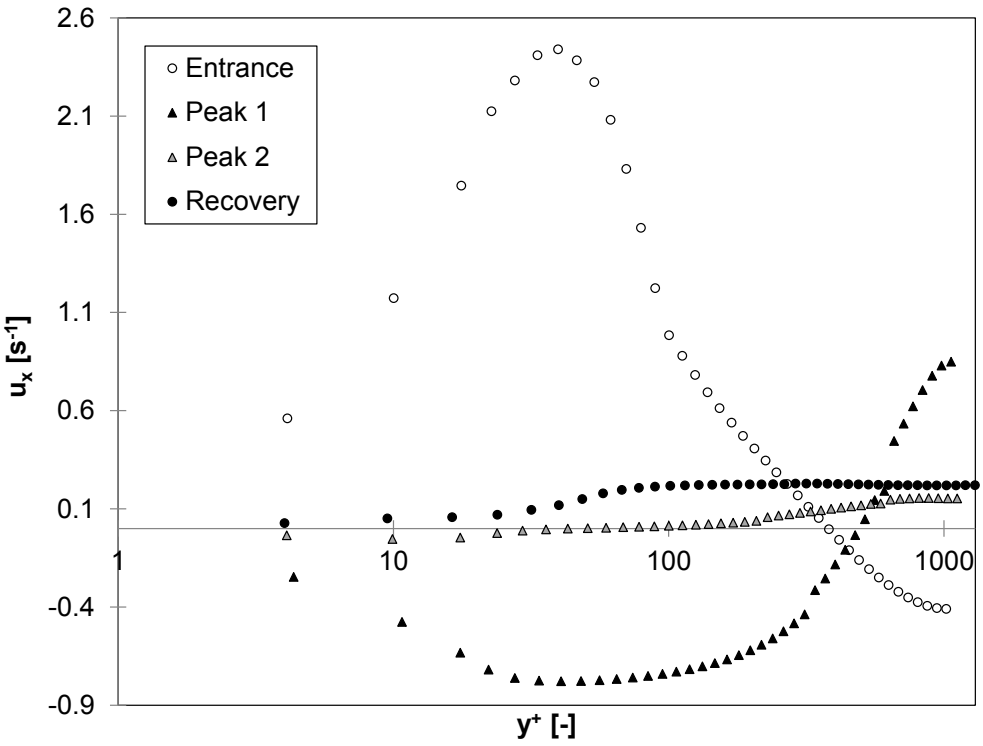

(b)

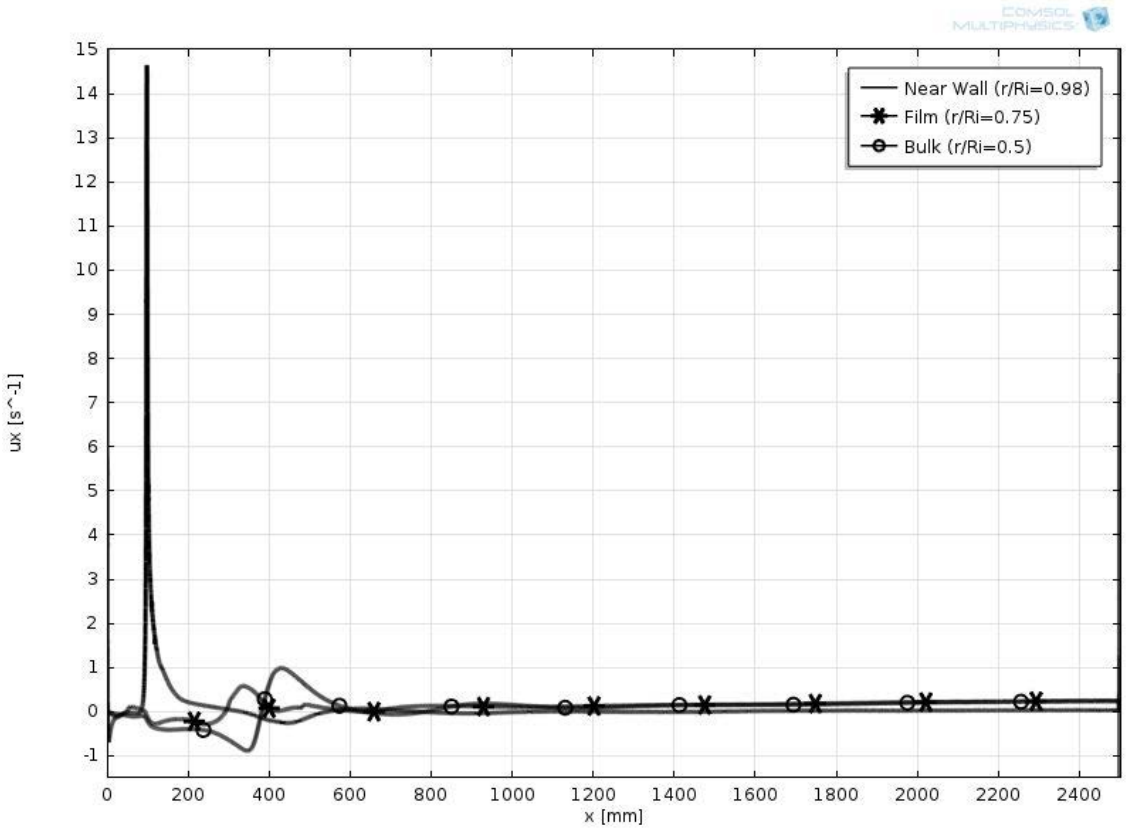

Figure 4.24 Radial (a) and axial (b) profiles of flow acceleration at different locations

4.3.3. 3D numerical study

The study cases 3D-F and 2D-D were selected for the 3D analysis and comparison with the equivalent system in 2D. The results are presented in Figure 4.25. The 3D simulation captured the same qualitative trends as those obtained in 2D, although the first peak of the HTC, approximately at x = 250 *mm* was smaller and located a bit more upstream, which agreed with the results obtained by Withag and collaborators, previously shown in Figure 4.11. Nevertheless the second HTC peak, protruding approximately at x = 600 *mm,* was slightly computed compared to the 2D case. Just like the case 2D-D, the case 3D-F was not capable of reproducing the recovery of the HTC within the axial region approximately between 1,250 *mm* and the outlet either, even considering the outlet value of T_b (415°C) had surpassed the PSC point. A finer mesh or a higher discretisation order would be required to appropriately represent this phenomenon.

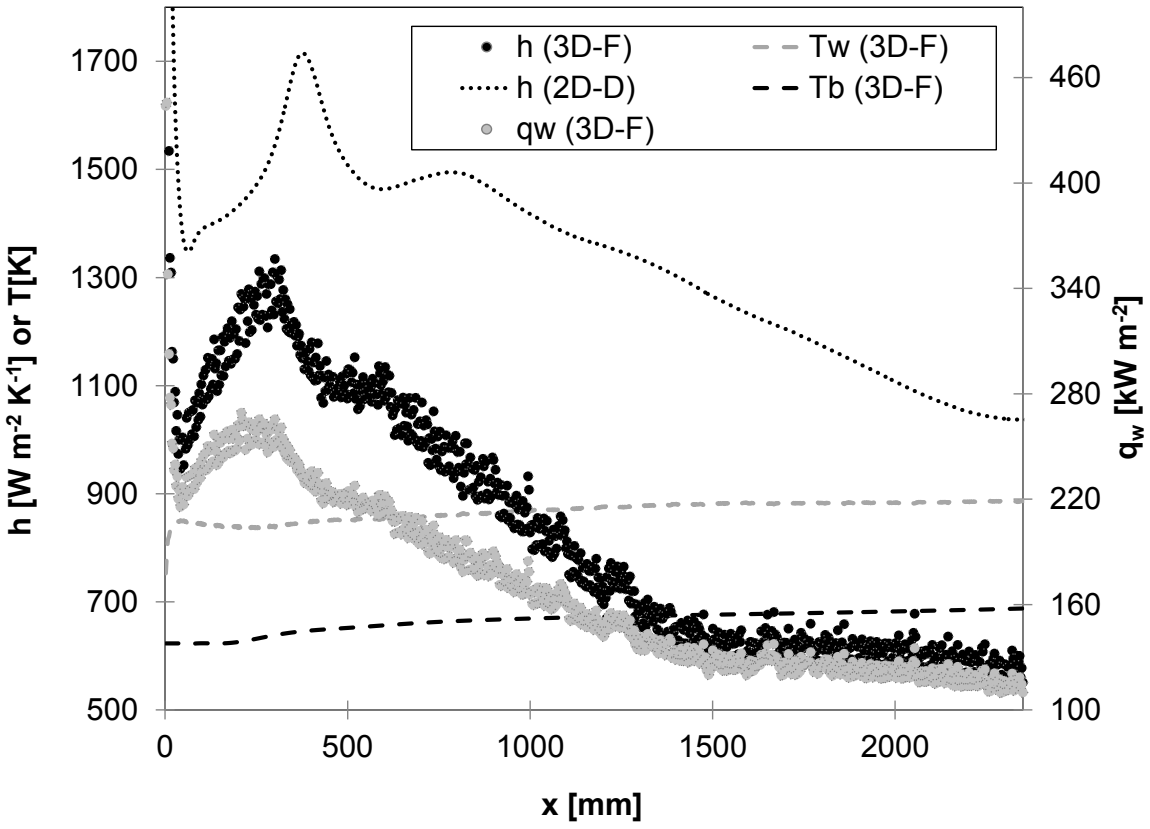

Figure 4.25 Axial values of h, T_{iw} and T_b (left y-axis) as well as q_w (right axis) for the study case 3D-F. The values of h from the case 2D-D were depicted as comparison

For further comparison with the IRTs, which possessed a L_{hot} of 400 *mm* only, a radial study was carried on the locations of case 3D-F involving the drop in the HTC value at the entrance region as well as the first HTC peak. In Figure 4.26, the results for I, U, laminar shear stress (τ_{lam}), turbulent shear stress (τ_{turb}) and flow acceleration (w_z) are presented for the aforementioned radial locations (entrance effect and HTC peak). As can be observed, the trends were very similar compared to the same parameters previously plotted for the same radial locations in case 2D-C. This was due to the use of very similar boundary conditions and therefore the flow reflected the same laminarisation in the entrance region near the wall, triggered by the buoyancy effect. This impaired turbulence and heat transfer, producing the readjustment of the

velocity profiles downstream in order to create shear (positive or negative) and reactivate turbulence.

(a)

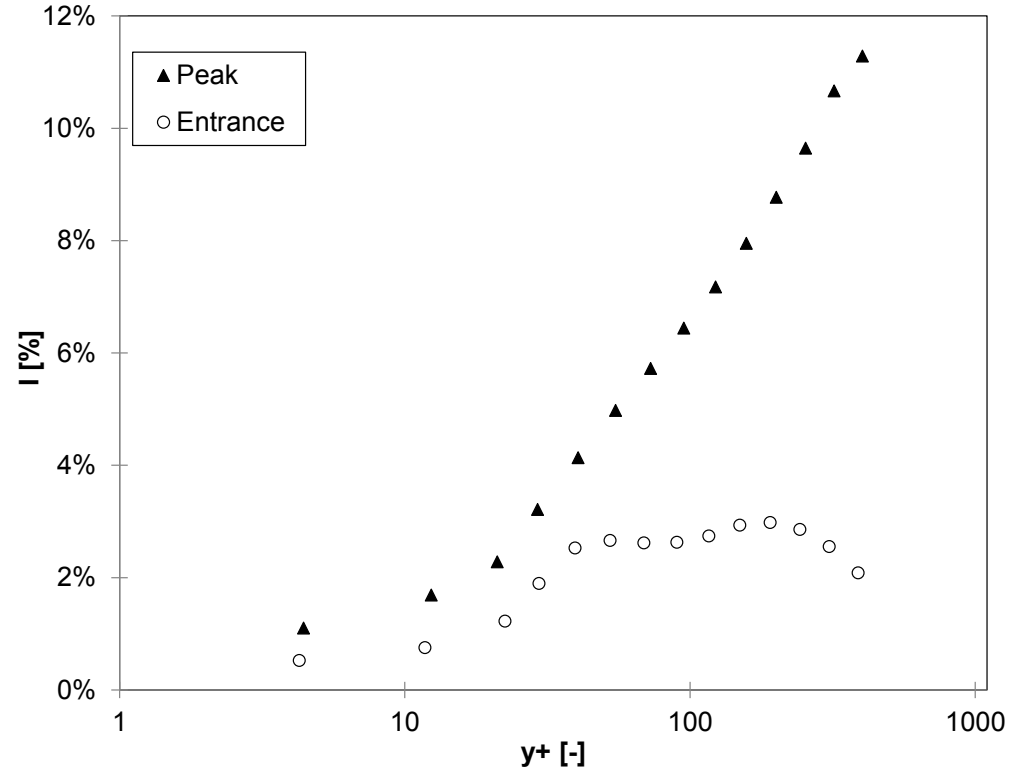

(b)

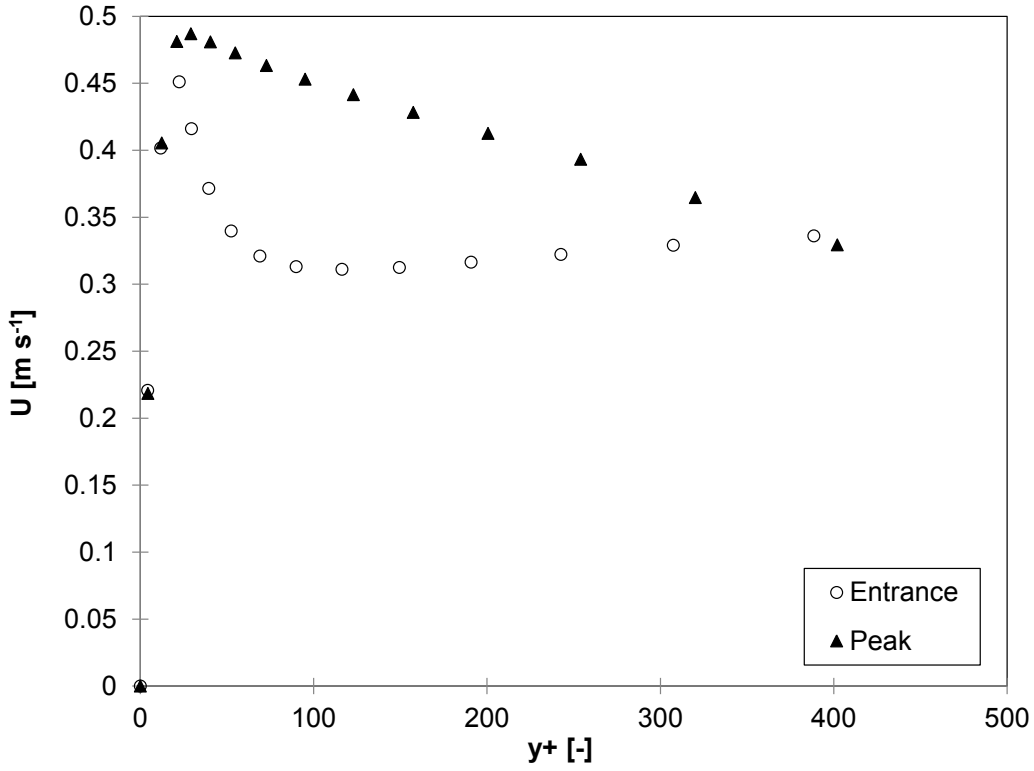

(c)

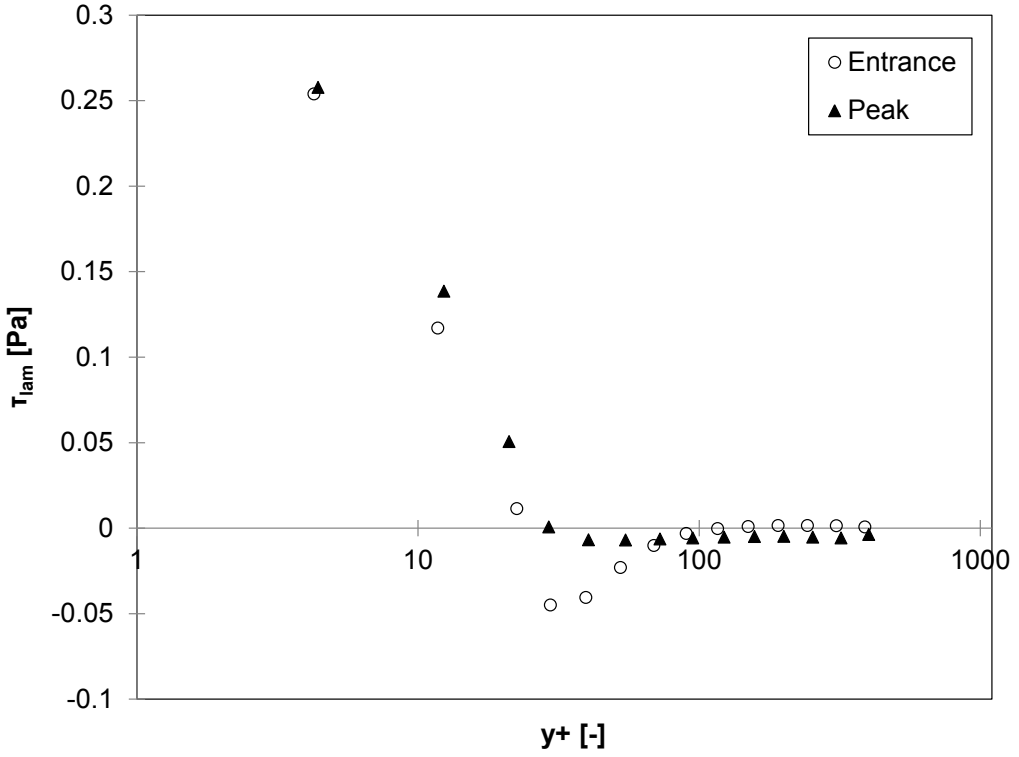
0.3
0.25
0.2
0.15
0.1
0.05
0
-0.05
-0.1
1
10
100
1000
τlam [Pa]
y+ [-]
Entrance
Peak

(d)

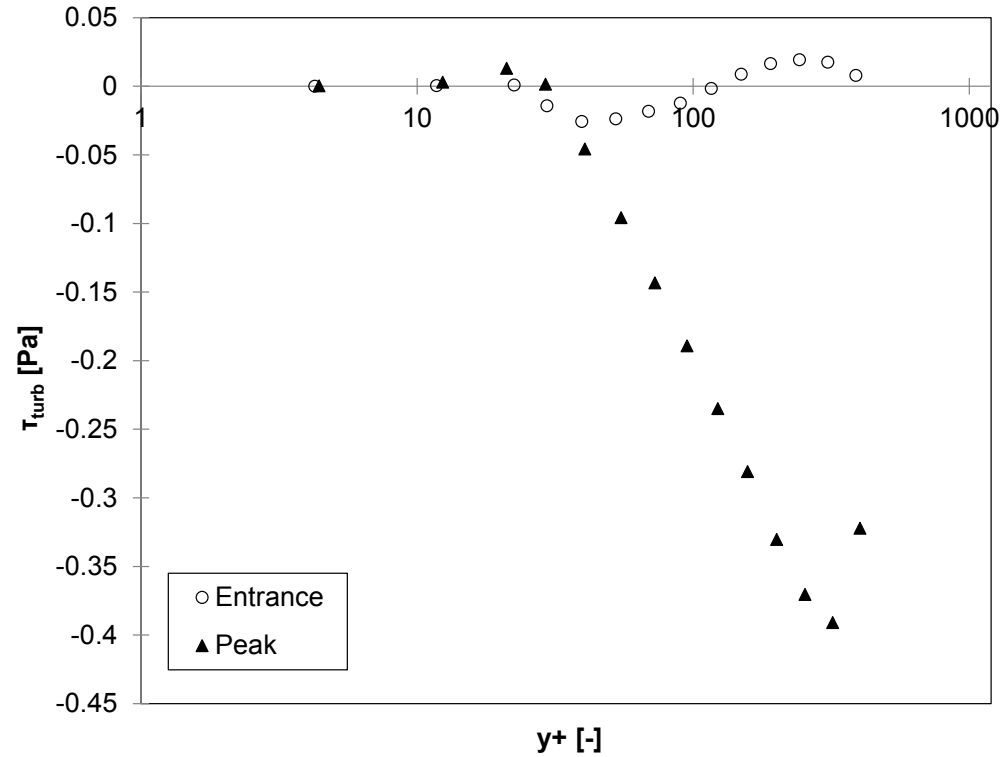
0.05
0
-0.05
-0.1
-0.15
-0.2
-0.25
-0.3
-0.35
-0.4
-0.45
1
10
100
1000
τturb [Pa]
y+ [-]
Entrance
Peak

(e)

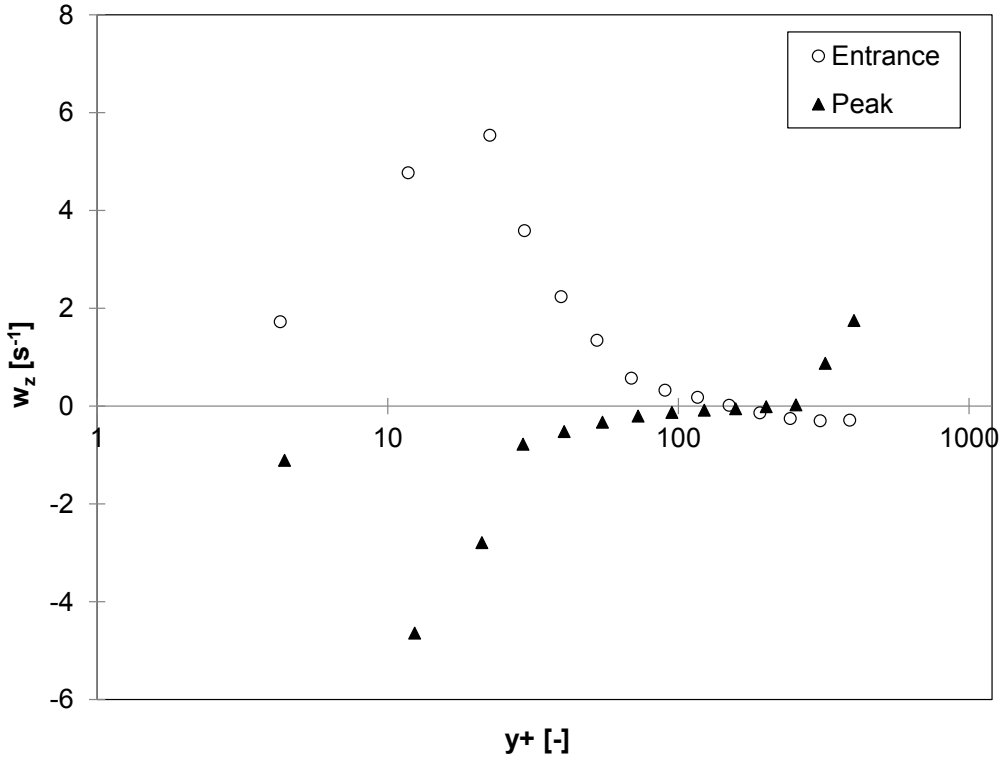

Figure 4.26 Radial profiles of I (a), U (b), τ_{lam} (c), τ_{turb} (d) and w_z (e) for the entrance and peak radial locations

The explanation of the laminarisation phenomena near the flow inlet was also supported by the 3D results plotted using the postprocessing tool in Comsol. Figure 4.27 shows four 3D images from the case 3D-F with the geometrical aspect ratio 1:1 and depicting G, I, the radial gradients of the velocity profile (w_y) and C_p (inflows on left side of picture). Again, these results were very similar to the 2D plots displaying the same parameters in case 2D-C, for the same reasons. The only difference is that the recovery region, in terms of turbulence and HTC, was not reproduced by the case 3D-F in the axial region approximately between 1,250 *mm* and the outlet.

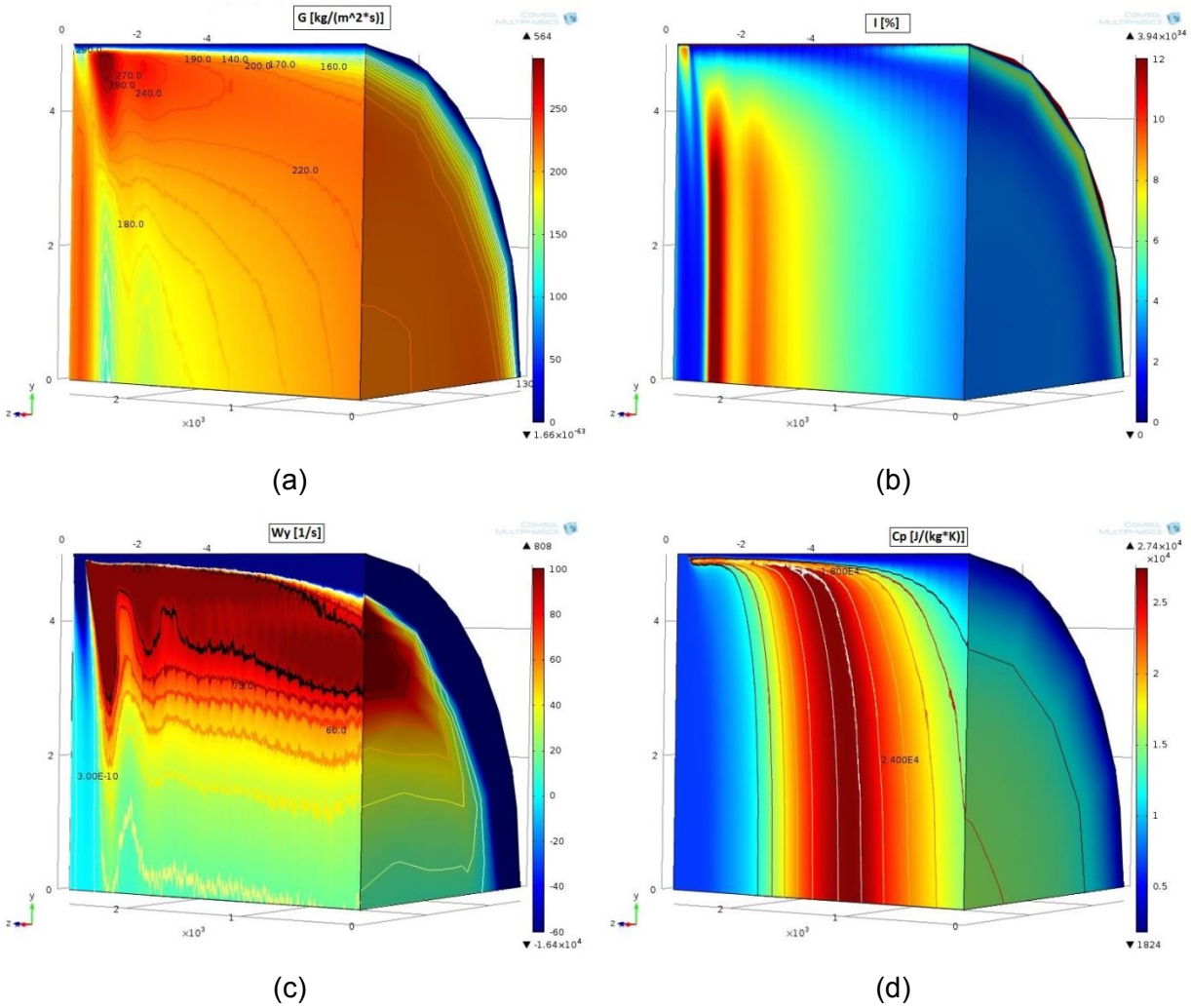

Figure 4.27 3D plots of the fluid domain from case 3D-F depicting G (a), I (b), w_y (c) and C_p (d)

4.3.4. 3D techniques for HTE

The case study 3D-H, which computes a pipe including straight ribs, is presented first. The mesh for the fluid domain, like in the case 3D-F for the smooth pipe did not employ rectangular elements but unstructured tetrahedral instead, which is convenient for irregular domains. Nevertheless, this case computed the full 3D domain of a shorter pipe (L= 500 *mm*) and thus the pipe centreline did not contain any edge, as observed comparing Figure 4.2 and Figure 4.3. This involved some challenges when exporting the results, because the points of data were located

always on edges. Therefore, two approaches were adopted. One, exporting data from the full volume of the meshed domains, so only the existing nodules (calculation points) were represented in the three space dimensions; and the other one exporting data from precise 1D cut lines which employed iterations when crossing mesh regions without nodules, as the pipe centreline. The former approach, while relying on mesh nodules, made the organisation of results in geometrical arrays complicated due to the unstructured mesh. On the other hand the 1D cut lines, although relying on iterations between nodules when the lines did not touch them in their path, it offered a more precise geometrical display.

Figure 4.28 shows the axial profiles of q_w, T_{iw}, T_b and HTC for the case 3D-H for two different locations of the internal wall, one along any of the ribs protruding into the fluid domain (ribbed section), and the other one along the smooth surface between ribs having the standard pipe diameter (smooth section). Moreover, the two different approaches were considered (volume data and cut line data). In Figure 4.28a, by observing the axial values of T_{iw} it was concluded that the ribbed sections display a lower temperature than the smooth sections, which is logical considering the ribs deepen more into the flow. Also, the temperature results obtained with both approaches reflected very similar values, even considering the fact that the temperature profiles using cut lines had to be supported by polynomial fits in order to match axial locations between the fluid and the solid domain meshes. However, the q_w profiles obtained at the solid-fluid interface offered disperse trends when using the volume data approach, on the smooth and ribbed surfaces. This was due to the higher sensitivity of this parameter towards the mesh performance (as described in

Section 3.2.6). For this reason, in the cut line data approach the value of q_w was obtained by drawing a 1D cut line on the solid outer wall, as it should be constant along the radial profile at steady state conditions. As observed in Figure 4.28a, the results obtained using the cut line where more stable and less disperse for the two surfaces (smooth and ribbed).

(a)

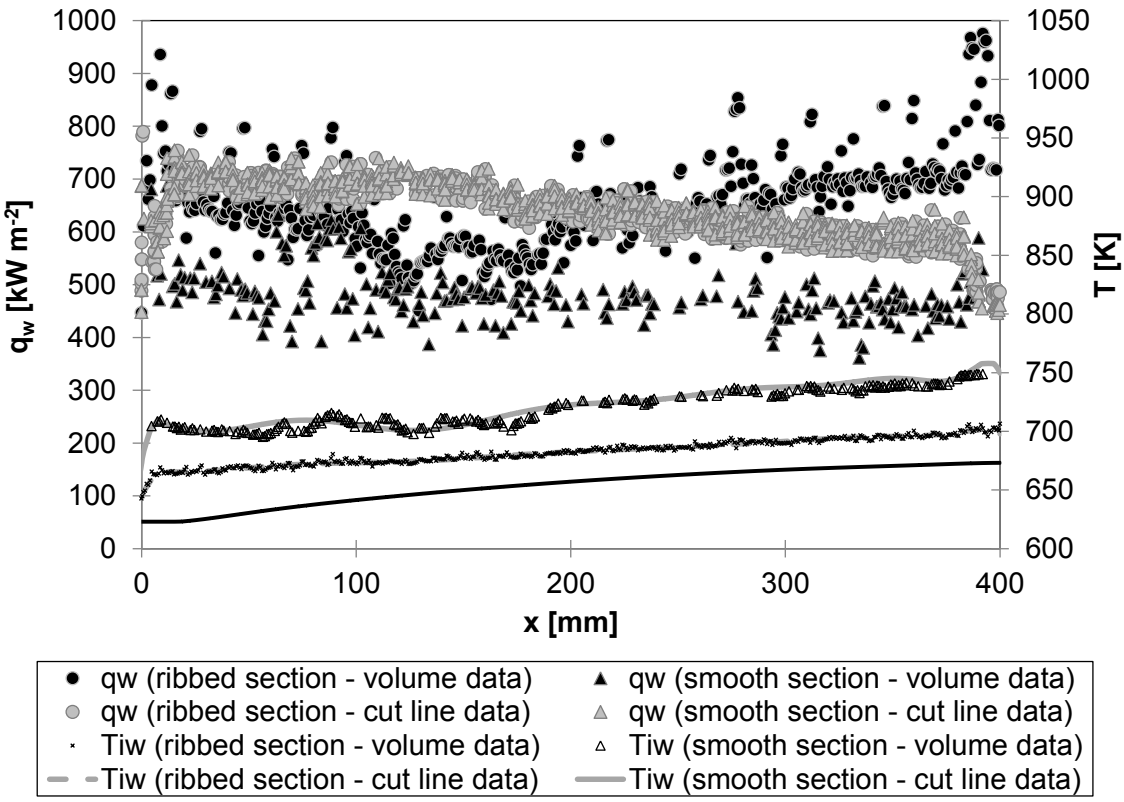

(b)

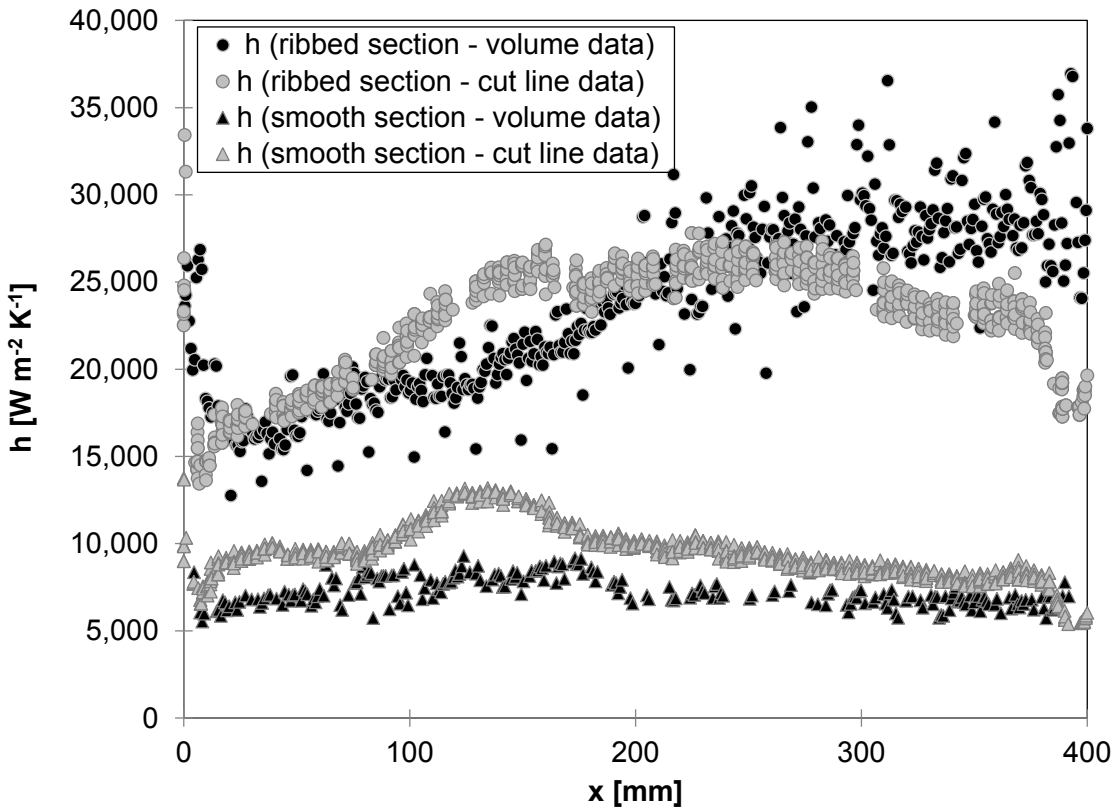

Figure 4.28 Values of HTC (a), and q_w, T_{iw} and T_b (b) for case 3D-H using two different data export methods

In Figure 4.28b, the respective values of HTC were displayed using both approaches for the two pipe sections. Both techniques (volume data and cut line data) provided similar ranges and trends, but the results from the ribbed section using the volume data were more disperse and the fact that the value of y_1^+ on the ribbed wall was higher than on the smooth wall was a key factor. Due to the smaller distance from the ribbed wall to the pipe centreline, the temperature difference was smaller and thus their values of HTC were much higher and sensible to the proximity of T_b to the LPV region, shown by an increase upstream that point (x=200 *mm* approximately). All the HTC values obtained were much higher than those from the smooth pipe in case 3D-F, and moreover none of the HTC profiles revealed any presence of HTD. The reason for this was not only due to the attachment of ribs on the inner wall increasing

turbulence and HTC values, but also due to the shorter pipe length employed in case 3D-H (straight IRTs) which diminished the effect of buoyancy on the upward flow. In order to make the cases 3D-F and 3D-H comparable the latter should have employed the same pipe length, which was unfeasible in terms of memory power.

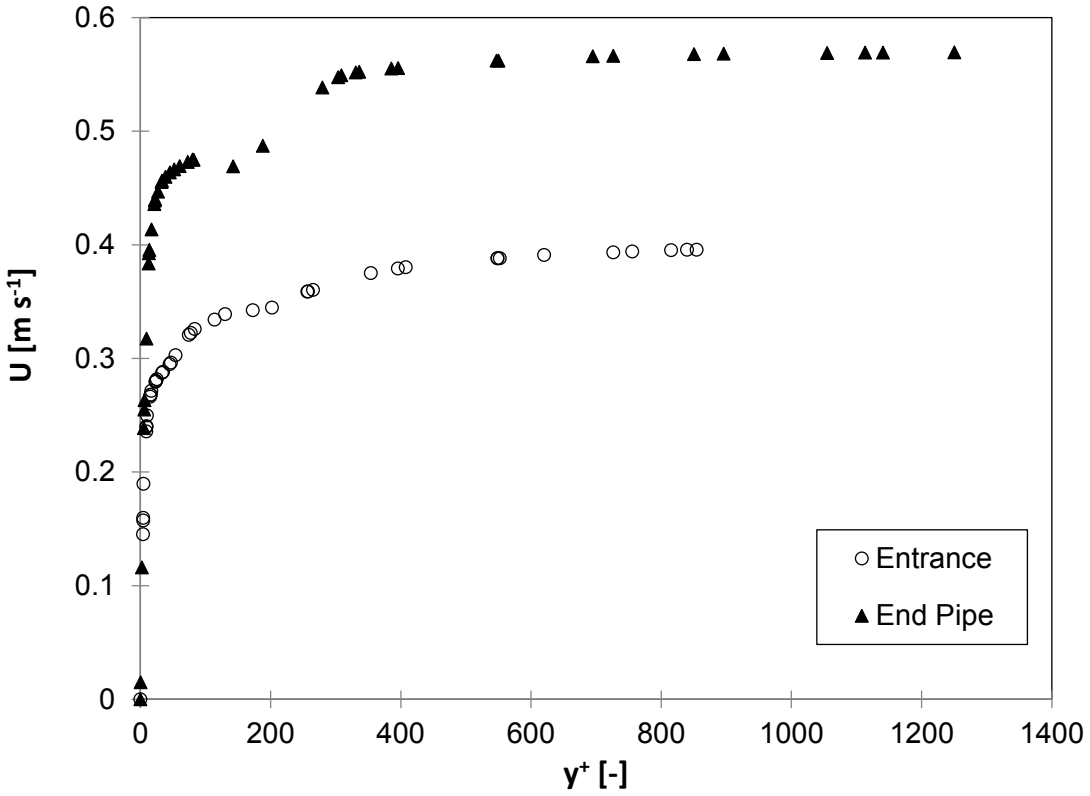

Figure 4.29 Radial profiles of flow mean velocity for the case 3D-H at two different locations

For a better understanding of the turbulence presence in the case 3D-H, radial profiles at the same two axial locations as in case 3D-F were selected for study, from the pipe centreline to the smooth internal wall surface located in the midpoint between two ribs (one near the pipe entrance and the other near the pipe outlet). Figure 4.29 depicts the velocity profiles and, as previously discussed observing the HTC profiles, the buoyancy forces did not affect the system as in the cases with a

longer pipe length, thus no M-shape profiles were observed. Figure 4.30 depicts the radial profiles for τ_{turb} and I, revealing stronger turbulence intensity than in any previous case. Additionally, the plot depicting I shows two turbulence peaks, one near the wall at $y^+ < 3$ approximately and another one at y^+ close to 200-300. Between the two peaks there was a drop at $y^+ = 9$ approximately. Moreover, turbulence at the entrance location was higher than at the outflow, which is in agreement with the HTC plots shown in Figure 4.28 that revealed a drop in HTC near the end of the pipe due to the T_b surpassing the PSC point.

(a)

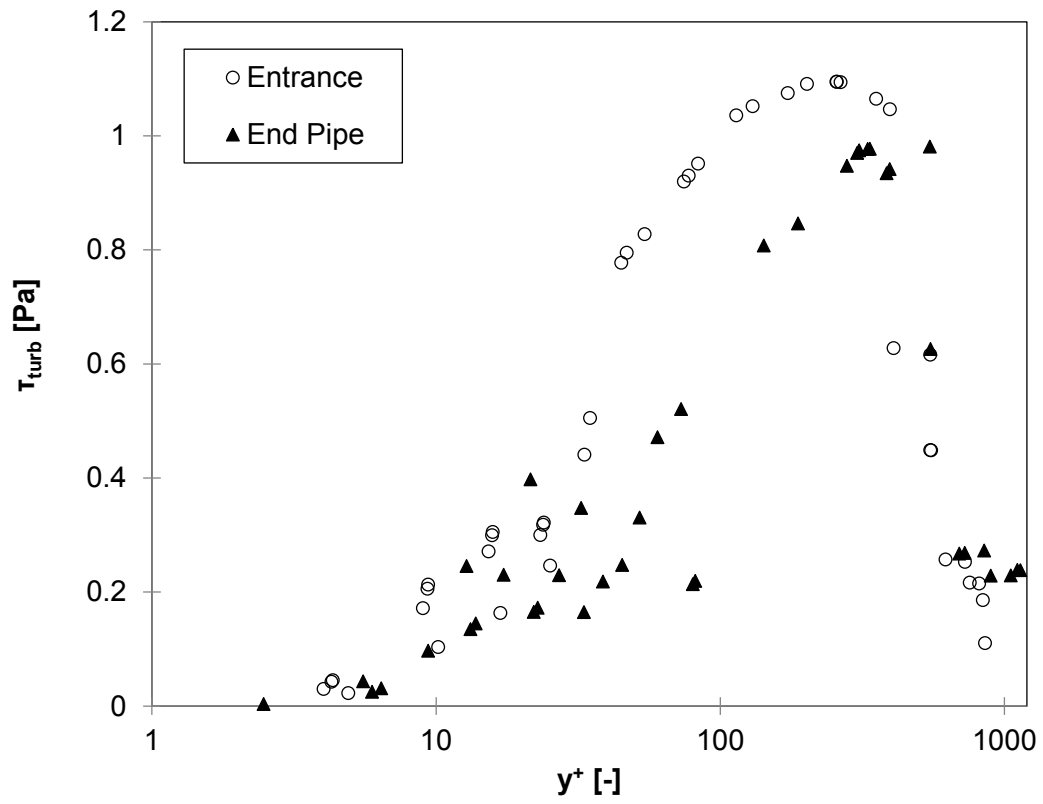

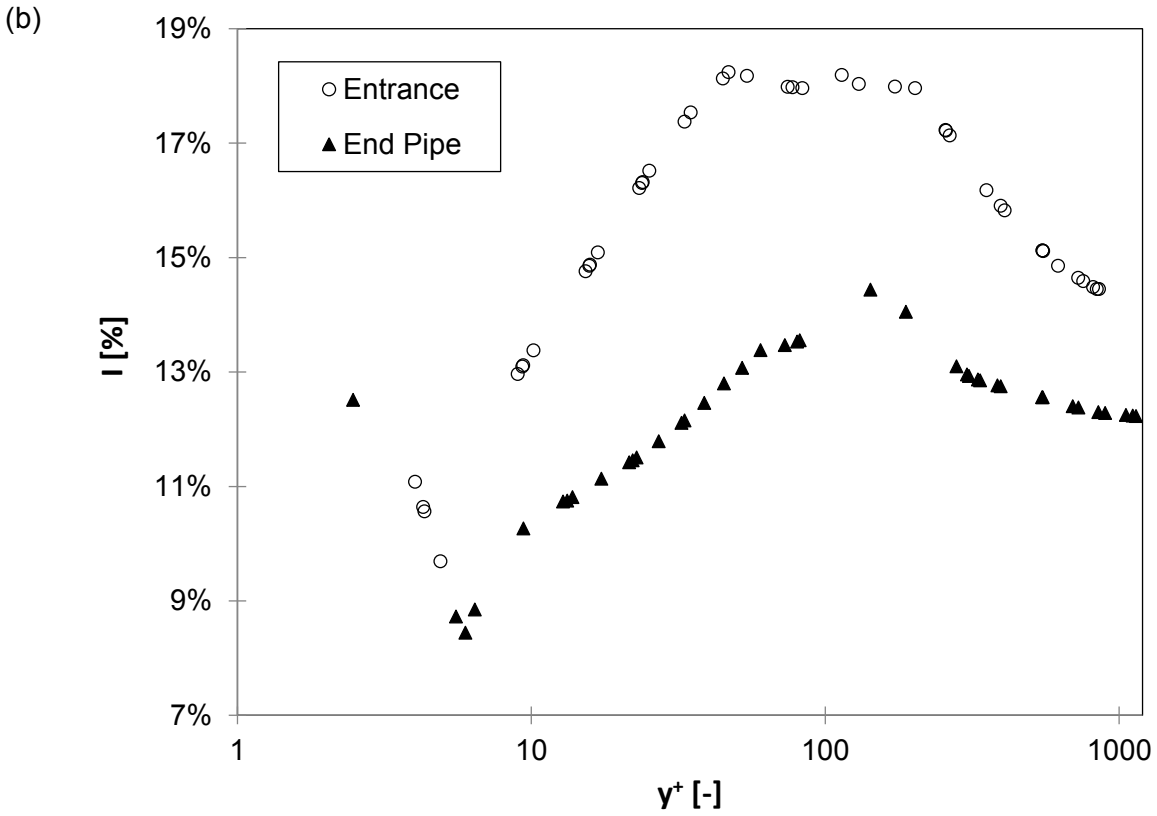

Figure 4.30 Radial profiles of τ_{turb} and I for the case 3D-H at two different locations

The plots presented in Figure 4.31 depict the 3D profiles of G and I by showing the fluid domain with a visually reduced geometrical aspect ratio and having the inlet section on the left side of the picture (a black perimeter line indicating the entrance of L_{hot} can be observed). Three planes were selected, the first upstream still within the unheated section and the other two downstream at the two axial locations previously studied on the radial analysis (entrance and end pipe). Smooth gradients in G confirm the absence of gravity effect in the flow, as well as the values of I show how turbulence declines towards the end of the pipe. Similarly, strong turbulence was located around all the rib edges.

(a)

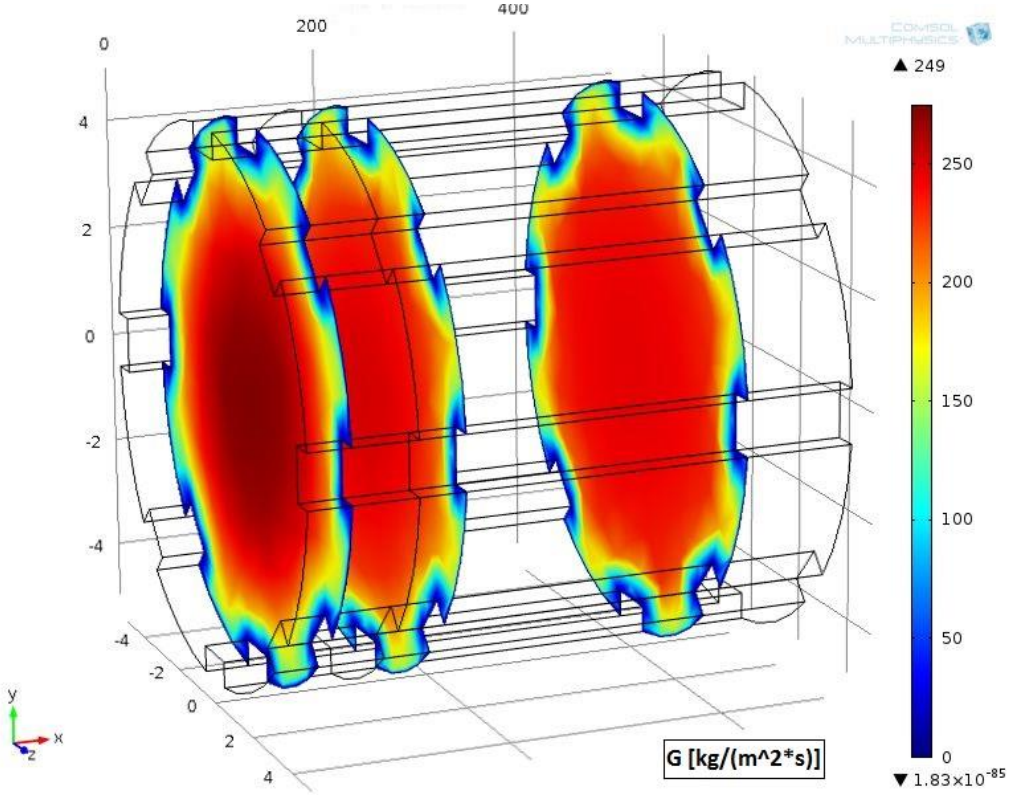

(b)

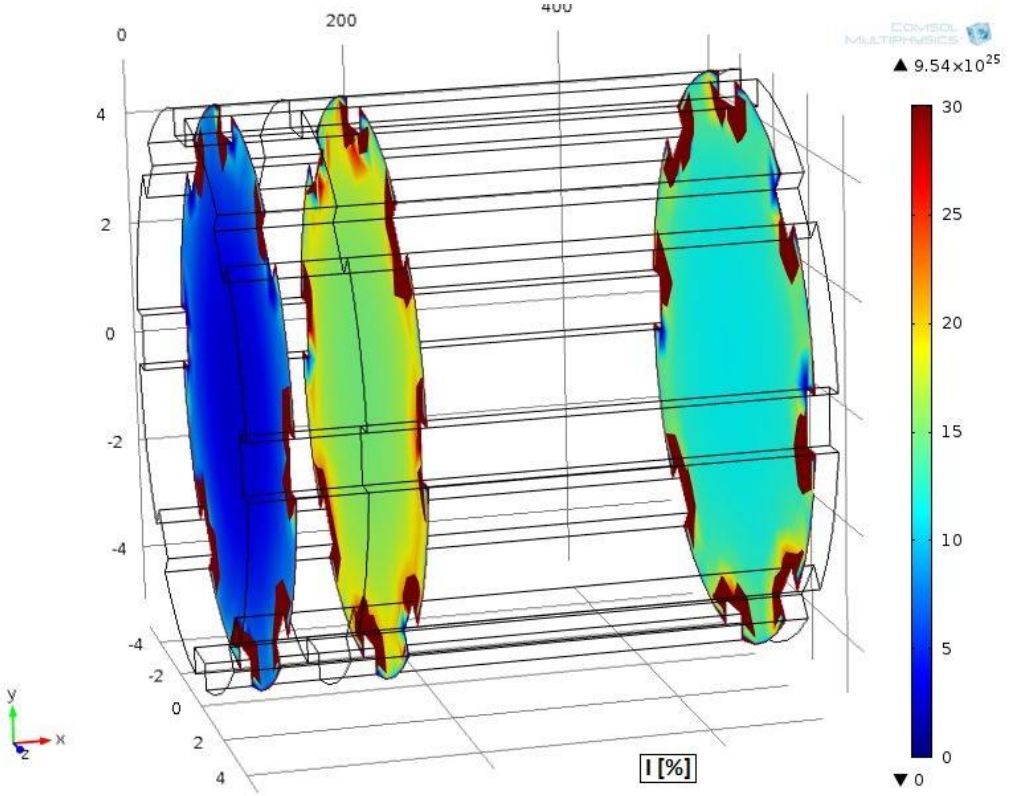

Figure 4.31 Postprocessed 3D plots of case 3D-H depicting values of G (a) and I (b)

In terms of thermal efficiency, Figure 4.32 represents the C_p profiles in the same fashion as in Figure 4.31. Another plane was added at the pipe outlet. As can be observed, the corners formed by the edge between the ribs and the smooth internal wall achieved higher temperature values earlier. Moreover, the LPV region spread towards the pipe centreline displaying an annular shape, until the full cross section at the pipe outlet achieved an almost uniform C_p profile when the Tb was close to the PSC point. By the time the PSC point was reached, the HTC value was meant to decrease again.

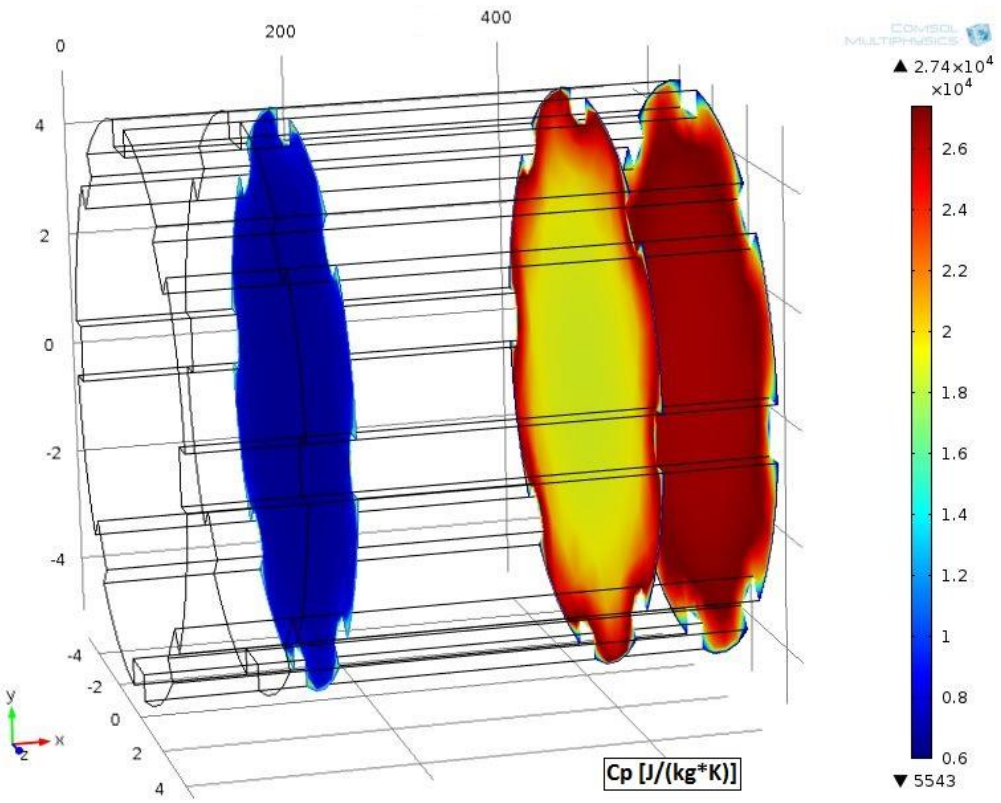

Figure 4.32 Postprocessed 3D plots of case 3D-H showing the C_p profiles

The efficiency of the ribs as turbulence enhancers is portrayed in Figure 4.33a with the axial velocity acceleration/deceleration and in Figure 4.33b with the velocity radial gradients. As depicted in Figure 4.33a, the region around the ribs showed a

combination of acceleration and deceleration patterns which was related to a turbulent process; consequently Figure 4.33b describes how the velocity radial gradients (shear rates) were larger around the ribs, a clear indication of the presence of turbulence.

(a)

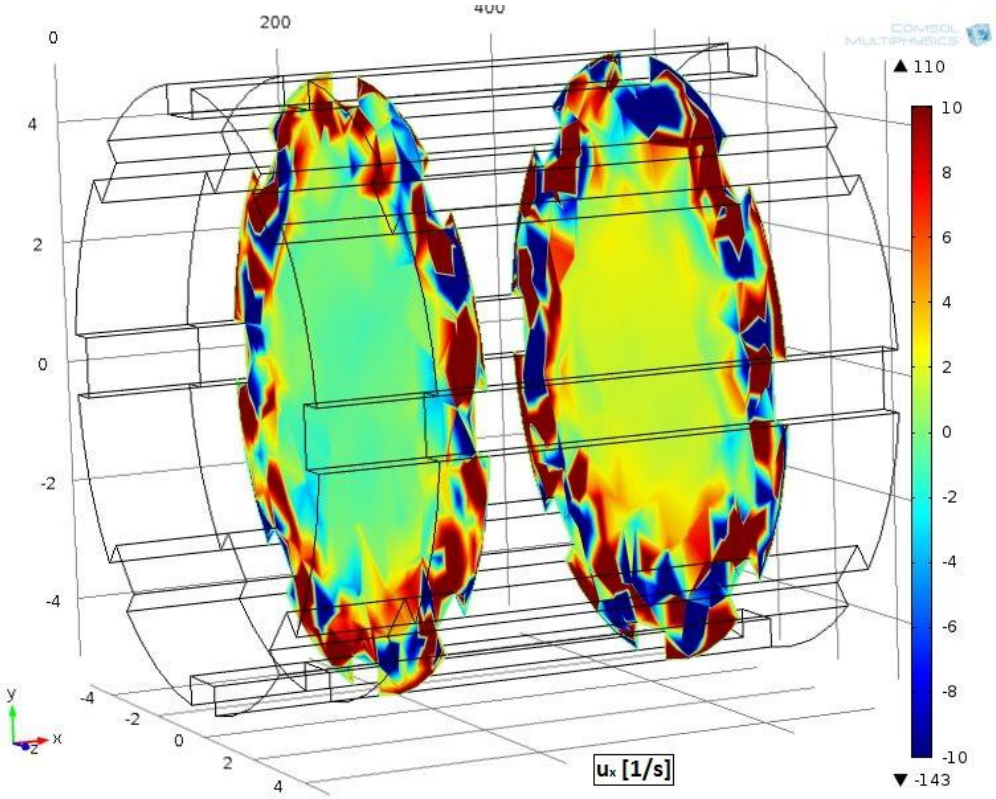

(b)

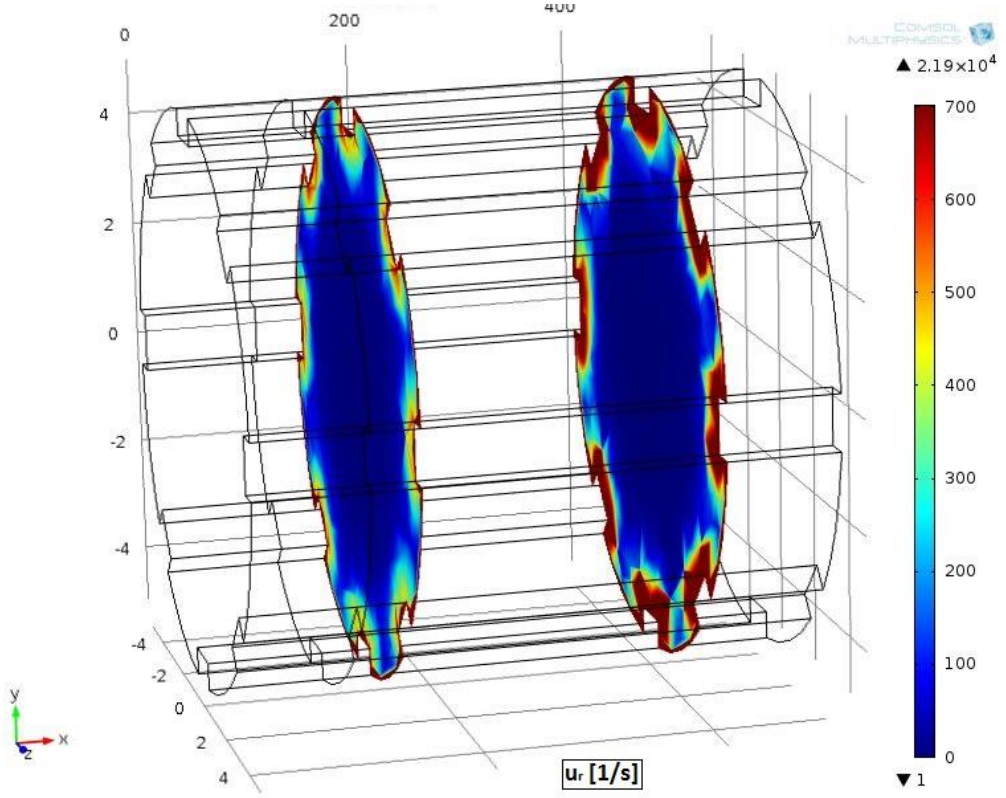

Figure 4.33 Postprocessed 3D plots of case 3D-H revealing profiles of u_x (a) and u_r (b)

The straight ribs from case 3D-H were helically twisted 15° along the axis in order to observe if the turbulence and HTC improve, conforming the case 3D-I. Due to the geometrical complexity of the ribbed pipe and the good results in the case 3D-F exporting cut line data, this approach was selected. Figure 4.34 provides a schematic of the solid geometry showing a cut line (in red).

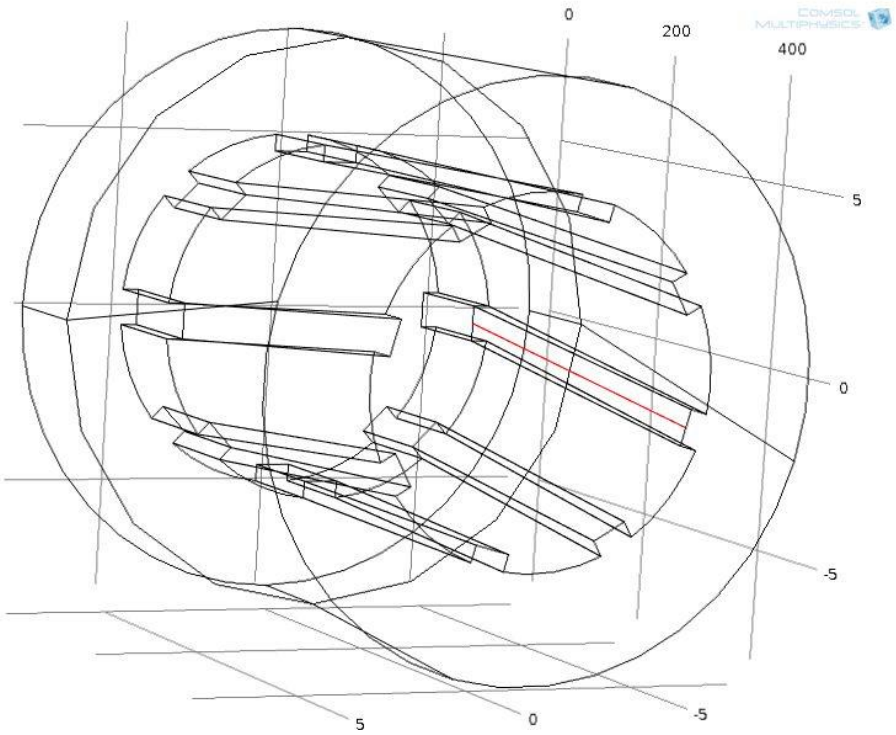

Figure 4.34 Solid domain of case 3D-I showing a cut line to import data (in red)

The calculated values of HTC are presented in Figure 4.35 and compared to the results from the straight IRT, also distinguishing the ribbed surface and the smooth pipe surface. Again, the ribbed surface offered higher values of HTC compared to the smooth sections from the same pipe. The HTC profile described the same trend as the one from the straight IRT, i.e., increasing when the flow achieves temperatures near the PSC point, decreasing when the T_b was about to surpass that point, and absence of external forces. In terms of magnitude, the helical ribbed surfaces showed slightly smaller values of HTC within the axial region approximately between the inlet and 200 *mm* compared to the straight IRT; while within the axial region approximately between 200 *mm* and the outlet this trend was reversed. The smooth surfaces depicted more similar values of HTC, although the helical IRT revealed a larger peak in the centre of the pipe. As a consequence, it could be concluded that

twisting the straight ribs an angle of 15° did not considerably improve the HTC for the pipe length considered, and longer pipes as well as larger helix angles should be tested.

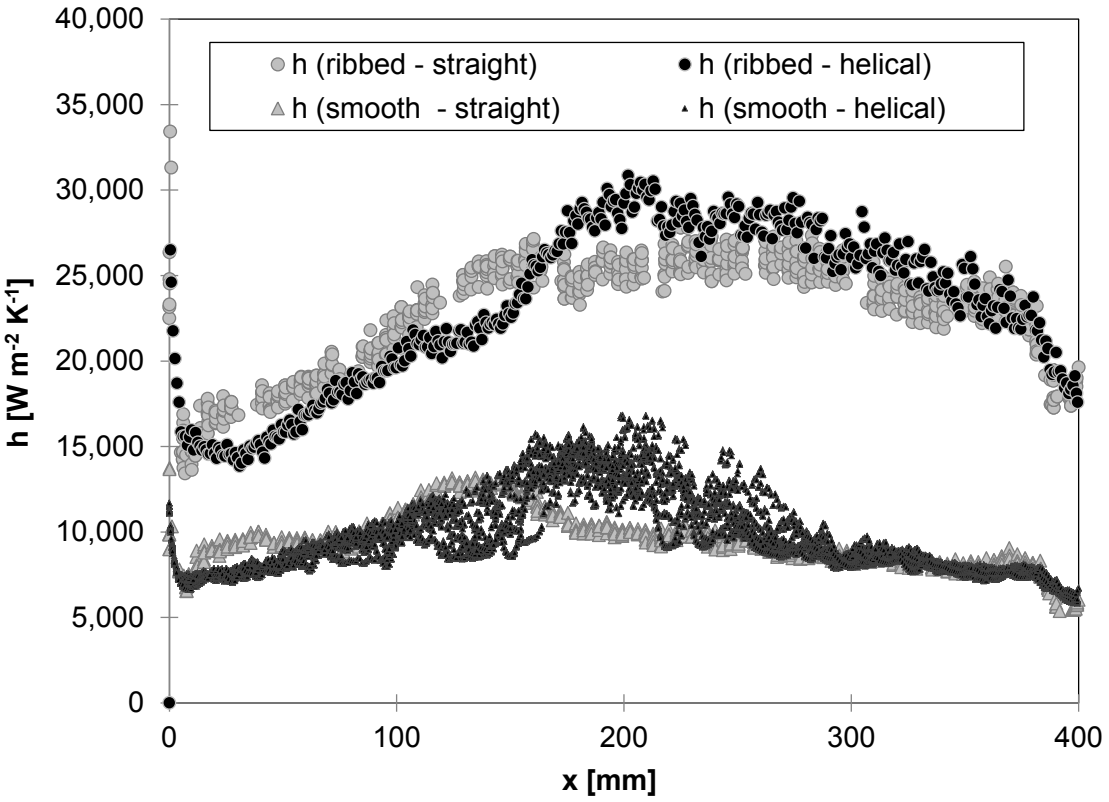

Figure 4.35 Comparison of HTC values between cases 3D-H and 3D-I

In order to obtain a radial comparison with the straight IRT, the cut lines were placed in the same axial locations as before and also from the pipe centreline to the smooth internal wall surface located in the midpoint between two ribs. This involved the consideration of the local angle displacement with respect to the total angle displacement of 15° along L_{hot}, as shown in Figure 4.36. If the cut line did not twist along with the rib helix, it would end up being too close to the rib, where turbulence was much higher, and thus the comparison would not be in the same conditions.

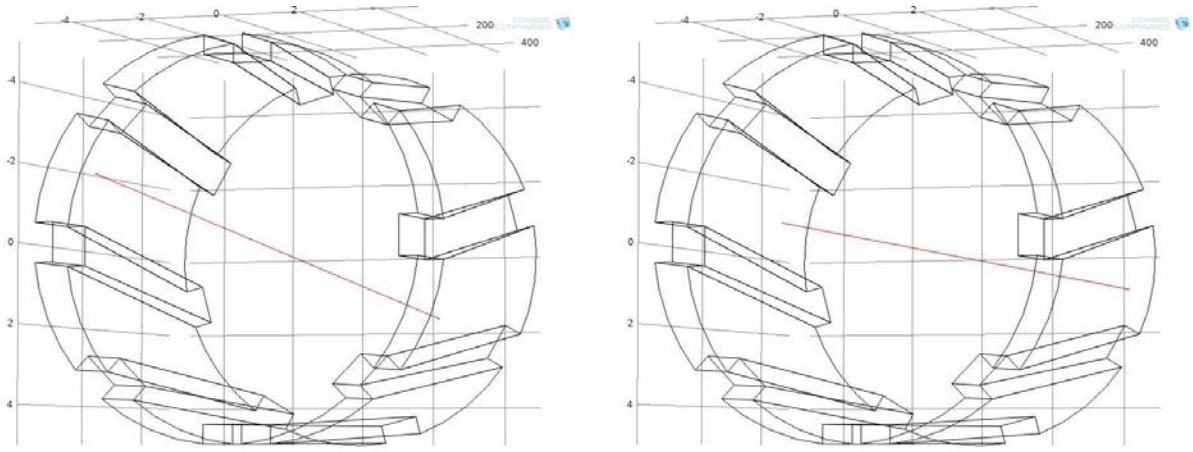

(a) (b)

Figure 4.36 Radial cut lines from case 3D-H, at the entrance (a) and near the outlet (b)

The comparison of radial velocity profiles between cases 3D-H and 3D-I (straight and helical ribs) is shown in Figure 4.37 in logarithmic scale for visual convenience. The close similarity between both cases and the weak effect of twisting the ribs 15° was confirmed. Nevertheless, at values of y^+ between 10 and 200 the velocity profiles for the case 3D-I were slightly smaller for both axial locations. This area coincides with the radial locations of the ribs, thus showing influence over the velocity magnitude. Further on towards the pipe centreline this trend was inverted, so the mean velocities turned slightly higher compared to the case displaying straight ribs.

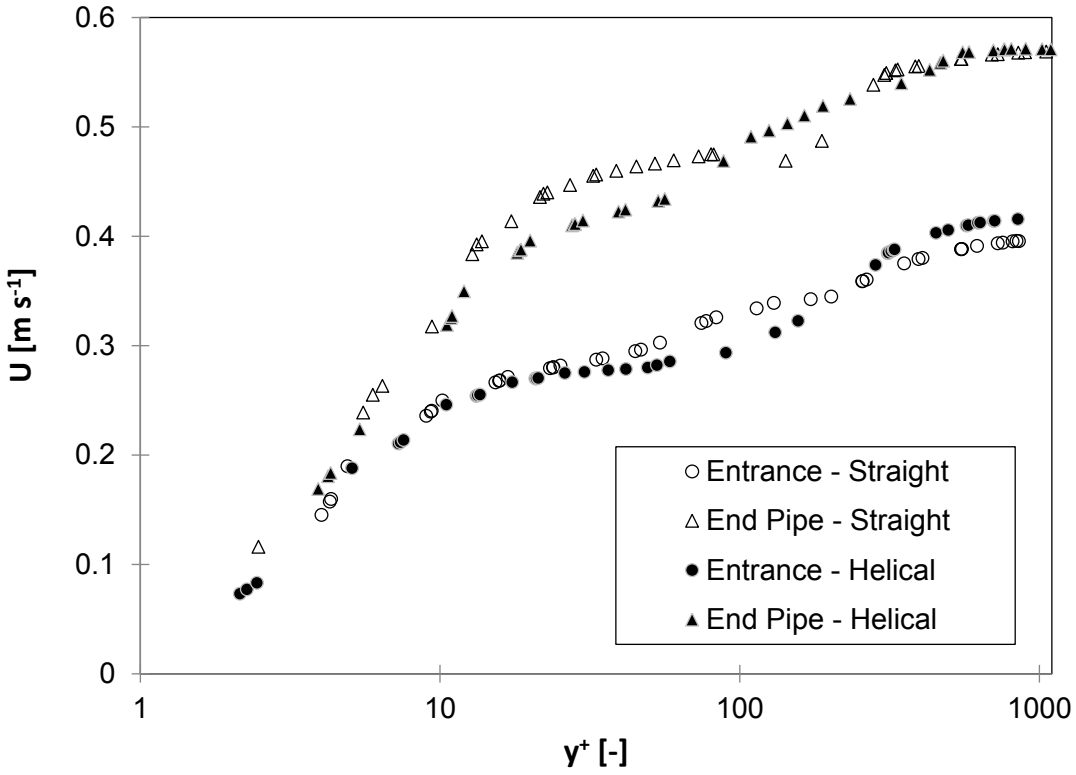

Figure 4.37 Radial profiles of flow mean velocity for the entrance and outlet axial locations from cases 3D-H (straight) and 3D-I (helical)

As the HTC profiles previously revealed in Figure 4.35, in Figure 4.38 the turbulence efficiency depicts slightly better values at the entrance section for the case with straight ribs while in Figure 4.39 the same parameters represent an inverted trend at the outlet pipe section although the differences were smaller.

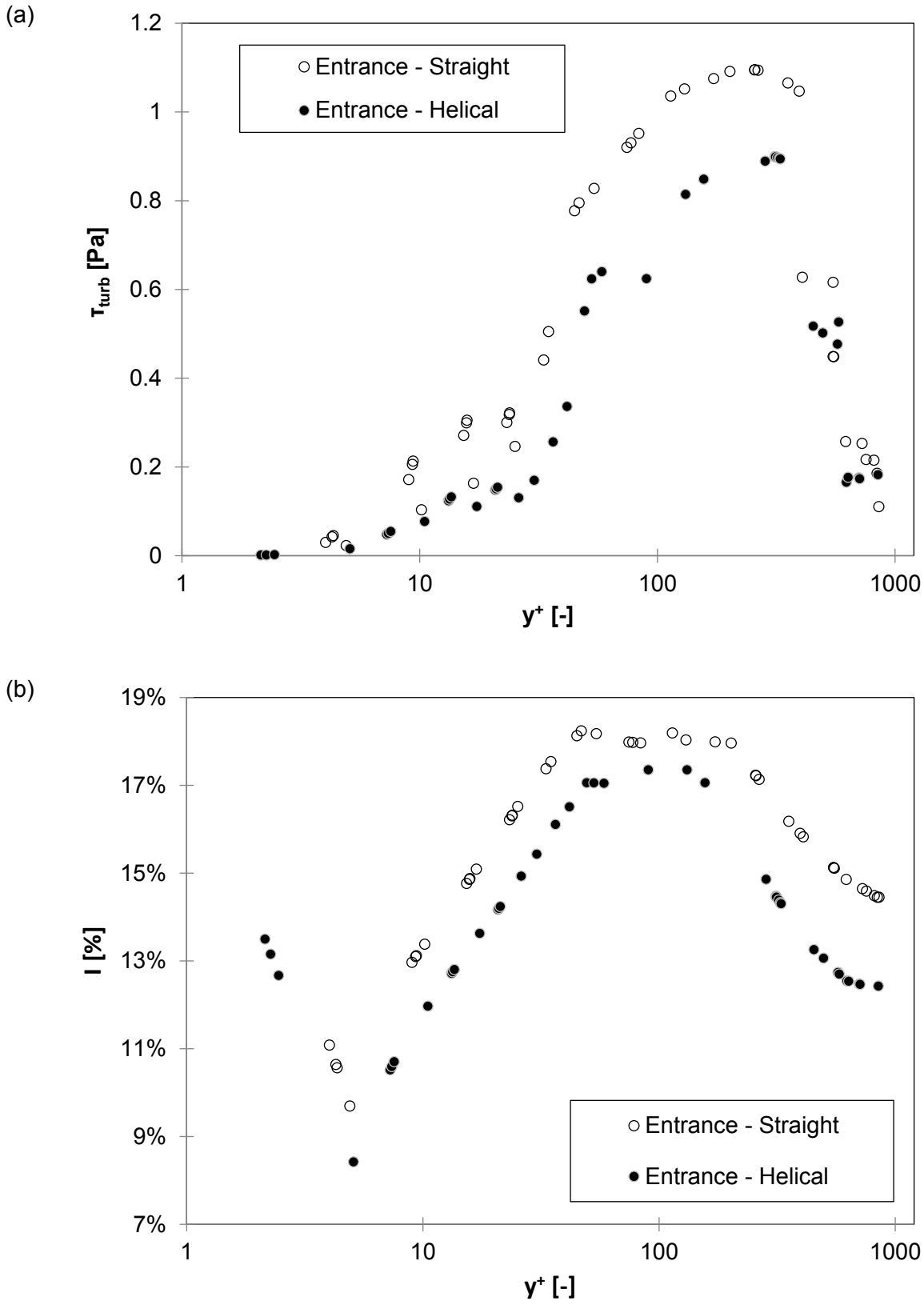

Figure 4.38 Radial profiles of τ_{turb} (a) and I (b) for the entrance location of cases 3D-H and 3D-I

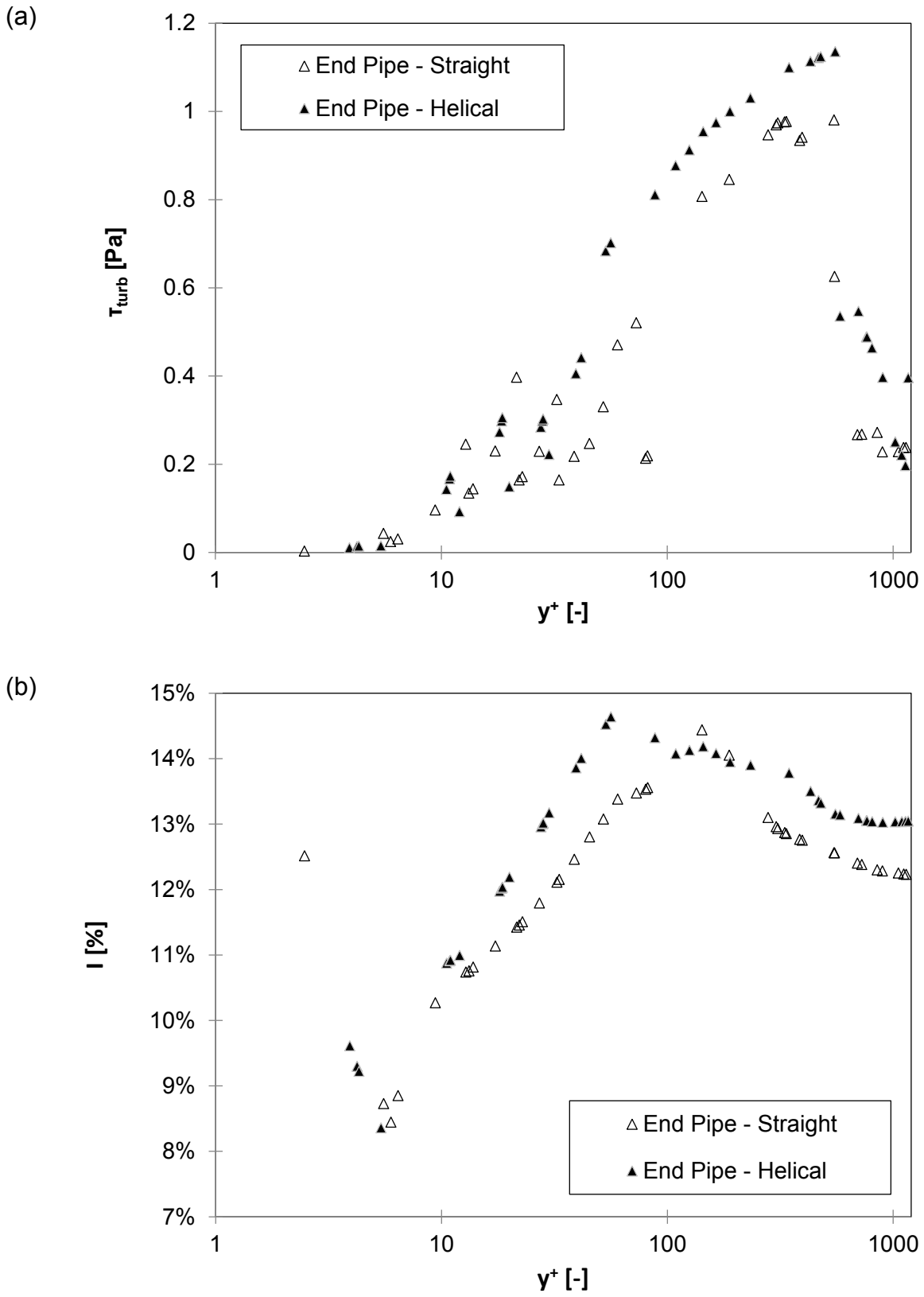

Figure 4.39 Radial profiles of τ_{turb} (a) and I (b) for the pipe outlet location of cases 3D-H and 3D-I

Once the axial and radial analyses were performed on the results from case 3D-I, the main trends on heat transfer and turbulence were spotted. Additionally, other parameters were postprocessed and plotted in 3D together with the same plots from case 3D-H as reference to confirm the aforementioned trends. In order to highlight the differences between the results from the two last cases, in Figure 4.40 and Figure 4.41 the 3D plots are displayed visually decreasing the L:D aspect ratio on the yx plane view and employing a slice at z=0 (middle of the plane) to represent the results. Thus, the flow inlets were located on the left edge of the slices. Figure 4.40a and Figure 4.40b show the values of G for the cases 3D-H and 3D-I, respectively. As can be seen in the colour scale, despite they were very similar, the values of G on case 3D-I were a few kg m^{-2} s^{-1} higher in the bulk of the flow. This was due to the fact that the fluid in case 3D-I left the pipe with a bulk temperature slightly lower than case 3D-H and thus a higher value of density considering how sensitive thermophysical properties are near the PSC point. This was confirmed by Figure 4.40c and Figure 4.40d where the values of C_p, although both of them in the LPV region at the pipe outlet, were a bit higher for case 3D-H, which verified the inability of the selected helical ribs to improve the thermal performance of the system.

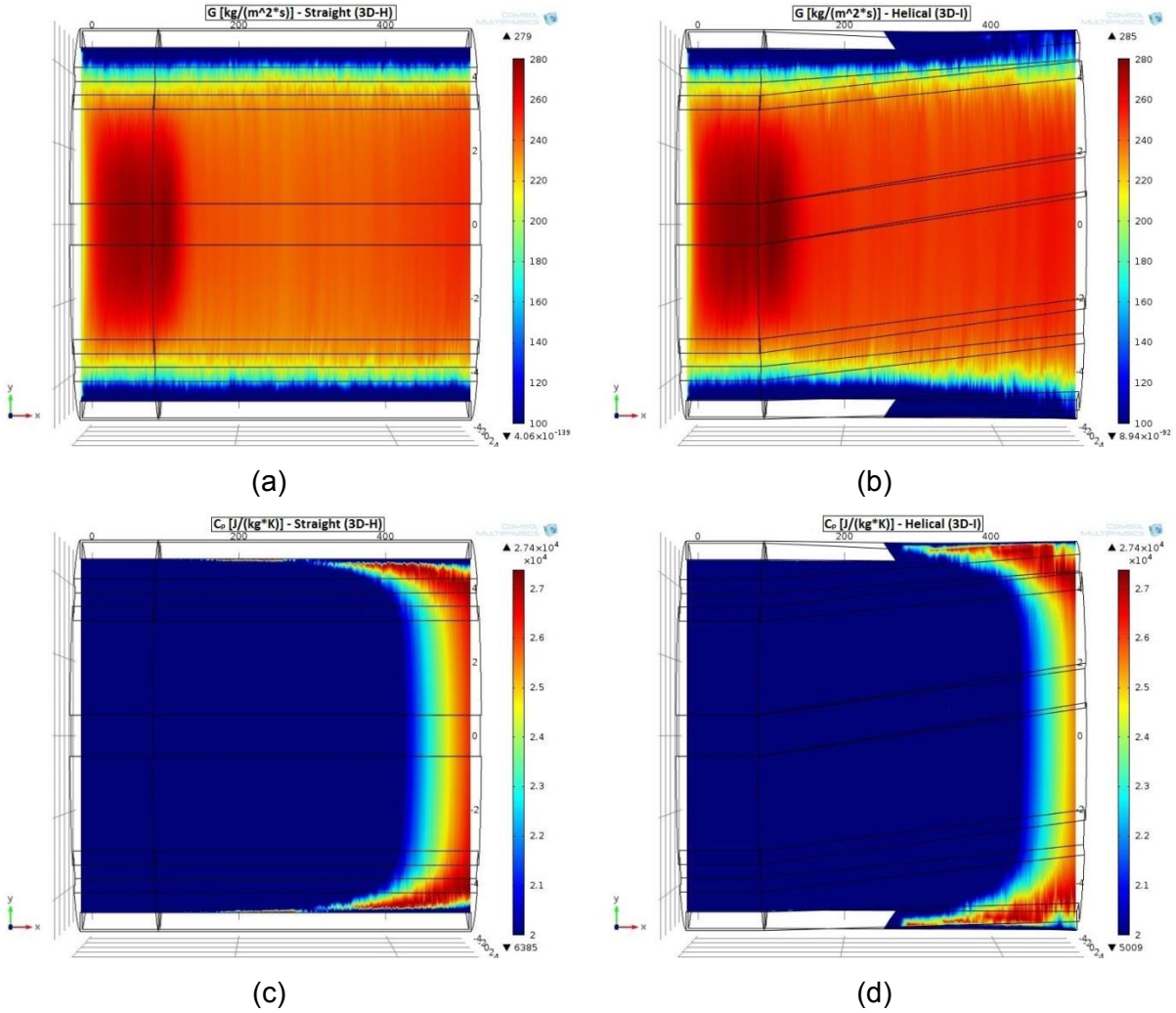

Figure 4.40 Slices in the 3D geometry showing the values of G and C_p for cases 3D-H in (a) and (c); and 3D-I (b) and (d) respectively

Figure 4.41 depicts the turbulence efficiency in the two systems and the results were in agreement with the radial analyses. Figure 4.41a and Figure 4.41b confirm in both cases the existence of larger radial velocity gradients (u_r) at the entrance section extending further into the bulk of the flow, compared to the outlet region. On the other hand, Figure 4.41c and Figure 4.41d represent the values of I in two radial slices (flow inlet still on the left side of each picture) at the entrance and outlet regions. These results supported the previous statements, and moreover revealed that the highest turbulence efficiency took place at the entrance region of case 3D-H with an

intensity of 15-16% approximately, although the outlet region of case 3D-I possessed a slightly better turbulence intensity (around 14%) compared to the equivalent location in case 3D-H, with a 13% approximately. Therefore, although turbulence was becoming stronger at the end of the helical IRT, the overall performance of the straight IRT was better and therefore the outlet value of T_b was slightly higher. It is expectable that with a larger pipe length or a higher helix angle to further develop turbulence, the thermal performance in the helical IRT would exceed that from the straight IRT.

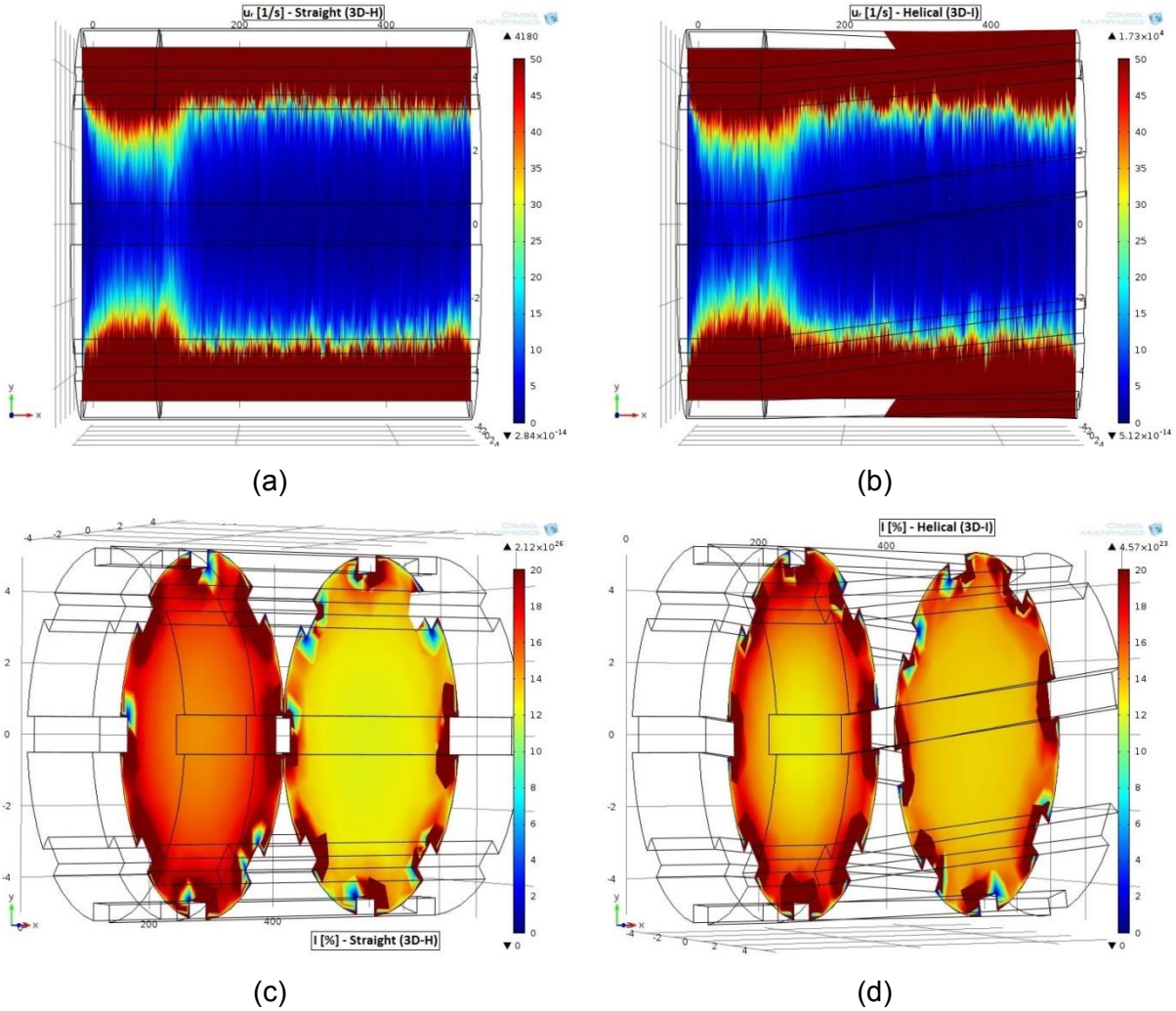

(a) (b)

(c) (d)

Figure 4.41 Slices in the 3D geometry showing the values of u_r and I for cases 3D-H in (a) and (c); and 3D-I (b) and (d) respectively

4.4. Summary

In order to assess the performance of the simulation software Comsol Multiphysics in conditions of deteriorated SCHT, a numerical verification was undertaken employing the boundary conditions from the computational study of Withag (2013) as reference. Among all the 2D study cases selected, the case 2D-C showed a better performance due to the use of a second-order discretisation. The other 2D cases captured the qualitative trends at the axial range approximately between the inlet and 1,250 *mm*, but they were unable to represent the expected trends at axial range approximately between 1,250 *mm* and the outlet, where the LPV region was taking place. Thus, finer meshes were recommended.

A HTD study was carried using the case 2D-C, employing different Nu ratios and specific parameters to highlight the influence of different phenomena. A sharp drop in property changes at the beginning of the heated section triggered HTD. On the other hand, strong buoyancy and flow acceleration/deceleration effects were detected near the heated pipe inlet due to the high q_w/G ratio, generating flow laminarisation but at the same time showing Nu ratios above 1 as both parameters had surpassed the thresholds at which impairment or deterioration took place entering the free-convective regime. This was due to the velocity profiles adopting an M-shape as a means to readjust the flow imbalance, which at the same time produced cyclic stages of shear and turbulence and thus inducing a series of diminishing peaks in the HTC along the pipe. Nevertheless, buoyancy and flow acceleration only affected the axial region approximately between the inlet and x/D= 125 and quickly dissipated along

the pipe, turning the flow into the forced convective regime. On the axial region approximately between x/D= 125 and the outlet, the onset of T_b values prior to the PSC point triggered an improvement of the HTC coefficient.

In the 3D numerical study a smooth pipe was computed employing axial symmetry to only compute a quarter of the geometry. The HTC plot obtained on the region affected by buoyancy (axial region approximately between the inlet and 1,250 *mm*) was more approximate in magnitude and radial location to the results from Withag and colleagues than the 2D plots. Moreover, the radial studies reflected the same effects of buoyancy and acceleration as the 2D simulations did in this region. However the HTC recovery occurring on the forced-convective section (axial region approximately between 1,250 *mm* and the outlet) was not properly computed, which calls for a refined mesh or a second discretisation order.

In order to see the efficiency of HTE techniques improving the HTC values, the computations from the smooth 3D pipe were meant to be compared to two different arrays of IRTs (straight and helical ribs). For this purpose, the boundary conditions and pipe diameter employed were the same as in the previous studies. However, axial symmetry could not be applied on the helical IRT and a full 3D geometry had to be meshed instead, which due to computational limitations forced the shortening of the IRTs length from 2500 *mm* to 500 *mm*. This modification neglected the influence of buoyancy, which was also dependent on the pipe length and thus any comparison with the previous case studies was rendered unfeasible. For this reason, it was decided to compare the results of the two IRTs using the same pipe length instead.

Although not comparable, the straight IRT results showed higher values of HTC and turbulence than the smooth 3D pipe, the ribbed surfaces displaying larger values of HTC than the smooth internal walls in the same axial location. Stronger turbulence was found around the ribbed surfaces than anywhere else in the flow. Moreover, the section at the beginning of the heated length provided better results of turbulence than the outlet region, which was due to the fact that the T_b at the outlet had reached the PSC point, inducing deterioration. The selected helical IRT did not show improvements in turbulence or HTC compared to the straight IRT, although it revealed better values of turbulence at the end of the pipe compared to the straight IRT. It is expected that a longer pipe of this kind, or displaying a larger helix angle, would improve the hydrothermal performance.

References

Du Z, Lin W, Gu A (2010). Numerical investigation of cooling heat transfer to supercritical CO_2 in a horizontal circular tube. *The Journal of Supercritical Fluids*; 55: 116-21

Forooghi P, Hooman K (2013). Numerical study of turbulent convection in inclined pipes with significant buoyancy influence. *International Journal of Heat and Mass Transfer;* 61: 310-22

Forooghi P, Hooman K (2013). Effect of buoyancy on turbulent convection heat transfer in corrugated channels – A numerical study. *International Journal of Heat and Mass Transfer;* 64: 850-62

Hall WB, Jackson JD (1969). Laminarization of a pipe flow by buoyancy forces. *ASME;* paper 69-HT-55

He S, Jiang P, Xu Y, Shi R, Kim WS, Jackson JD (2005). A computational study of convection heat transfer to CO_2 at supercritical pressures in a vertical mini tube. *International Journal of Thermal Sciences;* 44: 521-30

He S, Kim WS, Bae JH (2008). Assessment of performance of turbulence models in predicting supercritical pressure heat transfer in a vertical tube. *International Journal of Heat and Mass Transfer;* 51: 4659-75

Huang D, Wub Z, Sunden B, Li W (2016). A brief review on convection heat transfer of fluids at supercritical pressures in tubes and the recent progress. *Applied Energy*; 162: 494-505

Jackson JD, Hall WB (1979), Influences of buoyancy on heat transfer to fluids flowing in vertical tubes under turbulent conditions. In: Kakac S (editor). Turbulent forced convection in channels and bundles. *Hemisphere Publishing Corporation*; pp. 613-40

Jackson JD (2009). Progress in developing an improved empirical heat transfer equation for use in connection with advanced nuclear reactors cooled by water at supercritical pressure. In: ASME (editor). Proceedings of the 17th International congress on advances in nuclear power plants. *Nuclear Engineering Division*

Jaromin M, Anglart H (2013). A numerical study of heat transfer to supercritical water flowing upward in vertical tubes under normal and deteriorated conditions. *Nuclear Engineering and Design;* 264: 61-70

Lemmon EW, McLinden MO, Friend DG (2015). Thermophysical Properties of Fluid Systems. In: Linstrom PJ (editor). NIST Standard Reference Database Number 69. *NIST Chemistry WebBook*

Li H, Kruizenga A, Anderson M, Corradini M, Luo Y, Wang H, Li H (2011). Development of a new forced convection heat transfer correlation for CO_2 in both heating and cooling modes at supercritical pressures. *International Journal of Thermal Sciences*; 50: 2430-42

Li H, Zhang Y, Zhang L, Yao M, Kruizenga A, Anderson M (2016). PDF-based modeling on the turbulent convection heat transfer of supercritical CO_2 in the printed circuit heat exchangers for the supercritical CO_2 Brayton cycle. *International Journal of Heat and Mass Transfer*; 98: 204-18

Li Z, Wu Y, Lu J, Zhang D, Zhang H (2014). Heat transfer to supercritical water in circular tubes with circumferentially non-uniform heating. *Applied Thermal Engineering;* 70: 190-200

Li Z, Wu Y, Tang G, Zhang D, Lu J (2015). Comparison between heat transfer to supercritical water in a smooth tube and in an internally ribbed tube. *International Journal of Heat and Mass Transfer*; 84: 529-41

Li Z, Wu Y, Tang G, Lu J, Wang H (2016). Numerical analysis of buoyancy effect and heat transfer enhancement in flow of supercritical water through internally ribbed tubes. *Applied Thermal Engineering;* 98: 1080-90

Mokry S, Pioro I, Farah A, King K, Gupta S, Peiman W, Kirillov P (2011). Development of supercritical water heat-transfer correlation for vertical bare tubes. *Nucl. Eng. Des.;* 241 (4): 1126-36

Nemati H, Patel A, Boersma BJ, Pecnik R (2015). Mean statistics of a heated turbulent pipe flow at supercritical pressure. *International Journal of Heat and Mass Transfer;* 83: 741-52

Podila K, Rao YF (2015). CFD analysis of flow and heat transfer in Canadian supercritical water reactor bundle. *Annals of Nuclear Energy;* 75: 1-10

Podila K, Rao Y (2016). CFD modelling of supercritical water flow and heat transfer in a 2 × 2 fuel rod bundle. *Nuclear Engineering and Design;* 301: 279-89

Shang Z, Yao Y, Chen S (2008). Numerical investigation of system pressure effect on heat transfer of supercritical water flows in a horizontal round tube. *Chemical Engineering Science;* 63: 4150-58

Shang Z, Chen S (2011). Numerical investigation of diameter effect on heat transfer of supercritical water flows in horizontal round tubes. *Applied Thermal Engineering;* 31: 573-81

Sharabi M, Ambrosini W, He S, Jackson JD (2008). Prediction of turbulent convective heat transfer to a fluid at supercritical pressure in square and triangular channels. *Annals of Nuclear Energy;* 35: 993-1005

Taklifi A, Hanafizadeh P, Behabadi MAA, Aliabadi A (2016). Experimental investigation on heat transfer and pressure drop of supercritical water flows in an inclined rifled tube. *J. of Supercritical Fluids;* 107: 209-18

Tang R, Yin F, Wang H, Chen T (2007). An investigation into the heat transfer characteristics of spiral wall with internal rib in a supercritical sliding-pressure operation once-through boiler. *Front. Energy Power Eng. China;* 1(3): 300-04

Urbano A, Nasuti F (2013). Conditions for the occurrence of heat transfer deterioration in light hydrocarbons flows. *International Journal of Heat and Mass Transfer;* 65: 599-609

Van der Kraan M, Peeters MMW, Fernandez-Cid MV, Woerlee GF, Veugelers WJT, Witkampa GJ (2005). The influence of variable physical properties and buoyancy on heat exchanger design for near- and supercritical conditions. *J. of Supercritical Fluids;* 34: 99-105

Wang J, Li H, Yu S, Chen T (2011). Comparison of the heat transfer characteristics of supercritical pressure water to that of subcritical pressure water in vertically-upward tubes. *International Journal of Multiphase Flow;* 37: 769-76

Wang H, Bi Q, Yang Z, Wang L (2015). Experimental and numerical investigation of heat transfer from a narrow annulus to supercritical pressure water. *Annals of Nuclear Energy;* 80: 416-28

Wang K, Xu X, Wu Y, Liu C, Dang C (2015). Numerical investigation on heat transfer of supercritical CO_2 in heated helically coiled tubes. *J. of Supercritical Fluids*; 99: 112-20

Wen QL, Gu HY (2010). Numerical simulation of heat transfer deterioration phenomenon in supercritical water through vertical tube. *Annals of Nuclear Energy;* 37: 1272-80

Withag JAM (2013). On the gasification of wet biomass in supercritical water. PhD thesis at the University of Twente, Enschede, The Netherlands

Withag JAM, Sallevelt JLHP, Brilman DWF, Bramer EA, Brem G (2012). Heat transfer characteristics of supercritical water in a tube: Application for 2D and an experimental validation. *J. of Supercritical Fluids;* 70: 156-70

Yamagata K, Nishikawa K, Hasegawa S, Fujii T, Yoshida S (1972). Forced convective heat transfer to supercritical water flowing in tubes. *International Journal of Heat and Mass Transfer*; 15: 2575-93

Zhang G, Zhang H, Gu H, Yang Y, Cheng X (2012). Experimental and numerical investigation of turbulent convective heat transfer deterioration of supercritical water in vertical tube. *Nuclear Engineering and Design;* 248: 226-37

Zhang Q, Li H, Zhang W, Li L, Lei X (2015). Experimental study on heat transfer to the supercritical water upward flow in a vertical tube with internal helical ribs. *International Journal of Heat and Mass Transfer;* 89: 1044-53

5. Numerical study of a water-cooled wall in a supercritical boiler

Gil-Garcia AA, Kings IN, Al-Duri B

Abstract

In order to optimise the supercritical boiler performance, many different studies have been performed using process simulators focused on the thermal-hydraulic side, while computational fluid dynamics had been mostly focused on the exhaust gases side. In the present study, the heat transfer performance of a supercritical fluid in a test element was investigated using the software Comsol Multiphysics. The test element represented one pipe of the water wall of the thermal-hydraulic side in a vertical position with upward flow. The fluid performance in the test element was simulated using the Conjugate Heat Transfer and the SST turbulence models, using a two-dimensional geometry. The boundary conditions were obtained by applying similarity equations in order to make the simulation feasible in terms of meshable geometry, and as a consequence the hydrothermal conditions increased. The results obtained for two different thermal boundary conditions revealed that in none of the scenarios the flow was significantly affected by buoyancy, although thermal acceleration had a sensible impact on the heat transfer performance once the bulk of the flow surpassed PSC point. The main phenomenon controlling the heat transfer performance was the property changes, given the strong forced-convective nature of the system. When increasing the temperature of the furnace chamber, the system improved the heat transfer behaviour, showing better hydrothermal properties and producing a better heat transfer coefficient. More results using finer meshes and reduced wall distances must be undertaken in order to verify the trends obtained.

Keywords: supercritical coal-fired power plant, two-dimensional turbulence modelling, Comsol Multiphysics, conjugate heat transfer, fluid-to-fluid scaling.

Industrial Relevance

When investigating utility boilers using supercritical water cycles, the acquisition of experimental data is expensive if possible and laden with many uncertainties because often the techniques or procedures to be tested would have never been implemented before in these systems. Thus, the use of computational fluid dynamics in power systems is paramount for the evolution of the power industry towards a cleaner, efficient and affordable production of electricity. Once a simulation program is validated and verified to be capable of reproducing the performance of a system whose response is well documented, the desired working conditions in terms of research can be applied for the production of new data. In this study, boiler conditions were scaled down applying fluid-to-fluid supercritical equations to comply with computing limitations while still considering it hydrodynamically and thermally equivalent.

Abbreviations

2D	two-dimensional
CFD	computational fluid dynamics
DB	Dittus-Boelter
DOF	degrees of freedom
HTC	heat transfer coefficient
HTD	heat transfer deterioration
LPV	large property variation
NHT	normal heat transfer
PDE	partial differential equation
PSC	pseudo-critical
SCHT	supercritical heat transfer
SST	shear stress transport

Dimensionless numbers

Bo	buoyancy parameter
Gr	Grashof number
K_v	thermal acceleration parameter
Nu	Nusselt number

Greek symbols

α	thermal diffusivity [$m^2\ s^{-1}$]
μ	dynamic viscosity [$kg\ m^{-1}\ s^{-1}$]
ν	kinematic viscosity or momentum diffusivity [$m^2\ s^{-1}$]
π_c	dimensionless parameter measuring thermophysical changes [-]
ρ	density [$kg\ m^{-3}$]
τ	shear stress [Pa]

Geometric definitions

D_i, D	inner tube diameter [mm]
D_o	outer tube diameter [mm]
L	total length of pipe [mm]
S	pipe cross-sectional area [m^2]
x	axial coordinate within the heated section [mm]
x/D	dimensionless heated pipe length [-]
y	radial coordinate [mm]
y^+	dimensionless wall distance [-]
y_1^+	dimensionless wall distance of first layer to the wall [-]

Roman symbols

C_p	isobaric heat capacity [J kg^{-1} degC^{-1}]
G	mass flux of water [kg m^{-2} s^{-1}]
g	gravitational acceleration [m s^{-2}]
h	heat transfer coefficient [W m^{-2} degC^{-1}]
I	turbulence intensity [%]
k	thermal conductivity [W m^{-1} degC^{-1}] or turbulent kinetic energy [m^2 s^{-2}]
n	number of water wall pipes
p	absolute pressure [bar]
q	heat flux [kW m^{-2}]
T	temperature [K or °C]
u	axial flow velocity [m s^{-1}]
v	radial flow velocity [m s^{-1}]
U	mean flow velocity [m s^{-1}]
W_m	water mass flow [kg s^{-1}]

Subscripts

$(\dots)_b$	at bulk conditions
$(\dots)_{entr}$	at the pipe entrance section
$(\dots)_{hot}$	at the heated section
$(\dots)_i$	at inner pipe diameter conditions
$(\dots)_{in}$	at inlet conditions
$(\dots)_{iw}$	at inner wall conditions
$(\dots)_o$	at outer pipe diameter conditions
$(\dots)_{out}$	at outlet conditions
$(\dots)_{ow}$	at outer wall conditions
$(\dots)_{pc}$	at pseudo-critical conditions
$(\dots)_{SD}$	at scaled down conditions
$(\dots)_T$	at turbulent conditions
$(\dots)_{turb}$	at turbulent conditions
$(\dots)_{ww}$	at water-wall conditions
$(\dots)_x$	increment of property in axial direction
$(\dots)_y$	increment of property in radial direction
$(\dots)_\infty$	at furnace chamber conditions

5.1. Background

In Chapters 3 and 4 the modelling software Comsol Multiphysics was validated and verified using experimental and numerical data respectively, in two and three dimensions, in order to confirm its applicability when studying supercritical heat transfer in a test element at laboratory conditions. The aim of such validation and verification was to give way to a new research, applying boiler conditions, in order to understand the occurrence of enhancing and deteriorating phenomena in heat transfer in these systems as a means to optimise the boiler efficiency and provide a better scenario to comply with the UK Grid Code.

Previous studies were carried employing computational fluid dynamics (CFD) software to simulate supercritical coal-fired power plants systems, and the majority of these simulations were focused on the calculation of heat fluxes and temperatures on the water wall in order to avoid thermal stress and ash deposition. It was found that ANSYS FLUENT and ANSYS CFX were the most popular CFD codes used among authors to simulate such systems, besides a series of “in-house” programs. Also, most of the considered authors employed steady state conditions in their simulations in contrast to more complicated time dependent studies.

Sankar *et al.* (2016) published a review on the numerical techniques to measure and predict the heat fluxes applied on the water wall pipes of the boiler, and they concluded that most researches devoted solely to the furnace side (exhaust gases) while only a few focused on the thermal-hydraulic performance of the water wall

cycle. This was because of the computational cost of meshing such a large and complex system. As a consequence, the data necessary from the thermal-hydraulic side (water cycle) must be obtained by several methods. One was the integration of the CFD software with process simulator programs. Another alternative implied using empirical correlations at supercritical conditions obtained in experimental works using rigs for the calculation of the heat transfer coefficient (HTC) for the water cycle. Also, data for the water cycle could be obtained by the measurement of steam parameters in similar experimental systems or by undertaking CFD simulations focused solely on the water cycle (obtaining numerical correlations).

In terms of integrated systems, Edge *et al.* (2011) studied the generation of steam in a subcritical power plant by employing a thermosiphon system (natural circulation). At steady state conditions they combined the simulator gPROMS on the water cycle to provide values of HTC, with ANSYS FLUENT to obtain the wall temperatures of the furnace and radiative heat exchangers. This study was later extended to include a carbon capture system (Edge *et al.,* 2012). Moreover, Park *et al.* (2010) successfully validated their simulation using the experimental data from a power plant in South Korea. For this purpose, they combined a CFD program to study the furnace side (ANSYS CFX), coupled with a process simulator to model the water side of a steady state system (PROATES from E.ON Engineering).

With respect to the use of CFD programs only in studies employing correlations or importing data from other sources, Xu *et al.* (2016) employed CFD to calculate heat fluxes in a circulating fluidised bed boiler at supercritical conditions by using ANSYS

FLUENT on the furnace side for the gas-particle hydrodynamics coupled with Nusselt correlations for the estimation of the HTC on the thermal-hydraulic side. On the other hand, Badur *et al.* (2012) estimated the degradation of the water walls in a pulverized-coal boiler using a finite element software (ABAQUS) employing steam parameters by undertaking a previous simulation in ANSYS code. Similarly, Piotr *et al.* (2009), developed a method to obtain the heat flux in the water wall pipes using ANSYS as CFD software and utilising experimental data previously measured on the inner surfaces of the pipes.

As mentioned before, the number of studies found employing CFD on the thermal-hydraulic side was limited, and to the author's knowledge no simulations have been yet performed using Comsol Multiphysics to study the water cycle of supercritical coal-fired power plants. Therefore, the aim of this work was to perform a two-dimensional (2D) computational study with the CFD software Comsol Multiphysics, previously validated in Chapters 3 and 4, by scaling down working conditions taken from boiler operations while keeping hydrodynamic and thermal equivalence. Water wall pipes from the thermal-hydraulic side were selected to investigate in order to capture the occurrence of the pseudocritical transition and the complex phenomena involved.

5.2. Scale-down of water-wall conditions

The working conditions at the water-wall of supercritical boilers include a wide range of values depending on various aspects, such as the boiler type (pulverised-coal or circulating fluidised bed), the water wall configuration (smooth spiral upwards or ribbed upwards) and the boiler load (% of capacity). Complete information is scarce, thus in an attempt to capture standard values to be scaled down, these were obtained combining parameters from the studies carried by Huilin *et al.* (2013) on a ribbed upward water wall and Zima *et al.* (2010) studying a spirally upward configuration, presented in Table 5.1.

Table 5.1 Selected working conditions at the water wall

Characteristic	Magnitude
Steam mass flow (W_m)	1900 $t\ h^{-1}$
Water pressure at inlet (p_{in})	300 bar
Average thermal load of water walls (q_{ow})	1450 kW m^{-2}
Number of water-wall pipes (n)	1500 (smooth)
Orientation	Upward & inclined (20° approx.)
Pipe internal diameter (D_i)	22 *mm*
Pipe external diameter (D_o)	35 *mm*
Length of pipe (L)	123 *m*
Water inlet temperature (T_{in})	350°C
Furnace chamber temperature (T_∞)	700° - 900°C

With the working conditions defined, similarity equations were employed to keep the same hydrodynamic and thermal performance. In this case the fluid was the same, but the pipe geometry was reduced at the expense of increasing the hydrothermal conditions as a means to reduce the computational domain and make the simulation

feasible. The similarity equations, based on inlet conditions, are shown in Table 5.2. The symbols employed and their units were properly summarised on the nomenclature section.

Table 5.2 Similarity equations based on inlet conditions (Pioro & Duffey, 2007)

Similarity	Equation	
Geometry	$\left(\frac{x}{D_i}\right)_{WW} = \left(\frac{x}{D_i}\right)_{SD}$	**(5.1)**
Mass flux	$\left(\frac{G \cdot D_i}{\mu_b}\right)_{WW} = \left(\frac{G \cdot D_i}{\mu_b}\right)_{SD}$	**(5.2)**
Heat flux	$\left(\frac{q_{ow} \cdot D_i}{k_b \cdot T_b}\right)_{WW} = \left(\frac{q_{ow} \cdot D_i}{k_b \cdot T_b}\right)_{SD}$	**(5.3)**

To obtain the simulation conditions, the geometric similarity was first calculated in equation (5.1). A balance between $(D_i)_{SD}$ and the pipe length (L_{SD}) had to be maintained in order to decrease the computational requirements. A scaled-down length of 20 *m* was selected, and applying the aforementioned equation an inner diameter of 3.58 *mm* was obtained. In order to maintain the same D_o/D_i ratio in the simulation, the equivalent $(D_o)_{SD}$ was 5.69 *mm*.

$$(w_m)_{WW} = (G \cdot S)_{WW} \quad \textbf{(5.4)}$$

For the mass flux similarity, the equivalent mass flux for one single pipe must be calculated first at water wall conditions (G_{ww}). With the water mass flow (W_m) provided in Table 5.1 and equation (5.4), the obtained value of G for one pipe of section S was equal to 925 kg m^{-2} s^{-1}. Using equation (5.2) and considering the thermodynamic properties were the same for both systems at inlet conditions, a

value of 5.684 kg m^{-2} s^{-1} was obtained for G_{SD}. Applying the same considerations on the heat flux similarity in equation (5.3) and redefining heat flux with equation (5.5), a new expression for thermal similarity was produced in equation (5.6) if both the same values of h_∞ and T_{ow} were imposed in both scales.

$$q_{ow} = h_\infty \cdot (T_\infty - T_{ow}) \quad \textbf{(5.5)}$$

$$(T_\infty)_{SD} = \frac{(D_i)_{WW}}{(D_i)_{SD}} \cdot (T_\infty)_{WW} - \left(\frac{(D_i)_{WW}}{(D_i)_{SD}} - 1\right) \cdot (T_{ow})_{SD} \quad \textbf{(5.6)}$$

The final equation of thermal similarity, equation (5.6), forced the need to increase the furnace chamber temperature on the scaled-down system, which is logical considering the increased value of G_{SD} compared to G_{WW} to offset a smaller pipe diameter. When applying similarity equations, the effect of the new balance of parameters cannot be completely predicted due to the sensitivity of factors like buoyancy or thermal acceleration to those modifications at supercritical conditions. These parameters were the pipe diameter, the fluid mass flux and heat flux on the convective nature of the system.

For the calculation of the external heat transfer coefficient (h_∞), a standard value at furnace chamber conditions of 4800 W m^{-2} $degC^{-1}$ was estimated using equation (5.5). Based on the average thermal load included in Table 5.1, a furnace chamber temperature of 900°C and an outer water wall pipe temperature of 600°C were considered. A summary of the scaled-down working conditions is presented in Table 5.3.

Table 5.3 Working conditions after scaling-down the system

Scaled-down parameter	Magnitude
Mass flux (G_{SD})	5684 kg m^{-2} s^{-1}
Water pressure at inlet (p_{in})	300 bar
External heat transfer coefficient (h_{∞})	4800 W m^{-2} $degC^{-1}$
Orientation	upward
Pipe internal diameter ($(D_i)_{SD}$)	3.58 *mm*
Pipe external diameter ($(D_o)_{SD}$)	5.69 *mm*
Length of pipe (L_{SD})	20 *m*
Water inlet temperature (T_{in})	350°C
Furnace chamber temperature ($(T_{\infty})_{SD}$)	1000° and 2200°C

A low value (700°C) and a high value (900°C) of chamber temperatures ($(T_{\infty})_{WW}$) were considered. Two scaled furnace chamber temperatures of 1000° and 2200°C, $(T_{\infty})_{SD}$ were obtained by estimating an average temperature for the outer water wall $(T_{ow})_{SD}$ of 650°C. It was acknowledged that, given their high values, the temperatures obtained by similarity would not have practical application in prospective experimental works; however they were considered only in a computational context.

Initially, two pipe configurations were selected to reproduce the standard types employed in supercritical boilers, namely vertical upward flow and inclined pipe positions (20° approx.). However, the property profiles obtained for the two orientations at the respective scaled chamber temperatures of 1000° and 2200°C showed negligible difference, revealing buoyancy was completely overcome by the inertial forces at the working conditions produced by the similarity equations.

5.3. Computational methods

5.3.1. Physical model and modelling techniques

A test element representing one of the 1500 pipes and carrying 5,684 kg m^{-2} s^{-1} of water was modelled in 2D including the solid domain and applying axial symmetry, as shown in Figure 5.1.

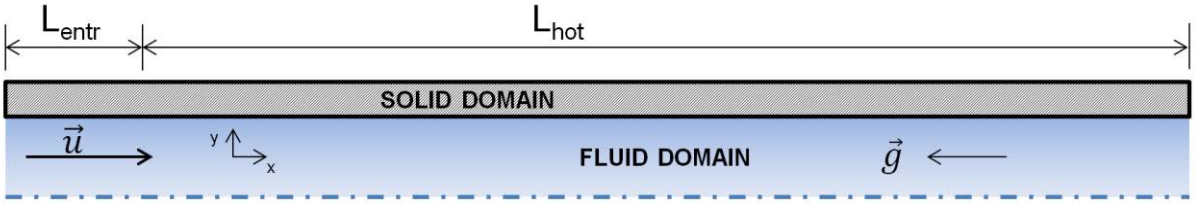

Figure 5.1 Computational domain of the system to be modelled

The present study involved the use of the conjugated heat transfer (CHT) module, as heat conduction in the solid domain transferred the heat flux to the fluid domain, where convection also occurred. The CHT module was coupled with the shear stress transport model (SST) for the flow turbulence. Thus, the governing equations, the turbulence model and the solution methodology employed were the same as those described in Chapter 4.

5.3.2. Boundary conditions

The present computational study was not based on laboratory conditions where an AC power supply would provide an average value of heat flux. Instead, the system was considered at furnace chamber conditions with hot flue gases from combustion

surrounding the pipes. Thus, the thermal boundary condition imposed in this case would be convective heat flux, defined by an external HTC (h_∞) at furnace chamber temperature (T_∞). The average thermal load of the water walls defined in Table 5.1 was included among the working conditions though the furnace chamber temperature was also defined, as a means to calculate h_∞.

Because it was an upward flow, axial symmetry was applied to both the flow and the heat transfer. The inlet flow was developed, meaning the boundary layer was already formed. A certain distance was left unheated at the entrance to allow the flow to fully develop prior to the heating. The details are shown in Figure 5.2.

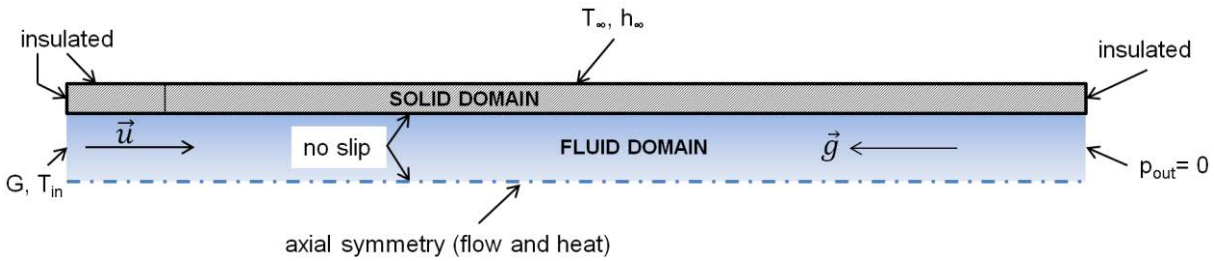

Figure 5.2 Boundary conditions of the model

5.3.3. Initial conditions

In order to gain computational stability, a developed flow at the inlet was used. As described in Chapters 3 and 4, an isothermal model with the same diameter and a finer mesh produced a developed flow at the outlet, and thus the velocity profiles and turbulent parameters obtained were mapped into the inlet of the CHT module. This pre-model could use a different turbulence model and any pipe length as long as the

pipe diameter was the same compared to the heated pipe and the boundary layer was developed at the outlet.

The following step was the ramped technique employed in Chapters 3 and 4 for the thermal boundary condition, progressively increasing the temperature and using the results as initial conditions for the following simulation.

5.3.4. Material properties and implementation

The materials involved in the simulations were the same as those selected in Chapter 4, i.e. water at 300 bar for the fluid domain and Inconel 625 for the solid domain. Because of the physics related to CHT, Comsol forced the implementation of those properties from both materials relevant to the physics to compute, namely density, thermal conductivity, heat capacity and dynamic viscosity. They were defined as functions of temperature in a range of values wide enough to safely contain all the working temperatures defined in the boundary conditions. As previously described in Chapter 3, water was considered at isobaric conditions due to the small pressure drops and because the thermodynamic properties are weak functions of pressure.

Due to the high temperatures employed in the present study, the material properties of water at 300 bar, defined as a function of temperature, were obtained from several sources. From the inlet temperatures to 1000°C, the NIST database (Lemmon *et al.,* 2015) was employed as in Chapters 3 and 4, while the material data was collected

from Wagner *et al.* (2008) from 1000° to 2000°C. However, from 2000° to 2200°C the property functions were implemented using trend lines (extrapolation).

5.3.5. Mesh distribution and solver performance

Details about mesh characteristics and solver performance for the computations using the two selected values of T_∞ are presented in Table 5.4. As can be observed, it was the most demanding computation among the chapters undertaking simulation cases. As a consequence, first-order discretisation was used. The solver technique was similar as in Chapters 3 and 4, although due to the strong turbulence and intense heating, the segregated groups including the partial differential equations (PDEs) employed modified damping factors in order to gain stability.

Table 5.4 Mesh characteristics and solver performance

Residual error	DOF	Solid elements	Fluid elements	Memory [GB] (physical/virtual)	Solution time [h]
$1x10^{-3}$	$7.5x10^{6}$	$2x10^{5}$	$1.2x10^{6}$	30.7/38.4	5.5

The 2D mesh was implemented using a coarse free triangular distribution in the solid domain as a means to save computational power, as seen in Figure 5.3a. For the fluid domain, a method to simplify the mesh was approached as in Chapter 4, by which the boundary layer was not defined as such using the node offered by the program applying a stretch factor. Instead, a mapped mesh (quadrilateral elements) was displayed and refined close to the wall by manual selection. The radial mesh was composed of 30 elements applying a distribution method to refine the mesh near

the wall. The axial mesh was composed of 40,000 elements with a refinement sequence towards the outlet, as seen in Figure 5.3b, in order to improve the mesh performance near the hottest sections of the system.

(a)

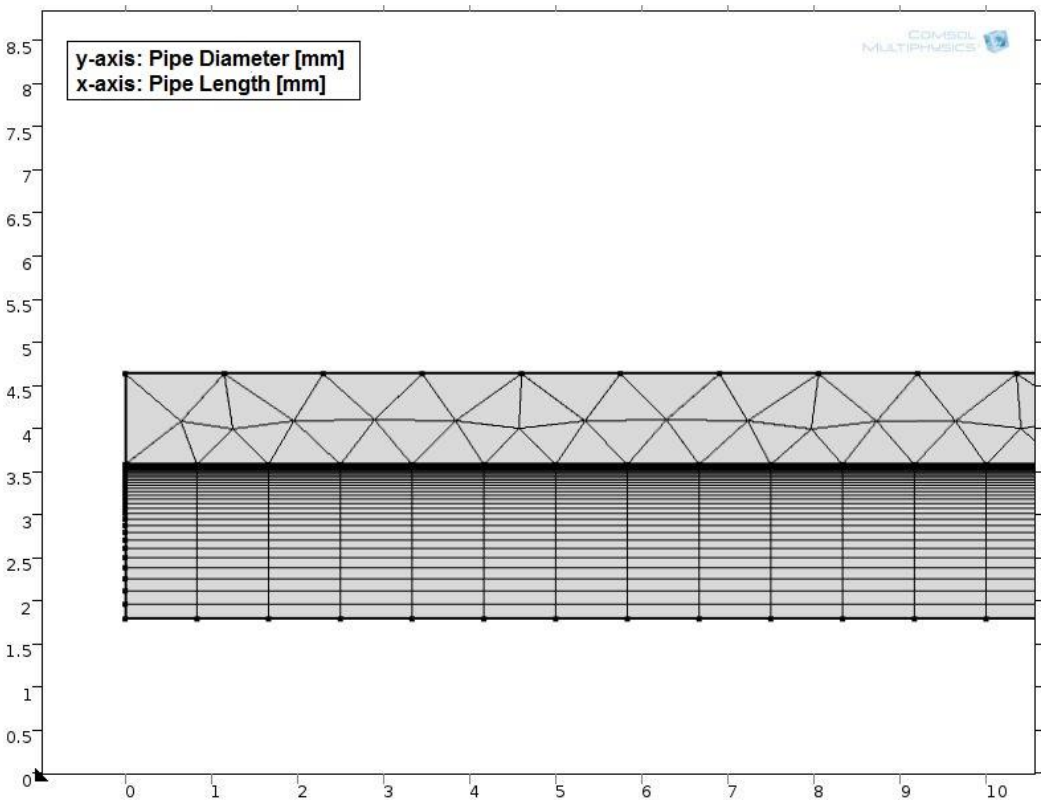

(b)

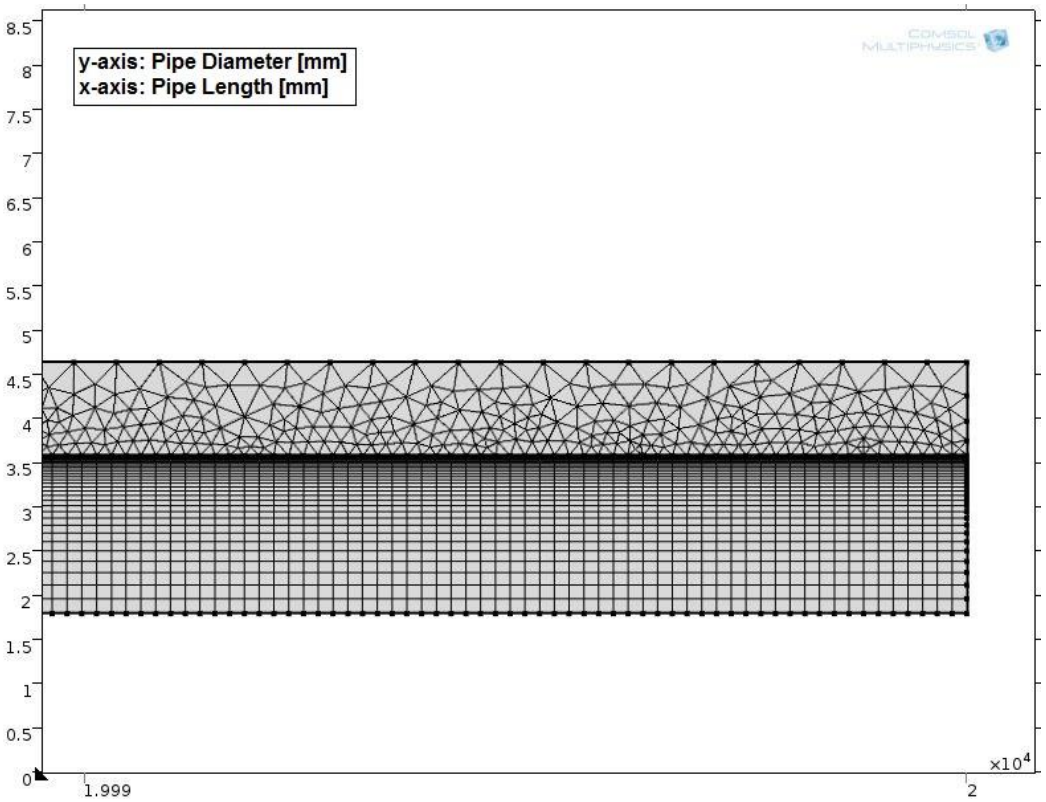

Figure 5.3 Mesh at inlet (a) and outlet (b) sections for solid and fluid domains (axes in *mm*)

The Law of the Wall described in the Appendix reflected the fact that the value of G has a strong impact in the calculation of the distance of the first layer to the wall (y_1^+), through the flow velocity component. Thus, the larger the value of G, the higher the y_1^+ produced and as a consequence the accuracy of the quantitative results was negatively affected. In order to keep a low value of y_1^+, the first layer could be located closer to the wall, however this would increase the computational time as the phenomena occurring near the wall would be captured in higher detail. There are three main features that will determine the accuracy and computational time when computing turbulent convective heat transfer; namely (1) the mesh refinement expressed by the number of degrees of freedom (DOF), (2) the discretisation order and (3) wall the value of y_1^+.

In Chapter 3, the mesh near the wall presented a considerable wall refinement (y_1^+ values below 1) while G had a value of 1,260 kg m^{-2} s^{-1}. In Chapter 4, the first layer next to the wall was located further away, but the value of G was only 200 kg m^{-2} s^{-1} and thus the values of y_1^+ remained below 4-5. In the present study, the mesh had a finer radial distribution compared to the 2D simulation employed in Chapter 4; with 30 radial elements over an internal radius of 1.79 *mm* compared to 40 radial elements over an internal radius of 5 *mm*, respectively. Nevertheless, the large value of G used (5,684 kg m^{-2} s^{-1}) produced values of y_1^+ around 25. An attempt to decrease the value of y_1^+ was performed by relocating the first layer closer to the wall, but the computational time escalated prohibitively for a ramped technique. Therefore, efforts were made to keep y_1^+ in the log-law region, away from the buffer zone (values of y_1^+ between 5 and 15), where the Law of the Wall could not be applied as explained in the Appendix. As a consequence of the resulting value of y_1^+, the approach of the present study was more qualitative rather than quantitative.

5.4. Results and discussion

5.4.1. Study of axial profiles

In order to observe the trends of the HTC and the effects of the thermophysical property changes, buoyancy and thermal acceleration on the heat transfer behaviour, the results from the two computations using different values of T_∞ were firstly analysed along the axial length. It is worth highlighting that, as a result of the existing computational limitations, the investigation was focused on qualitatively capturing the main trends, rather than performing a quantitative study.

Specific phenomena affecting the system were captured, as in Chapter 3, by applying different Nusselt numbers (Nu) displayed as a series of ratios for comparison (henceforth expressed as *Nu ratios*). To this purpose, and in addition to the simulations results, the empirical correlations by Dittus-Boelter (Winterton, 1998) and Mokry *et al.* (2011), henceforth named as DB and Mokry correlations respectively, were selected. The Nu values from the Mokry correlation were meant to account for the large property changes occurring at supercritical conditions by comparing them to the Nu values obtained from the DB correlation for subcritical systems. It is worth noting that as a consequence of the subcritical approach, the Nu or HTC values obtained from the DB correlation were only valid within the normal heat transfer regime (NHT), i.e. away from the peaks produced in the HTC during the PSC transition. At the same time, the Nu values from the computation were compared to the Nu values from the Mokry correlation in order to reveal possible

buoyancy or thermal acceleration effects, considering the Mokry correlation was produced at forced-convective conditions in absence of heat transfer deterioration (HTD).

Similarly, it was acknowledged that, differently from Chapters 3 and 4, the boundary conditions in the present study belonged to scaled hydrothermal conditions considered extreme and unfeasible from an experimental point of view. Thus, both correlations were applied at conditions considerably far from the working condition ranges they were created for. For this reason and in addition to the computational limitations in terms of mesh performance, the resulting quantitative values of HTC or Nu ratios involving such correlations and the computational results were not assessed as such. Instead, their purpose in the present study was devoted to the comprehension of the system performance by obtaining the qualitative trends of the different phenomena.

The different Nu ratios were plotted against certain dimensionless parameters that affected supercritical heat transfer (SCHT); namely property changes (π_c) buoyancy (Bo) and thermal acceleration (K_v). Considering the thermal boundary condition was expressed as a convective heat flux and not as a temperature, the formulae to obtain the aforementioned parameters were the same as those employed in Chapters 3 and 4. The results for the simulation at a chamber temperature of 1000°C were presented in Figure 5.4, showing the HTC values obtained using the computational results and both empirical correlations. The HTC values from the computation (HTC Comsol) revealed a sharp peak produced slightly upstream the point where the bulk of the

flow achieved the pseudocritical (PSC) temperature (401.9°C), at a dimensionless heated pipe length (x/D) of 800 approximately.

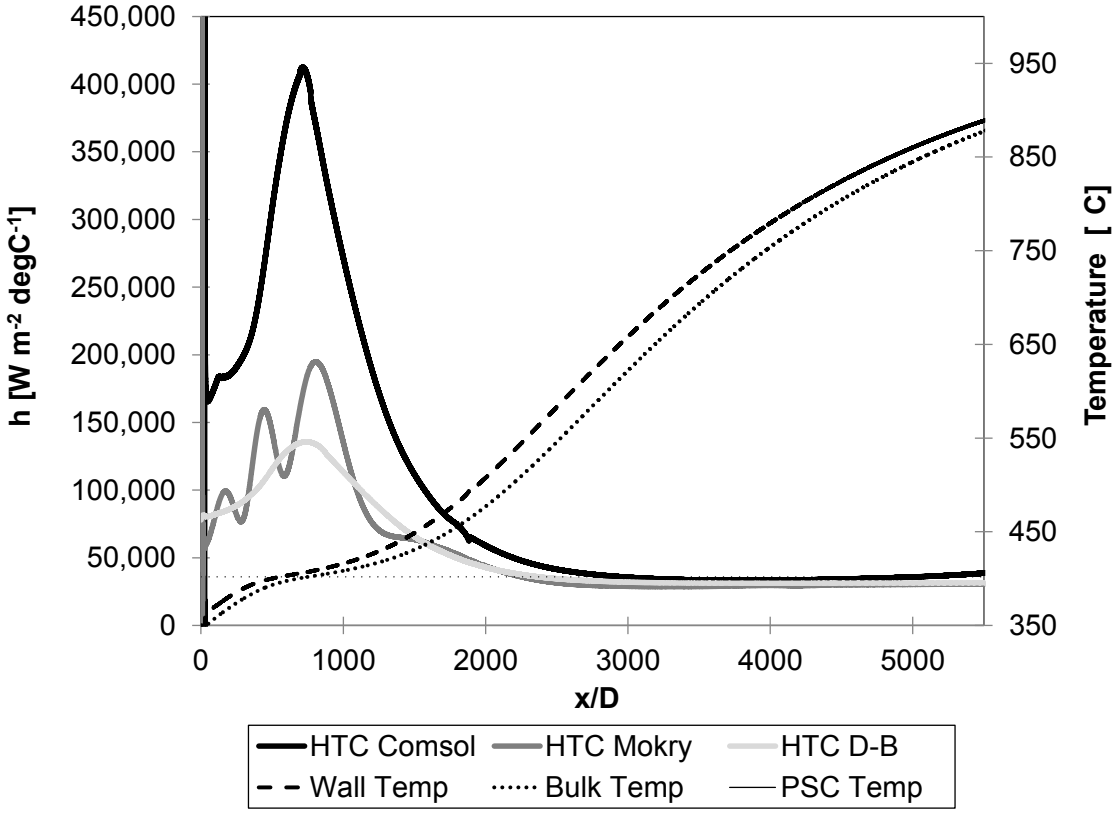

Figure 5.4 HTCs from computation and correlations, with wall-bulk temperatures (chamber at a T_∞ of 1000°C)

The Mokry correlation captured this HTC peak as well, although as expected the values obtained were much smaller than the computation values due to the extreme working conditions that nullified their quantitative interpretation. The DB correlation also experienced this peak at the same axial location, but in this case the quantitative value was damaged by the working conditions and also due to the inability to accurately predict away from the NHT regime, which is recovered from a x/D of approximately 3000 onwards. In fact, from that point on the three values of HTC converged, and thus the flow had negligible influence of property changes, buoyancy

or thermal acceleration as it was completely governed by forced convection. As a consequence, from that point on the condition of applicability of the similarity equations was satisfied (Jackson, 2013), and was achieved due to the relatively small pipe diameter and the high value of G.

(a)

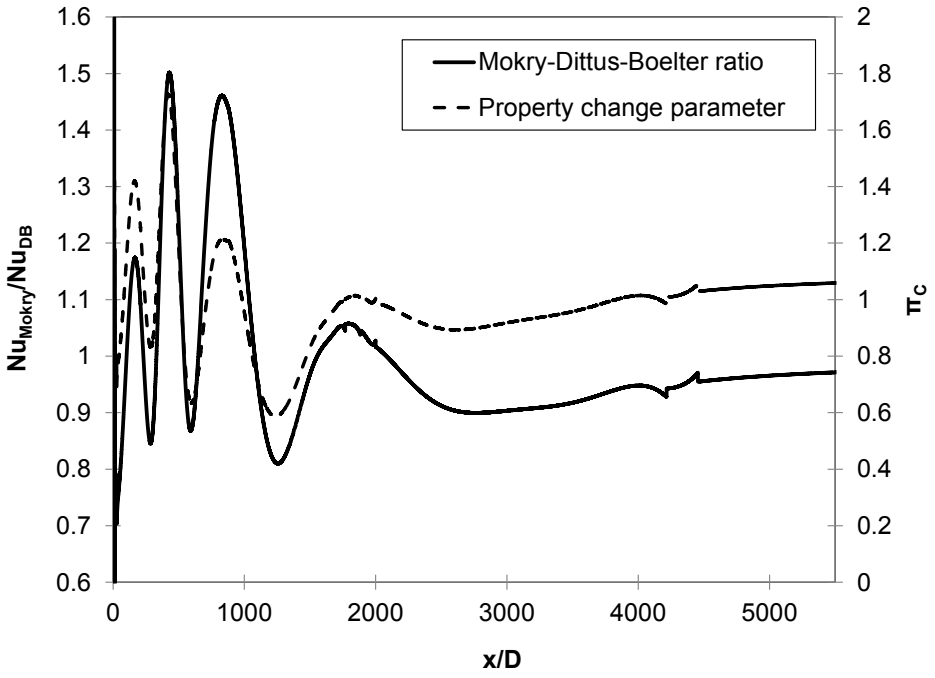

(b)

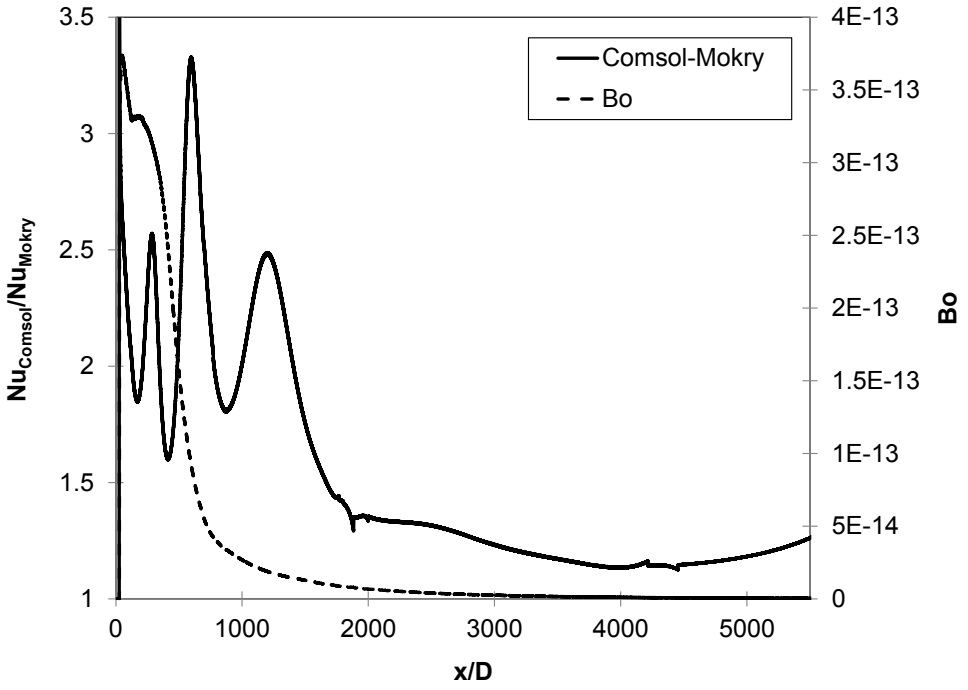

(c)

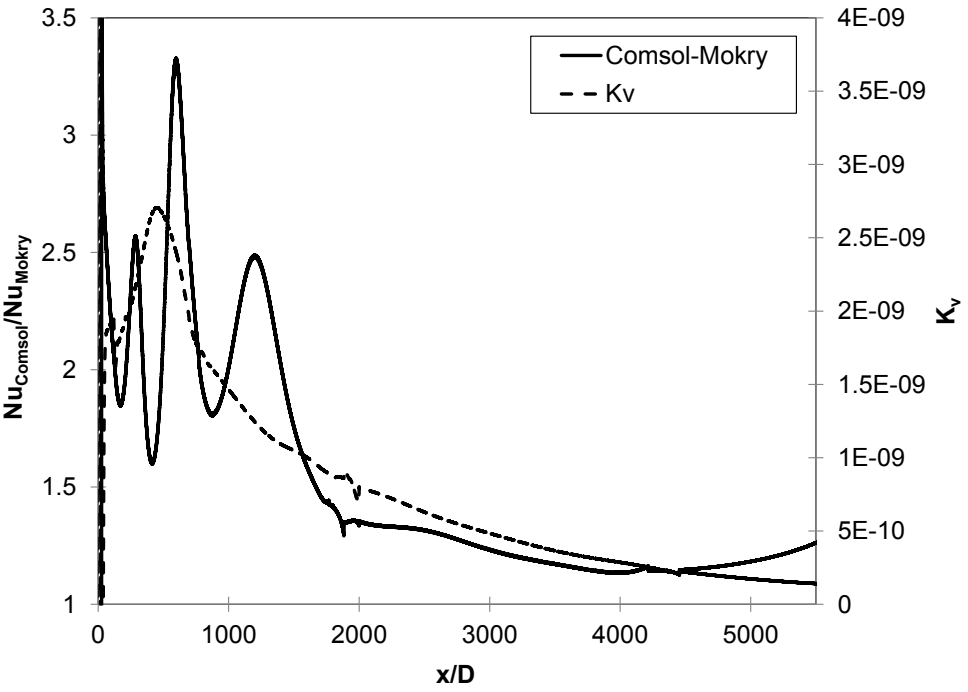

Figure 5.5 Effects of property changes (a), buoyancy (b) and acceleration (c) for chamber at a T_∞ of 1000°C

Figure 5.5a shows that the relation between Nu ratio expressing the extent of property changes (Nu_{Mokry}/Nu_{DB}) and the property change parameter was strong due to their similar profile. Buoyancy and thermal acceleration effects were triggered

before the bulk temperature reached the PSC value; and even though the relation between the Nu ratios and the respective parameters is not accurate, the overall trend is maintained as shown in Figure 5.5b and c. As explained in Chapter 3, simulating 2D geometries of horizontal systems involving SCHT phenomena in the presence of buoyancy effects would produce misleading results due to the unrealistic computation of gravity. However, it was confirmed that gravity had no effect on the overall performance of the present computations as inclining the pipe from 90° (vertically upwards) to almost a horizontal direction did not produce tangible differences (not represented due to the identical results obtained).

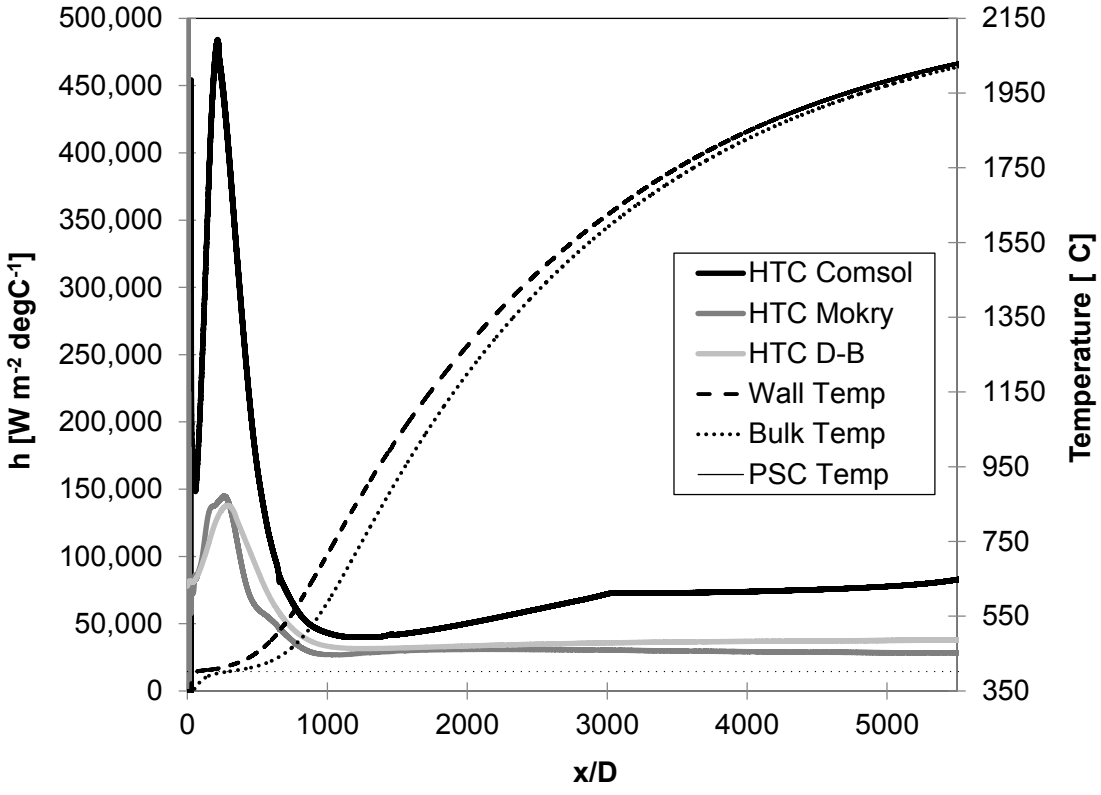

Figure 5.6 HTCs from computation and correlations, with wall-bulk temperatures (chamber at a T_∞ of 2200°C)

When the chamber temperature was increased to 2200°C, the results obtained were different but the heat flux-mass flux ratio was still not large enough to induce gravitational effects in the flow. 2D simulations with inclined angle did not show remarkable differences either. The values of the different HTC are depicted in Figure 5.6. As expected, when comparing the results to the simulation at a T_∞ of 1000°C, the PSC temperature was achieved in the bulk of the flow more upstream and closer to the flow inlet. The HTC peak from the simulation (HTC Comsol) was larger than the one produced at 1000°C, shown in Figure 5.4. Also, from x/D=1000 onwards the computed HTC smoothly increased again downstream a sharp drop triggered after the peak, which was due to a slight recovery of the thermal conductivity (k) in a similar fashion at such temperature range, represented in Figure 5.7.

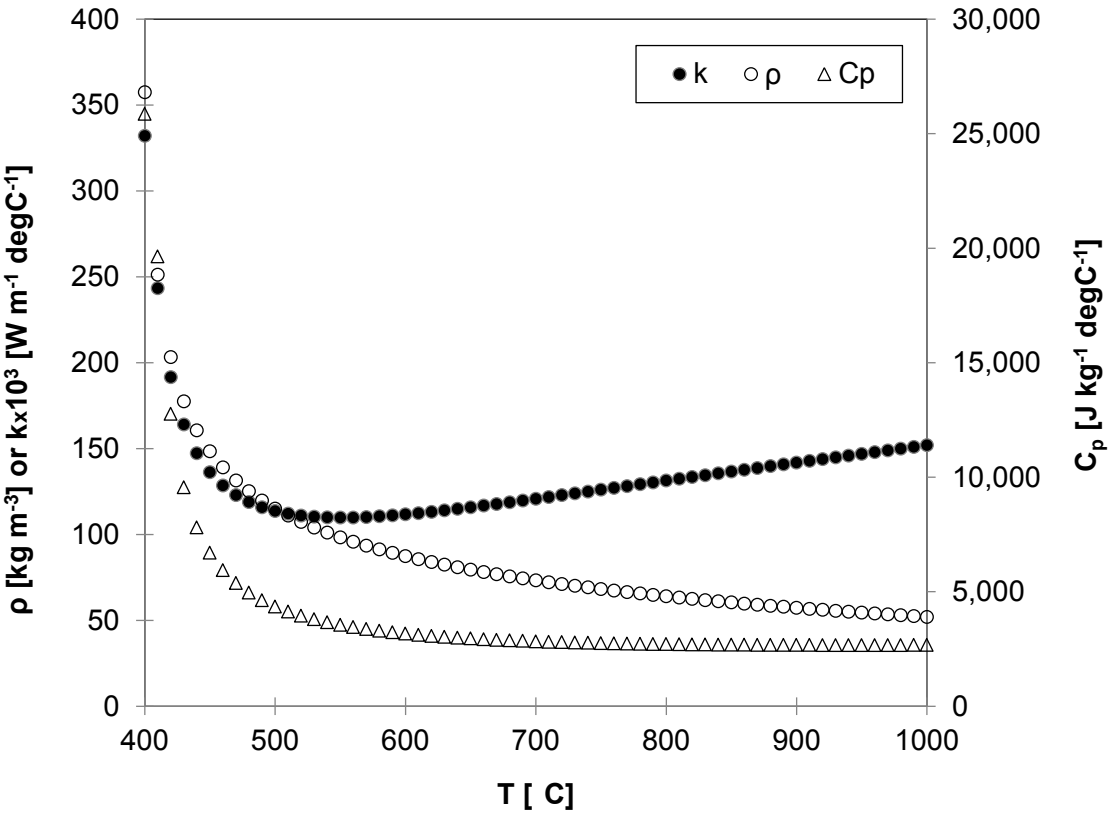

Figure 5.7 Isobaric temperature dependence (300 bar) of thermodynamic properties related to thermal diffusivity after surpassing the PSC point (Lemmon *et al.*, 2015)

The steeper drop at 2200°C in the HTC after the peak was achieved occurred due to a stronger presence of thermal acceleration (u_x), as shown in Figure 5.8a. This influence of u_x downstream the HTC peak was not predicted by the K_v parameter in none of the two computations; thus u_x as a local parameter is revealed as a better choice to represent flow acceleration than K_v. On the other hand, the values of HTC obtained from the two correlations using a T_∞ at 2200°C revealed a contradiction, being smaller than those at a T_∞ of 1000°C despite their good prediction of the peak location (see Figure 5.8b). This was related to the extreme temperatures computed, so the mesh performance and the applicability of such correlations were more limited employing a T_∞ at 2200°C. However, and as previously stated at the beginning of this chapter, this is a study focused on qualitative trends rather than quantitative values.

(a)

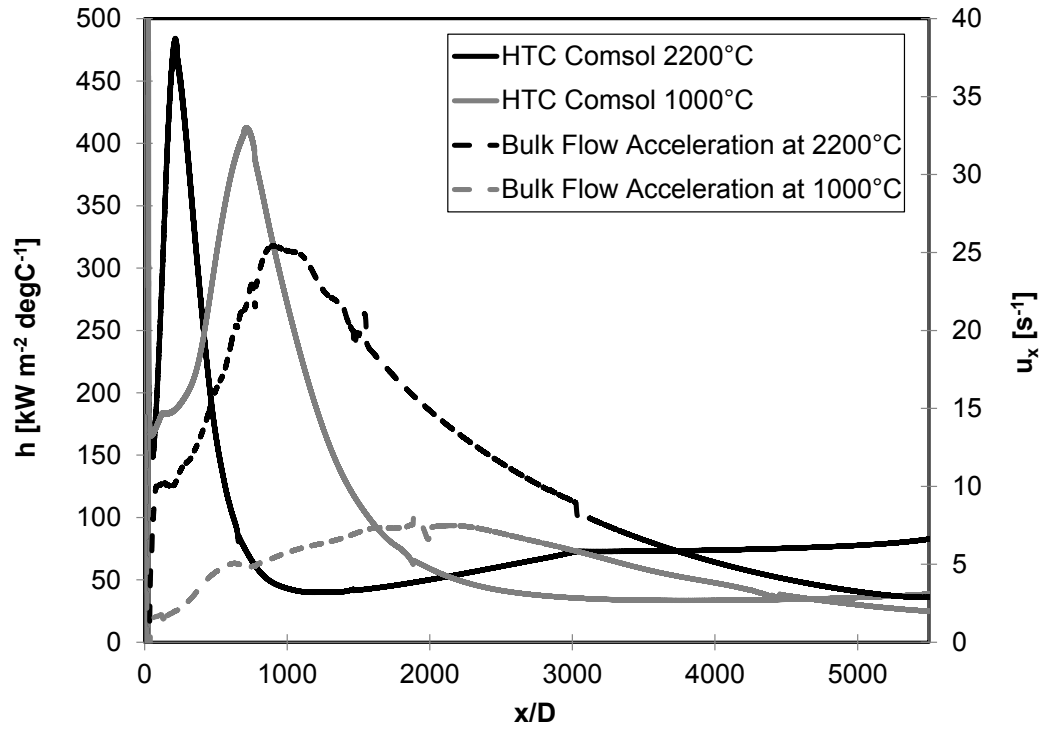

(b)

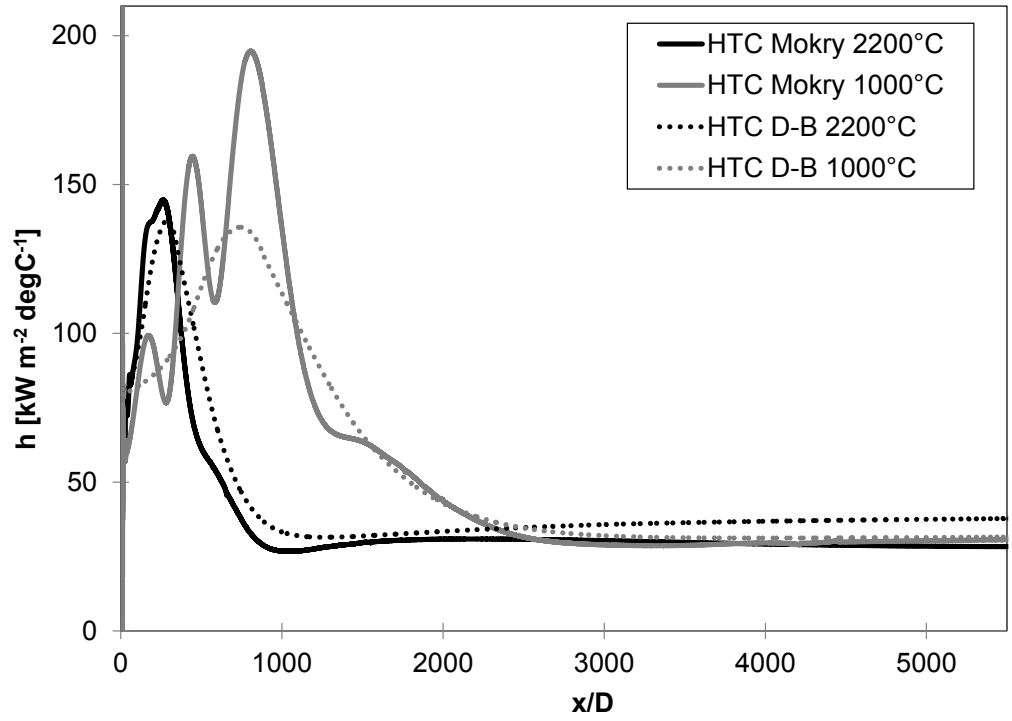

Figure 5.8 Values of HTC at T_∞=1000° and 2200°C from simulation and plotting u_x (a) and only from correlations (b)

With respect to the effect of the SCHT parameters on Nu ratios at a T_∞ of 2200°C, they revealed the same trends compared to the previous simulation at a T_∞ of 1000°C. A strong dependence of Nu ratio towards the property changes was also observed. The buoyancy and thermal acceleration parameters were not relevant enough to induce visible changes in the heat transfer performance, despite their increased effect at a higher heat flux-mass flux ratios as seen in Figure 5.9. Nevertheless, it can be concluded again that plotting u_x is a better technique to evaluate the thermal acceleration at local positions, while K_v represents the behaviour of the whole flow.

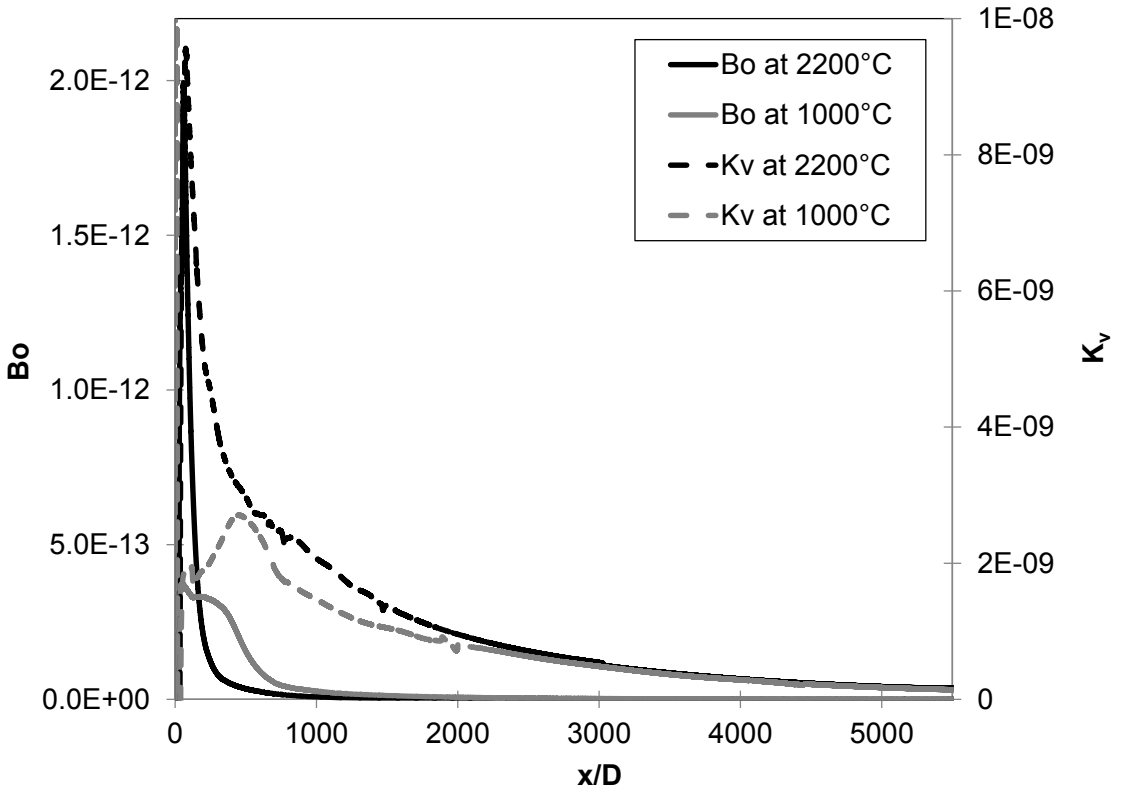

Figure 5.9 Buoyancy and acceleration parameters along the pipe at different temperatures

On the other hand, when depicting the parameter π_c for both simulations (Figure 5.10), it can be seen that they had very similar values despite the different thermal conditions applied. This was due to the simplicity of the formula to calculate this parameter, relying only on enthalpy and heat capacity, and thus being limited to a qualitative approach rather than to quantitative for comparison purposes between systems using different values of T_∞. For the two cases large property changes were observed during the PSC transition and downstream this point their magnitude stabilised.

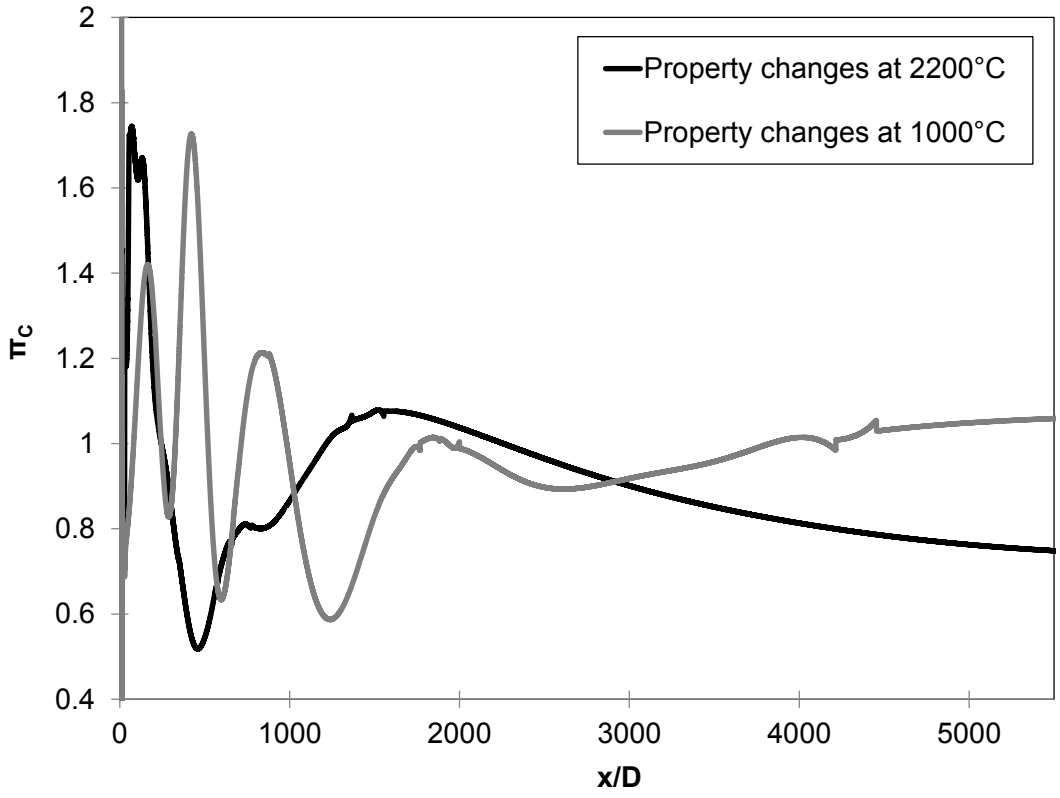

Figure 5.10 π_c for both simulations at T_∞=1000° and 2200°C

Once all the parameters commonly employed in SCHT studies at both temperatures have been investigated, it was concluded that buoyancy only affected the system at

the pipe inlet and quickly dissipated downstream, while the thermal acceleration effect extended until approximately x/D=2500 as Figure 5.8a suggested. Moreover, HTC peaks were observed in the entrance region, so no HTD was triggered due to the aforementioned phenomena. On the other hand, property changes dictated the performance of the system during the PSC transition.

5.4.2. Study of radial profiles

The axial studies were compared to a radial analysis of the flow at specific locations by employing hydrodynamic parameters for the study of turbulence, such as turbulent shear stress (τ_{turb}), turbulence intensity (I), u_x and the radial gradient of velocity (u_y). Also, thermal parameters were selected for the study of heat transfer such as momentum diffusivity (ν) and thermal diffusivity (α). The equations defining all the aforementioned parameters were appropriately described in Chapter 3 and their units displayed on the nomenclature section.

The radial locations were selected with the feedback from the former axial analysis at both furnace temperatures, thus the first point was located relatively close to the pipe inlet (x/D=279), also in order to account for HTC peak at a T_∞ of 2200°C. The second location was placed nearby the HTC peak obtained by the simulation at a T_∞ of 1000°C (x/D=838). The remaining radial locations were studied in the middle section of the pipe (x/D=2793) and near the outlet (x/D=5028). For the simulation at a T_∞ of 1000°C, the parameters selected to investigate the presence of turbulence are shown in Figure 5.11 and Figure 5.12.

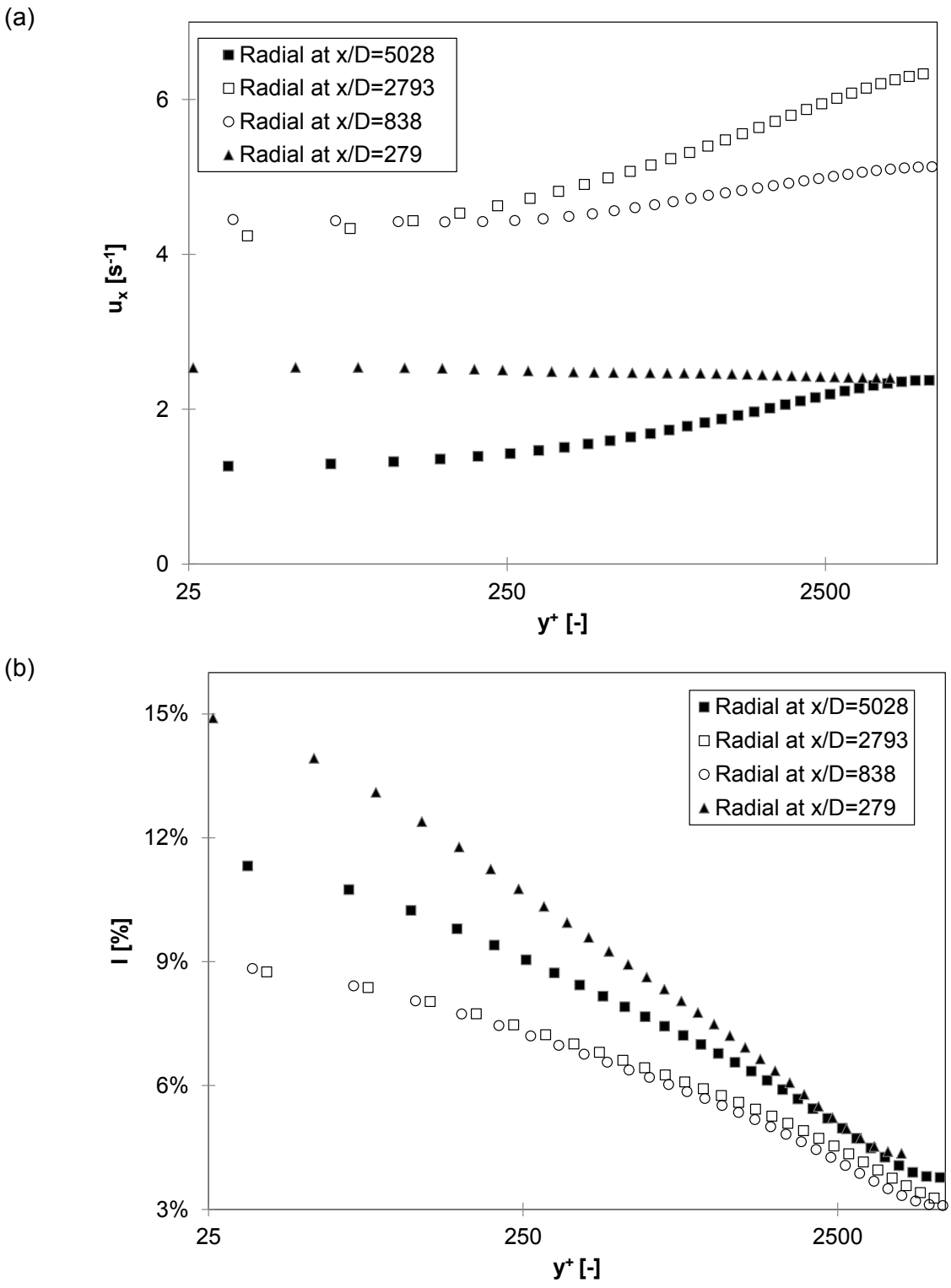

Figure 5.11 Radial profiles of velocity axial increase (a) and turbulence intensity (b) at a T_∞ of 1000°C

Figure 5.11a depicted lower acceleration near the inlet and outlet areas, and thus these areas reported better turbulence (Figure 5.11b). Near the entrance, at x/D= 279, the flow had not begun to accelerate and laminarise yet, but turbulence was produced near the wall due to the inlet effect triggered by the heat source combined with the proximity of the large property variation (LPV) region near the inlet at the bulk of the flow. At x/D=5028 the turbulent intensity was recovered again along with loss of flow acceleration produced downstream the middle section, where the flow had accelerated as a consequence of the bulk of the flow surpassing the PSC point.

Figure 5.12 shows how the u_y and τ_{turb} progressively increased along the pipe, favouring turbulence. These results agreed with Figure 5.11a where the outlet region (x/D=5028) showed good turbulent condition due to larger profile gradients while the inlet region reported flat profiles due to the high values of G employed and the developed inflow, reducing the velocity gradients and so the shear rates despite the proximity of the LPV region. This situation dissipated as the flow was laminarised along the flow, as seen in Figure 5.11a, showing larger acceleration gradients at the core near x/D=2793.

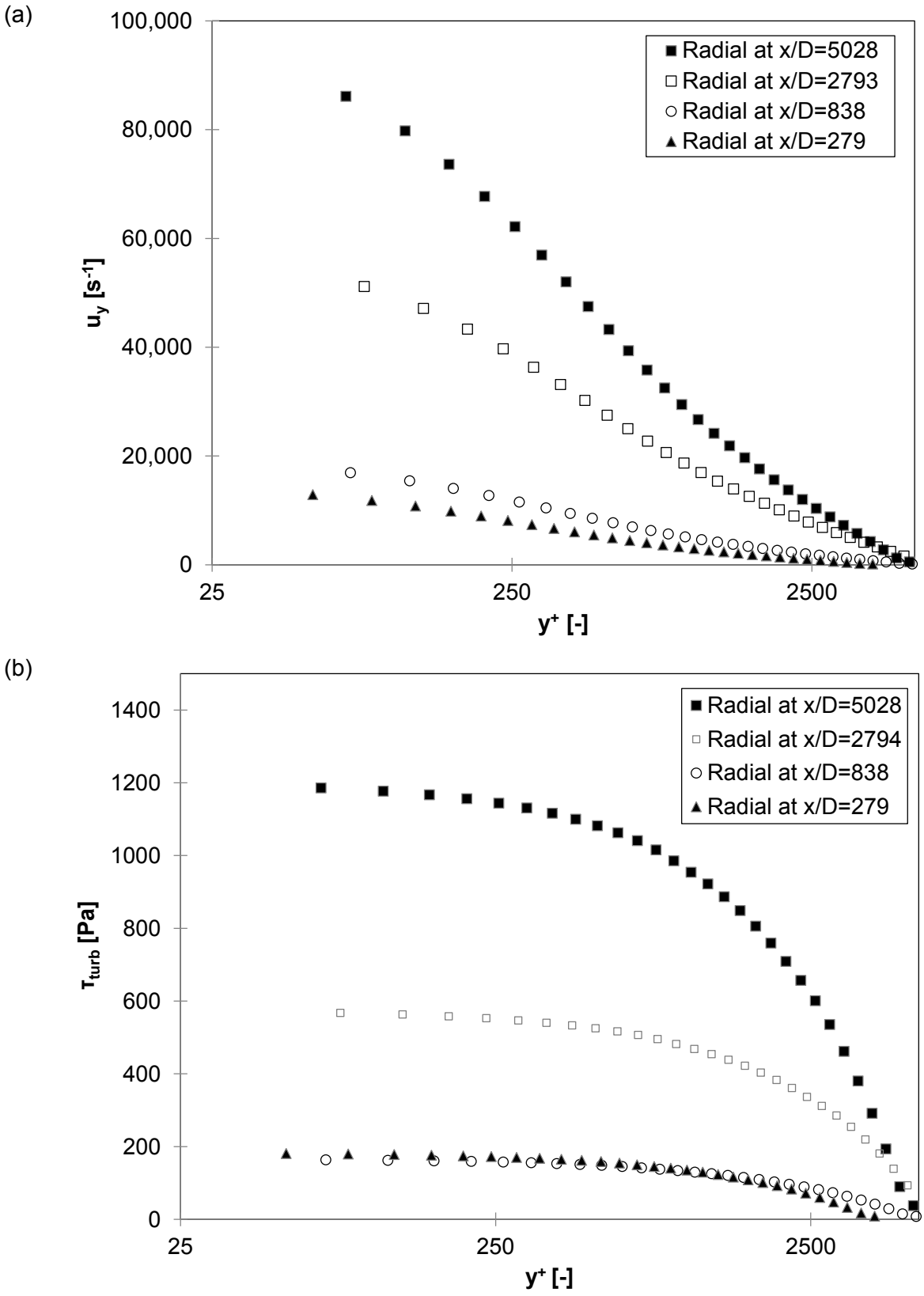

Figure 5.12 Radial profiles of u_y (a) and τ_{turb} (b) at a T_∞ of 1000°C

In order to fully understand the system performance, the hydrodynamic results were evaluated together with the thermal parameters, displayed in Figure 5.13. Both diffusivities (ν and α) showed an improvement for both the convective and conductive performance along the pipe respectively. This good thermal condition towards the end of the pipe and the recovery of turbulence in this region once thermal acceleration decreased triggered a slight increase in the HTC curve at the flow outlet. The only exception in this general performance was the value of α at the PSC transition, as seen on Figure 5.13b at x/D= 838. This drop was due to the increase of the heat capacity (C_p) which dramatically increased the amount of energy necessary to increase the fluid temperature, insulating the flow nearby in terms of temperature gradients.

(a)

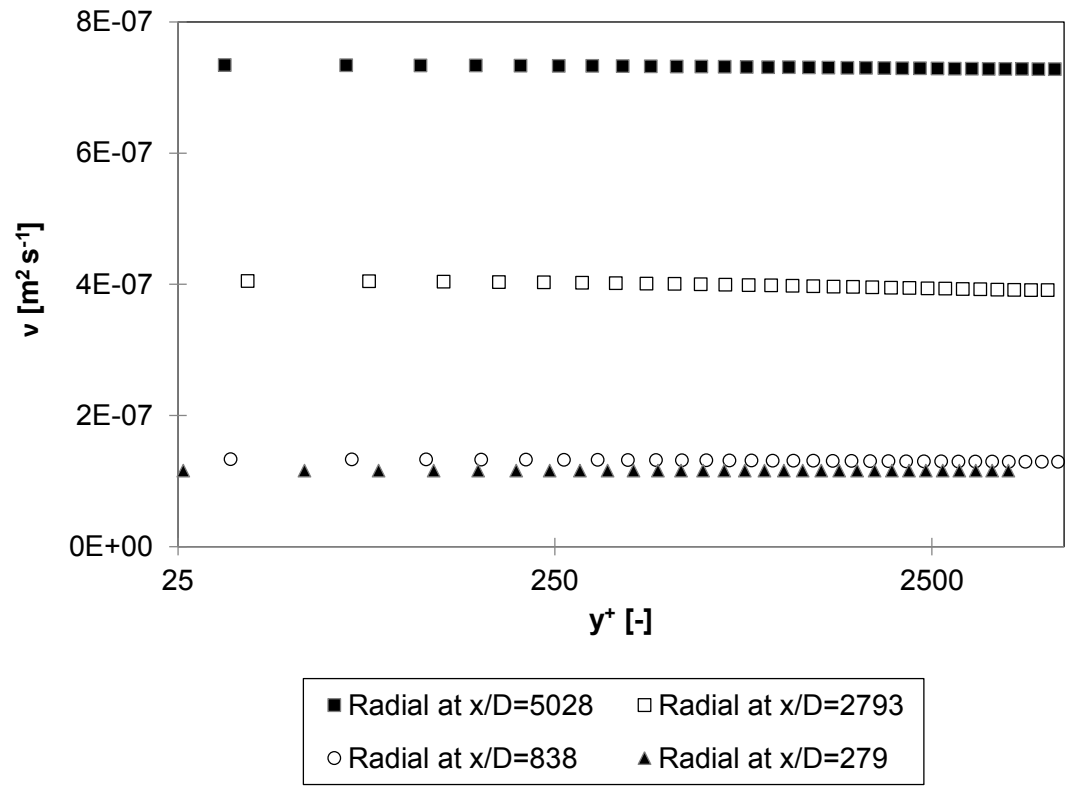

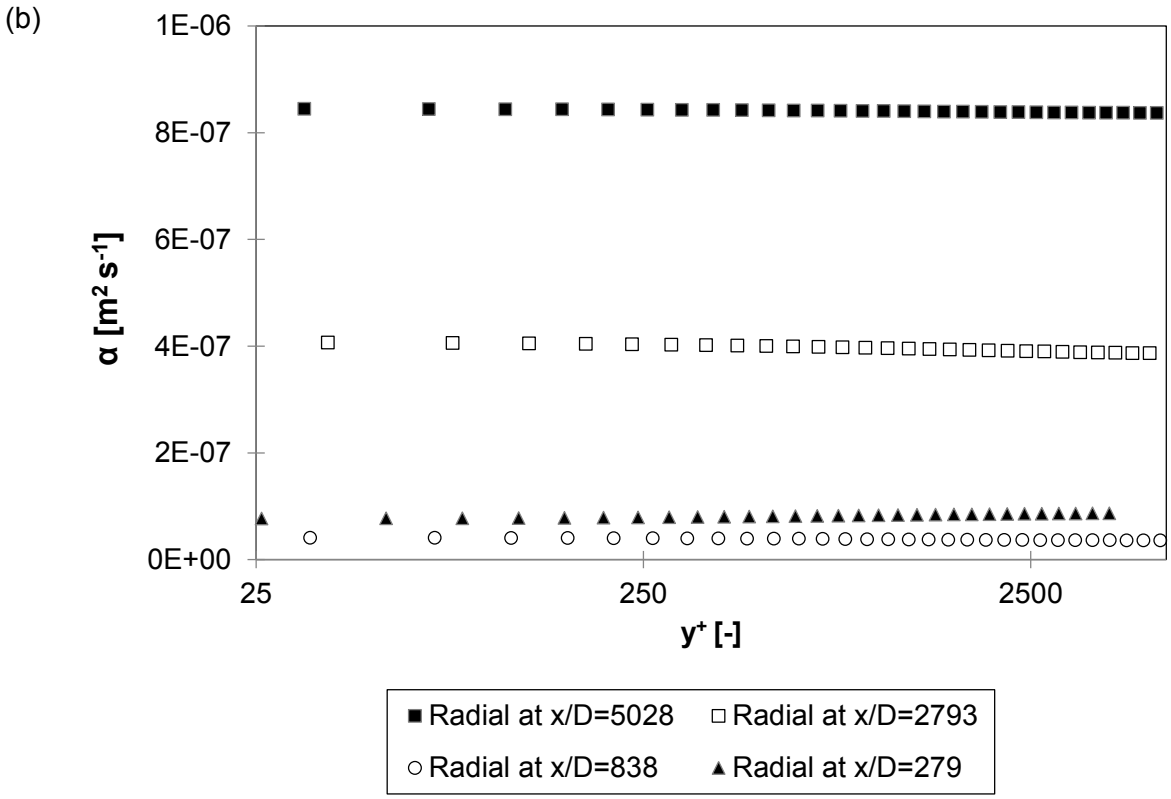

Figure 5.13 Radial profiles of ν (a) and α (b) at a T∞ of 1000°C

In order to observe the hydrothermal response of the system and if any kind of HTD was triggered, all the previous results were then compared to the computation at a T∞ of 2200°C. The results for the hydrodynamic parameters are shown in Figure 5.14. As can be observed in Figure 5.14a, the I of the system at a T∞ of 2200°C was much higher towards the end of the pipe than at a T∞ of 1000°C, almost doubling the percentage of intensity. On the other hand, the value of I had decreased considerably at the radial location near the inlet (x/D=279) because of the displacement of the HTC peak towards the entrance. At this radial location, the HTC peak had just been surpassed, thus thermal acceleration was peaking and heat transfer was deteriorated. This response was verified by the u_x profiles at a T∞ of 2200°C as displayed on Figure 5.14b, showing small values of u_x at the end of the pipe and a sharp increase at x/D=279 and 838 coinciding with the sharp drop of the HTC

downstream the peak. Figure 5.14c shows the τ_{turb}, which had considerably increased towards the end of the pipe, reflecting a good turbulent condition.

(a)

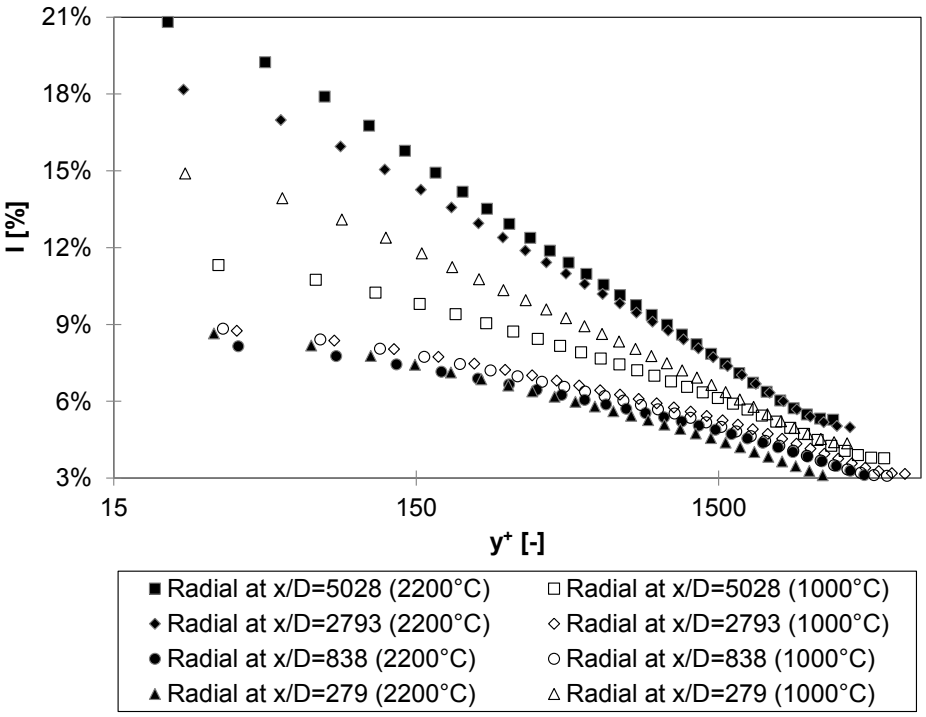

(b)

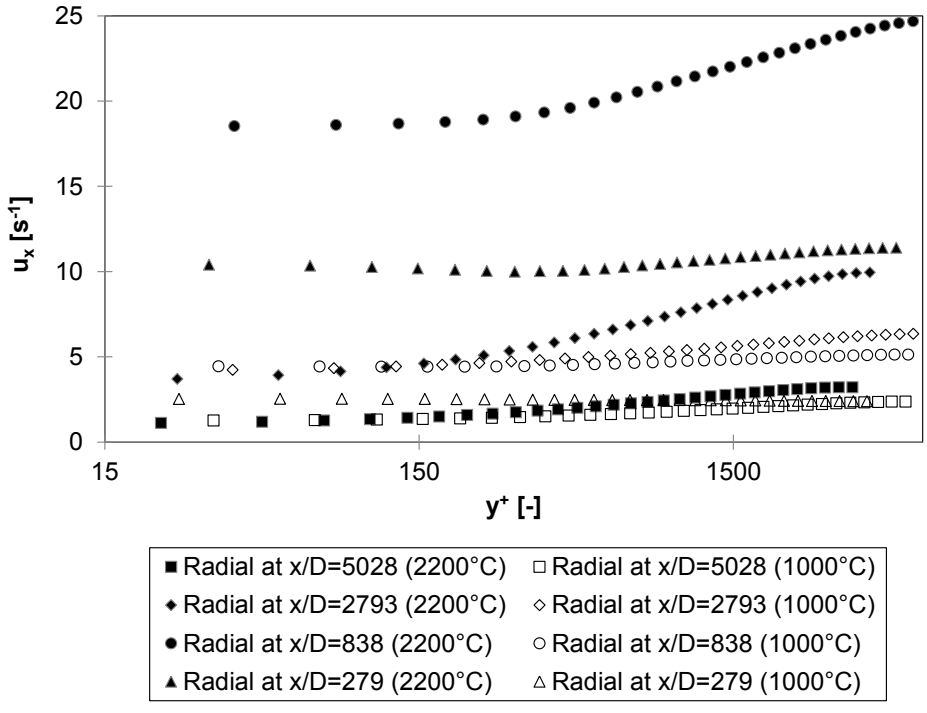

(c)

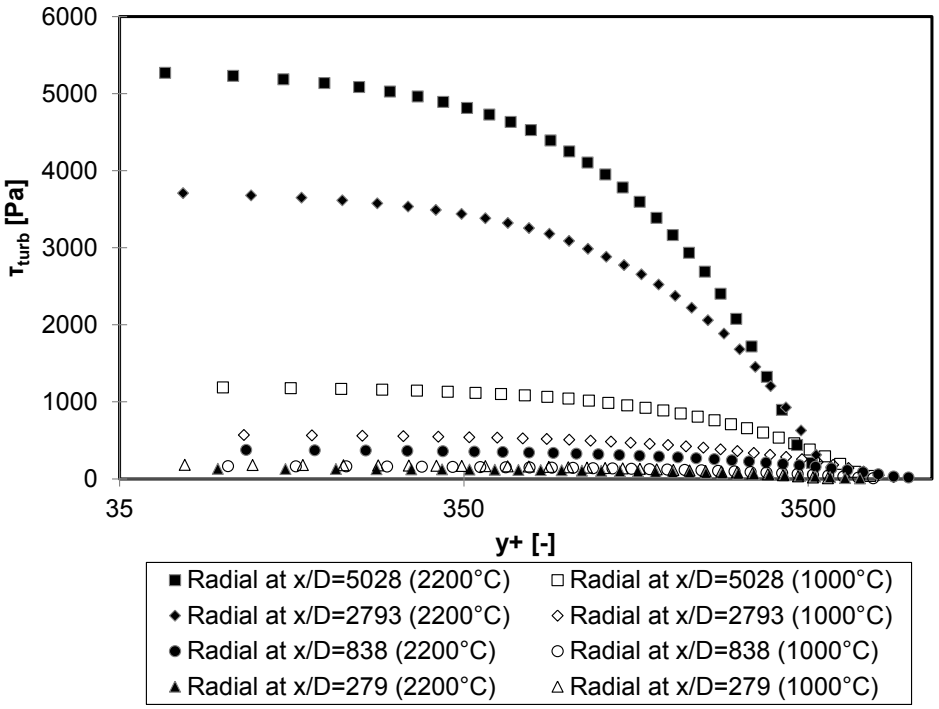

Figure 5.14 Comparison of radial profiles of I (a), u_x (b) and τ_{turb} (c) for the computations at a T_∞ of 1000° and 2200°C

The thermal parameters for the computation at a T_∞ of 2200°C are represented on Figure 5.15. Both diffusivities were much larger compared to the results obtained in the simulation at a T_∞ of 1000°C due lower values of density (ρ) achieved earlier upstream as a consequence of the stronger heat flux. This improved the convective heat transfer and the magnitudes of k, triggering a considerable recovery of the HTC downstream the drop from the PSC transition. Additionally, with higher values of temperature for the same G, the region of high C_p shrank and thus the thermal diffusivity in this area was impaired to a lesser extent.

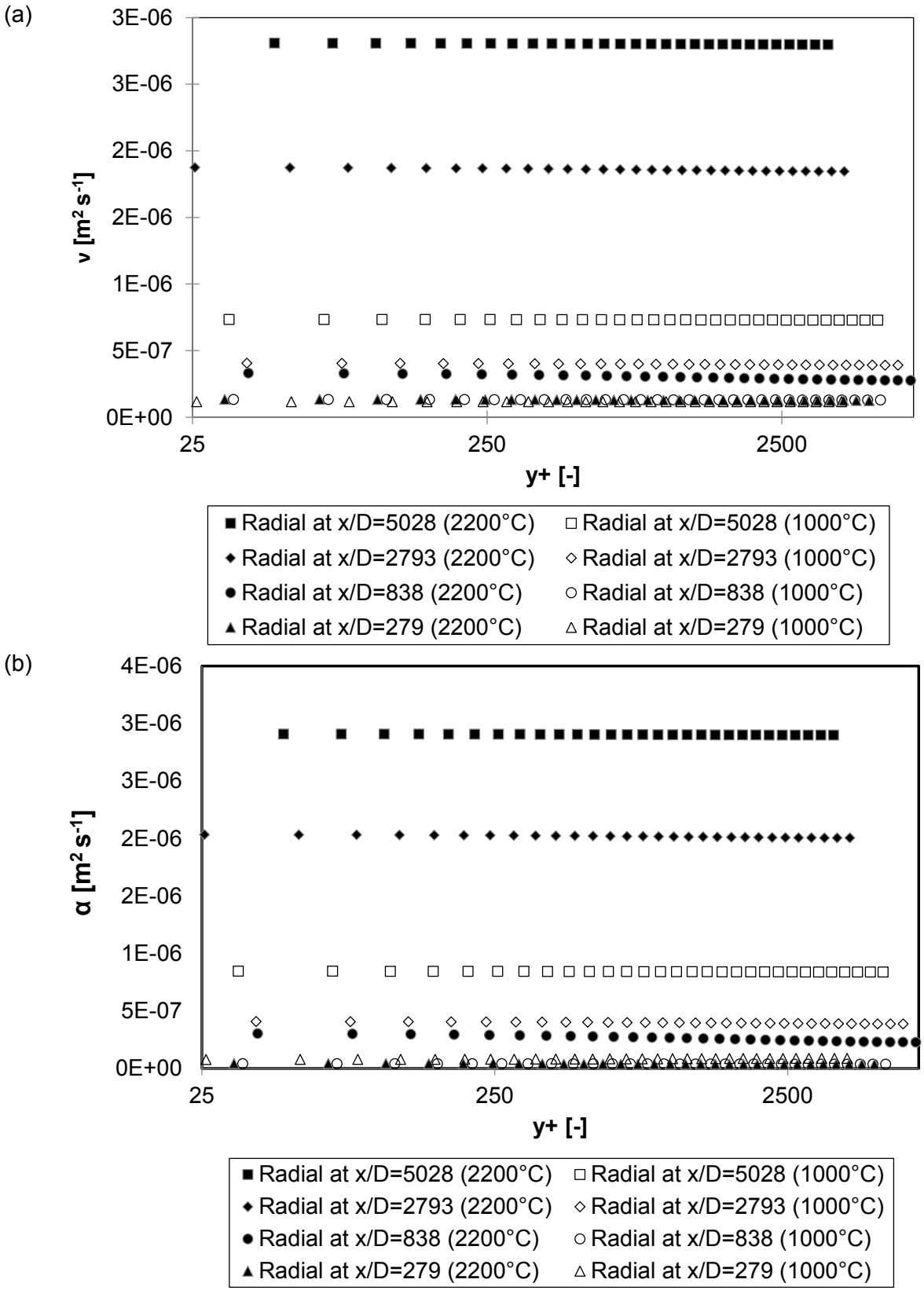

Figure 5.15 Radial profiles of ν (a) and α (b) for the computations at a T_∞ of 1000° and 2200°C

5.4.3. Study of 2D images

Several hydrodynamic parameters, obtained from the two computations at a T_∞ of 1000° and 2200°C, were postprocessed in 2D plots, as Figure 5.16 shows. For depiction convenience the fluid domain was represented with the L:D aspect ratio visually reduced to 1:1 for convenience. In every 2D plot the flow entered the pipe on the left edge of the geometry and the outlet was represented on the right edge, while the pipe wall was located at the top boundary and the bulk of the flow was at the bottom due to axial symmetry. Figure 5.16a and b reveal the G profiles at a T_∞ of 1000° and 2200°C, respectively. The profile at a T_∞ of 2200°C was slightly more laminarised towards the end of the pipe compared to the simulation at a T_∞ of 1000°C, as the G near the core was slightly higher and slightly lower near the wall. As can be observed near the inlet at the flow core of both computations, the G sharply decreased in this area upstream the point where the bulk flow reached the PSC temperature, which improved the turbulence and the respective HTC values. Downstream this area towards the outlet, the bulk velocity steadily increased while the ρ remained low, thus making the core recover high values of G again and turning the flow into a forced-convective regime. At these high values of G the velocity profile was considerably flattened at the pipe inlet and thus turbulence was higher near the wall, where the velocity gradients and thus the shear rates were larger as previously shown in the radial studies. In Figure 5.16c and d the values of I similarly reflected these phenomena, with stronger turbulence at the inlet and outlet regions. However, at a T_∞ of 2200°C the turbulence near the wall was larger towards the end of the pipe

because this area had smaller values of G compared to the core, while the outlet at a T_∞ of 1000°C had a more homogeneous profile.

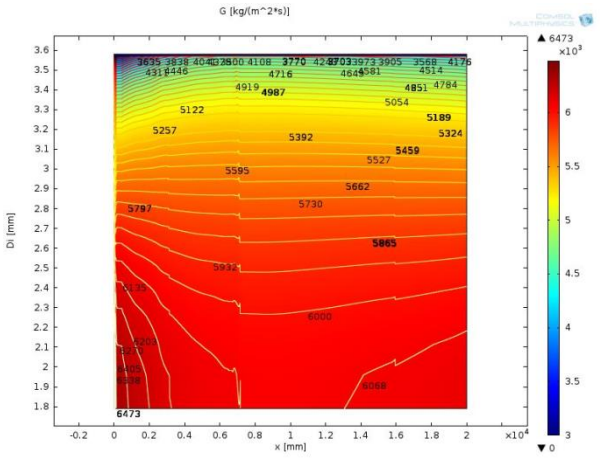

(a) G at a T_∞ of 1000°C

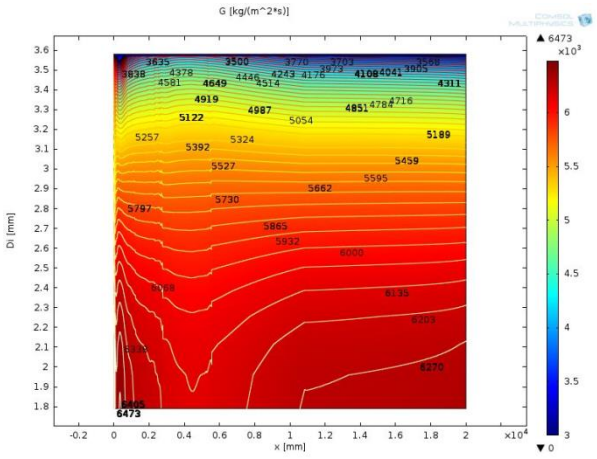

(b) G at a T_∞ of 2200°C

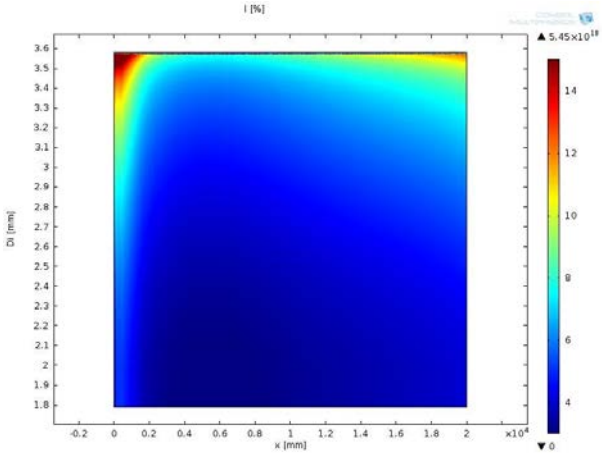

(c) I at a T_∞ of 1000°C

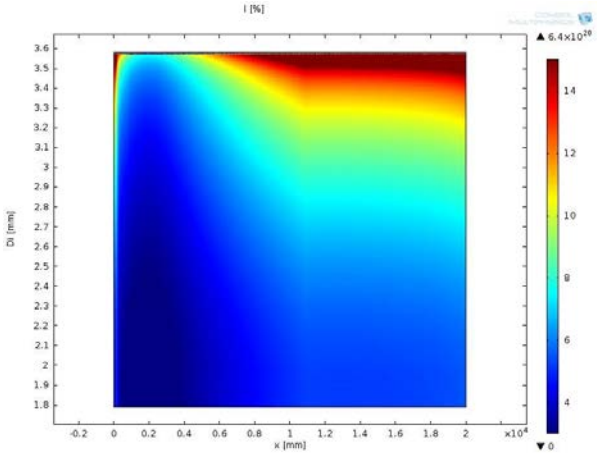

(d) I at a T_∞ of 2200°C

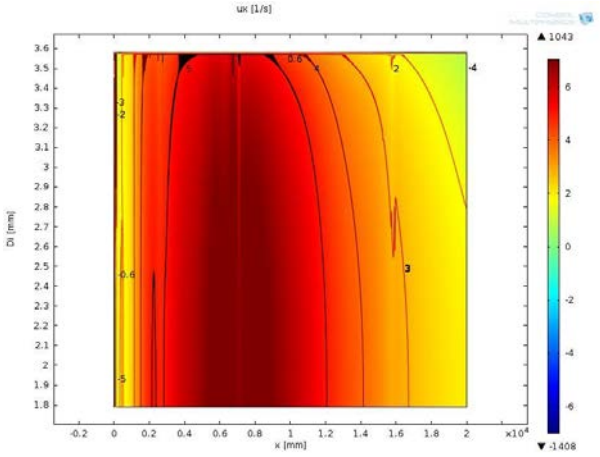

(e) u_x at a T_∞ of 1000°C

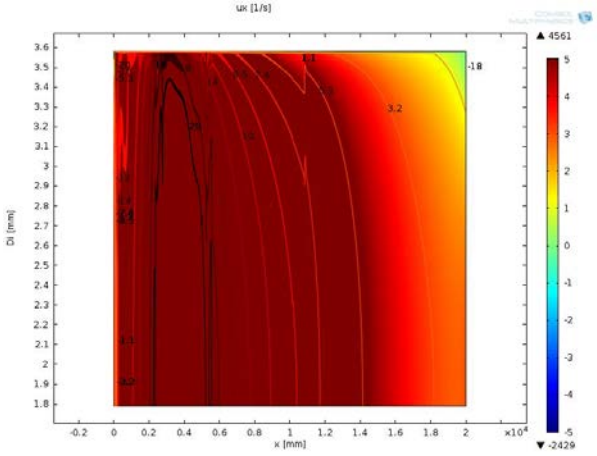

(f) u_x at a T_∞ of 2200°C

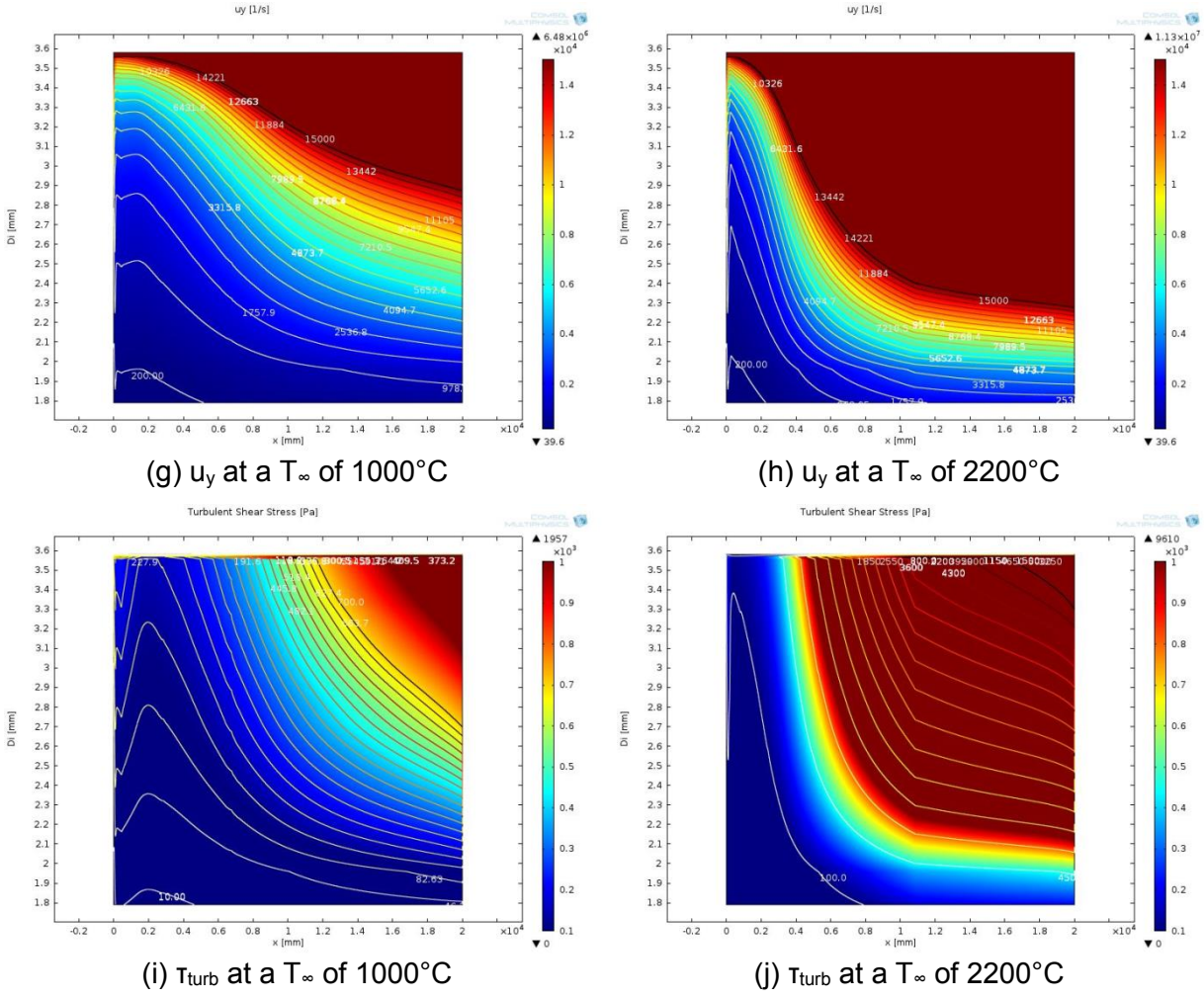

(g) u_y at a T_∞ of 1000°C

(h) u_y at a T_∞ of 2200°C

(i) τ_{turb} at a T_∞ of 1000°C

(j) τ_{turb} at a T_∞ of 2200°C

Figure 5.16 Postprocessed images of several hydrodynamic parameters

The aforementioned phenomena were verified by Figure 5.16e and f, depicting the values of u_x. The inlet and outlet regions displayed the lowest accelerations while the flow sharply accelerated downstream the location where the bulk reached the PSC point. The results at a T_∞ of 2200°C showed stronger acceleration due to higher extents of laminarisation triggered by the stronger heat flux. The postprocessed results of u_y (Figure 5.16g and h) and τ_{turb} (Figure 5.16i and j) confirmed these trends, displaying stronger turbulence due to shear near the wall and increasing towards the end of the pipe as a result of the laminarisation, which was stronger at a T_∞ of 2200°C.

Moreover, thermal performance was similarly postprocessed in 2D plots for the two simulation cases, as presented in Figure 5.17. The selected thermal parameters also reflected the influence of the high values of G, and thus Figure 5.17a and b depict almost flat radial profiles of C_p for the two working temperatures. The region displaying the highest values of C_p, or LPV region, was narrower and closer to the inlet at a T_∞ of 2200°C as a consequence of the stronger heat flux inducing an earlier, more violent transition of the thermophysical properties through the PSC point. Figure 5.17c and d describe the axial temperature gradients (T_x). As expected, in both cases the LPV region coincided with the lowest values of T_x due to higher energy required to increase the flow temperature in this region. Downstream the LPV region, the C_p and ρ decreased considerably, while the k smoothly increased as seen in Figure 5.7. As a consequence, the overall balance of these properties increased the value of α towards the end of the pipe, reducing the temperature gradients.

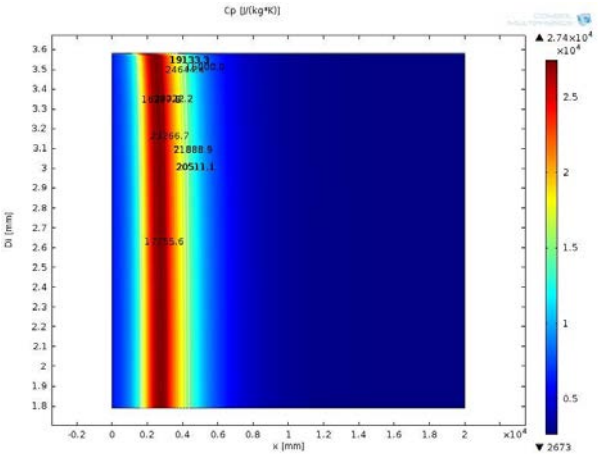

(a) C_p at a T_∞ of 1000°C

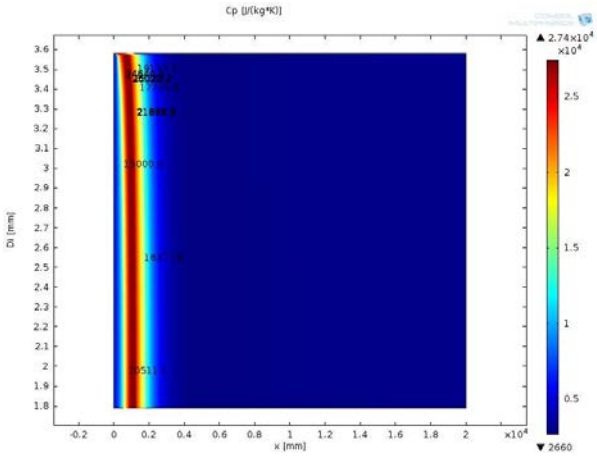

(b) C_p at a T_∞ of 2200°C

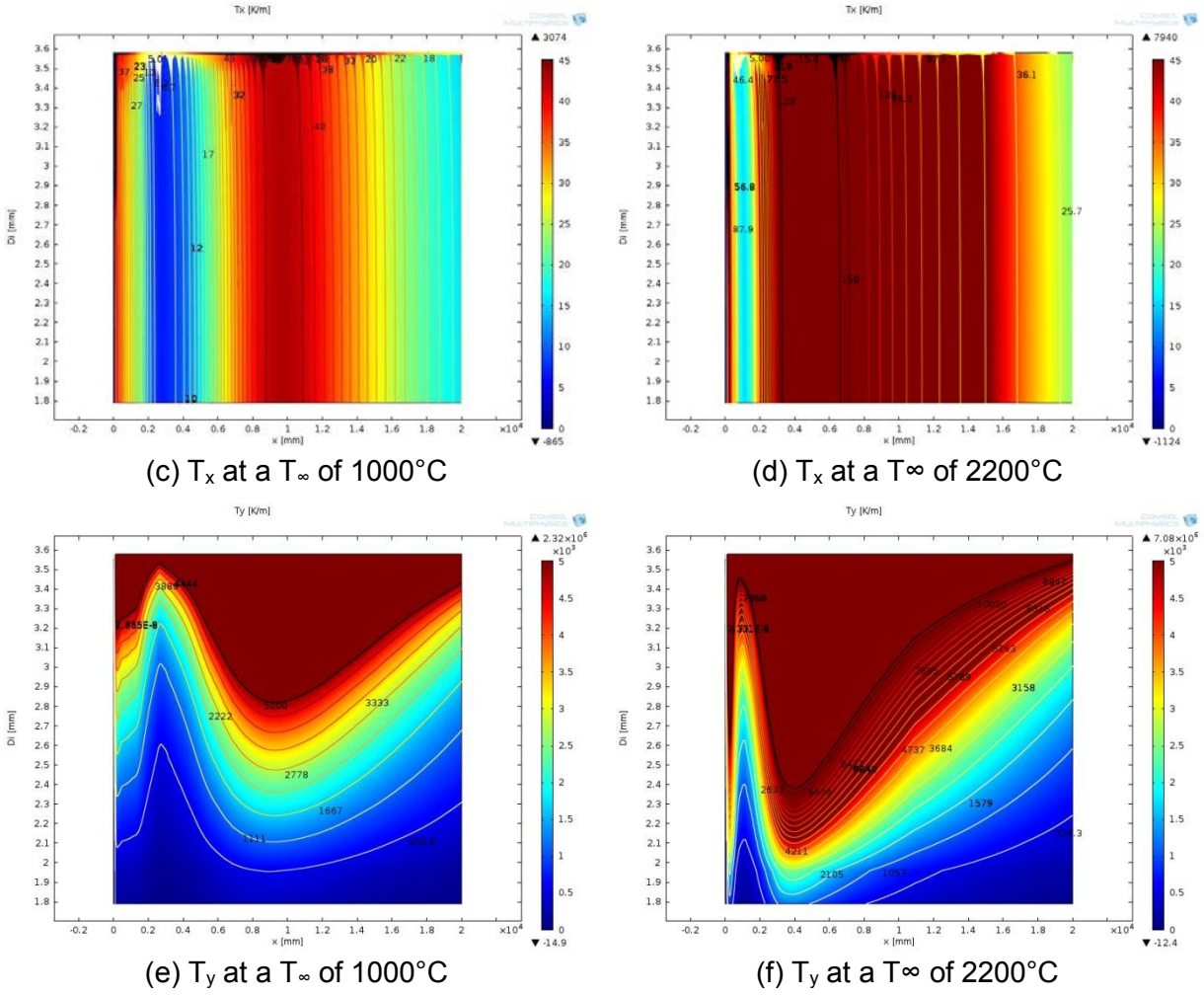

(c) T_x at a T_∞ of 1000°C

(d) T_x at a $T\infty$ of 2200°C

(e) T_y at a T_∞ of 1000°C

(f) T_y at a $T\infty$ of 2200°C

Figure 5.17 Postprocessed 2D images of several thermal parameters

The radial temperature gradients (T_y) behaved in a similar trend as T_x, as observed in Figure 5.17e and f. The narrower LPV region in the results using the T_∞ of 2200°C induced more dramatic changes in the properties due to the stronger heat flux, which triggered a peak in the HTC displaying a higher value but also steeper slopes. Due to the low values of C_p upstream and downstream the LPV region, larger gradients of T_y were triggered. Downstream that point, the α progressively increased due to the recovery of the k, forcing homogeneous temperature profiles near the core but not near the wall due to proximity of the heat source.

5.4.4. Effect of heat transfer behaviour in the boiler efficiency

The outcome of the present research based on the qualitative capture of the main trends occurring within the water wall reflected a system where buoyancy effects were only present at the entrance section. However, the scaling of the hydrothermal conditions led to an overestimation of the forced-convective regime, inducing a low heat flux to mass flux ratio (q_w/G). Thus, buoyancy did not show considerable influence on the water wall thermal performance.

Still, the entrance of the water wall pipe displayed good thermal behaviour due to the early onset of the PSC transition. The drawback of this phenomenon was that a strong thermal acceleration was triggered downstream, deteriorating the heat transfer for a considerable portion of the pipe. This effect was magnified by the reduced pipe diameter and the large value of G obtained from the scaling process.

In these circumstances, decreasing G as a means to increase buoyancy beyond the deterioration range would be beneficial for the overall heat transfer performance of the water wall, as seen in Chapter 4. Additionally, the drop in heat transfer efficiency downstream the PSC transition due to thermal acceleration would decrease. In this case and as stated in Section 1.3.3, upward rifled pipes are ideal to operate at lower values of G without inducing HTD in the flow. Increasing the pipe diameter would also facilitate buoyancy. In simulations terms, these procedures would reduce the extent of scaling to approach a more realistic research. However, the meshable domain would become computationally prohibitive.

From a thermal point of view and based on the results obtained, two approaches to increase heat transfer efficiency in a real water wall section are suggested. One would involve decreasing the inlet temperature, delaying the onset of the PSC transition and thus thermal efficiency would improve upstream that point. In the other approach, the thermal load applied would be increased as a means to rise the fluid temperature beyond 500°C. As it has been shown in the present chapter, the k of the fluid would progressively increase past this temperature, improving thermal performance towards the end of the pipe. Moreover, the latter approach would synergise with an induced decrease of G as well as with the use of vertical rifled pipes.

5.5. Summary

A 2D simulation of an upward test element representing a water wall pipe from a supercritical boiler was undertaken using Comsol Multiphysics, in order to study the hydrothermal performance at different conditions. The water flow inlet was near the pseudocritical point and the boiler conditions were scaled down employing similarity equations while keeping the mass flux constant and using two thermal boundary conditions as convective heat transfer; at a T_∞ of 1000°C and at 2200°C furnace chamber temperature.

The study of the axial profiles through the measurement of SCHT parameters and the use of empirical correlations revealed that buoyancy effects were present mostly near the pipe inlet and visibly stronger at a T_∞ of 2200°C; while thermal acceleration extended from the inlet until the PSC was surpassed, approximately at x/D=2500. However, buoyancy was not strong enough to represent a remarkable impact on the heat transfer performance. The property changes in both cases were closely related to Nu ratios, which predicted the trends accordingly though the empirical correlations gave different predictions compared to the computed results. This could be due a combination of factors such as the limitations of the mesh, the extreme hydrothermal conditions employed and the correlations being specifically produced for much milder conditions than the ones selected for the present investigation.

Investigation of the radial profiles employing hydrothermal parameters showed more details about the heat transfer performance, revealing a sharp increase of the axial

flow acceleration at the middle sections of both pipes (x/D=2800 approximately), always following the HTC peak. For both temperatures, the outlet section revealed favourable conditions for heat transfer and fluid flow. On the other hand, simulation at a T_∞ of 1000°C revealed better turbulence condition on the inlet section due to the existence of the LPV region prior to the HTC peak, while at a T_∞ of 2200°C the peak, although larger than the one produced at a T_∞ of 1000°C, occurred much closer to the inlet, leaving a wider section post-peak with stronger flow acceleration. Nevertheless, the heat transfer performance was significantly better at a T_∞ of 2200°C not only because of the HTC peak, but also due to the k progressively increasing after dropping when the bulk surpassed the PSC temperature.

The postprocessed 2D plots of hydrothermal properties from the two simulation scenarios agreed with the previous results in Sections 5.4.1 and 5.4.2, highlighting better turbulence in the entrance and outlet regions of the flow and strong acceleration downstream the location where the bulk of the flow achieved the PSC point. Thermal performance was revealed to improve towards the end of the pipe once the LPV region was surpassed, but the lack of turbulence at the central section of the pipe (around x/D=2800 approximately) impaired the good hydrothermal performance.

The heat transfer behaviour in the water wall reflected a good performance near the entrance due to the onset of the PSC point. Deterioration followed downstream, triggered by thermal acceleration and a recovery of the thermal efficiency towards the end of the pipe, along with an increasing thermal conductivity of the fluid. As a means

to increase boiler efficiency, lower values of G and larger pipes diameters were suggested in a simulation scenario in order to observe if the buoyancy produced was strong enough to induce more turbulence through larger velocity gradients and shear stress. Additionally, lower inlet temperatures at the water wall as a means to extend the LPV region or higher thermal loads in order to increase the thermal conductivity downstream the PSC transition were suggested in real water wall conditions as methods to increase the thermal efficiency.

References

Badur J, Ziołkowski P, Sławinski D, Kornet S (2015). An approach for estimation of water wall degradation within pulverized-coal boilers. *Energy;* 92: 142-52

Duda P & Taler J (2009). A new method for identification of thermal boundary conditions in water-wall tubes of boiler furnaces. *International Journal of Heat and Mass Transfer*; 52 1517-24

Edge PJ, Heggs PJ, Pourkashanian M, Stephenson PL (2013). Integrated fluid dynamics-process modelling of a coal-fired power plant with carbon capture. *Applied Thermal Engineering*; 60: 456-64

Edge PJ, Heggs PJ, Pourkashanian M, Williams A (2011). An integrated computational fluid dynamics–process model of natural circulation steam generation in a coal-fired power plant. *Computers and Chemical Engineering*; 35: 2618-31

Huilin F, Zhengchun C, Xiaozhong Y, Jinqiao H, Yucai Z (2013). Failure Analysis of 600 MW Supercritical Boiler Water Wall. *Research Journal of Applied Sciences, Engineering and Technology*; 6: 1726-31

Jackson JD (2013). Fluid flow and convective heat transfer to fluids at supercritical pressure. *Nuclear Engineering and Design;* 264: 24-40

Lemmon EW, McLinden MO, Friend DG (2015). Thermophysical Properties of Fluid Systems. In: Linstrom PJ (editor). NIST Standard Reference Database Number 69. *NIST Chemistry WebBook*

Mokry S, Pioro I, Farah A, King K, Gupta S, Peiman W, Kirillov P (2011). Development of supercritical water heat-transfer correlation for vertical bare tubes. *Nuclear Engineering and Design*; 241:1126-36

Park HY, Faulkner M, Turrell MD, Stopford PJ, Kang DS (2010). Coupled fluid dynamics and whole plant simulation of coal combustion in a tangentially-fired boiler. *Fuel*; 89: 2001-10

Pioro IL & Duffey RB (2007). Practical prediction methods for heat transfer at supercritical pressures. In: Pioro IL & Duffey RB (editors). Heat transfer and hydraulic resistance at supercritical pressures in power–engineering applications. *Asme Press;* pp. 172-73

Sankar G, Chandrasekhara Rao A, Seshadri PS, Balasubramanian KR (2016). Techniques for measurement of heat flux in furnace waterwalls of boilers and prediction of heat flux – A review. *Applied Thermal Engineering*; 103: 1470-79

Wagner W, Kretzschmar HJ (2008). Table 4 - High-temperature region (800°C to 2000°C). In: Wagner W (editor). International Steam Tables. Properties of water and steam based on the industrial formulation IAPWS-IF97. *Springer;* pp. 289-96

Winterton RHS (1998). Where did the Dittus and Boelter equation come from? *International Journal of Heat Mass Transfer*; 41: 809-10

Xu L, Cheng L, Cai Y, Liu Y, Wang Q, Luo Z, Ni M (2016). Heat flux determination based on the waterwall and gas–solid flow in a supercritical CFB boiler. *Applied Thermal Engineering*; 99: 703-12

Zima W, Grądziel S, Cebula A (2010). Modelling of heat and flow phenomena occurring in waterwall tubes of boilers for supercritical steam parameters. *Archives of thermodynamics*; 31: 19-36

6. Design aspects of a supercritical carbon dioxide rig

Gil-Garcia AA, Kings IN, Al-Duri B

Abstract

Considering future experimental validations of the numerical results obtained in previous chapters, some supercritical design aspects were presented. Hydrothermally equivalent conditions to those of the water-wall section of a supercritical boiler as described in Chapter 5 were calculated using CO_2 as surrogate fluid. Fluid-to-fluid modelling was applied and the working conditions for the $SCCO_2$ rig were obtained. The pipe diameters of a prospective test element were imposed due to safety and supplier constraints, while the necessary heat rates and the length of the test element were estimated using control volume analysis. A subsequent differential analysis was performed, which produced temperature profiles along the pipe length. The results of both analytical methods were compared. The first method considerably overestimated the necessary pipe length at high values of mass flux and pipe diameter, although at smaller values of mass flux the two methods showed converging results. A graphical approach to verify the formation of dry ice at the system outlet of $SCCO_2$ rigs was described, and the scaled conditions obtained for the surrogate fluid were employed as case study.

Keywords: fluid-to-fluid modelling, $SCCO_2$ rig, differential analysis, Joule-Thomson effect.

Abbreviations

1D	one-dimensional
CVA	control volume analysis
DB	Dittus-Boelter
DFA	differential analysis
DHT	deteriorated heat transfer
HTC	heat transfer coefficient
LHS	left-hand side
LPV	large property variation
NHT	normal heat transfer
NPS	nominal pipe size
PDE	partial differential equation
PID	piping and instrumentation design
PSC	pseudo-critical
RANS	Reynolds-averaged Navier-Stokes
RHS	right-hand side
SCF	supercritical fluid
SCH	schedule (pipe wall thickness)
SCHT	supercritical heat transfer
VDE	volume differential element

Dimensionless numbers

Nu	Nusselt number; $Nu = \frac{h \cdot D}{k}$
Pr	Prandtl number; $Pr = \frac{C_p \cdot \mu}{k}$
Re	Reynolds number; $Re = \frac{\rho \cdot u \cdot D}{\mu}$

Greek symbols

δ	infinitesimal change in a variable [-]
Δ	gradient operator [-]
μ	fluid dynamic viscosity [kg m^{-1} s^{-1}]
ρ	fluid density [kg m^{-3}]

Geometric definitions

A	heat transfer area of volume differential element [m^2]; $A = \pi \cdot D \cdot \delta x$
D, D_i	inner tube diameter [mm]
D_o	outer tube diameter [mm]
L	total length of pipe [m]

S pipe cross-sectional area [m^2]
V volume of differential element [m^3]; $V = \frac{\pi \cdot D^2}{4} \cdot \delta x$
x axial coordinate [mm]

Roman symbols

C_p fluid isobaric heat capacity [J kg^{-1} $degC^{-1}$]
G fluid mass flux [kg m^{-2} s^{-1}]
h fluid enthalpy [J kg^{-1}]
k fluid thermal conductivity [W m^{-1} $degC^{-1}$]
p system absolute pressure [bar]
$\dot{q}_{in}$ heat rate [J s^{-1}]
q heat flux [W m^{-2}]
R_f fouling factor [m^2 degC W^{-1}]
t time [s]
T fluid temperature [K or °C]
u fluid velocity [m s^{-1}]
U overall heat transfer coefficient [W m^{-2} $degC^{-1}$]
W_m fluid mass flow [kg s^{-1}]

Subscripts

$(\ldots)_b$ at bulk conditions
$(\ldots)_{cr}$ at critical conditions
$(\ldots)_i$ at inner pipe diameter conditions
$(\ldots)_{in}$ at inlet conditions
$(\ldots)_m$ log mean temperature difference
$(\ldots)_o$ at outer pipe diameter conditions
$(\ldots)_{out}$ at outlet conditions
$(\ldots)_{pc}$ at pseudo-critical conditions
$(\ldots)_w$ at pipe wall conditions

6.1. Background

Before considering a modelled system to be capable of producing independent and reliable data through numerical analysis, validation is a first step. For that purpose, boundary (working) conditions must be first imported from previously validated experimental or numerical data, and thus the results from these references would be used to verify the quality of the computed results. This was the objective of Chapters 3 and 4, as a means to validate and verify the production of numerical data in Chapter 5.

As a third step, experimental work should be performed using the boundary conditions of the computed system as a means to produce empirical data and validate the quality of the new numerical results.

On the other hand, when researching supercritical heat transfer (SCHT) this practice is not always possible due to operational or economic constraints. Nevertheless, some authors have undertaken experimental validation after numerically researching SCHT using water as thermal fluid. Two main approaches have been considered. One consists of building a test rig employing water at the same operational conditions as the simulation. However, if this approach is not feasible, CO_2 could be employed as surrogate fluid (Bae & Kim, 2009; Bae *et al.,* 2010; Gu *et al.,* 2015). This is due to the fact water systems are more energy demanding and costly, as the working conditions to achieve the critical point are higher than in CO_2 systems (221.2 bar and 374.14°C for water; 73.8 bar and 31.05°C for CO_2). Fortunately, all the

thermophysical properties of fluids perform similarly when approaching the critical or pseudo-critical (PSC) points and thus are proportional when related to reduced pressures (P/P_{cr}; P/P_{pc}) and temperatures (T/T_{cr}; T/T_{pc}) as seen in Figure 6.1.

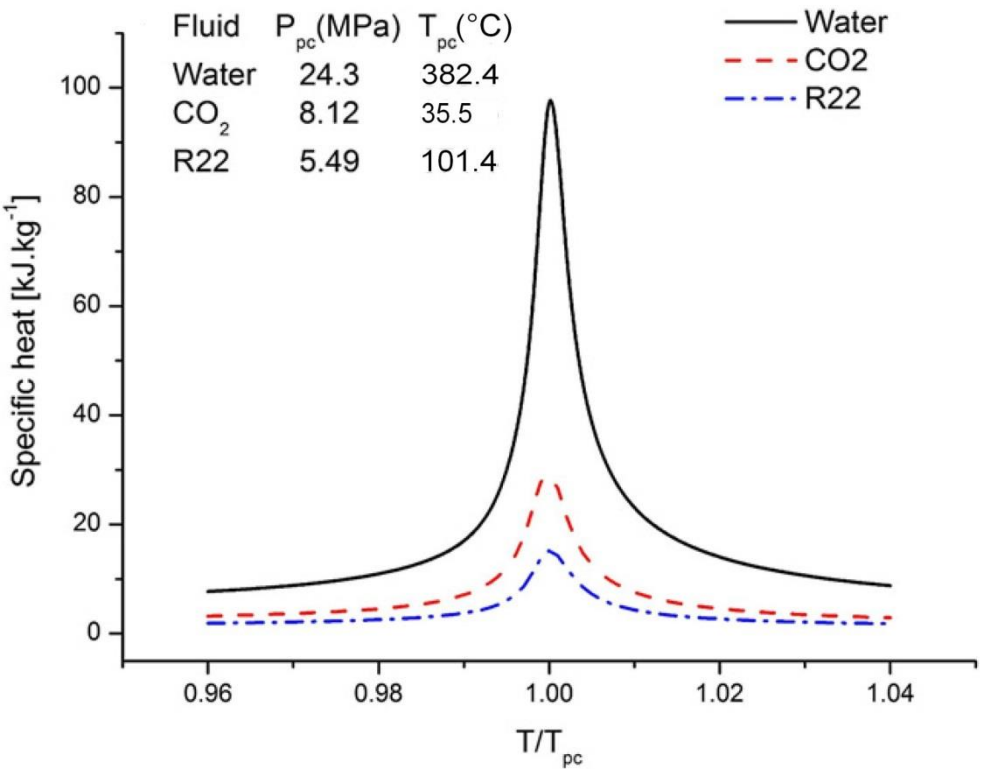

Figure 6.1 Heat capacity profile of several fluids along the T/T_{pc} at a pressure of 1.1 P_{cr} (adapted from Bae *et al.*, 2010)

Jackson (2007) established that, before considering an upward flow of a fluid experiencing large property variations at supercritical pressure similar to another system using the same fluid, steady-state and forced-convective conditions had to apply. In other words, the pipe diameters had to be small enough to avoid buoyancy but large enough to prevent the dominance of viscosity effects. Moreover, he defined a scaling law for the wall heat flux (q_w) at inlet properties, and specified that both systems had to use the same inlet pressure (P_{in}), inlet temperature (T_{in}), pipe length

(L) to inner diameter (D) ratio (L/D) and inlet Reynolds (Re_{in}). Additionally, thermal expansion and compressibility effects had to be negligible. In similar terms, Song *et al.* (2008) researched a criterion of similarity in SCHT, and found that if both systems possessed the same L/D and q_w to mass flux (G) ratio, the heat transfer performance would be maintained in normal heat transfer (NHT) and deteriorated heat transfer (DHT) regimes.

Zwolinski *et al.* (2011) extended the scaling laws of Jackson (2007), scaling SCHT between two different fluids (water and CO_2) and establishing fluid-to-fluid modelling. Their similarity equations were those used in the numerical analysis of Chapter 5 (Section 5.2). At the same time, Cheng *et al.* (2011) proposed different scaling laws for SCHT in vertical flows between water and CO_2 using a constant q_w. In their specifications, both systems would have the same D and conditions would not be evaluated at the inlet but locally at the bulk. Moreover, they created another dimensionless group for the temperature.

Upon empirical investigation of fluid-to-fluid modelling in SCHT, Zahlan *et al.* (2014) created alternative scaling laws and improved the ones from Cheng and colleagues. In their research, they avoided some limitations from previous works and utilised an empirically adjusted correlation of Dittus-Boelter (DB) in the similarity equations, applicable at supercritical and high subcritical conditions.

More recently, and due to the development of numerical methods, Pucciarelli and Ambrosini (2016) investigated fluid-to-fluid scaling of supercritical fluids (SCFs) using

Reynolds-averaged Navier-Stokes (RANS) calculations in DHT conditions. They produced validated numerical results from experimental cases, and afterwards replaced the fluid with a surrogate and forced the system to maintain the enthalpy trends at the wall and the bulk.

Nonetheless, the use of surrogate fluids by applying scaling laws is a recent technique under development, and as Bae (2013) pointed out still bears inherent problems. One of them is the lack of experimental data of many fluids within comparable parameter ranges in order to validate the fluid-to-fluid techniques (Zhang *et al.,* 2014).

Due to the inherent complexities in the design of rigs employing SCFs, the objective of the present chapter was to approach some supercritical design aspects. First, the hydrothermal conditions at the water-wall section of a supercritical boiler were scaled to produce an equivalent system employing supercritical CO_2 ($SCCO_2$) as surrogate fluid. Afterwards, two analytical procedures were described as a means to estimate the input heat rates ($\dot{q}_{in}$) and pipe length necessary to achieve supercritical temperatures in a pressurised once-through pass within the test element. The first procedure applied control volume analysis (CVA) based on inlet and outlet conditions, and the second was a differential analysis (DFA) where a simplified partial differential equation (PDE) was derived and integrated. Finally, a graphical approach was described in order to avoid the formation of dry ice when venting compressed CO_2 out of the system. These design aspects can be considered as guidelines for future extensions of the current research, prior to the acquisition of rig

equipment, if experimental validation of the numerical results employing a surrogate fluid was undertaken.

6.2. Fluid-to-fluid scaling

In Table 6.1 the desired working conditions for a test rig employing supercritical water (SCW) are shown along with the scaled conditions for a rig employing CO_2 as surrogate fluid. The hydrothermal parameters of the SCW rig were chosen similar to those at boiler water-wall conditions, as described in Chapter 5. However, the geometric parameters were imposed due to operational constraints. Two values of G were chosen in order to observe the effect of the q_w/G ratio. The values of G for the $SCCO_2$ rig were assigned considering operational limitations, and it was verified that the corresponding value of G_{max} for the water system was similar to that of the boiler water-wall conditions in Chapter 5.

Table 6.1 Working parameters for the SCW test loop and the scaled $SCCO_2$ rig

Characteristic	SC Water rig	SC CO_2 rig	Magnitude
Water pressure at inlet (p_{in})	300	100	[bar]
Water inlet temperature (T_{in})	350	20	[°C]
Water outlet temperature (T_{out})	450	67	[°C]
Minimum mass flux (G_{min})	~260-400	1800	[kg m^{-2} s^{-1}]
Maximum mass flux (G_{max})	~600-900	4000	[kg m^{-2} s^{-1}]
Pipe external diameter (D_o)	¼ NPS (13.72)	1.6/2.4	[mm]
Pipe internal diameter (D)	SCH 30 (10.01)	6.35	[mm]

The scaling laws used to calculate the surrogate conditions were obtained by Zwolinski *et al.* (2011) and summarised by Pioro & Duffey (2007) in Figure 6.2. The symbols presented were properly described in the nomenclature section. In the equations, the suffix A represents the working fluid conditions and suffix B is related to the surrogate fluid equivalent. The thermodynamic properties are considered at

pipe inlet bulk conditions. Ideally, in experimental conditions all the scaling equations would provide values for the surrogate system; however the similarity criteria for the geometry and heat flux were not applied due to the fact the SCW rig did not exist for comparison. Thus, these parameters (pipe length and heat flux) were estimated in Section 6.3.

Similarity Criteria	Equation
Geometric Similarity	$\left(\frac{x}{D}\right)_A = \left(\frac{x}{D}\right)_B$
Pressure	$\left(\frac{p}{p_{cr}}\right)_A = \left(\frac{p}{p_{cr}}\right)_B$
Bulk Fluid Temperature (all temperatures in K)	$\left(\frac{T_b}{T_{cr}}\right)_A = \left(\frac{T_b}{T_{cr}}\right)_B$
Heat Flux or Wall Superheat	$\left(\frac{q\,D}{k_b\,T_b}\right)_A = \left(\frac{q\,D}{k_b\,T_b}\right)_B$ or $\left(\frac{T_w - T_b}{T_{cr}}\right)_A = \left(\frac{T_w - T_b}{T_{cr}}\right)_B$
Mass Flux	$\left(\frac{G\,D}{\mu_b}\right)_A = \left(\frac{G\,D}{\mu_b}\right)_B$
Heat Transfer Coefficient	$\mathbf{Nu}_A = \mathbf{Nu}_B$

Figure 6.2 Scaling laws for the calculation of working conditions in a $SCCO_2$ rig (Pioro & Duffey, 2007)

The nominal pipe size (NPS) for the D_o and wall thickness (SCH) of the SCW rig were selected so the pipe material (an austenitic nickel-chromium-based super alloy, Inconel 625) could withstand the high conditions of pressure and temperature. Inconel 625 is widely employed in SCHT rigs because it allows applying the heat source by passing an alternate current (AC) along the metal pipe using two terminals attached to the inlet and outlet sections. The characteristic low electrical conductivity of the Inconel alloys induces high rates of energy dissipation by the Joule effect, and thus heating the flow if the pipe is thermally insulated on the outside. However, the values of D_o and D for the $SCCO_2$ rig were imposed due to supplier restrictions, offering two test elements with the same D_o and different D in order to investigate the diameter effect. Due to the lower energy demand of the $SCCO_2$ rig, two heating methods were recommended. One involved an induction coil that would heat an iron sheath (ferromagnetic material) and the stainless steel pipe would be located inside. The other could be a tracer heater containing an electrical resistance as a wire that would be tightly wrapped around the pipe wall. The former method would be more efficient in terms of applying homogeneous heat along the pipe, although the latter would be more economic.

6.3. Length of test element

6.3.1. Control volume analysis

The CVA was employed as a first design approach to achieve supercritical temperatures at the outlet of the test element. Therefore, only working conditions at the inlet and outlet of the system were considered as seen in Figure 6.3 as a means to estimate the necessary ($\dot{q}_{in}$), pipe lengths and thus heat fluxes.

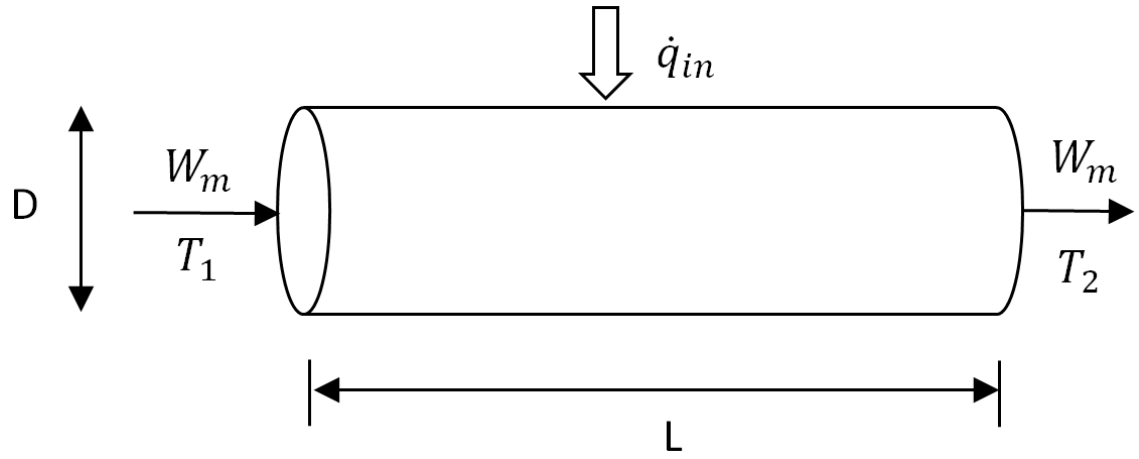

Figure 6.3 CVA based on inlet (1) and outlet (2) conditions

Moreover, a procedure to estimate the pressure drop was presented. For this purposes, the scaled parameters for the $SCCO_2$ obtained in Section 6.2 were used. Employing equation (6.2) from the general energy equation for steady flows (Çengel & Cimbala, 2006), the values of $\dot{q}_{in}$ can be calculated for the considered mass flow (W_m). The values of the internal energy ($\bar{u}$) at the inlet or outlet, as well as any other thermodynamic property can be obtained from the NIST database (Lemmon *et al.,* 2015) at the operational values of temperature and pressure.

$$(Energy)_{in} + \dot{q}_{in} = (Energy)_{out} \quad \textbf{(6.1)}$$

$$\dot{q}_{in} = W_m \cdot (\bar{u}_2 - \bar{u}_1) \quad \textbf{(6.2)}$$

$$\dot{q}_{in} = W_m \cdot \left(\left(\bar{h}_2 - \frac{p_2}{\rho_2} \right) - \left(\bar{h}_1 - \frac{p_1}{\rho_1} \right) \right) \quad \textbf{(6.3)}$$

$$W_m = G \cdot S \quad \textbf{(6.4)}$$

Similarly, the $\dot{q}_{in}$ could be calculated if the test element was considered to behave like a heat exchanger (Incropera *et al.,* 2007), using equation (6.5). In this and the following equations, all the parameters and symbols were defined in the nomenclature.

$$\dot{q}_{in} = A \cdot U \cdot \Delta T_m \quad \textbf{(6.5)}$$

$$A = \pi \cdot D \cdot L \quad \textbf{(6.6)}$$

$$U = \frac{1}{D_o} \cdot \frac{1}{\frac{1}{h_{air} \cdot D_o} + \frac{(R_f)_{air}}{D_o} + \frac{\ln\left(\frac{D_o}{D}\right)}{2 \cdot k_{pipe}} + \frac{(R_f)_i}{D} + \frac{1}{(h_{convective})_{ave} \cdot D}} \quad \textbf{(6.7)}$$

$$\Delta T_m = \frac{(T_w - T_{m,out}) - (T_w - T_{m,in})}{\ln\left(\frac{T_w - T_{m,out}}{T_w - T_{m,in}}\right)} \quad \textbf{(6.8)}$$

Combining all equations from (6.5) to (6.8), the L of the pipe was calculated, as shown in (6.9). It is worth mentioning that, the resistance coefficients involving the heat transfer coefficient (HTC) of the air (h_{air}) and the fouling factor between the air and the pipe ($(R_f)_{air}$) in equation (6.7) were considered negligible. Also, the thermal conductivity of the pipe (k_{pipe}) was estimated considering an average value of temperature at the wall, and the HTC of the flow was estimated as an average of the

inlet and outlet values by employing the DB correlation (Winterton, 1998), defined in equation (6.10).

$$L = \frac{\dot{q}_{in}}{\pi} \cdot \left(\frac{\ln\left(\frac{D_o}{D}\right)}{2 \cdot k_{pipe}} + \frac{\left(R_f\right)_i}{D} + \frac{1}{\frac{(Nu_D)_{in} \cdot k_{in} + (Nu_D)_{out} \cdot k_{out}}{2}} \right) \cdot \frac{1}{\Delta T_m} \quad \textbf{(6.9)}$$

$$Nu_D = 0.023 \cdot Re_D^{0.8} \cdot Pr^{0.4} \quad \textbf{(6.10)}$$

With the values of $\dot{q}_{in}$ and L calculated, the heat flux (q_w) can be obtained. As explained at the beginning of this section, this procedure was a first approximation to obtain L and q_w, and thus several assumptions were made. For instance, equation (6.5) considers the fluid to have a constant value of heat capacity (C_p) along the pipe. Similarly, Reynolds number (Re) and Prandtl (Pr) were obtained as averages of inlet and outlet values. Finally, the DB correlation was employed to define the HTC of the flow ($h_{convective}$), which is meant only for subcritical conditions.

In terms of hydraulic resistance, the total pressure drop of a forced-convective flow passing through a test element was defined by Pioro and Duffey (2007) as shown in equation (6.11).

$$\Delta p = \sum \Delta p_{fr} + \sum \Delta p_l + \sum \Delta p_{ac} + \sum \Delta p_g \quad \textbf{(6.11)}$$

The first summation terms on the right-hand side (RHS) of equation (6.11) represent, from left to right, the pressure drop due to fictional resistances, local flow obstructions, acceleration effects and gravitational forces, respectively. As design

considerations, the pressure drop due to obstructions was considered negligible due to the absence of accessories or observable changes in D along the test element. Moreover, the pressure drop due to gravity was not included as a consequence of the short straight lengths expected in a pipe fitting inside a conventional laboratory. Thus, the pressure drop due to frictional resistance and acceleration was represented in equations (6.12) and (6.14), respectively.

$$\Delta p_{fr} = \xi_{fr} \cdot \frac{L}{D} \cdot \frac{G^2}{2 \cdot \rho} \quad \textbf{(6.12)}$$

$$\xi_{fr} = \frac{1}{(1.82 \cdot \log_{10} \cdot Re_b - 1.64)^2} \quad \textbf{(6.13)}$$

$$\Delta p_{ac} = G^2 \cdot \left(\frac{1}{\rho_{out}} - \frac{1}{\rho_{in}}\right) \quad \textbf{(6.14)}$$

As can be seen, the value of L employed in equation (6.12) would be obtained from the results of equation (6.9). The frictional coefficient (ξ_{fr}) would be estimated using equation (6.13). These hydraulic resistance equations reveal that higher values of wall temperature (T_w) reduce the pressure drop, while high values of G trigger larger pressure losses. On the other hand, smaller pipe diameters would induce larger values of pressure drop. As a consequence, they are useful to validate the assumption of isobaric performance, not only in experimental works but also in numerical studies.

6.3.2. Differential analysis

A procedure to calculate the flow temperature at different axial locations of the heated pipe (and thus the necessary length to achieve a certain temperature at the outlet) was described in the present analysis. First, an energy balance was performed to a volume differential element (VDE) of the heated pipe (Çengel & Cimbala, 2006), as seen in Figure 6.4.

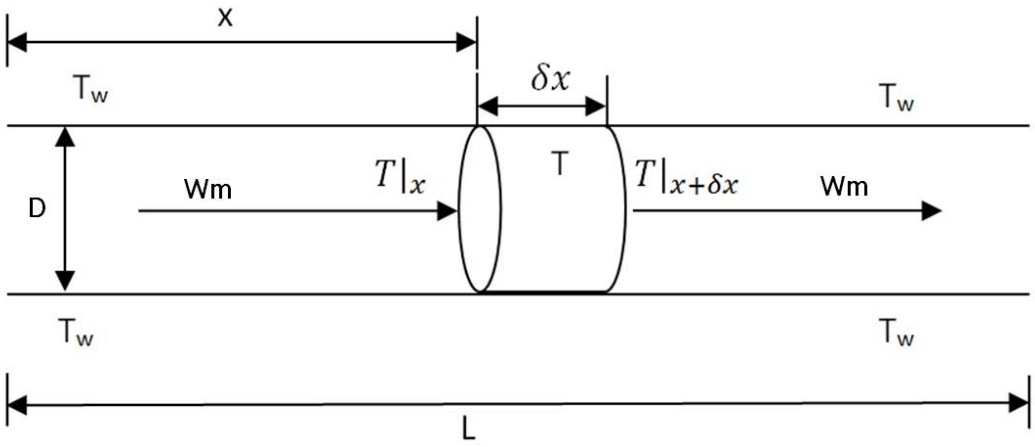

Figure 6.4 Analysis of the system using a volume differential element

A series of assumptions were made in the analysis. T_w was considered constant and the same as that of the surroundings. The velocity profile would be flat inside the volume element due to turbulence, as well as the temperature profile (one-dimensional approach). C_p was assumed unaffected by the differential temperature increase and the pressure losses. No frictional losses and heat dissipation would be accounted for. As a following step, the law of conservation of energy was applied to the VDE, as seen from equations (6.15)-(6.18).

$$Accumulation = Input - Output \quad \textbf{(6.15)}$$

$$Input = \left[W_m \cdot C_p \cdot T|_x + h \cdot A \cdot (T_w - T)\right] \cdot \delta t \quad \textbf{(6.16)}$$

$$Output = W_m \cdot C_p \cdot T|_{x+\delta x} \cdot \delta t \quad \textbf{(6.17)}$$

$$Accumulation = V \cdot \rho \cdot C_p \cdot \delta T \quad \textbf{(6.18)}$$

Once all the terms were rearranged, a partial differential equation (PDE) was produced to describe the system performance, as seen in equation (6.19). The fluid HTC (h) was forced to be solved using a subcritical correlation, i.e. equation (6.10). This was due to the assumption of flat radial temperature profiles, which prevented the application of supercritical correlations as they rely on temperature values at the bulk of the flow and at the inner wall of the pipe. Thus, equation (6.20) was produced.

$$\frac{dT}{dt} = -\frac{4 \cdot W_m}{\rho \cdot \pi \cdot D^2} \cdot \frac{\partial T}{\partial x} - \frac{4 \cdot h}{\rho \cdot D \cdot C_p} \cdot (T - T_w) \quad \textbf{(6.19)}$$

$$\frac{dT}{dt} = -\frac{4 \cdot W_m}{\rho \cdot \pi \cdot D^2} \cdot \frac{\partial T}{\partial x} - \frac{4 \cdot k \cdot (T - T_w)}{\rho \cdot D^2 \cdot C_p} \cdot 0.023 \cdot \left[\frac{4 \cdot W_m}{\pi \cdot D \cdot \mu}\right]^{0.8} \cdot \left[\frac{C_p \cdot \mu}{k}\right]^{0.4} \quad \textbf{(6.20)}$$

Assuming steady state, equation (6.20) was rearranged and the differentials were solved for the full length of the pipe, as equation (6.21) shows.

$$\int_{T_{in}}^{T_{out}} \frac{C_p \cdot \mu^{0.8}}{k \cdot Pr^{0.4} \cdot (T_w - T)} \cdot \partial T = 4 \cdot 0.023 \cdot \frac{(G \cdot D)^{0.8}}{G \cdot D^2} \cdot \int_{x=0}^{x=L} \partial x \quad \textbf{(6.21)}$$

As a result, the left-hand side (LHS) of equation (6.21) was composed of temperature-dependent parameters, while the RHS was hydrodynamic-dependent. In order to solve the temperature-dependent integral, the NIST database was used to fit all the thermophysical parameters into a single polynomial as a function of

temperature. The large property variations (LPVs) near the PSC point were represented via the use of two polynomials for an accurate fit, representing the sections of the pipe upstream and downstream the PSC point. This is observed in equations (6.22) and (6.23), respectively.

$$\int_{T_{in}}^{T_{PSC}} \frac{a + b \cdot T + c \cdot T^2 + \cdots}{(T_w - T)} \cdot \partial T = 4 \cdot 0.023 \cdot \frac{(G \cdot D)^{0.8}}{G \cdot D^2} \cdot \int_{x=0}^{x_{PSC}} \partial x \quad \textbf{(6.22)}$$

$$\int_{T_{PSC}}^{T_{out}} \frac{a' + b' \cdot T + c' \cdot T^2 + \cdots}{(T_w - T)} \cdot \partial T = 4 \cdot 0.023 \cdot \frac{(G \cdot D)^{0.8}}{G \cdot D^2} \cdot \int_{x_{PSC}}^{x=L} \partial x \quad \textbf{(6.23)}$$

Figure 6.5 shows the flow temperature profiles calculated along a test element using water at 300 bar as thermal fluid. Six different values of G between 100 and 1800 kg m^{-2} s^{-1} were employed and two different values of D were considered. The thermal conditions imposed were a T_{in} of 300°C and a T_{out} of 500°C, at two different values of T_w, at 600°C (Figure 6.5a) and 900°C (Figure 6.5b).

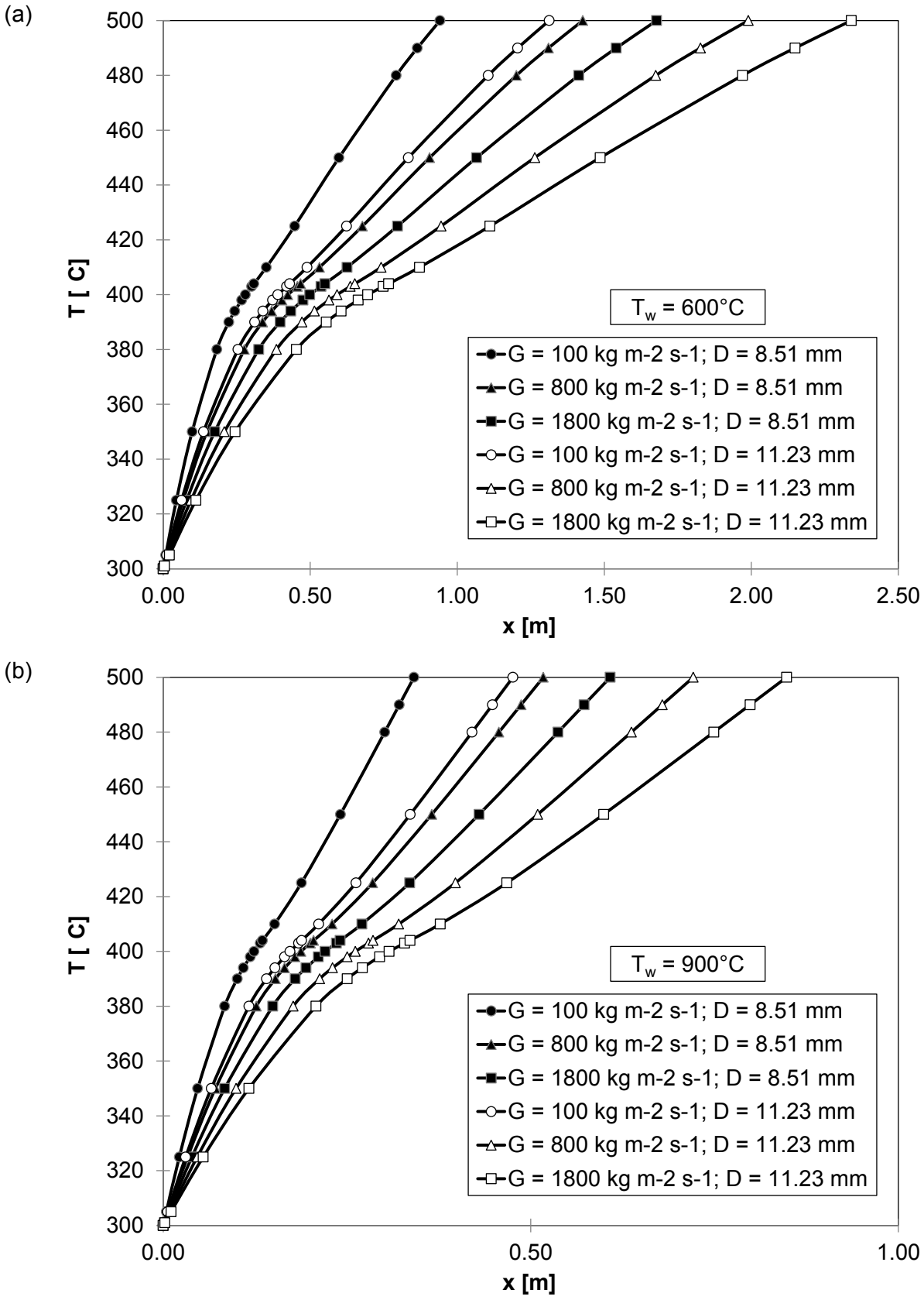

Figure 6.5 Temperature profile of water (300 bar) along the pipe at Tw = 600°C (a) and Tw = 900°C (b)

As can be observed, the calculated values of pipe length (L) to reach a T_{out} of 500°C were larger in Figure 6.5a compared to those in Figure 6.5b due to the lower T_w applied. Within each case, the temperature profiles obtained from conditions at lower values of G reflected shorter pipe lengths for the same D, as the q_w/G ratio was higher and thus the length requirement decreased. Similarly, pipes with a smaller D also required shorter pipes for the same values of G, as they employed lower values of W_m. Moreover, when the temperature reached the PSC temperature (402°C approximately) the temperature gradients decreased downstream the PSC point, showing lower heat transfer efficiency than the section upstream and thus requiring a longer pipe section. Nevertheless, the temperature profiles relied on a subcritical correlation for the calculation of the HTC besides the various assumptions considered, and thus their interpretation must be considered only as an approximative design approach.

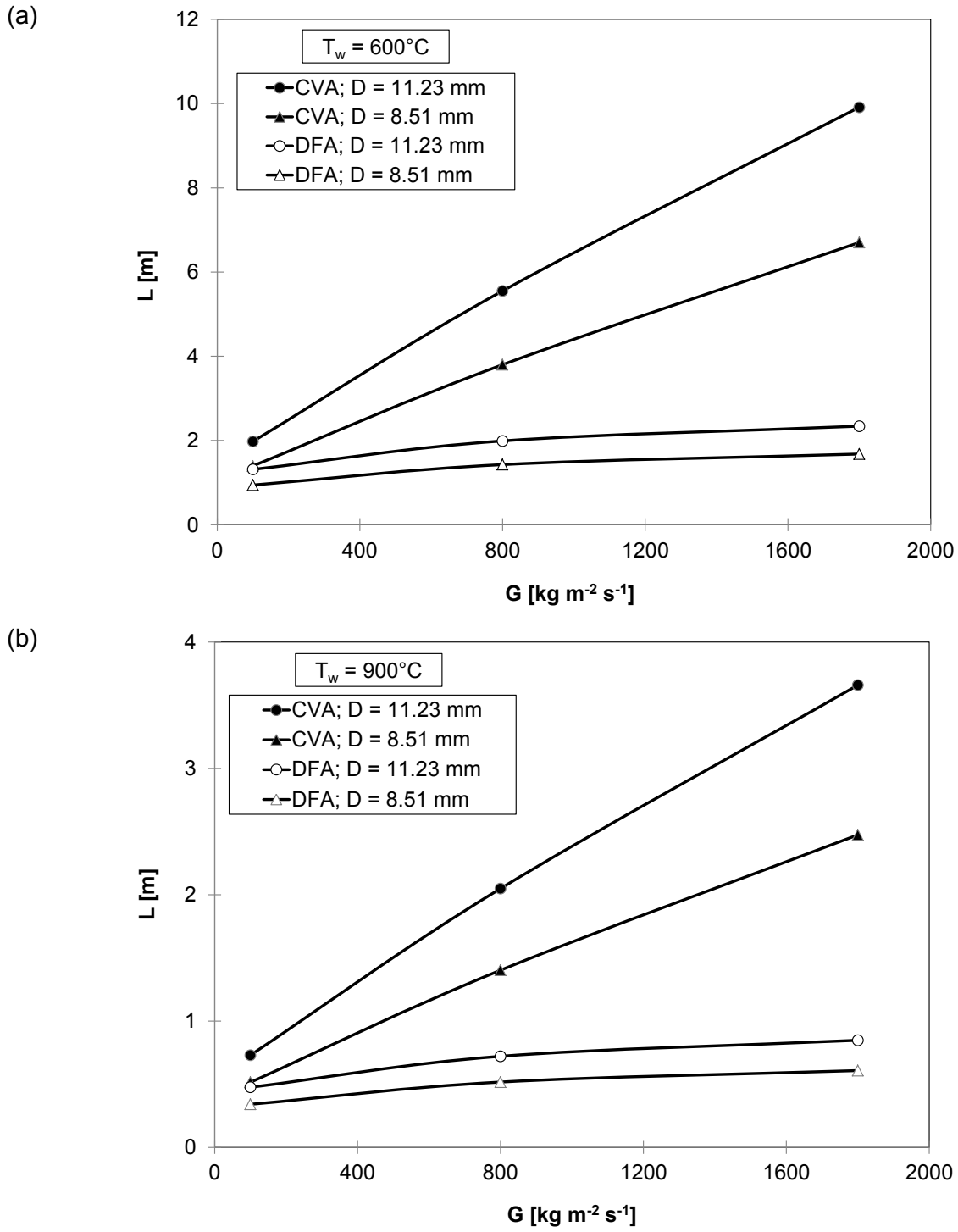

Figure 6.6 Comparison between the control volume and differential analyses for two different pipe diameters at T_w = 600°C (a) and T_w = 900°C (b) using water; T_{in} = 300°C and T_{out} = 500°C

In Figure 6.6, the calculated values of L using the DFA were compared to the results from the CVA at the same conditions described for Figure 6.5. In general, the CVA

overestimated the values of L when the G was increased, compared to more conservative results from the DFA. This overestimation with CVA was higher when the D employed was larger. One of the reasons for these deviations at large values of G and D was due to larger differences when averaging parameters such as Re at the inlet and the outlet. Nevertheless, at low values of G the calculations from both analyses converged regardless of the D and T_w, thus these methods are recommended for systems employing relatively low values of G.

6.4. SCCO2 decompression

When operating $SCCO_2$ demonstration rigs it is often more economic to vent the CO_2 out of the system and purchase new CO_2 bottles rather than using recompression in a loop. In this type of rigs, CO_2 is adiabatically expanded when leaving the system because the pipe is thermally isolated from the outside; and thus the fluid temperature decreases isenthalpically due to the Joule-Thomson effect (Menon, 2005). If the gas temperature drops below -78.5°C at room pressure (1 bar), CO_2 will solidify and form dry ice, which can deteriorate the piping system.

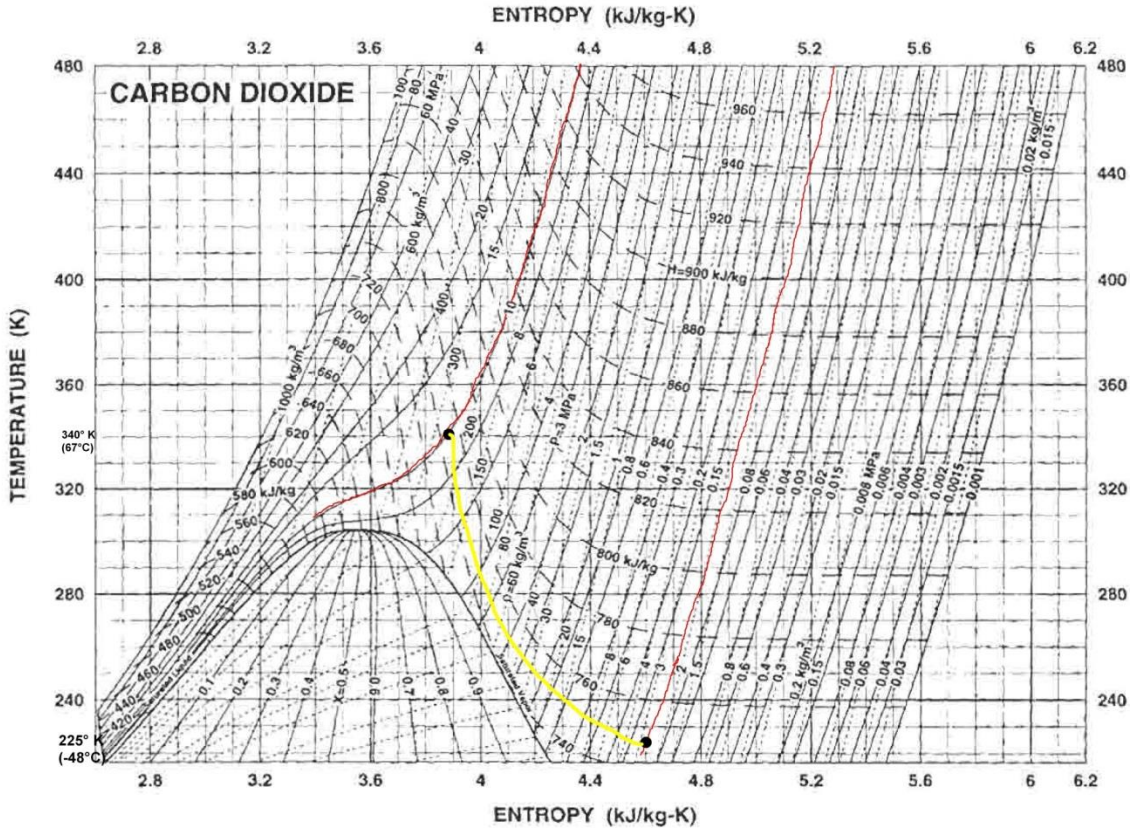

Figure 6.7 Temperature-entropy diagram for pure CO_2 (adapted from Jacobsen *et al.,* 1997)

Nevertheless, if the decompression conditions are known, it is possible to approximately establish if this phenomenon is likely to be triggered by using a temperature-entropy diagram for CO_2, as seen in Figure 6.7. The initial conditions considered for decompression are those at the test element outlet. As an example, the scaled outlet values obtained in Section 6.2 (67°C, 100 bar), were located in the diagram by intersecting this temperature from the y-axis with the isobar at 100 bar (10 MPa). Considering the process as isenthalpic, the enthalpy isoline was followed until it intersected the expected outlet pressure isoline, at 1 bar (0.1MPa, room conditions). This intersection provided a final temperature of -48°C approximately, achieved at the outlet system in ideal circumstances. Thus, it was safe to consider no dry ice to be formed.

To assure no dry ice would be formed during the decompression, the $SCCO_2$ could be vented out using two sequential back-pressure regulators and thus the flow temperature would decrease in two pressure-controlled steps. In the last step, heat could be added to prevent the formation of dry ice, such as applying hot air using a heat gun or wrapping the pipeline with heating tape. A simplified piping and instrumentation diagram (PID) of the $SCCO_2$ rig showing the two back-pressure regulators is suggested in Figure 6.8.

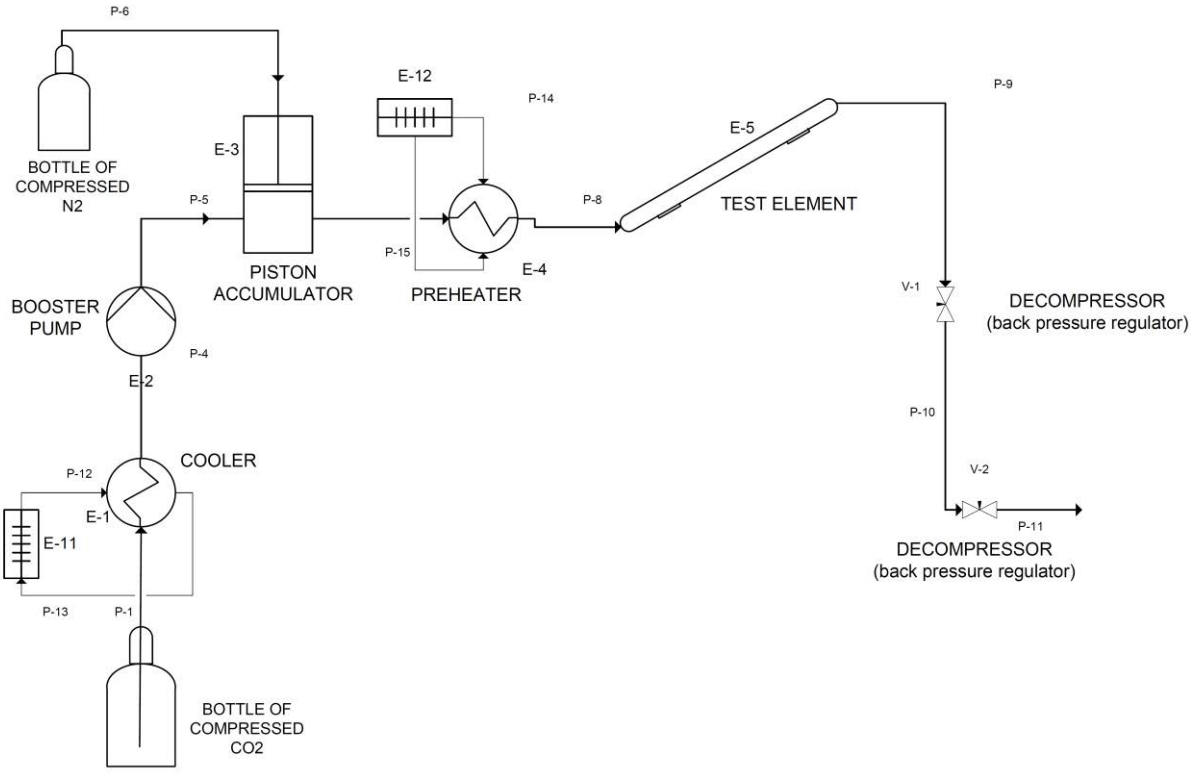

Figure 6.8 Simplified PID design for a SCCO2 rig

6.5. Summary

Using the scaling laws from by Zwolinski *et al.* (2011), hydrothermal conditions similar to those employed in Chapter 5 as a part of a water rig design were scaled to a system employing CO_2 as surrogate fluid in a $SCCO_2$ rig. The hydraulic similarity of the test element was constrained due to safety issues on the water rig and supplier limitations on the $SCCO_2$ rig.

The length of the test element and the values of $\dot{q}_{in}$ were calculated using two analytical methods for several values of G and D. The CVA only considered inlet and outlet conditions, combining the general energy and the heat exchanger equations as a means to estimate $\dot{q}_{in}$ and pipe length. The DFA used an energy balance on a VDE to produce a PDE that was simplified through several assumptions and axial temperature profiles were calculated. Both methods were compared using the water rig conditions as case study in order to estimate values of L at three different values of G and two different diameters. It was observed that relatively similar values of L were obtained when using low values of G, although higher values of G and D triggered a remarkable overestimation with the CVA.

A graphical method to determine the production of dry ice at the system outlet of a $SCCO_2$ rig was performed, and the scaled conditions obtained in Section 6.2 were used as example.

References

Bae YY, Kim HY (2009). Convective heat transfer to CO_2 at a supercritical pressure flowing vertically upward in tubes and an annular channel. *Experimental Thermal and Fluid Science;* 33: 329-39

Bae YY, Kim HY, Kang DJ (2010). Forced and mixed convection heat transfer to supercritical CO_2 vertically flowing in a uniformly-heated circular tube. *Experimental Thermal and Fluid Science;* 34; 1295-308

Bae YY (2013). Heat transfer in CO_2 at supercritical pressures in an eccentric annular channel. *Nuclear Engineering and Design;* 265: 1036-44

Çengel YA, Cimbala JM (2006). Energy analysis of steady flows. In: Jeans S (editor). Fluid Mechanics. Fundamentals and applications. *McGraw-Hill;* pp. 206-08

Cheng X, Liu XJ, Gu HY (2011). Fluid-to-fluid scaling of heat transfer in circular tubes cooled with supercritical fluids. *Nuclear Engineering and Design;* 241: 498-508

Gu HY, Zhao M, Cheng X (2015).Experimental studies on heat transfer to supercritical water in circular tubes at high heat fluxes. *Experimental Thermal and Fluid Science;* 65; 22-32

Incropera FP, Dewitt DP, Bergman TL, Lavine AS (2007). Heat exchanger analysis: use of the log mean temperature difference. In: Vargas VA (editor). Fundamentals of heat and mass transfer (Sixth Edition). *John Wiley & Sons;* pp. 675-85

Jackson JD (2007). Requirements for similarity in the case of heat transfer to fluids at pressures above the critical value and an approach to the correlation of experimental data. In: Sefiane S, Kew P, Wadekar VV (editors). Proceedings of the 10th UK National Heat Transfer Conference. *UK Heat Transfer Society;* paper G3

Jacobsen RT, Penoncello SG, Lemmon EW (1997). Thermodynamic properties of cryogenic fluids. In: Timmerhaus KD, Clark AF, Rizzuto C (editors). The International Cryogenics Monograph Series. *Springer US*; pp. 31-287

Menon ES (2005).Thermal Hydraulics. In: Taylor & Francis Group (editor). Gas pipeline hydraulics. *CRC Press*; pp. 249-74

Pioro IL & Duffey RB (2007). Practical prediction methods for heat transfer at supercritical pressures. In: Pioro IL & Duffey RB (editors). Heat transfer and hydraulic resistance at supercritical pressures in power–engineering applications. *Asme Press;* pp. 172-73

Pioro IL & Duffey RB (2007). General correlation for total pressure drop. In: Pioro IL & Duffey RB (editors). Heat transfer and hydraulic resistance at supercritical pressures in power–engineering applications. *Asme Press;* pp. 175-77

Pucciarelli A, Ambrosini W (2016). Fluid-to-fluid scaling of heat transfer phenomena with supercritical pressure fluids: results from RANS analyses. *Annals of Nuclear Energy;* 92: 21-35

Song JH, Kim HY, Kim H, Bae YY (2008).Heat transfer characteristics of a supercritical fluid flow in a vertical pipe. *J. of Supercritical Fluids;* 44: 164-71

Winterton RHS (1998). Where did the Dittus and Boelter equation come from? *International Journal of Heat Mass Transfer*; 41: 809-10

Zahlan H, Groeneveld DC, Tavoularis S (2014). Fluid-to-fluid scaling for convective heat transfer in tubes at supercritical and high subcritical pressures. *International Journal of Heat and Mass Transfer;* 73: 274-83

Zhang S, Gu H, Cheng X, Xiong Z (2014). Experimental study on heat transfer of supercritical Freon flowing upward in a circular tube. *Nuclear Engineering and Design;* 280: 305-15

Zwolinski S, Anderson M, Corradini M, Licht J (2011). Evaluation of fluid-to-fluid scaling method for water and carbon dioxide at supercritical pressure. 5th International Symposium on Supercritical Water-Cooled Reactors (SCWR5). *Canadian Nuclear Society*

7. Conclusions and recommendations for further work

7.1. Conclusions

The work presented herein was focused on understanding the heat transfer behaviour of a supercritical boiler belonging to a coal-fired power plant. This research will facilitate the means to increase the boiler thermal efficiency and eventually achieve compliance with the UK National Grid Code, in terms the dynamic response capabilities established during changes in power demand.

Numerical analysis was performed to study the hydrothermal behaviour of the water wall, as the section of the boiler where the fluid experiences large changes in thermophysical properties. The capacity of the simulation software Comsol Multiphysics to compute supercritical heat transfer was tested through validation and verification, prior to modelling the water wall conditions. Moreover, design aspects were considered for the construction of an experimental rig in order to validate the models produced. This section describes the main conclusions and findings of this research.

a) The models were validated by successfully reproducing experimental data:

- The trends expected in the heat transfer coefficient were obtained when applying identical boundary conditions as those from the experimental work, considering the working pressure was increased to observe boiler conditions.
- A near-wall treatment using a $y_1^+ < 1$ and a refined radial mesh were discovered as essential procedures to accurately model supercritical heat

transfer, because they provided the best agreement with the experimental data. Similarly, applying second-order discretisation showed better validation results at the expense of an increased computational time.

- The presence of additional forces affecting the heat transfer performance was confirmed: the experimental data showed the influence of factors related to pipe orientation. The model was capable of capturing the extent of influence of these factors, namely buoyancy forces, flow acceleration and large thermophysical changes.
- The heat transfer behaviour of the modelled system was investigated using a series of hydrodynamic and thermal parameters. Hydrothermal performance was good at the inlet and outlet of the pipe; however the outlet region showed laminarisation. Moreover, the region before the core flow reached PSC temperature displayed good thermal performance as a consequence of the favourable balance of the combined thermophysical property variations, especially the fluid heat capacity.

b) The model performance was verified employing numerical data under strong buoyancy conditions:

- The qualitative trends observed in the numerical system to be verified were successfully reproduced by computing a 2D model with the same boundary conditions and using second-discretisation order.
- The heat transfer behaviour obtained in the computed model was studied. The q_w/G ratio of the system was higher compared to the numerical validation,

which quickly triggered the PSC transition near the wall, and thus flow laminarisation was induced at the pipe inlet. Downstream, strong buoyancy forces led to M-shaped velocity profiles, which improved the thermal efficiency on the first axial half of the pipe until the flow progressively turned to the forced-convective regime. Near the pipe outlet, the core flow approached the PSC temperature and thus the heat transfer behaviour improved.

- The 2D model was converted to 3D; the computations performed showed that only the results representing the first axial half of the pipe were verified. It was observed that when the mesh employed was not refined enough, and first-discretisation order was employed, the model did not reproduce the results correctly at the end of the pipe. This was because the coupling of the PDEs was deteriorated by the increase in fluid temperature and turbulence near the wall, as well as by the acceleration triggered at the core downstream the PSC transition.
- Ribs displaying different axial patterns (straight, helical) were attached on the inner surface of the 3D geometry. Computations were made using identical boundary conditions, although the pipe length had to be reduced. This proved to be useful at promoting turbulence, thus increasing the heat transfer performance of the flow. The helical ribs presented the most favourable configuration for turbulence, but the improvement was only observed at the pipe outlet. It was concluded the twist angle of the helical ribs was not large enough to promote better turbulence than the straight ribs for the considered pipe length.

c) Knowledge about the thermal performance of a SCCFPP was expanded:

- In order to reduce the meshable domain and afford the numerical study of the heat transfer behaviour, the hydrothermal boundary conditions of a single pipe from the water wall were scaled and applied to a 2D test element in Comsol. The pipe diameter was reduced while the mass flux had to be increased to maintain the turbulence regime. This produced large values of y_1^+ that could not be decreased due to computational limitations. Nevertheless, the qualitative trends were still captured.
- Buoyancy affected the pipe inlet and turbulence was triggered, though the small pipe diameter limited the extent. Heat transfer performance was mainly improved near the entrance region by the large property changes prior to the onset of the PSC transition in the bulk.
- Once the bulk surpassed the PSC temperature, thermal conductivity progressively increased. However, the flow accelerated simultaneously and impaired shear turbulence, consequentially impairing heat transfer in this region. It was acknowledged that thermal acceleration had a relevant role impairing turbulence due to the reduction of the pipe diameter and the increase of mass flux in the scaling process.
- As a consequence of the induced thermal acceleration, the flow was laminarised at the pipe outlet, despite turbulence increased near the wall.
- Scaled thermal boundary conditions at 1000° and 2200°C were employed as furnace chamber temperatures for comparison. Each value triggered the PSC transition at a different location in the pipe. Despite suffering from stronger

flow acceleration effects past the PSC transition, the simulation at a T_∞ of 2200°C reflected a better heat transfer performance overall due to the fact that the LPV region produced near the pipe inlet was thinner and thus the impairment triggered in T_x and T_y was reduced. Moreover, the thermal conductivity of the flow further increased after dropping downstream the onset of the PSC temperature in the bulk.

- With the numerical analyses performed, it was suggested that decreasing the mass flux in the real water walls to induce a free-convective regime near the pipe inlet would improve thermal performance if M-shape velocity profiles were triggered. Additionally, the extent of thermal acceleration would decrease past the PSC transition. It was suggested that employing vertical rifled pipes would facilitate this operation as it would prevent heat transfer deterioration.
- Similarly, employing lower values of inlet temperature would delay the PSC transition and the large property variation region produced upstream would improve the heat transfer performance.
- It was observed that at 300 bar, the thermal conductivity of the fluid increased along with the temperature above 500°C. Therefore, increasing the fluid temperature beyond this value would positively affect thermal performance, if turbulence was favourable.

d) Two design approaches of the test element in a supercritical rig were presented:

- A control volume analysis applied on a heated pipe would use given inlet and outlet parameters as a means to calculate the corresponding heat rates and pipe lengths.
- On the other hand, a 1D differential analysis would provide pipe lengths and the flow temperatures achieved.
- Comparing the two methods, relatively similar pipe lengths were obtained when using low values of mass flux. Otherwise, the control volume analysis would overestimate the results.

7.2. Recommendations for further work

The present work gave way to a series of recommendations for future studies, as a means to benefit this area of research from the issues that arose and could not be possibly investigated in more detail.

a) Building an experimental rig to validate the models generated: this is a paramount step when performing numerical analyses as a means to complement and reinforce the computed results obtained using in-house data. The design guidelines offered in the present thesis could be used as starting point for the construction of a water rig if economically feasible, or a supercritical CO_2 rig instead by properly applying scaling laws.

b) Definition of thermophysical properties of supercritical water at several pressures: when validating a model prior to performing an independent numerical study, it

would be useful to produce two types of simulations. One would be performed with the fluid properties at the working pressure employed by the authors of the experiment to validate, and a second one using the same boundary conditions but specifying the fluid properties at the desired pressure for the independent study. Therefore, the model would be validated and at the same time the performance at two different pressures would be compared.

c) Use of 3D geometries without axial symmetries in supercritical heat transfer: computing full 3D domains would allow the study of horizontal pipes. Moreover, when assessing the performance of internally ribbed pipes compared to smooth surfaces, the computer employed should have enough memory to allow the computation of each system using the same pipe length.

d) Smaller values of dimensionless distance to the wall (y_1^+): modelled systems obtained by scaling boiler conditions involve large values of mass flux if the hydraulic similarity is maintained by decreasing the pipe diameter. As a consequence, the values of y_1^+ will increase considerably. In order capture the quantitative trends of the simulation, a low y_1^+ must be maintained and thus the refinement near the wall must be more intense. The computer employed must be capable of undertaking these analyses keeping reasonable simulation times. In addition, a computer powerful enough would allow larger pipe diameters and lengths so the system would approach working conditions closer to the real system, consequently reducing the scaling.

e) Use of second-order discretisation by default: numerical works related to supercritical heat transfer should be always performed using second order of discretisation. Thus, not only the qualitative trends of the system could be researched, but also the quantitative values obtained would be prone to interpretation.

f) Time-dependent studies: besides the steady state computations performed in the present thesis, time-dependent simulations would offer a valuable approach in terms of understanding the dynamic responses of the system if the thermal boundary condition or the mass flux changed their input at a given time.

g) Use of radiative heating in the simulation: due to the proximity of the water wall pipes to the furnace, where combustion takes place, most of the energy would be transferred to the water cycle in this section as radiation. It would be of high interest to carry simulations specifying the thermal boundary conditions as such.

h) Post-processing of 2D images using Matlab: the computed 2D images can be analysed in Matlab, using codes from mixing techniques as a means to research if the areas revealing a better mixing also reflect an improvement in the HTC.

i) Use of a different CFD software to approach simulations: other CFD codes, such as Ansys Fluent, are more popular in the literature review and thus it is highly desirable to carry the simulations employing the same working and boundary conditions as a means to verify the results between packages.

j) Dynamic process simulators: software packages such as SimSci DYNSIM or MATLAB SIMULINK could be focused on the dynamic responses of the thermal-hydraulic side of the water cycle. As a consequence, they would represent a useful complement for a numerical study of supercritical boilers combined with time-dependent simulations in Comsol Multiphysics.

Appendix. Methods in Comsol Multiphysics

Abbreviations

1D	one dimension
CFD	computational fluid dynamics
CHT	conjugate heat transfer
DOF	degrees of freedom
HTC	heat transfer coefficient
LHS	left-hand side
PSC	pseudo-critical
RANS	Reynolds-averaged Navier-Stokes
RHS	right-hand side
SCW	supercritical water
SST	shear stress transport (turbulence model)
TKE	turbulent kinetic energy

Dimensionless numbers

Pr	Prandtl number
Re	Reynolds number

Greek symbols

β_1	model constant [-]
Δ	del operator
σ	distance from the pipe wall to the buffer layer [m]
σ_w	model constant [-]
ε	rate of dissipation of kinetic energy [$m^2\ s^{-3}$]
λ	fluid thermal conductivity [$W\ m^{-1}\ degC^{-1}$]
μ	dynamic viscosity [$kg\ m^{-1}\ s^{-1}$]
ν	kinematic viscosity [$m^2\ s^{-1}$]
ρ	density [$kg\ m^{-3}$]
τ	shear stress [$N\ m^{-2}$]
ω	specific turbulence dissipation rate [s^{-1}]

Geometric definitions

D	inner diameter of pipe [m]
R	inner radius of pipe [m]
y	distance to wall [m]
y^+	dimensionless wall distance [-]
y_1^+	dimensionless wall distance of first mesh layer to wall [-]

Roman symbols

C_p	isobaric heat capacity [J kg^{-1} degC^{-1}]
F	volume force vector [m s^{-2}]
G	mass flux of fluid [kg m^{-2} s^{-1}] or reciprocal wall distance [m^{-1}]
g	gravitational acceleration [m s^{-2}]
h	convective heat transfer coefficient [W m^{-2} degC^{-1}]
I	identity matrix [-]
I_T	turbulence intensity [%]
k	turbulent kinetic energy [m^2 s^{-2}] or solid thermal conductivity [W m^{-1} degC^{-1}]
l_{ref}	reference length scale [m]
l_w	distance to the closest wall [m]
L_T	turbulent length scale [m]
n	normal vector of boundary [-]
p	absolute pressure [Pa or bar]
q	applied heat flux vector [W m^{-2}]
T	temperature [K or °C]
u	velocity field [m s^{-1}]
u^*	friction velocity [m s^{-1}]
v	radial flow velocity [m s^{-1}]
U	mean flow velocity [m s^{-1}]

Subscripts

$(\dots)_0$	at initial conditions
$(\dots)_{ext}$	at external/outer conditions
$(\dots)_{in}$	at inlet conditions
$(\dots)_o$	at outlet conditions
$(\dots)_{pc}$	at pseudo-critical conditions
$(\dots)_T$	at turbulent conditions
$(\dots)_w$	at inner wall conditions
$(\dots)_x$	axial increment or horizontal component
$(\dots)_y$	radial increment or vertical component

A.1. Main stages in CFD analysis

Modelling in computational fluid dynamics (CFD) is a step-wise process. These steps are normally the same regardless of the software employed, and can be observed in Figure A.1. Some CFD packages like Ansys CFX have created specific programs for each step, while in Comsol Multiphysics all the stages are included within the same program; and yet the purpose is the same.

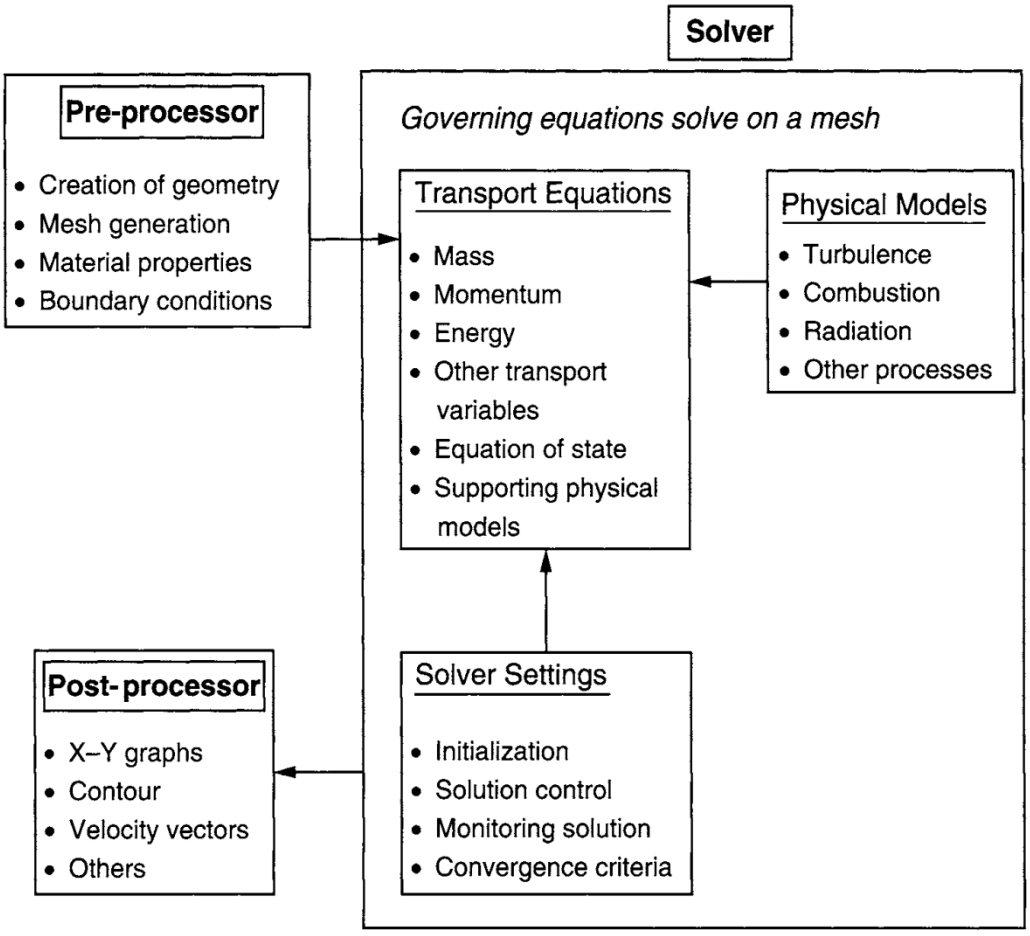

Figure A.1 The three main stages of CFD analysis and their interconnections (Tu *et al.,* 2008)

The main CFD stages are summarised as:

- Pre-processing: involves all the information the model equations need to grant convergence of the numerical calculation. Aspects such as process variables, material properties, geometry, boundary conditions or mesh are defined at this stage.
- Solver step: the model equations are defined and the software assembles all the information and goes through the numerical calculation using specific solver techniques. The process will finish when the convergence criteria are reached.
- Post-processing: after a solution has converged, all the results obtained are stored. Every CFD program has several tools in order to visualise and interpret the output data.

A.2. Pre-processing stage

A.2.1. Creation of a new simulation in Comsol Multiphysics

When creating a new simulation, Comsol offers the possibility to either choose a blank model or use a step-wise guide called “model wizard”. In the first case, Comsol will lead directly to the interface, and from the root everything necessary will have to be manually included. In the second case, Comsol will take the user through three specification steps in order to create and customise the model interface containing the most basic aspects of the pre-processing and solver stages. These specifications steps are space dimension, the physics relevant to the simulation and the study performance:

- Space dimension: Comsol offers a wide range of dimensions, from zero-dimension (points) to three-dimension (3D). For one and two dimensions (1D and 2D), an axisymmetric configuration is available as a means to save one level of dimension in computing resources when solutions are accepted as symmetrical around an axis. For the present thesis, 2D and 3D dimensions have been selected.
- Physics selection: among all the different modules offered by Comsol, the “Heat Transfer Module” and “CFD Module” were purchased for the present thesis, as the physics involved are related to convective heat transfer in turbulent flow within pipes. Figure A.2 shows the different options and the selected physics path.

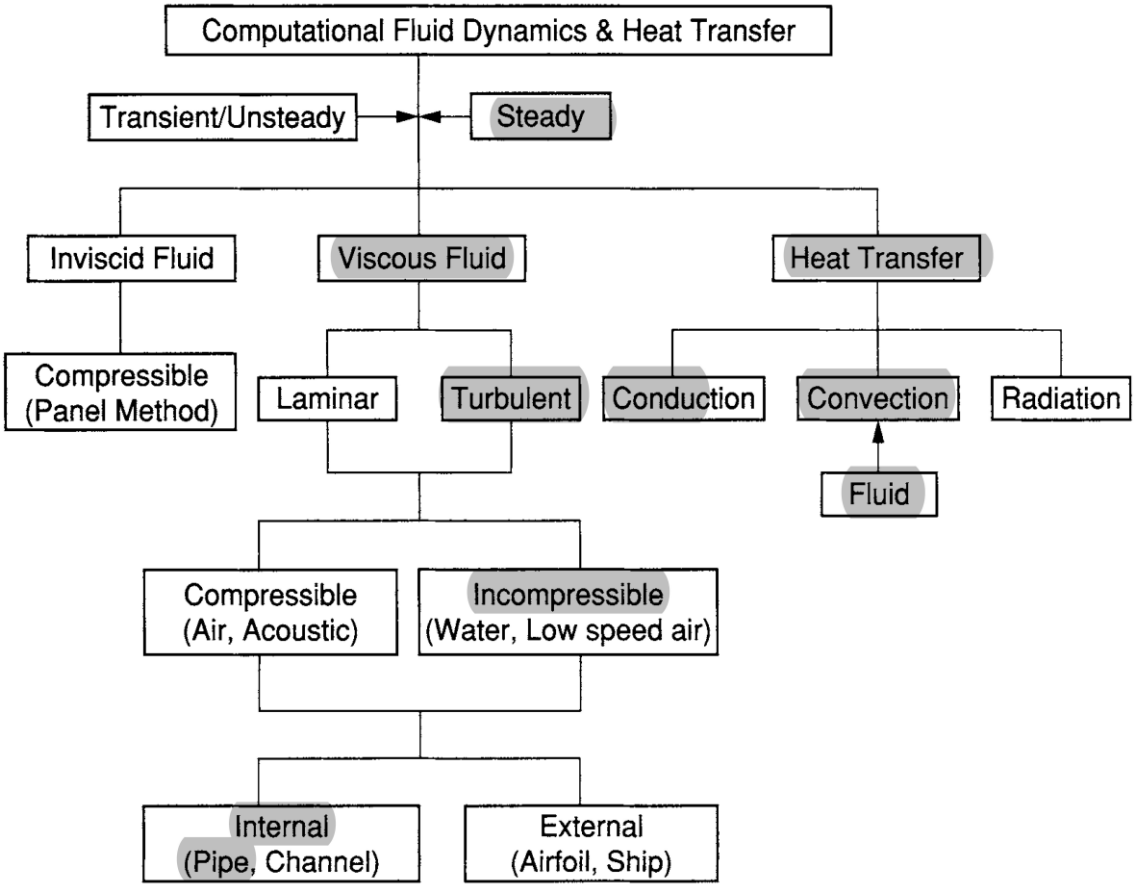

Figure A.2 Flowchart of physics related to CFD. Highlighted, those relevant to the present thesis (Tu *et al.,* 2008)

As will be explained in Section A.2.3, supercritical water (SCW) was created in Comsol as an isobaric material, because the thermodynamic properties are weak functions of pressure, and because the pressure drop in the system was firstly assumed and later confirmed as negligible for all the simulations. In addition, the flow velocity is very important to differentiate between compressible and incompressible fluid behaviour. Therefore, prior to doing any simulation a range of expected working temperatures was selected at a fixed pressure of 30 MPa making sure it was passing through the pseudo critical (PSC) point, and by using the National Institute of Standards and Technology (NIST) database. Two physics paths were offered for turbulent convective heat transfer in incompressible flows:

- Fluid flow > Non-isothermal flow > Turbulent flow.
- Heat transfer > Conjugate heat transfer > Turbulent flow.

Conjugate heat transfer (CHT) involves the coupling of conduction heat transfer in solids and convection heat transfer in fluids. In terms of simulation, non-isothermal flow and CHT are virtually the same, although the CHT physics includes by default a node for the heat transfer in solids, while in non-isothermal flow this node must be added if necessary. Moreover, the turbulent model must be considered.

- Study selection: this section defines the procedure that Comsol performs to go through the numerical calculation of the solution, depending on the physics previously selected. Moreover, the study can be performed at stationary (steady state) or time-dependent conditions.

With all this information provided the model wizard transfers all the selections to the simulation interface, containing three pull-down nodules, namely component, study and results. The first contains all the information for the pre-processing stage, the second stores the solver procedure and the third is still blank, prepared to display the data produced after computation.

A.2.2. Geometry

Due to a modular conception, Comsol includes a built-in CAD tool, which is useful for relatively simple geometries. In case of using complex geometries, the “CAD Import

Module" is strongly recommended as it allows importing geometries from different specialised CAD software (among them, AutoCAD, SolidWorks or SpaceClaim). For the undertaken research, straight pipe elements have been considered both in 2D and 3D, therefore using the Comsol CAD engine was convenient. In all simulations, the preferred length unit was *mm* for post-processing purposes and the angular unit was degrees. A default relative repair tolerance of $1x10^6$ is selected, which will determine when different geometric entities are merged or not.

Once all the relevant geometries have been created, Comsol offers the chance to finalise the process either forming a union or an assembly. In a union, domains will be created with boundaries in between and all their space can be meshed, assigning physics, boundary conditions, material properties, etc. This is the most common option for most geometries. An assembly will create a collection of independent parts where boundaries must be connected by using pairs and the applied mesh is different in every domain. This might be useful when importing complex geometries (COMSOL Multiphysics, 2013c).

- 2D geometries: for the simplest geometries where only the fluid domain was considered, only a rectangle entity was necessary. This represents half the fluid domain if symmetry is applied later on, or the entire fluid domain if not. An unheated entrance length can be applied as a means to allow the boundary layer to develop without the interference of temperature profiles for stability reasons. This is represented by creating a point entity on the wall boundary a certain distance from the inlet, in order to separate boundaries. When a solid domain is

also considered such as the metal section of the pipe, another rectangle of the same axial length but reduced height is placed next to the fluid domain.

- 3D geometries: creating 3D entities is a more complex process with the built-in CAD tool. The procedure starts by creating a work plane, where a plane geometry is defined containing all the 2D basic entities which, after using several Boolean operators (intersection, union, difference, etc.), will be combined to form the final 2D geometry and extruded in the normal axis of the work plane to produce the final 3D geometry. Smooth pipes were the simplest to create by extruding two concentric circles, while internally ribbed pipes were produced by a combining a circle with a series of rectangles displaying different inclination angles. To produce the spiral ribs, the extruded geometries for both fluid and solid domains were twisted 15^0, giving the appearance shown in Figure A.3.

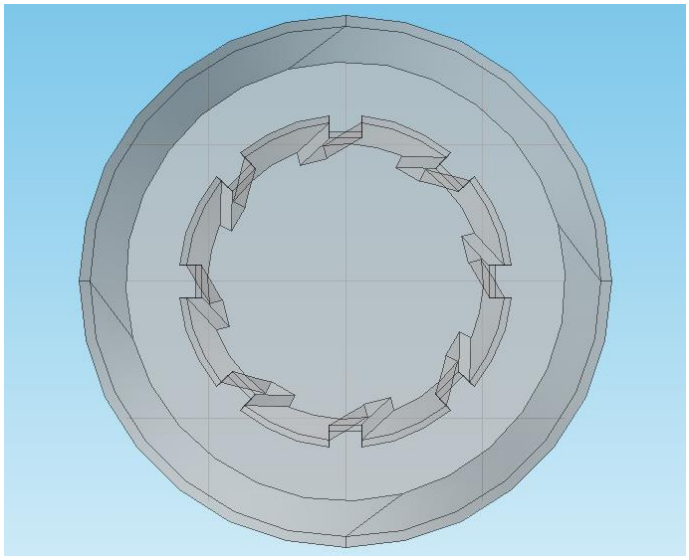

Figure A.3 Axial view of ribbed pipe geometry (inlet side)

A.2.3. Defining SCW properties in Comsol

The specifications of SCW for the fluid domain at 300 bar were based on real working conditions within the water wall section located in the furnace of supercritical boilers, gathered from the water cycle of a supercritical coal-fired power plant in Hebei (China). More detailed data for the computations at boiler conditions performed in Chapter 5 was provided by the research studies on water wall pipes performed by Zima *et al.* (2010) and Huilin *et al.* (2013).

The thermodynamic properties of water necessary for the computations, namely the fluid density, isobaric heat capacity, viscosity and thermal conductivity, were considered at isobaric conditions. This is due to the fact that the pressure drop experienced by water passing through the full length of water walls in the supercritical power plant in Hebei was observed to be around 20 bar; and the largest test element simulated was not longer than 20 metres. Considering that the thermodynamic properties of water are strong functions of temperature while pressure as a weaker effect, this assumption is reasonable. Therefore, using piece-wise polynomials dependent only on temperature, the material properties were defined within a range of 300-500°C for similarity with the water wall inlet-outlet conditions. Also, the polynomials had the temperature range expanded for the scaled boundary conditions in Chapter 5.

For the CHT simulations, the metal domain used thermodynamic properties similar to the Inconel alloy 625, described as linear polynomials dependent solely on temperature. This material was selected because it is widely used in experimental

studies with supercritical flows due to its high thermal resistivity, dissipating heat by the Joule effect to the flow when an electrical current is passed through with two terminals. It is also a heating option available in Comsol.

A.2.4. Boundary conditions

In Comsol Multiphysics or any other CFD software, boundary conditions are restrictions applied to the boundaries of the physical model in the form of equations that simplify the solutions to the governing equations. A summary of the most relevant is listed in Table A.1, considering the turbulence model SST was selected and that all the symbols contained in the equations are properly defined in the nomenclature section.

Table A.1 Summary of boundary conditions applied in the CHT simulations

Boundary Condition	Specification	Equation
Solid Heat Transfer	CHT	$\rho C_p u \cdot \nabla T = \nabla \cdot (k \nabla T)$;
Thermal insulation/Outflow	Prevented conduction (thermal sink)	$-n \cdot (-k \nabla T) = 0$;
Wall	No-slip condition	$u = 0$; $k = 0$; $\omega = \lim_{l_w \to 0} \frac{6\mu}{\rho \beta_1 l_w^2}$; $G = \frac{2}{l_{ref}}$;
Fluid	Wall Distance	$\nabla G \cdot \nabla G + \sigma_w G(\nabla \cdot \nabla G) = (1 + 2\sigma_w) G^4$; $l_w = \frac{1}{G} - \frac{l_{ref}}{2}$;
Volume force	Gravity in RANS	$F = \begin{pmatrix} g_x \\ g_y \end{pmatrix}$;

Inlet (velocity)	Unknown inlet k and ω: turbulent length scale (L_T) and intensity (I_T)	$k = \frac{3}{2}(U_0 I_T)^2$;	$\omega = \frac{k^{1/2}}{(\beta_0^*)^{1/4} L_T}$;
	Known inlet k and ω	$k = k_0$	$\omega = \omega_0$
Outlet	Pressure condition and viscous stresses	$\left[-pI + (\mu + \mu_T)(\nabla u + (\nabla u)^T) - \frac{2}{3}(\mu + \mu_T)(\nabla \cdot u)I - \frac{2}{3}\rho k I\right] n = -\widehat{p_0} n$	
	Zero pressure outlet	$p_0 = 0$;	
Thermal Boundary Conditions	Wall Temperature	$T = T_0$;	
	Heat flux	$-n \cdot (-k\nabla T) = q_0$;	
	Convective heat flux	$-n \cdot (-k\nabla T) = h \cdot (T_{ext} - T)$	

The SST model, including its turbulent parameters k and ω are further described in sections A.3.2 and A.3.3. In addition, a detailed analysis on the SST model is presented in the study by Podila *et al. (*2015). Further information about the existing boundaries is described in the reference manual (COMSOL Multiphysics, 2013c).

It is worth mentioning that symmetry was considered on certain boundaries, as a means to save computational cost when symmetry planes exist, mirroring fluid and heat flow phenomena across the plane (*Çengel & Cimbala,* 2006b). However, in cases with strong buoyancy effects in the flow (normally using high heat flux or large pipe diameters) it is not recommended to use symmetry in horizontal or inclined flows, as the gravity will have different effects on the top and bottom sides of the pipe.

A.2.5. Defining model parameters

It is a good practice when starting a simulation to previously define the most important parameters, as it saves time and effort. In this case, the most relevant parameters were:

- Dimensional: inner and outer pipe diameters, heated pipe length and unheated pipe entrance length.
- Thermal: inlet temperature, wall temperature (or wall heat flux).
- Hydrodynamic: inlet value for mass flux and corresponding inlet values for density and viscosity of water at the desired inlet temperature using the NIST database. With all these values, the inlet velocity (u_{inlet}) and Reynolds (Re_{inlet}) were calculated, as shown in equations (A.1) and (A.2), respectively.

$$u_{inlet} = \frac{G_{inlet}}{\rho_{inlet}} \quad \textbf{(A.1)}$$

$$Re_{inlet} = \frac{G_{inlet} \cdot D_{inlet}}{\mu_{inlet}} \quad \textbf{(A.2)}$$

  In equations (A.1) and (A.2), G represents the mass flux, ρ the flow density, D the inner pipe diameter and μ the flow viscosity.
- Turbulent: when the inlet turbulence parameters are not available the turbulent intensity (I_T) and the turbulent length scale (L_T), defined in equations (A.3) and (A.4) respectively, are used to define the extent of turbulence at the inlet (COMSOL Multiphysics, 2013a).

$$I_T = 0.16 \cdot Re_{in}^{-1/8} \quad \textbf{(A.3)}$$

$$L_T = 0.07 \cdot D_{in} \quad \textbf{(A.4)}$$

A.2.6. Creating a developed flow at the inlet boundary

When the flow inlet is defined using a constant value of inlet velocity, the velocity profile at the entrance is being defined as flat. As a consequence, velocity gradients will automatically appear downstream the inlet as a means to develop the boundary layer. On the other hand, if the inlet turbulence parameters are unknown they are normally replaced by approximations such as L_T and I_T. As a result, the computations of sharp velocity gradients at the inlet employing turbulent approximations can sometimes trigger instabilities. Additionally, if the pipe is being heated from the entrance or shortly after, the temperature profiles will develop as well. All these phenomena are known as inlet effects.

In cases of inlet instability it is desirable to have a fully developed turbulent flow at the entrance. To achieve this, a previous simulation (pre-model) can be performed at isothermal conditions as a means to produce a fully developed turbulent flow, and thus the flow parameters obtained at the outlet boundary can be transferred (mapped) to the inlet boundary of the heated pipe. As a consequence, the pre-model geometry must be identical as the model in terms of these two boundaries (flow outlet of pre-model and flow inlet of model).

In computational terms, a turbulent flow modelled with the Reynolds-averaged Navier-Stokes (RANS) equations is considered fully developed when the turbulent viscosity (μ_T) at the bulk of the flow remains constant (COMSOL Multiphysics,

2013d). The μ_T, also called eddy viscosity, does not have a physical meaning like the dynamic viscosity. Instead, it is a parameter created to describe turbulence in RANS models. As explained in Chapter 2, in most commercial CFD packages including Comsol, turbulence is modelled with RANS approximation rather than resolved, by using the linear eddy viscosity approach.

In order to allow the flow to be fully developed in the pre-model, the pipe length must be large enough. In many engineering scenarios, a length beyond 10 pipe diameters is enough to cover the hydrodynamic entry length (*Çengel & Cimbala*, 2006a). However, it strongly depends on the system and the best practice is to employ different pipe lengths until the μ_T at the bulk of the flow stabilises (COMSOL Multiphysics, 2013b). When the outlet properties of the pre-model are mapped to the flow inlet of the model, a coupling operator called *linear extrusion* is selected. This allowed exporting the established outlet boundary conditions as new inlet boundary conditions, such as the velocity profile or the turbulence variables.

A.2.7. Initial values

The initial conditions provide values for several parameters when time is zero as a means to stabilise the first iterations of the simulation until it reaches steady state. These parameters include the velocity field, pressure, turbulent parameters, reciprocal wall distance and temperature.

The thermodynamic properties were defined to depend only on temperature, and thus the initial value of pressure did not seem to affect the simulations sensibly. The

initial temperature is normally selected to be the one at isothermal conditions, which is the same as the inlet boundary. For aspects such as the turbulent parameters and the reciprocal wall distance, Comsol has a series of pre-defined formulae and do not need to be modified. The velocity field would seem an important initial condition, however it has been observed that setting a value (for instance the mapped outlet profile from the pre-model) or leaving this section blank does not affect the simulation performance in this research. Moreover, if the ramping technique is employed when applying a heat source (described in Section A.6.4), this step becomes unnecessary as the previous solution will be taken as initial condition.

A.2.8. Meshing

Once all the materials, initial values and boundary conditions have been specified within the geometry, the different computational domains will be discretised in cells (elements) by creating a grid or mesh (see Figure A.4). These elements contain the calculation points where the governing equations will be applied. In this case, heated, turbulent flows with several variables to compute are solved, which requires fine meshes. However, when meshing, the perfect balance involves simplifying the mesh as much as possible without losing too much detail, because otherwise the computing time would be prohibitive.

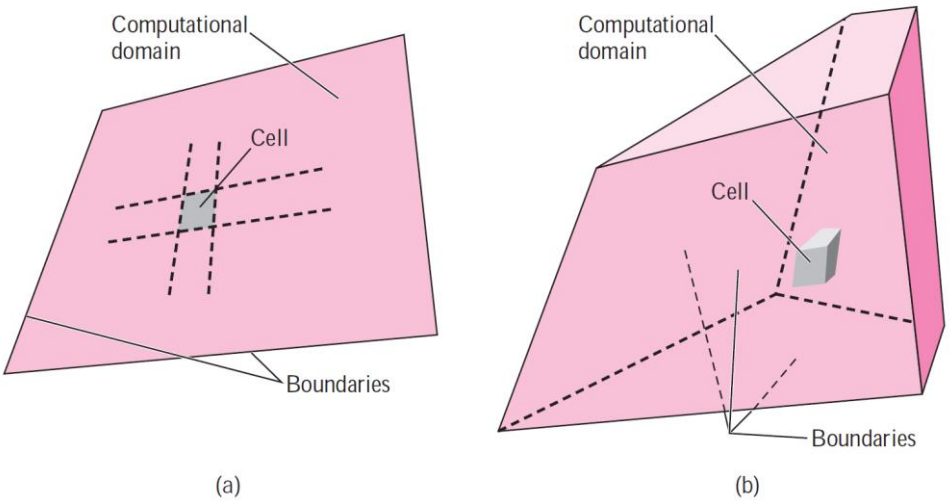

Figure A.4 Mesh elements (cells) in 2D (a) and 3D (b) computational domains (*Çengel & Cimbala,* 2006b)

- Meshing sequence: in Comsol, there are two types of meshing sequence:

  - Physics-controlled mesh: it is an automatic process, the only parameter to choose is the element size in a range from extremely coarse to extremely fine. Comsol will apply different meshing techniques depending on the information provided in the previous steps.
  - User-controlled mesh: if no mesh has been created the mesh nodule will still allow adding manually the different options, or if a previous physics-controlled mesh has been created the nodule will expand and will show the different features automatically selected. When learning how to mesh, it is often convenient to apply first a physics-controlled mesh and afterwards switch to user-controlled to manually modify the default meshing sequence.

- Meshing elements:

  - Free triangular (2D) or pyramid (3D): it is the default element in 2D. A flexible mesh with no pre-established arrangement (called unstructured, as seen in Figure A.5) and consequentially adaptable to all geometries.
  - Free quadrilateral (2D) or hexahedron (3D): it is an unstructured mesh, more convenient for rectangular geometries.
  - Free tetrahedral (tetrahedron): it is also an unstructured mesh, only available for 3D geometries. It is selected by default in 3D geometries.
  - Mapped: a structured, customisable mesh for 2D rectangular geometries.

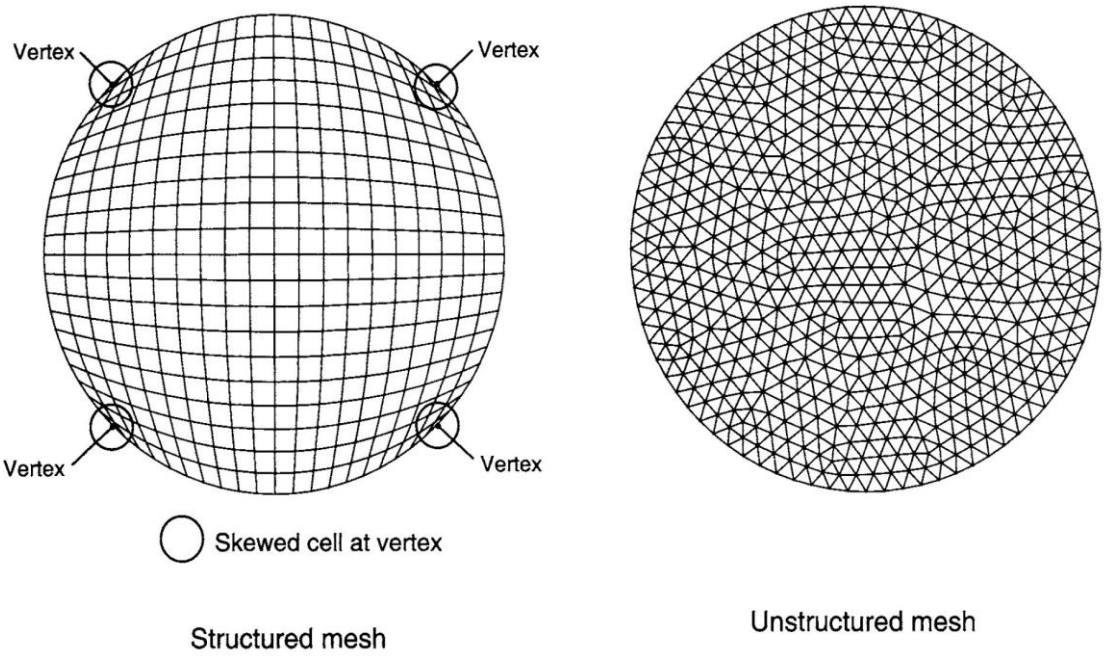

Figure A.5 Structured and unstructured 2D mesh elements (*Tu et al.*, 2008)

In this thesis, mapped elements were employed because all 2D geometries are rectangular and provide good control. For 3D and due to complexities in certain

meshes such as ribbed pipes, an unstructured, free tetrahedral mesh was selected.

- Element size and distribution: when manually controlling the mesh nodule, elements are added as sub-nodules during the meshing sequence and they can include a “size” option. Here, aspects such as maximum or minimum element size can be applied as well as maximum element growth rate (from an area with smaller elements to another region with bigger elements). Similarly, by right-clicking the element sub-nodule a “distribution” option can be activated to modify the number of elements on the boundaries. These two options allow controlling unstructured meshes to make them more structured, as well as manually refine the mesh.
- Boundary layer mesh: the best procedure to capture the steep velocity and temperature gradients occurring in the viscous sublayers of the developed boundary layer is to refine the grid in this region, applying a special mesh composed of narrow rectangles (2D) or prisms (3D) with high aspect ratio such that these elements display the short edges normal to the wall and the large edges parallel to the wall. It is worth noting that although this mesh is known as “boundary layer” in Comsol, it should not be mistaken for the real boundary layer, which develops from the inlet until it fills the entire flow domain. Although this mesh can be manually expanded to occupy the full flow domain, it will be automatically placed such that it focuses on the viscous and buffer sublayers by default.

In 2D, this boundary layer mesh is formed of layered quadrilateral elements, while in 3D it is formed of hexahedron elements. By using the boundary layer properties option, its performance can be manually controlled:

- Number of boundary layers: defines the amount of calculation points normal to the wall.
- Boundary layer stretching factor: helps making a progressive transition to the interior mesh (bulk flow). By controlling this parameter and the number of boundary layers, the thickness of the boundary layer can be established.
- Thickness of the first layer (y_1^+): it can be adjusted automatically with a factor; however when setting the y_1^+ it is much better to manually input a thickness obtained from the Law of the Wall explained in Section A.3.4.

▪ Setting an initial value for y_1^+: when internal flow is first modelled in Comsol, the exact values of y_1^+ cannot be known until the first results are obtained. Thus, the normal procedure when trying to set a good value for y_1^+ is as follows:

- Choose an initial value of y_1^+, as described in section A.3.4.
- Use an online calculator (www.pointwise.com/yplus/) or the set of equations seen in the Law of the Wall, in order to obtain the thickness of the first layer (in *mm*) as necessary input in Comsol.
- Choose an appropriate stretching factor for the boundary layer mesh to expand as desired. In this case, the pipe radius and the number of radial elements must be considered. Within the Comsol environment this is

achievable in 2D geometries, although in 3D there has to be always a tetrahedral mesh as support below the boundary layer mesh, and it is tougher to control.

A.3. Solver stage: turbulence model selection

A.3.1. Wall-function vs. Low-Re models

Although the eddy viscosity models are not the most accurate of numerical approaches, their memory demand is satisfied by most computers purchased by CFD users, hence their popularity. Inside the eddy viscosity models, there is a wide range of turbulence models, depending on the procedure to calculate μ_T. As a rule of thumb, the higher the number of variables to solve the μ_T, the more accurate the model but the less robust it is. Thus, the RANS models using two equations to solve the transport equations (two-variable models) were selected in Comsol due to the good balance between accuracy, robustness and computational time. Depending on how these two-equation turbulence models approach the mesh treatment near the wall, there are two groups: wall-function models, and Low-Re models.

Table A.2 Two-equation turbulence models offered by Comsol (based on near-wall treatment)

Variables to solve μ_T	Wall-function models	Non wall-function models
2	k-ε k-ω	Low Re k-ε SST
1	-	Spallart-Allmaras
0	-	L-VEL yPlus

In Table A.2 a summary of the two-equation turbulence models in Comsol is observed. Turbulence models computing stable flows and predictable boundary layers preferably use semi-empirical equations near the wall, known as “wall

functions". These functions assume the flow in the layers near the wall to behave like the fully developed turbulent boundary layers further form the wall (see Figure A.6) instead of considering the no-slip condition (hence their name high-Re models). This automatically sets a nonzero solution for the velocity at the wall, and thus links directly with the velocity profiles at the boundary layers further away from the wall (log-law region). As a consequence the model is simplified, saving memory power.

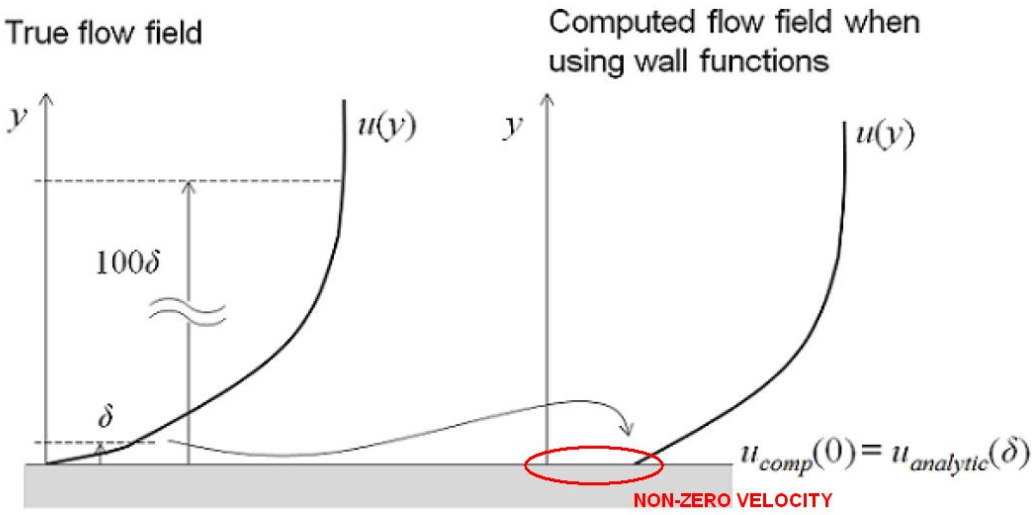

Figure A.6 Performance of wall functions (adapted from Frei, 2013b)

Nevertheless, due to the computations performed in the present thesis related to turbulent convective heat transfer at supercritical conditions, the flow within the viscous regions of the boundary layer will suffer considerable modifications and thus the boundary layer will expand and contract. These modifications in the viscous layers will affect the temperature profiles in the entire flow domain, and thus a refined mesh is needed near the wall to additionally solve the viscous regions of the boundary layer.

The models computing the viscous region near the wall apply the no-slip condition, and thus the Re achieves very low values in this zone (hence the name Low-Re models). They allow refining not only the first layer, but also the subsequent inflation layers within the boundary region. Overall, they are considerably more precise than wall-function models, and therefore they were selected to perform the simulations in the present thesis, namely the Low-Re k-ε and the Shear Stress Transport (SST) models.

A.3.2. Low-Re k-ε

It has the same features as the wall-function k-ε model, i.e. includes transport equations for two variables commonly employed in the RANS approach: the turbulent kinetic energy (k, or TKE) and the rate of dissipation of kinetic energy (ε). However, it solves the flow in the entire domain. It is more computationally expensive and unstable, thus performing a k-ε simulation first for an initial condition is advisable.

A.3.3. SST

This model combines the k-ε model in the free flow and k-ω near the wall, harnessing the best features of each. Like the k-ω model, the transport equations in the SST model include the TKE and the specific rate of dissipation, called omega (ω). But it does not use wall functions, and like the Low-Re model, it is more expensive in memory usage in exchange of accuracy. To compensate a lack of robustness, it is often advisable to use a first solution from the k-ε or k-ω models as initial condition. This is the main turbulence model employed in the thesis.

A.3.4. Law of the Wall

When defining the treatment near the wall for Low-Re models, y^+ is an essential tool. Conceptually it is a dimensionless distance between the first cell and the wall; thus y_1^+ is the height of the first cell from the wall. As a means to understand its application, the necessity to create a special mesh for the laminar region of the turbulent boundary layer must be explained first.

In any developed internal turbulent flow, velocity profiles do not change relatively much in the axial direction (parallel to the wall). However, velocity profiles change sharply normal to the wall (or radially inside a pipe), especially in the laminar region of the turbulent boundary layer where viscous effects are strong next to the wall, as previously discussed in Chapter 2. Additionally, velocity fluctuations after passing the laminar sublayers represent a considerable percentage of the mean flow velocity, which highly affects when modelling with the RANS approach of turbulence. As a consequence, this section of the turbulent boundary layer must be well represented when computing any turbulent convective flow. The value of y^+ is important because will define these limits within the boundary layer, dividing it in a series of regions or sublayers (see Figure A.7).

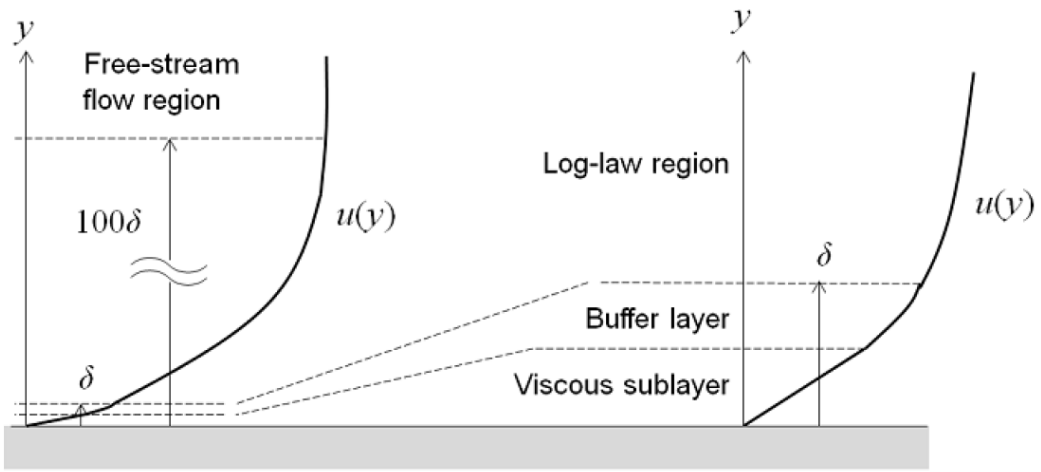

Figure A.7 Boundary layers (adapted from Frei, 2013b)

Considering the boundary layer fully developed, the sublayers are as follow:

a) Laminar or viscous sublayer ($0 < y^+ < 5$): also known as Low-Re region due to the fact that at this small distance from the wall the flow is completely laminar and thus inertial forces are weak related to viscous forces. In this zone, the shear stress is fully laminar (proportional to viscosity), as there are no eddies to interact with the flow. Despite being a thin layer, the velocity gradients are large in this area and thus they affect the performance of the rest of the flow. In that sense, any roughness on the wall would affect this sublayer and therefore the entire flow. A wall is considered rough (not smooth) when the height of these irregularities surpasses the thickness of the viscous sublayer. The higher the value of Re in the mean flow, the thinner the viscous layer, and the more protruding and important the wall roughness becomes. This is why in turbulence regime the friction factor depends highly on the wall roughness.

Because in this region the velocity profile is almost linear as it decreases approaching the wall, $^{du}/_{dy} = {}^{u}/_{y}$, being u the axial flow velocity and y the distance from the wall. Wall shear (τ_w) becomes $\tau_W = \mu \cdot \frac{u}{y}$, or $^{\tau_w}/_{\rho} = \nu \cdot {}^{u}/_{y}$, being ρ the density and ν the kinematic viscosity. Reorganising this equation, the friction velocity (u_*) is produced as equation (A.5).

$$u_* = \sqrt{{}^{\tau_w}/_{\rho}} \tag{A.5}$$

Equation (A.5) provides the formulation of the velocity profile, known as Law of the Wall for the viscous layer, shown in equation (A.6).

$$\frac{u}{u_*} = \frac{y \cdot u_*}{\nu} \tag{A.6}$$

Using dimensionless values is much more convenient, thus $y^+ = \frac{y \cdot u_*}{\nu}$ and $u^+ = \frac{u}{u_*}$ to produce the final form as equation (A.7).

$$y^+ = u^+ \tag{A.7}$$

As explained before, the dimensionless thickness of the viscous layer is no larger than a distance of $y^+ = 5$. As a consequence, $y^+ = 5 = \frac{y \cdot u_*}{\nu}$ and thus the real thickness is set as $y = \frac{5 \cdot \nu}{u_*}$. This means that the thickness of the laminar sublayer is proportional to the fluid viscosity and inversely proportional to the mean flow

velocity. Therefore, the larger the value of Re, the thinner this sublayer and the flatter the velocity profile will be.

b) Buffer sublayer ($5 < y^+ < 30$): viscous effects still dominate, however turbulence increases as this transition sublayer is located further from the wall. Unlike the viscous and the log-law sublayers, there is no accurate velocity profile formulation for this region. Thus, this region must be avoided when defining y_1^+.

c) Log-law sublayer ($y^+ > 30$): also known as overlap, inertial or the high-Re sublayer. Turbulent forces are even more important but still not overcoming the viscous effects. As seen in Chapter 2, in this region the turbulence peaks due to the eddies strongly interacting with the dynamic velocity gradients, and therefore turbulent shear stress also peaks. This region is much wider than the viscous and buffer layers, so if the distance from the wall until the end of the buffer layer is σ, the log-law region will exist until 100·σ. In this zone the average velocity is proportional to the logarithm of the distance to the wall, this formulation being called the logarithmic law, as represented in equation (A.8). The parameters κ and B represent experimental coefficients, set to 0.4 and 5, respectively.

$$u^+ = \frac{1}{\kappa} \cdot \ln y^+ + B \qquad \textbf{(A.8)}$$

d) Outer (or turbulent) sublayer: existing beyond the log-law layer, in the remaining section of the boundary layer towards the centreline. Here, inertial forces completely overcome the weak viscous effects (molecular diffusion), almost

negligible at this distance from the wall. Thus, turbulence and turbulent shear stress decrease back again as the velocity profile is flattened and the gradients disappear. The formulation of the velocity profile for a pipe of internal radius R would be defined as equation (A.9).

$$\frac{u_{max} - u}{u_*} = 2.5 \cdot \ln \frac{R}{R - r} \qquad \textbf{(A.9)}$$

In equation (A.9), u_{max} is the maximum velocity at the core. This is called the velocity defect law, because of the deviation u_{max}-u. As observed, the dimensionless velocity depends only on the distance from the core, and has nothing to do with the fluid viscosity, obviously due to the negligible viscous effects in this point, and the dominance of the eddy diffusivity.

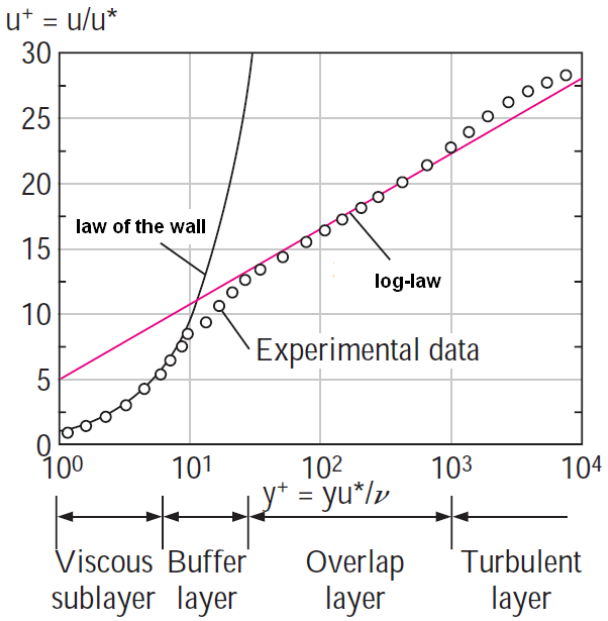

Figure A.8 Boundary layer regions defined by y+ (*Çengel & Cimbala,* 2006b)

In Figure A.8, all the regions described can be seen. The value of y_1^+ employed in the computation will determine if the first cell centre is located near the viscous layer, the buffer layer or the log-law layer. This is critical, because y_1^+ should always be placed away from the buffer layer, which is the transition region and is undefined by any equation and might lead to mistakes. Instead, it is recommended to locate it either in the viscous or in the log-law regions (5 > y_1^+ > 15, approximately).

As described before, controlling the value of y_1^+ will define how much of the real boundary layer is being computationally considered. This is even more important when simultaneously computing convective heat transfer, because y_1^+ will dictate the extent to which the heat diffusivity and the velocity fluctuations occurring within the viscous regions of the boundary layer are being resolved, and ultimately the validity of the heat transfer coefficients (HTCs). It is worth mentioning, that due to the importance of y_1^+, the refinement of the subsequent y^+ within the sublayers under study is crucial to fully capture all the effects.

In simulations of turbulent convective heat transfer, turbulence models will have different requirements for y_1^+ depending on the approach to compute the viscous region of the boundary layer. In wall-function models, the y_1^+ values will be at least 15 as a means to avoid computing in the buffer layer. Thus, the boundary layer mesh will be entirely positioned from the log-law region towards the pipe centre. Compared to grids using smaller values of y_1^+, these models call for coarser meshes, and thus the computing time decreases. It is worth noticing that if using these models the mesh is manually refined near the wall, the value of y_1^+ could decrease from 15 and

fall into the buffer layer, thus damaging the results. Setting an initial y_1^+ in the buffer layer must be avoided at all times. Similarly, selecting a y_1^+ too large ($y^+ > 30$) might locate the first calculation points too far from the wall, missing most of the strong turbulence phenomena within the log-law region and thus inducing errors in the wall-functions. Nevertheless, these results can be used as good initial conditions for non-wall function models if they are applied afterwards.

On the other hand, non-wall function models will need a refined mesh to achieve accuracy in exchange of increased memory resources, and should have a $y_1^+ < 5$ to include the laminar sublayer. That is why they are also called “Low-Re” models, because their y_1^+ values must be located in the viscous sublayer. As a rule of thumb, in turbulent convective heat transfer simulations when using non-wall function models the y_1^+ is normally kept at 1 or below if accuracy is required on the results. As mentioned before, often the number of calculation points in the boundary layer mesh is more important than the y_1^+ itself (at least between 10 and 20 points).

In the present simulations, in addition to the heat source applied on the wall there is always a turbulent flow experiencing large property variations throughout the velocity profile. These property changes are triggered when the flow is approaching the PSC temperature due to the heat applied. This will induce strong wall effects that will modify the viscous regions in the boundary layer. Therefore, solving this region is highly recommended using a Low-Re turbulence model such as the SST, and thus y_1^+ should be located within the viscous layer for better accuracy.

A.4. Solver stage: governing equations

Because the properties of SCW have been defined as a series of piece-wise polynomials dependent on temperature, they rely on the solution for the temperature field and therefore the problem is taken as non-linear. After having selected the relevant physics for the model, the equations extracted from the Comsol code for a steady, incompressible, two-dimensional flow are described here, thus time-dependent terms and dependence of density on pressure are neglected. Vector arrows have been removed for simplicity.

A.4.1. Equations describing a fluid in motion: mass and momentum

- Continuity of mass (mass conservation):

$$\nabla \cdot (\rho u) = 0 \tag{A.10}$$

- Momentum: this is the Navier-Stokes equation using the RANS approach.

$$\rho(u \cdot \nabla)u = \nabla \cdot \left[-pI + (\mu + \mu_T)(\nabla u + (\nabla u)^T) - \frac{2}{3}(\mu + \mu_T)(\nabla \cdot u)I - \frac{2}{3}\rho k 2I\right] + F \tag{A.11}$$

The left hand side (LHS) of equation (A.11) displays the acceleration due to convective effects (advection), while the right hand side (RHS) shows the diffusion effects including the divergence of stress with pressure (p) and viscosity

as well as the effect of body forces (F), gravity in this case. This is the RANS formulation with the use of the Boussinesq assumption described in Chapter 2, therefore contains the eddy viscosity term, μ_T. The identity matrix (I) is often written with the notation δ_{ij}. The volume force vector (F) defines the effect of gravity, as shown in equation (A.12), containing the horizontal and vertical vectors.

$$F = \begin{pmatrix} g_x \\ g_y \end{pmatrix} \quad \textbf{(A.12)}$$

A.4.2. Equations describing heat transfer: conduction and convection

For the conservation of energy, the terms offered by Comsol involving pressure work and viscous heating have been neglected as the pressure drop is always small and the friction energies are also irrelevant compared to the heat source applied on the wall, also because of the viscosity drop near the wall.

- For heat convection in the flow, equation (A.13) couples the fluid flow temperature (T) with the heat flux applied (q) depending on the flow properties.

$$\rho C_p u \cdot \nabla T = -\nabla \cdot q \quad \textbf{(A.13)}$$

- For heat conduction through the solid pipe, the q in equation (A.13) is provided by Fourier's law as shown in equation (A.14), where k is the solid thermal conductivity.

$$q = -k\nabla T \quad \textbf{(A.14)}$$

A.4.3. Equations describing the turbulence model

As discussed in Section A.3.3, the eddy viscosity model SST was adopted for the research. The transport equations for turbulent energy, represented as (A.15) and (A.16), account for the dissipation of kinetic energy occurring during the turbulence phenomenon due to viscous forces. In these equations, the turbulence model parameters μ_T, P, and f_{v1} are calculated using auxiliary equations included within the model, while β_0^*, σ_ω and σ_k are fixed coefficients.

- For the TKE (k):

$$\rho(u \cdot \nabla)k = \nabla[(\mu + \mu_T\sigma_k)\nabla k] + P - \beta_0^*\rho\omega k \quad \textbf{(A.15)}$$

- For the turbulent dissipation rate for energy (ω):

$$\rho(u \cdot \nabla)\omega = \nabla[(\mu + \mu_T\sigma_\omega)\nabla\omega] + \frac{\gamma}{\mu_T}\rho P - \beta\rho\omega^2 + 2(1 - f_{v1})\frac{\sigma_\omega\rho}{\omega}\nabla k \cdot \nabla\omega \quad \textbf{(A.16)}$$

- Heat transport turbulence model (turbulent conductivity): the Prandtl number (Pr) is useful to define the velocity and thermal boundary layers in the laminar region (ratio of laminar diffusion of momentum to heat transfer). Similarly, the turbulent Prandtl number (Pr_T) defines the relation between the additional shear stress $\left(-\overline{u'v'}\right)$ and the heat flux $\left(-\overline{v'T'}\right)$ present in turbulent flow.

$$-(\overline{u'v'}) = \varepsilon_M \frac{\partial \bar{u}}{\partial y} \quad \textbf{(A.17)}$$

$$-\left(\overline{v'T'}\right) = \varepsilon_H \frac{\partial \bar{T}}{\partial y} \quad \textbf{(A.18)}$$

The parameters ε_M in equation (A.17) and ε_H in equation (A.18) represent the turbulent (or eddy) diffusivities of momentum and heat transfer, respectively. Therefore:

$$Pr_T = \frac{\varepsilon_M}{\varepsilon_H} \quad \textbf{(A.19)}$$

These diffusivities cannot be resolved, because contain the fluctuations of turbulence. Thus, in Comsol Pr_T is modelled by using the Kays-Crawford equation, which is a good approximation for most wall-bounded turbulent flows (COMSOL Multiphysics, 2013a).

$$Pr_T = \left(\frac{1}{2Pr_{T\infty}} + \frac{0.3}{\sqrt{Pr_{T\infty}}} \frac{C_p \mu_T}{\lambda} - \left(0.3 \frac{C_p \mu_T}{\lambda}\right)^2 \left(1 - e^{-\lambda / (0.3 C_p \mu_T \sqrt{Pr_{T\infty}})}\right) \right)^{-1} \quad \textbf{(A.20)}$$

In equation (A.20), the value of Pr at infinity is $Pr_{T\infty}$=0.85, λ is the fluid conductivity and C_p is the fluid heat capacity.

A.5. Solver stage: discretisation order and stabilisation methods

A.5.1. Discretisation order

All the mesh elements displayed to define the domain(s) are composed of calculation points on their boundaries, where all the governing equations are solved by using the finite element method (FEM). In every calculation point, one or more unknowns are contained depending on the physics to be solved. In this case, with a heated turbulent flow, the unknowns would be temperature, velocity and pressure as well as the turbulence variables (TKE and ω).

The discretisation order will set the number of calculation points along the element boundaries and in the interior. As an example, a tetrahedral element solving only for temperature (Figure A.9) will display 4 calculation points for a discretisation of first order; however 10 calculation points for a discretisation of second order. Second-order discretisation subdivides the elements into additional calculation points which, although not visible in the mesh interface, replace interpolation polynomials between the initial nodules, therefore increasing accuracy in expense of computational time.

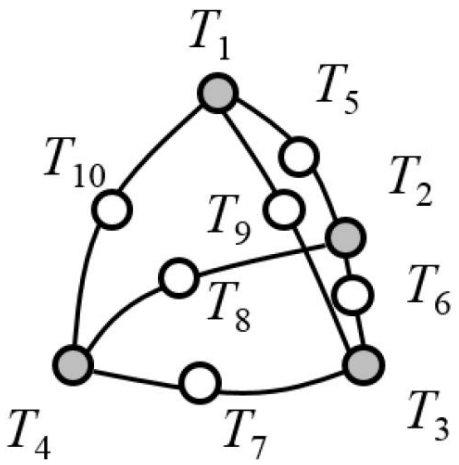

Figure A.9 Tetrahedral element with first (grey) and second (white) discretisation order (adapted from Frei, 2014)

Within the CHT module, Comsol splits the discretisation order tool in fluids (calculation points for velocity and pressure) and temperature. For a global first-order discretisation, Comsol will display the option “P1+P1” for the fluid (namely, first order for velocity + first order for pressure) and temperature will have a “linear” description. However, for second order discretisation, only “P2+P1” is available (still first order for pressure) while temperature will be described as “quadratic”. Due to computational limitations, first-order discretisation was normally selected over second-order, although some computations were made using second-order for the sake of observing differences.

A.5.2. Stabilisation methods

Numerical methods such as the FEM need stabilisation techniques when using transport models controlled by convection rather than diffusion, because otherwise oscillations appear and robustness is at risk. These instabilities are triggered when

the Péclet number (ratio of convective to diffusive effects) becomes higher than 1, which happens in large convective or small diffusive simulations.

$$Pe = \frac{\|\beta\| h}{2c} > 1 \quad \textbf{(A.21)}$$

In equation (A.21), β is the convective velocity, h is the mesh element size and c is a diffusive coefficient. As can be observed, also the mesh refinement affects the Péclet number, and thus coarse meshes will have a higher Péclet number (producing instabilities) while refined meshes will be more stabilised, at the expense of increasing computational time.

In order to stabilise a convection-driven system such as heat transfer or fluid flow without significantly increasing computational time, a certain quantity of artificial diffusion is always added by default as a stabilisation method to decrease the Péclet number. This can be achieved in two manners:

- Inconsistent stabilisation (isotropic diffusion): the artificial diffusion coefficient is adjustable and applies in all directions. Regardless of how close the computation is approaching the exact solution, the additional diffusion never changes. As previously explained, the artificial diffusion also depends on the mesh element size. As a consequence, finer meshes will require less artificial diffusion to produce a good solution despite consuming much computational resource. On the other hand, coarser meshes will converge much faster by applying more artificial diffusion, but the physical meaning will be distorted.

- Consistent stabilisation: as the simulation approaches the exact solution, the artificial diffusion is decreased. Thus, if the mesh is fine enough, there will be almost no artificial diffusion added. All heat transfer and fluid flow apply this technique by default, using two kinds of diffusions combined:

  - ❖ Streamline diffusion: artificial diffusion is added in the streamline direction, eliminating amplifying oscillations.
  - ❖ Crosswind diffusion: when sharp local gradients appear, this can lead to local instabilities (over and undershoots, i.e. values above and below the bounded solution, respectively). This diffusion applies cross-directionally and includes discontinuities, avoiding over and undershoots.

  This stabilisation is better than the inconsistent method, because it allows obtaining reasonably accurate solutions in less computational time. When modelling fluid flow, the NS equations are always unstable when using first order discretisation for both velocity and pressure (P1+P1) regardless of the Péclet number. Thus, consistent stabilisation is always activated. Only when the velocity discretisation order is higher than the pressure order (P2+P1 or P3+P2) the Péclet number will be small enough to make the stabilisation unnecessary.

A.6. Solver stage: computation

The code compiles all the gathered input data to assemble a non-linear system of coupled equations defining the model. Algorithms are applied to linearise the non-linear system into a square matrix, whose size is called degrees of freedom (DOF) and depends on the number of mesh elements, the discretisation order selected for the physics, and the total number of variables to be solved. The matrix sparsity-density (how full of zeros it is) is determined by factors like the elements shape or the existence of couplings between nodes. It is the matrix size (DOF) along with its sparsity what determines the computational cost of the simulation. Because the turbulence model employed does not apply wall-functions, the solver scheme needs to be split in a two-step process. In the first step, a wall-distance equation is performed for wall treatment. The second step computes the solution at steady state conditions, because a boiler devotes most of the operational time in this mode as a means to be efficient.

A.6.1. Step one: Wall distance initialisation (WDI)

The code computes the distance to the wall for every mesh element because of the wall-bounded nature of the turbulence. The protocol is as follows:

- Wall distance equations are compiled.
- Dependent variables to the former equations are addressed.
- Solver stage at stationary conditions: depending on the number of DOF, a direct or iterative solver will be employed to linearise the non-linear equation system.

Due to the relative simplicity of this step, a fully coupled approach is selected to solve the linear equations. A damped version (modified to avoid instabilities in the iteration process) of the Newton-Raphson iteration method is used to solve the non-linear system, as seen in Figure A.10.

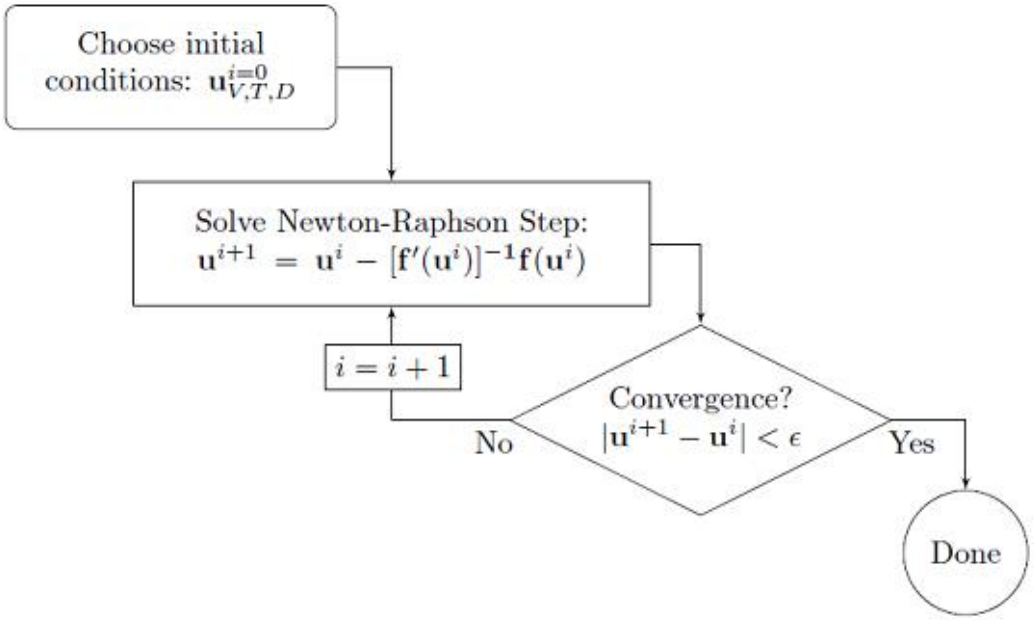

Figure A.10 Fully coupled solver approach for the WDI (Frei, 2013a)

- In this sub-step, the convergence criterion (relative tolerance) is automatically set to $1x10^{-3}$, however for academic purposes it is advisable to reduce it to $1x10^{-6}$.
- Solution is stored as it will be used in the next step.

A.6.2. Step two: Stationary solver

Once the wall distance is calculated for every mesh element, the main simulation is performed in the next step, following a similar protocol.

- All the governing and additional equations are compiled.

- All the dependent variables to the CHT are accounted for.
- Solver stage at stationary conditions: a direct solver will be always preferred over an iterative regardless of the number of DOF, due to the complexity of the system. The equations will not be fully coupled but segregated instead, as a means to divide the solution procedure in sub-steps, each of them using the damped version of the Newton-Raphson iteration method, as seen in Figure A.11.

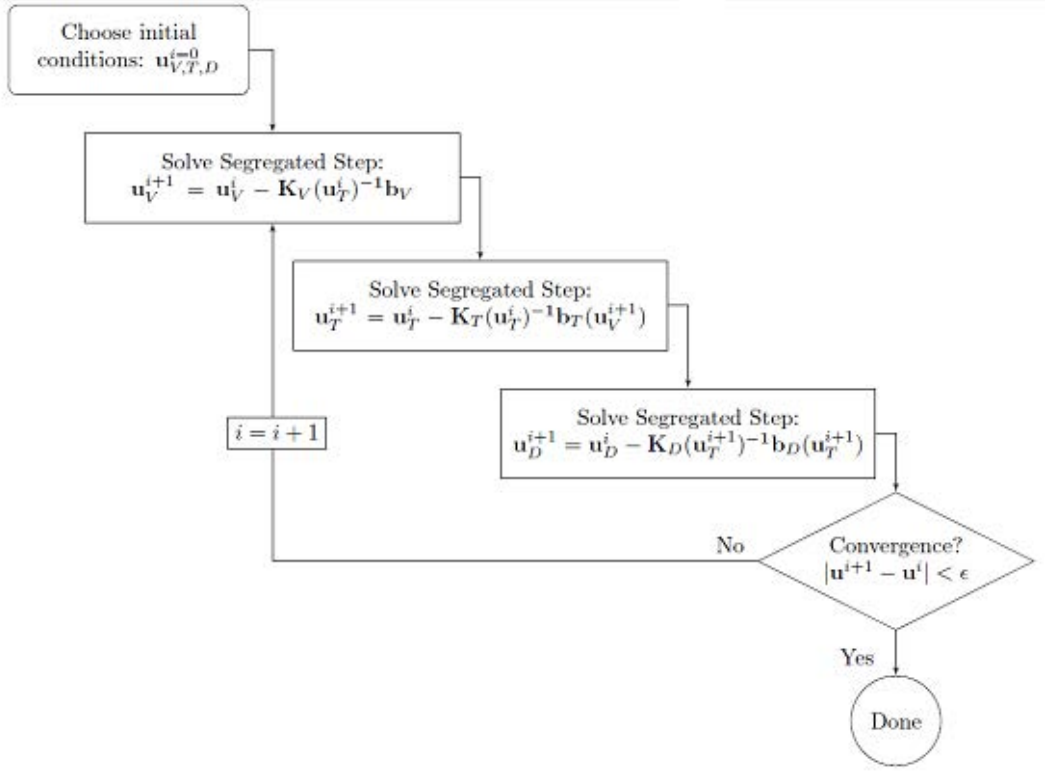

Figure A.11 Segregated approach for the stationary solver (Frei, 2013a)

- The segregated groups can be customised, and thus the following configuration was selected for the present thesis:

  - ❖ Segregated group 1: velocity, pressure and temperature variables.
  - ❖ Segregated group 2: TKE.

- ❖ Segregated group 3: ω.

- Because it is an incompressible flow, the equation for pressure is not independent and thus the solver will apply the SIMPLE scheme (Semi-Implicit Method for Pressure Linked Equations) to couple velocity and pressure (Tu *et al.,* 2008), as can be seen in Figure A.12.

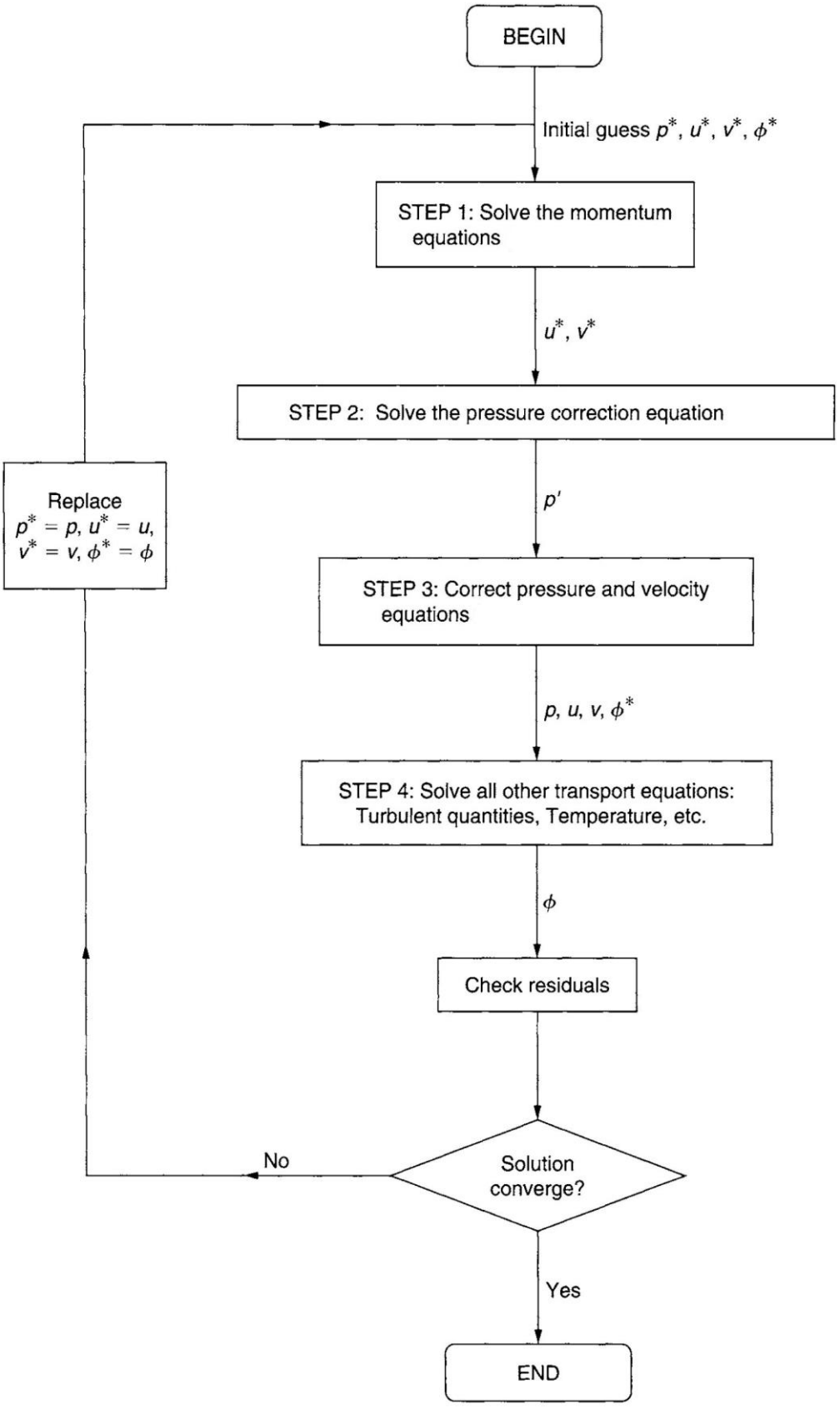

Figure A.12 SIMPLE scheme to solve incompressible systems (adapted from Tu *et al.*, 2008)

- Three different direct solver nodules were created for every segregated group, as can be seen in Figure A.13b. Within each segregated group, the damping factor was reduced to deal with the convergence complexities, and the termination technique was set as iterations or tolerance. The convergence criterion, as in the previous step, was decreased to $1x10^{-6}$.

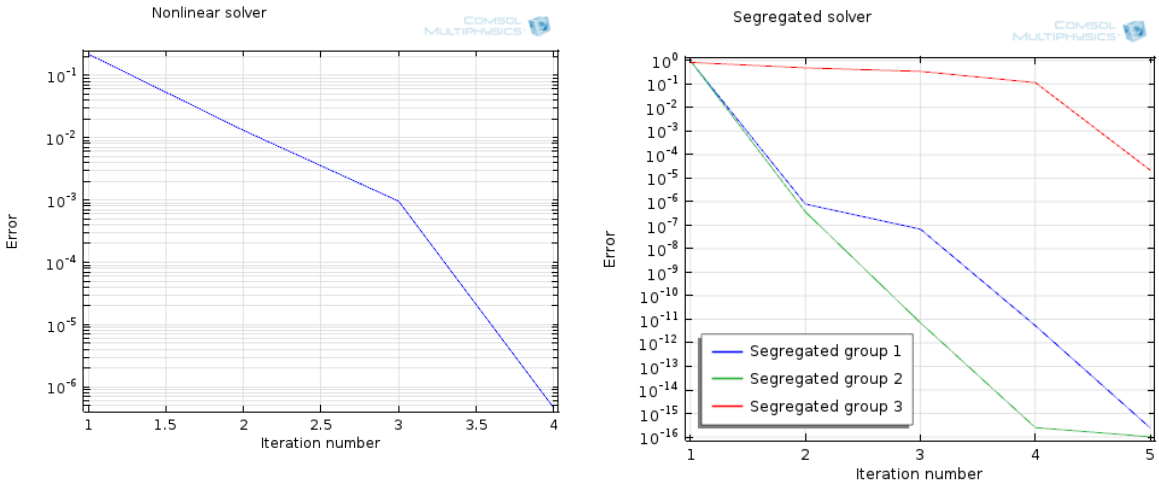

(a) (b)

Figure A.13 Convergence plots for the fully coupled (a) and segregated (b) approach (Frei, 2013a)

- The results in this step are transferred to the post-processing stage (results node).

A.6.3. Direct or iterative solvers

Once the sparse matrix containing the linearised equations is formed and the solver procedure in the two previous steps is established, the iterations can be solved using direct or iterative solvers.

- Direct solvers: these are stable, robust solvers that take in exchange longer computational times. It is worth noting that when the DOF increase the scaling of computational resources and time will be almost quadratic (Frei, 2014). Although they require high demand on memory and time, they are preferred for multi-physics problems employing small-sized 2D and 3D models due to their stability. There are four direct solvers available in Comsol and all will achieve the same solution; however the difference is the solver speed. PARDISO is the fastest, however demands the highest memory while SPOOLES is the slowest and least memory consuming. Additionally, the MUMPS solver allows cluster computing, i.e. employ several computers to provide more memory for the simulation.
- Iterative solvers: these solvers do not require as much memory and time as the direct solvers to solve the same problems, however they are more sensitive to instabilities in exchange. Therefore, they need appropriate adjustment, otherwise the simulation will take longer or the convergence will oscillate. In this case, the scaling for memory and time when increasing the DOF is linear (Frei, 2014). They are preferred for large models employing single physics as the matrices produced will be simple. Iterative solvers approach a gradual solution, instead of solving the iterations in large steps as direct solvers do (one plot). Thus, the error estimated can be monitored every iteration using two plots.

Choosing between direct or iterative solvers depends on the computational resources and the physics that are being simulated (Marra, 2013). In the present thesis, because of the relatively simple geometries and the model sizes, and because of the

multi-physics model having to solve turbulent flow and heat transfer at the same time, the direct solver PARDISO was employed.

A.6.4. Ramping the heat source

The equations employed by the turbulence models are highly nonlinear. When dealing with turbulent convective equations, a very good practice is ramping the heat source, which actually reduces viscosity stepwise and therefore stabilises the RANS equations in the turbulence model (Straccia, 2016)

When using ramping with a heat source, the procedure starts with an isothermal simulation and higher values of viscosity, thus stabilising convergence. Afterwards, the solutions obtained will be used as initial conditions for the next simulation where the heat source will be applied for the first time, and so forth while progressively increasing the magnitude of the heat source. Other ways to achieve a stable convergence involve applying ramping to any parameter that would initially decrease turbulence, such as inlet velocity, the viscosity itself, or buoyant forces if these are relevant.

Ramping can be automatised with an auxiliary sweep tool applied on the stationary step, by setting a ramping coefficient for the heat source that overrides every new simulation with the new value while using the previous simulation as initial condition. However, given the high instabilities of the study when approaching the PSC transition, a manual control was preferred as any convergence error would stop the sweep process.

In this case, the solver sub-step where the dependent variables to the wall distance equations are listed becomes user-defined after the first simulation in the “Initial Values of Variables Solved For” section (IVVSF) and the “Values of Variables Not Solved For” section (VVNSF). Thus, both of them will be set to use the solutions obtained from the previous simulation in order to facilitate the new calculation. The first section (IVVSF) is meant for the variables listed in that precise sub-step. The second one (VVNSF) is used in multi-physics computations between interconnected steps, with many variables solved in a sequential approach, so not all are listed as dependent variables.

A.7. Post-processing

A.7.1. Data sets (storage of solutions)

When the convergence criterion is reached in a computation, all the information produced is transferred to the results nodule and stored within the data sets sub-nodule. From this nodule, all the solutions previously obtained can be accessed and used as reference when trying to plot variables. Additionally, desired regions of the computed domains can be targeted using a "cut-tool" in order to focus the results, for instance:

- 1D: cut points.
- 2D: cut points, cut lines.
- 3D: cut points, cut lines, cut planes.

A.7.2. Plot groups

By right-clicking on the results node, and depending on the dimensions of the model, plot groups can be created to display all the parameters Comsol can offer. For instance, with a solved 3D model, 3D, 2D or 1D plot groups can be obtained and inside them more plotting options are available, such as contours, streamlines or arrow lines. 3D plot groups can display the cut planes defined in the data sets and slices, 2D plot groups can show surfaces, and 1D plot groups display line graphs (for cut lines) and point graphs (for cut points).

A.7.3. Checking the quality of the turbulence model in the wall

In convective heat transfer systems, the near-wall results need to be analysed as well when the computation is finished. For non-wall-function turbulence models, Comsol produces by default with the solution a parameter named *dimensionless distance to cell centre,* which should have a value of order one everywhere, preferably below 0.5 or otherwise the mesh must be refined here.

In the present thesis, another procedure was followed in order to verify the performance near the wall. The obtained radial profiles of y^+ were observed along the pipe (as these values rely on the local velocity profiles); and thus compared to the theoretical value of y_1^+ initially desired and established as a means to ensure they are not excessively different. Non wall-function models should locate y_1^+ in the viscous region in order to obtain accurate results.

References

Çengel YA, Cimbala JM (2006a). Flow in pipes. In: Çengel,Yunus A. Fluid Mechanics. Fundamentals and applications. *McGraw-Hill*; pp. 321-98

Çengel YA, Cimbala JM (2006b). Introduction to computational fluid dynamics. In: Çengel, Yunus A. Fluid Mechanics. Fundamentals and applications. *McGraw-Hill*; pp. 817-84

Comsol Multiphysics (2013a). CFD module user's guide (version 4.3b), Stockholm, Sweden, COMSOL AB

Comsol Multiphysics (2013b). Flow through a pipe elbow. (version 4.4), Stockholm, Sweden, COMSOL AB

Comsol Multiphysics (2013c). Reference manual (version 4.4), Stockholm, Sweden, COMSOL AB

Comsol Multiphysics, (2013d). Turbulent flow over a backward facing step (version 4.4), Stockholm, Sweden, COMSOL AB

Huilin F, Zhengchun C, Xiaozhong Y, Jinqiao H, Yucai Z (2013). Failure Analysis of 600 MW Supercritical Boiler Water Wall. *Research Journal of Applied Sciences, Engineering and Technology*; 6: 1726-31

Podila K, Rao YF (2015). CFD analysis of flow and heat transfer in Canadian supercritical water reactor bundle. *Annals of Nuclear Energy;* 75: 1-10

Tu J, Yeoh GH, Liu C (2008). Computational fluid dynamics. A practical approach. In: Butterworth-Heinemann (editor). *Elsevier*

Zima W, Grądziel S, Cebula A (2010). Modelling of heat and flow phenomena occurring in waterwall tubes of boilers for supercritical steam parameters. *Archives of thermodynamics*; 31: 19-36

Websites

Frei W (2013a). Improving convergence of multiphysics problems. In: *Comsol blog* (https://www.comsol.com/blogs/improving-convergence-multiphysics-problems/)

Frei W (2013b). Which Turbulence Model Should I Choose for My CFD Application? In: *Comsol blog* (https://www.comsol.com/blogs/which-turbulence-model-should-choose-cfd-application/)

Frei W (2014). How much memory is needed to solve large Comsol models. In: *Comsol blog* (https://www.comsol.com/blogs/much-memory-needed-solve-large-comsol-models/)

Marra V (2013). On solvers: multigrid methods. In: *Comsol blog* (https://www.comsol.com/blogs/on-solvers-multigrid-methods/)

Straccia A (2016). Viscosity ramping improves the convergence of CFD models. In: *Comsol blog* (https://www.comsol.com/blogs/viscosity-ramping-improves-the-convergence-of-cfd-models/)